

Center for Radiological Research – 630 W. 168th St., New York, NY 10032 –
crr.columbia.edu

CENTER FOR RADIOLOGICAL RESEARCH ANNUAL REPORT 2017



DAVID J. BRENNER
Director

SALLY A. AMUNDSON
and
HOWARD B. LIEBERMAN
Co-Editors



COLUMBIA UNIVERSITY
College of Physicians and Surgeons



Table of Contents

CONTENTS.....	1
COLLABORATING DEPARTMENTS AND INSTITUTIONS	4
ACKNOWLEDGEMENT OF SUPPORT.....	5
WEBSITES	5
INTRODUCTION – RARAF, 50 YEARS ON	6
STAFF NEWS	7
LABORATORY COLLOQUIA AND SEMINARS	8
FACULTY AND STAFF.....	9
FACULTY AND STAFF PHOTO.....	10
RESEARCH REPORTS	
<u>ION BEAM DEVELOPMENT</u>	
Super Microbeam at RARAF	
Andrew Harken, Veljko Grilj, Guy Garty, Gerhard Randers-Pehrson, and David J. Brenner	12
Microbeam at a Distance: Remote Control and Operations at the RARAF Microbeam	
Andrew D. Harken, Alejandro Carabe-Fernandez, Consuelo Guardiola, and Gerhard Randers-Pehrson	13
DREEBIT Heavy Ion Source at RARAF	
Christian Siebenwirth, Andrew D. Harken, Gerhard Randers-Pehrson, and David J. Brenner.....	15
Ultrahigh Dose-rate Ion Beam Irradiations	
Veljko Grilj, Manuela Buonanno, Brian Ponnaiya, and David J. Brenner	18
High LET Ion Beam Dosimetry with Unlaminated Radiochromic Films	
Veljko Grilj and David J. Brenner	20
Design Study of a Heavy Ion Particle Accelerator	
Malek Haj Tahar, David J. Brenner, and Gerhard Randers-Pehrson.....	22
Simultaneous Detection of Multiple Reactive Species	
Guy Garty and David J. Brenner.....	24
<u>FAR-UVC STUDIES</u>	
222-nm Light Prevents MRSA Infection of Superficial Wounds <i>in vivo</i>	
Brian Ponnaiya, Manuela Buonanno, David Welch, Igor Shuryak, Gerhard Randers-Pehrson, and David J. Brenner.....	28
Quantification of Killing MRSA with Far-UVC Light Using an Optical Diffuser	
David Welch, Manuela Buonanno, Igor Shuryak, Gerhard Randers-Pehrson, Henry M. Spotnitz, and David J. Brenner.....	30
Efficacy of Far-UVC for Inactivation of Aerosolized Influenza Virus	
David Welch, Manuela Buonanno, Veljko Grilj, Igor Shuryak, Connor Crickmore, Alan W. Bigelow, Gerhard Randers-Pehrson, Gary W. Johnson, and David J. Brenner.....	32
<u>CELLULAR AND MOLECULAR STUDIES</u>	
Cytokine Storm in Human Glioblastoma Cells after Combined Treatment with Gamma-irradiation, ATM Inhibitor and Cannabidiol	
Vladimir N. Ivanov, Jinhua Wu, and Tom K. Hei.....	36

X-ray Irradiation has a Strong Effect on Human HSC and Progenitor Populations Engrafted in the Immunodeficient Mouse	
Monica Pujol Canadell and Lubomir Smilenov.....	39
MEK Downregulation Sensitizes Human Prostate Cancer Cells to Etoposide Treatment	
Constantinos G. Broustas, Axel J. Duval, and Howard B. Lieberman.....	42
RAD9 Silencing Impairs Anchorage-independent Growth through the Suppression of AGR2	
Constantinos G. Broustas, Kevin M. Hopkins, Li Wang, Sunil K. Panigrahi, and Howard B. Lieberman	44
NBS1 and H2AX Complement Each Other in the DNA Damage Response	
Yuan-Cho Lee, Junjie Chen, and Jingsong Yuan	46
Mitochondrial Fission Protein DRP1 Regulates Tumor Immunogenicity through PD-L1 Expression	
Jinhua Wu and Tom K. Hei	52
<u>POPULATION AND CLINICAL STUDIES</u>	
A Dose Dependence of Accelerated Repopulation in Head and Neck Cancer: Supporting Evidence and Clinical Implications	
Igor Shuryak, Eric J. Hall, and David J. Brenner	56
Association between Non-melanoma and Melanoma Skin Cancer Rates, Vitamin D and Latitude	
Miguel Rivas, Elisa Rojas, and Gloria M. Calaf.....	58
Edith Quimby; A Pioneer in Nuclear Medicine as well as Medical Physics	
Eric J. Hall, David J. Brenner, and Sally A. Amundson.....	65
Guidelines for Moderate Hypofractionation in Prostate Cancer Radiotherapy	
David J. Brenner and Eric J. Hall	68
<u>RADIATION BIOSIMETRY</u>	
VADER: a Variable Dose rate External irradiator for Internal Emitter and Low Dose Rate Studies	
Guy Garty, Yanping Xu, Lubomir Smilenov, Gary Johnson, and David J. Brenner	72
RABiT-II: Development of Accelerated High-throughput Micronucleus Biodosimetry Assay	
Mikhail Repin, Sergey Pampou, Charles Karan, David J. Brenner, and Guy Garty	74
Chromosomal DNA Damage in Human Lymphocytes from Humanized Mice Exposed to Neutrons and X rays	
Helen C. Turner, Qi Wang, Younghyun Lee, Igor Shuryak, Monica Pujol Canadell, Jay R. Perrier, Lubomir B. Smilenov, Andrew Harken, Brian Ponnaiya, Guy Garty, and David J. Brenner	76
Combination of Imaging Flow Cytometry with High-throughput Automated Robotic Systems for Cytokinesis-block Micronucleus Assay	
Qi Wang, Mikhail Repin, Matthew Rodrigues, Sergey Pampou, Jay Perrier, Lindsay A. Beaton-Green, Ruth C. Wilkins, David J. Brenner, and Helen C. Turner.....	78
In Vivo Blood Cell Sub-type Changes after Irradiation via Deconvolution of the Gene Expression Response using CIBERSORT	
Shanaz A. Ghandhi, Shad R. Morton, Nils Rudqvist, and Sally A. Amundson.....	80
Protein Markers for Radiation Exposure in in-vivo Irradiated Humanized Mouse Model	
Younghyun Lee, Monica Pujol Canadell, Igor Shuryak, Jay R. Perrier, Purvi Patel, Antonius Koller, Lubomir B. Smilenov, David J. Brenner, Emily I. Chen, and Helen C. Turner.....	82
RABiT-II DCA: Optimization of the Fluorescent-based Dicentric Chromosome Assay for High-throughput Radiation Biodosimetry	
Ekaterina Royba, Mikhail Repin, Sergey Pampou, Charles Karan, David J. Brenner, and Guy Garty.....	85
Assessment of Mouse Pulmonary Function through Whole-body Plethysmography for the Study of Radiation-induced Late Pulmonary Injury	
Sanjay Mukherjee, Lubomir Smilenov, Evangelia C. Laiakis, Albert J. Fornace, and Sally A. Amundson	88

Comparison of Radiation Biodosimetry Studies Based on Microarray Analyses from the Transcriptomics Group of the Columbia CMCR
 Shad R. Morton, Shanaz A. Ghandhi, and Sally A. Amundson 90

Identification of Differentially Expressed Genes and Pathways in Mice Exposed to Mixed Field Neutron/X-ray Radiation
 Constantinos G. Broustas, Andrew D. Harken, Guy Garty, and Sally A. Amundson 93

The Influence of Inflammation on Transcriptomic Signatures of Radiation Exposure: Mouse Model of Inflammatory Bowel Syndrome
 Sanjay Mukherjee, Evangelia C. Laiakis, Albert J. Fornace, and Sally A. Amundson 96

THE RADIOLOGICAL RESEARCH ACCELERATOR FACILITY – an NIH-Supported Resource Center
 Dir., David J. Brenner, PhD, DSc; Assoc. Dir. Guy Garty, PhD

Research using RARAF 100

Development of Facilities 102

Singletron Utilization and Operation 105

Training 106

Dissemination 106

Personnel 107

PUBLICATIONS 110

Collaborating Departments and Institutions

Individuals from the following departments and institutions collaborated with the Center's faculty and staff in the research reports included in this year's publication (for individual attributions see specific reports):

Collaborating Columbia University Departments:

- Department of Surgery
- Genome Center High Throughput Screening Facility
- Proteomics Shared Resource, Herbert Irving Comprehensive Cancer Center

Collaborating Institutions:

- Consumer and Clinical Radiation Protection Bureau, Health Canada, Ottawa, ON, Canada
- Department of Biochemistry and Molecular and Cellular Biology, Georgetown University, Washington, DC
- Department of Experimental Radiation Oncology, University of Texas, MD Anderson Cancer Center, Houston, TX
- Department of Radiation Oncology, University of Pennsylvania
- Department of Physics, Faculty of Science, Tarapaca University, Arica, Chile
- Instituto de Alta Investigación, Universidad de Tarapacá, Arica, Chile
- MilliporeSigma, Seattle, WA
- St. Edmund Hall, Oxford University, Oxford, UK ■



Top (l to r): Tom Hei, Cheng-Shie Wu, Guy Garty, David Brenner, Gary Johnson, and Lubo Smilenov assemble the VADER. Bottom (l to r): David Brenner, Eric Hall, Hirohiko Tsujii, Tom Hei. Tom Hei (center) receives an honorary D.Sc. from Amity University in India.

Acknowledgement of Support

In 2017 the Center for Radiological Research was supported by competitively awarded grants from the following agencies:

- Department of Defense
 - Defense Threat Reduction Agency
- Department of Energy
 - Office of Science, Office of Biological and Environmental Research [Low Dose Radiation Research Program]
- Department of Health and Human Services
 - Biomedical Advanced Research and Development Authority
 - National Institutes of Health:
 - National Cancer Institute
- National Institute of Biomedical Imaging and Bio-engineering (P41)
- National Institute of Allergy and Infectious Disease (U19)
- National Institute of Environmental Health and Safety (R01s and R21)
- National Institute of General Medical Sciences (R01)
- National Aeronautics and Space Administration

Websites

- Center for Radiological Research.....<http://www.cumc.columbia.edu/crr/>
- Radiological Research Accelerator Facility.....<http://www.raraf.org>
- Center for High-Throughput Minimally-Invasive Radiation Biodosimetry.....<http://cmcr.columbia.edu>
- Department of Radiation Oncology.....<http://www.cumc.columbia.edu/dept/radoncology>
- CRR Annual Reports (1999-present)..... <http://crr.columbia.edu/events/annual-reports>

It is with great sadness that we note the passing of two of our own.



Lance Redford (left), our Director of Development since 2015, died in November of 2017 after a prolonged illness. He guided us through the early days of forming our development Advisory Board, and helped us to learn how to work with them for the best benefit of the center. Despite his frequent assertion that he was not an event planner, he flawlessly organized several events for us, including the major event celebrating our center’s centennial. We miss his friendliness, warmth, and inimitable laughter.

In early 2018, we also learned of the sudden death of Yanping Xu (right). Yanping joined the RARAF team as a post-doc in 2007, and spearheaded the development of both the world’s first neutron microbeam and our improvised nuclear device (IND) spectrum neutron irradiator. He left the lab in 2016 for a tenure track assistant professor position at East Carolina University, where he was embarking on an exciting and promising career. We miss him as both friend and colleague.



RARAF, 50 Years On

In 2017 we celebrated the 50th anniversary of our Radiological Research Accelerator Facility (RARAF). When RARAF was commissioned, much of radiobiological thinking and research was focused on neutrons, and so the original RARAF concept was as a source of monoenergetic neutrons with energies ranging from 200 keV to 14 MeV. RARAF moved to Columbia Nevis Labs in 1980. At that time there was increasing interest in the development of single charged-particle microbeams, and over the next 4 decades RARAF has become a world center for charged particle microbeam radiobiology. We started with a beam of a few microns, the size of a cell nucleus, and we have used different technologies to develop smaller and smaller beams, which we can deliver faster and faster. We have hosted three International Microbeam Symposia, as well as instituting an Annual Microbeam Training Course, and microbeam radiobiology is now a well-established and productive research area.

We always knew we were pushing against Mother Nature. As our microbeams became smaller and smaller, their diameter has now become comparable to the range of the delta ray penumbra ejected by our charged particles. The physics tells us that we really can't go too much smaller than our current ~100 nanometers.

So while our microbeam facilities will remain for researchers to use, we have started to develop a third major application of RARAF – as a tool for pre-clinical

studies to answer key questions underlying Heavy-Ion Radiation Therapy (HIRT). There is strong interest in the introduction of HIRT to the U.S., largely based on the experience of carbon-ion radiotherapy in Japan and Germany, where very encouraging survival rates have been reported for a number of hard-to-treat cancers such as pancreas, rectum and sarcomas. Just as an example, 2-year survival of 50 to 65% has been reported after combined carbon-ion and chemotherapy for locally-advanced pancreatic cancer, remarkably encouraging at a post-treatment time when survival is dominated by distant metastases.

So there has been much discussion that, as well as producing local effects to the tumor, HIRT may also be inducing long-range systemic anti-cancer effects. However, the underlying mechanisms for such high-LET-induced long-range systemic effects are not understood and there is evidence that the classic radiobiological phenomena underlying the efficacy of conventional x-ray radiotherapy, while still potentially relevant for local tumor control, are not the dominant phenomena driving the potential systemic efficacy of HIRT. Rather the data suggest different high-LET-induced mechanisms underlying radiation-induced long-range anti-cancer effects – and what is not known is the LET dependence of these long-range effects – and that is what we want to find out at RARAF.

-David Brenner ■



A Director's eye view of the open Singletron accelerator.

Staff News

Dr. David Brenner gave a talk on the use of far UV-C to combat the spread of superbugs in a session entitled “Bugs and Bodies” at the TED2017 conference (“The Future You”), in Vancouver, British Columbia. He continued to serve as a member of the National Academy of Sciences Nuclear and Radiation Studies Board. He is also a member of the New York City Radiological Advisory Committee, and continues to serve as an Associate Editor of the journal *Radiation and Environmental Biophysics*.

Dr. Tom Hei received the Distinguished Alumni Award for Professional Achievement from his alma mater, the University of Wisconsin-Whitewater and an honorary Doctor of Science (D.Sc.) degree for his contributions to radiological and environmental sciences from the Amity University in India. Dr. Hei holds an Adjunct Professorship at the Chinese Academy of Sciences and a Chair Professorship at the Soochow University. He serves as Editor in Chief of *Life Sciences in Space Research*, and as an Associate Editor of the *Journal of Radiation Research* and of *Translational Cancer Research*. He served as an external reviewer for the Hiroshima University Phoenix Education Program as well as the Helmholtz Center program. Dr. Hei serves as a member of the NIH Cancer Etiology Study Section and as the vice-chair of the Radiation Research Foundation.

Dr. Howard B. Lieberman was a member of the Israel Cancer Research Fund Scientific Advisory Board. He continued to serve as Associate Editor for the *Journal of Cellular Physiology*. In addition, he has been appointed Senior Editor for the journal *Radiation Research*. He also served as an invited Guest Editor for a special issue of the *International Journal of Radiation Biology*.

Dr. Sally Amundson continued to serve on the Scientific Committee of MELODI, the European Union low dose radiation program, and the EPA Science Advisory Board. She also continued as a member of NCRP and as an Associate Editor of *Radiation Research*. She returned to the Radiation Effects Research Foundation (RERF) Science Advisory Council in 2017 as a Special Advisor.

Dr. Eric Hall was the guest lecturer at the Annual meeting of the American Society of Nuclear Medicine and Molecular Imaging. He discussed the pioneering work in Nuclear Medicine carried out by Dr. Edith Quimby, who was on the faculty of our Center from 1919 to 1978. He also received the Lifetime Achievement Award by Marquis Who’s Who in America.

Dr. Guy Garty was named the Associate Director of RARAF.

During the year, Igor Shuryak was promoted to Assistant Professor at CUMC, David Welch was promoted to Associate Research Scientist, and Margaret German was promoted to Administrative Assistant.

Postdocs Malek Haj Tahar, Christian Siebenwirth, and Qi Wang joined the Center in 2017, as did graduate student Sofia Barbieri.

Mr. Haseeb Durrani also left the center in 2017. ■



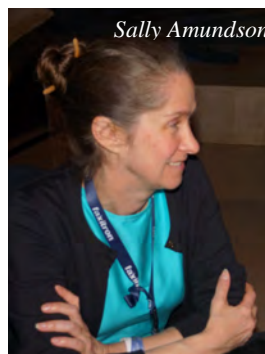
David Brenner
Photo: Bret Hartman / TED reproduced under Creative Commons License CC BY-NC 2.0



Tom Hei



Howard Lieberman



Sally Amundson



Guy Garty

Laboratory Colloquia and Seminars

Periodically, the Center organizes morning-long colloquium sessions featuring presentations of recent work by Center researchers and guest speakers. These colloquia are attended by Center professional and technical staff and graduate students, as well as by physicians and scientists from other departments at CUMC. They serve as a forum for discussions and forging future collaborations. The 2017 Colloquium Series was organized and coordinated by Dr. Lubomir Smilenov.

March Colloquium:

- Dr. Helen Turner, Center for Radiological Research: “Mind Map for High-throughput Biodosimetry.”
- Dr. Howard B. Lieberman, Center for Radiological Research: “Targeting RAD9 Signaling for Precision Prostate Cancer Diagnosis and Therapy.”
- Dr. John Ng, Dept. of Radiation Oncology, Weill Cornell Medical Center, New York, NY: “High LET Charged Particle Irradiation Leads to Increased Expression of In Vitro Markers of Immunogenic Cell Death.”

June Colloquium:

- Dr. Erik Young, Dept. of Mechanical Engineering, Columbia University: “smFET-CMOS Arrays for Single-molecule Bioelectronics.”
- Dr. David Welch, RARAF: “Anatomically Accurate Mouse Phantoms.”
- Dr. Carol Johnstone, Fermi National Accelerator Laboratory: “Innovations and Progress on Ion Therapy in the US.”

In addition to our colloquium series, the CRR also participated in the research retreat of our parent department, Radiation Oncology, in October:

- Dr. Lee Goldman, Dean of P&S: “A 250th Birthday for P&S and the Future of Academic Medicine.”
- Dr. Eileen Connolly, Radiation Oncology
- Dr. Christine Chen, Radiation Oncology: “Impact of pembrolizumab and high dose radiation on the tumor micro- environment in treatment naïve TNBC.”

- Dr. Simon Cheng, Radiation Oncology: “Therapeutic resistance pathways in lung cancer.”
- Dr. Fred Wu, Radiation Oncology: “Focused ultrasound-mediated BBB-opening and brain tumors.”
- Dr. Constantinos Broustas, CRR: “Targeting MEK5 sensitizes prostate cancer cells to genotoxic stress.”
- Dr. Sandra DeMaria, Dept. of Radiation Oncology, Weill Cornell Medical Center, New York, NY: “Novel insights into the interaction of radiotherapy with immunotherapy.”
- Dr. Katherine Spina, Radiation Oncology: “Prognostic implications of hematologic response to chemoradiation therapy in glioblastoma.”
- Dr. David Brenner, CRR: “Do we know whether the immune system plays a significant role in Radiation Oncology?”
- Dr. Gloria Su, Dept. of Surgery: “Genetic and environmental influences on pancreatic tumorigenesis.”
- Dr. Raúl Rabadán, Dept. of Systems Biology: “Medical Bioinformatics and Precision Medicine.”
- Dr. Lawrence Schwartz, Dept. of Radiology: “Radiomics in the Practice of Radiology.”
- Dr. Guy Garty, CRR: “RABIT-II: Using commercial robotic platforms for high throughput screening.”
- Dr. Andy Xu: “Superparamagnetic nanoparticles in ultra-low field magnetic resonance imaging and magnetic hyperthermia.”
- Dr. Yi-Fang Wang, Radiation Oncology: “Dosimetric Verification and Commissioning for A Small Animal Radiation Research Platform (SARRP).”
- Dr. David Welch, CRR: “Mouse phantom applications.”

A guest lecture was also given at RARAF in 2017:

- Drs. John Warmenhoven and Nicholas Henthorn, University of Manchester, UK: “Progress in developing nanodosimetry models in Geant4-DNA for proton induced DNA damage and NHEJ repair.” ■



Micaela Cunha



Jay Perrier



Gloria Calaf and Tom Hei



Charles Geard



David Brenner

Faculty and Staff

Faculty:

DAVID J. BRENNER, Ph.D., D.Sc.

Director

RARAF Director

Higgins Professor of Radiation Biophysics
 Professor of Radiation Oncology
 Professor of Environmental Health Sciences

TOM K. HEL, Ph.D.

Associate Director

Vice-Chairman, Dept. of Radiation Oncology

Professor of Radiation Oncology
 Professor of Environmental Health Sciences

ERIC J. HALL, D.Phil., D.Sc., FACR, FRCR, FASTRO

Higgins Professor Emeritus
 Special Lecturer in Radiation Oncology
 Special Research Scientist

CHARLES R. GEARD, Ph.D.

Professor Emeritus of Clinical Radiation Oncology

HOWARD B. LIEBERMAN, Ph.D.

Professor of Radiation Oncology
 Professor of Environmental Health Sciences

SALLY A. AMUNDSON, Sc.D.

Associate Professor of Radiation Oncology

JINGSONG (JASON) YUAN, M.D., Ph.D.

Assistant Professor of Radiation Oncology

GUY GARTY, Ph.D.

Associate Professor of Radiation Oncology (in the
 CRR) at the Columbia University Medical Center

HELEN TURNER, Ph.D.

Associate Professor of Radiation Oncology (in the
 CRR) at the Columbia University Medical Center

CONSTANTINOS BROUSTAS, Ph.D.

Assistant Professor of Radiation Oncology (in the
 CRR) at the Columbia University Medical Center

PETER GRABHAM, Ph.D.

Assistant Professor of Radiation Oncology (in the
 CRR) at the Columbia University Medical Center

IGOR SHURYAK, M.D., Ph.D.

Assistant Professor of Radiation Oncology (in the
 CRR) at the Columbia University Medical Center

LUBOMIR SMILENOV, Ph.D.

Assistant Professor of Radiation Oncology (in the
 CRR) at the Columbia University Medical Center

YONGLIANG ZHAO, Ph.D.

Adjunct Assistant Professor

Research Staff:

GERHARD RANDERS-PEHRSON, Ph.D.

Senior Research Scientist

VLADIMIR IVANOV, Ph.D.

Special Research Scientist

BRIAN PONNAIYA, Ph.D.

Research Scientist

MANUELA BUONANNO, Ph.D.

Associate Research Scientist

SHANAZ GHANDHI, Ph.D.

Associate Research Scientist

ANDREW HARKEN, Ph.D.

Associate Research Scientist

SANJAY MUKHERJEE, Ph.D.

Associate Research Scientist

MIKHAIL REPIN, Ph.D.

Associate Research Scientist

DAVID WELCH, Ph.D.

Associate Research Scientist

GLORIA CALAF, Ph.D.

Adjunct Associate Research Scientist

ENYUAN SHANG, Ph.D.

Adjunct Associate Research Scientist

LI WANG, Ph.D.

Adjunct Associate Research Scientist

KEVIN M. HOPKINS, M.S., Senior Staff Associate

M. HASEEB DURRANI, M.S., Staff Associate

DENNIS FARRELL, Staff Associate

JAY PERRIER, Staff Associate

MARIA TAVERAS, R.N., Research Nurse

Post-Doctoral Research Scientists:

MONICA PUJOL CANADELL, Ph.D.

MICAELA CUNHA, Ph.D.

VELJKO GRILJ, Ph.D.

MALEK HAJ TAHAR, Ph.D.

MIKE YUAN-CHO LEE, Ph.D.

YOUNGHYUN LEE, Ph.D.

STANLEY LUE, Ph.D.

GLICELLA SALAZAR-DE SIMONE, Ph.D.

CHRISTIAN SIEBENWIRTH, Ph.D.

QI WANG, Ph.D.

DANNIS JINHUA WU, Ph.D.

VIVIAN QING ZHOU, Ph.D.

Graduate Student:

SOFIA BARBIERI

Design & Instrument Shop:

GARY W. JOHNSON, A.A.S., Senior Staff Associate

Design & Instrument Shop Director

DAVID CUNIBERTI, B.A., Instrument Maker

ROBERT C. MORTON, Instrument Maker

Technical Staff:

CUI-XIA KUAN, Technical Assistant

JOHANNA STEINBRECHER, Technician B

Administrative & Secretarial Staff:

MARGARET ZHU, M.A., Center Administrator

LANCE REDFORD, B.A., Director of Development

ANNERYS RODRIGUEZ, Junior Accountant

MARGARET GERMAN, B.A., Administrative Assistant

Faculty and Staff Photo

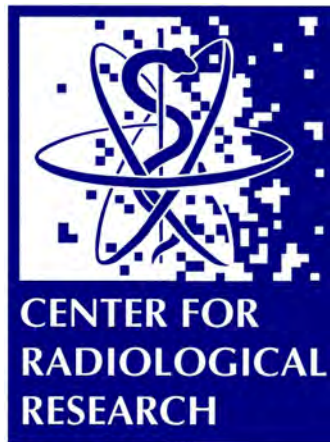


Front Row (l-r): Dr. Jingsong Yuan, Dr. Guy Garty, Dr. Howard Lieberman, Dr. David Brenner, Dr. Tom Hei, Dr. Lubomir Smilenov, Ms. Margaret Zhu.

2nd Row: Dr. Vivian Qing Zhou, Dr. Constantinos Broustas, Dr. Ekatarina Royba, Dr. Qi Wang, Dr. Younghyun Lee, Lidia Cunha, Ms. Cui Xia Kuan, Dr. Micaela Cunha, Dr. Monica Pujol Canadell, Dr. Helen Turner, Dr. Shanaz Gandhi, Ms. Annerys Rodriguez.

3rd Row: Dr. Mikhail Repin, Dr. Igor Shuryak, Ling Feng Ye, Dr. Veljko Grilj, Dr. Kunal Choudhary, Dr. Christian Siebenwirth, Dr. Mike Yuan-Cho Lee, Mr. Shad Morton, Dr. Sanjay Mukherjee, Dr. Andrew Harken, Mr. Jay Perrier, Dr. David Welch, Mr. Robert Morton.

ION BEAM DEVELOPMENT



Super Microbeam at RARAF

Andrew Harken, Veljko Grilj, Guy Garty, Gerhard Randers-Pehrson, and David J. Brenner

The Super Microbeam at RARAF is designed to couple a particle beam with a diameter less than 100 nanometers to STED super resolution imaging with resolution of the same dimensions. This would allow for the RARAF users to target sub-resolution sub-cellular features of interest. This system will be building off the technology previously developed at RARAF in our electrostatic microbeam and our multi-photon microscope.

Super Microbeam

The super microbeam is designed to be completed in two phases. Phase 1 is the installation of the superconducting solenoid as a solo focusing lens with a 250 nm beam. Phase 2 is the installation of the electrostatic double triplet, as the initial focusing element for focusing down to 75 nm.

This past year has been dedicated to the completion of Phase 1 alignment, and the continuation for the Phase 2 design completion and start of construction.

Solenoid chilling operations

The super conducting solenoid operations were disrupted in the early summer with a breakdown in the cryostat cooling system. The solenoid requires nearly 500 W of cooling capacity for cooling from room temperature to 4 K for operations. The building cooling capacity at RARAF is sufficient for this operation; however, as with any closed loop cooling system, there is an issue with air gaps when new equipment is added. After consulting with Cryomagnetics and Cryomech, our solenoid and cryochiller manufacturers, a modification was made to the cooling system to eliminate potential air gaps in the heat exchangers from shutting the system down. We also integrated secondary chiller monitoring to re-establish the cooling of the solenoid. We returned to operations in late June.

Microbeam operations

We have restarted microbeam operations with our users. The current beam size is 2 μm for He^{++} and 2.5 μm for protons. These sizes are consistent and sufficient for standard microbeam operations. The model and design for Phase 1 is to have a 250 nm beam size for He^{++} . The current size is due to the alignment of the internal aperture system to the solenoid field and the alignment of the solenoid field to the beam pathway. Figure 1 is the projection of the proton microbeam onto a plastic scintillator imaged using the microbeam endstation with a 50x objective. This image shows that the beam is oblong diagnosing that the solenoid field is not perfectly aligned with the beam direction. Modeling of this misalignment shows that the solenoid will need to be aligned within a

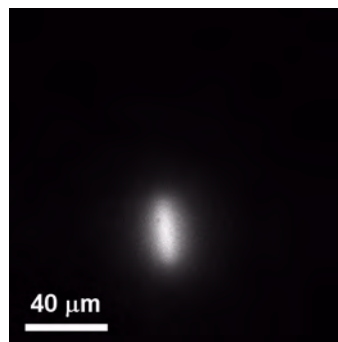


Figure 1. 50x image of proton beam slightly out of focus on plastic scintillator with the oblong shape visible. This predicts misalignment of the magnetic field in rotation with respect to the beam direction. The best focus for this alignment was 2.5 μm

milliradian, or less, of the correct angle to achieve best focusing. Currently, resolution of angular adjustment is in the 10's or milliradian accuracy. We are working on developing fine control of the solenoid table and positioning system to allow us to make adjustments at this resolution. Correction of the angular resolution and alignment should provide most of the last stages of best size optimization.

Phase 2 design

We are continuing with the Phase 2 design. This is primarily the re-installation of the electrostatic double lens as the first focusing element of a compound lens system with the solenoid. The primary object of this design is a custom vacuum tight box situated below the optical table where the circular mount cup for the double triplet can be positioned in alignment with the solenoid. This box also requires the high voltage feedthroughs for the electrostatic lens power and the high vacuum couplings that work within the existing order scheme. We are still iterating this design working with Gary Johnson in our Instrument Shop and Ralph Gardner, Nevis Machine Shop vacuum welding specialist, for component orientation and physical space requirements. We anticipate that this will be completed and ready for installation in the summer of 2018. The final build out of Phase 2 will occur in the Fall, with the re-installation of the double triplet.

Super Resolution Imaging

Super resolution imaging of ~ 75 nm is required to match the resolution of the super microbeam for accurate targeting of fluorescent targets. Stimulated emission depletion (STED) microscopy was chosen as it builds on our previously developed multi-photon microscope.

The lasers were co-aligned on the microbeam endstation in 2016, before the Phase 1 reconstruction. The optical bench was preserved as aligned and remounted as a unit in 2017. The endstation reconstruction was completed and the re-alignment of the multi-photon laser and STED laser recommenced.

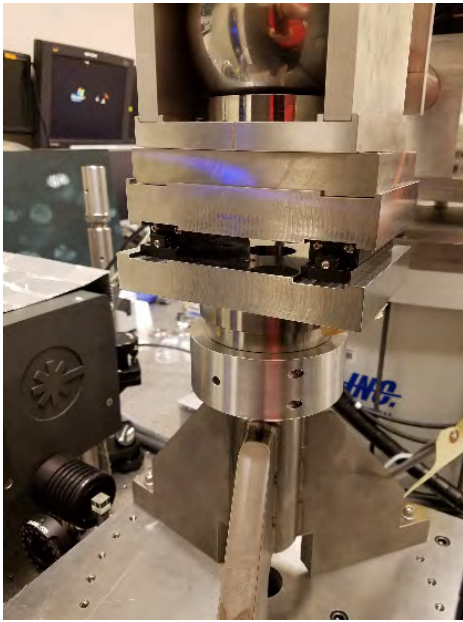


Figure 2. The split coupling in the spine of the end station. The multi-photon laser passes through the hole in the center of the bottom plate up through the rotation sphere to the upper optical bench.

Alignment of the two lasers is ongoing and will be a daily process. The new design of the endstation used a split spine, shown in Figure 2, that allows for lateral motion of the primary support bar away from the solenoid through expansion or adjustment motion. The split spine design means that the multi-photon laser, passing through

the body of the spine, needs to be re-aligned on a daily basis as the spine alignment changes due to room temperature (slight adjustments) and solenoid movement for ion beam alignments (large adjustments). While not ideal, this alignment procedure has already been reduced to a 40 minute procedure (from 3 hours) and will be reduced further once the ion beam alignments are complete.

Time-gated gSTED

Last year we made the decision to go directly to time gated STED (gSTED). This utilizes the pulsed nature of the multi-photon excitation with the CW STED to increase signal to noise in the STED images, while allowing the reduction in overall laser power delivered to the samples.

To that end we purchased a control card for Time Correlated Single Photon Counting (TCSPC) and a matching fast timing preamplifier for our PMT output signals. This hardware was tested by our REU student and the process of integrating these into the microbeam endstation began. The proprietary control software of the TCSPC card allows for integration with outside control programs, but the main work of the imaging is done in its own control space. While not ideal for high-speed irradiations, this will be sufficient for our super-resolution needs as currently envisioned.

We anticipate that we will have gSTED imaging capabilities before the start of the Phase 2 construction in the summer of 2018. ■

Microbeam at a Distance: Remote Control and Operations at the RARAF Microbeam

Andrew D. Harken, Alejandro Carabe-Fernandez^a, Consuelo Guardiola^a, and Gerhard Randers-Pehrson

Introduction

The remote operations and control at the RARAF microbeam, allowing users to control their experiments without physically being present at RARAF, have been a long-term goal. The integration of high-speed Internet with new telecommunications software allows us to offer these remote sessions to the RARAF users.

This report is on the first of these interactions around the collaboration with the University of Pennsylvania.

^aDepartment of Radiation Oncology, University of Pennsylvania

Project overview

The RARAF collaboration with the Department of Radiation Oncology at the University of Pennsylvania is working on the development of micro-miniature silicon-based solid-state diode detectors for beam characterization and microdosimetry at the UPenn Roberts Proton Therapy Center. They are using the RARAF microbeam and track segment facilities for irradiating single devices or an array of devices looking for LET dependence on the detector signals. The LET of the RARAF proton beams is similar to the LET of protons stopping in the tissue in therapy situations, i.e. the LET delivered at depth to the therapy target of interest. The ultimate goals are to use the RARAF microbeam to map the detector sensitive regions; correlate the detector

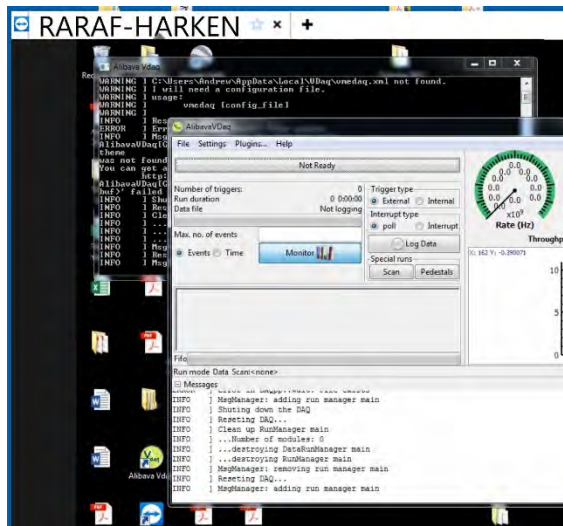


Figure 1. Screenshot of a user's desktop view through TeamViewer. The window labeled RARAF-HARKEN is the view of the remote desktop where control of the experiment takes place.

output to particle LET; and correlate particle LET, detector output, and biological response of irradiation to model clinical RBE factors.

The group that has developed this detector technology is an international collaboration involving UPenn, the Centro Nacional de Microelectronica (IMB-CMN, CSIC) in Bellaterra, Spain, and the Departamento de Fisica Atomica, Molecular y Nuclear at the University of Sevilla, Spain. This group worked together to develop the detectors, the support hardware, and the systems control

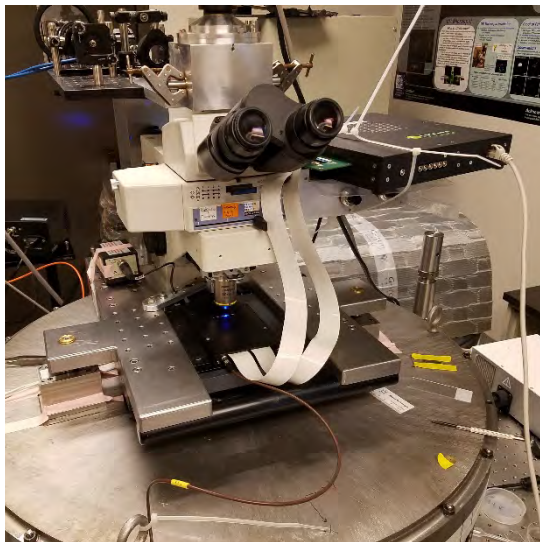


Figure 2. Detector system mounted at the microbeam endstation. The detector array is in the black box mounted on the stage. The white cross on the box and the light through the microscope are fiducials for aligning the detectors to the beam port. The control electronics area is mounted on the multiphoton PMT box and secured temporarily with cable ties. The control communications were run through the CAT5 cable coming out of the right-hand side of the electronics box to the control laptop on the bench.

programming for the detector arrays [1]. These systems are in the process of being commercialized by Alibava Systems, Inc., for the Spanish National Research Council (CSIC) through IMB-CMN. For the irradiations performed at the RARAF facility, having the many team members access the control hardware for the detector arrays and perform real time analysis was invaluable for a smooth operation.

Telecommunications program

We made use of a desktop sharing telecommunications program, TeamViewer, for the remote telecommunications. This program allows users to sign in to a remote computer and, in a windowed environment, control that computer as if they are sitting at its own keyboard. The TeamViewer program allows multiple users to be signed on to a single computer simultaneously, allowing all collaborators to control the operations, making adjustments and comments as needed. TeamViewer also provides for voice communications and text chat with all that are connected. Figure 1 is a screenshot of what a signed in user would see for the experiment. The remote desktop is in the window and remote mouse control applies when dragging over that window.

Experiment Layout and Operation

The irradiation experiments were performed at the microbeam endstation and the track segment facility, sampling several different proton energies. At the microbeam, the detector system is mounted in a custom housing on the micro positioning stage over the beam port, with the associated electronics package mounted high on the endstation (Fig. 2) to avoid the magnetic fields from the solenoid magnet. At the Track segment facility, the dosimetry wheel was removed and the detectors were manually positioned over the beam window with the electronics package on the wheel space (Fig. 3). In both locations, the electronics were controlled

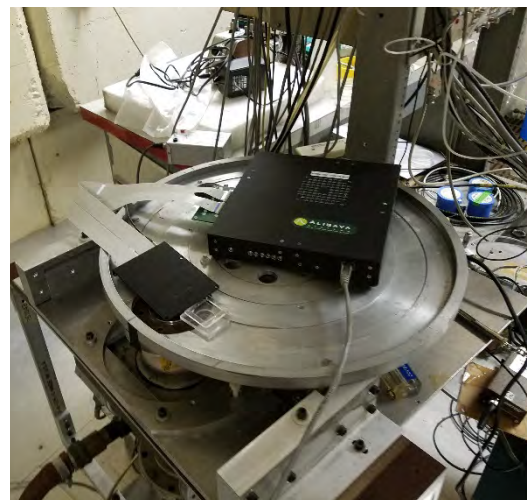


Figure 3. Detector system positioned above the track segment beam exit window. The CAT5 communications cable extended out of the track segment cave and to the RARAF console for control interactions.

by an Internet connected laptop running the Alibava control software and TeamViewer communications software.

The control of the detector system was managed through TeamViewer and the communications that system provides. Accelerator and microbeam positioning control remained under local RARAF control for beam operations and sample locating. Future iterations of this experiment may provide access to positioning control, but accelerator control will always be at the local RARAF level.

Conclusion

We have successfully performed irradiations at RARAF with remote control of the experimental

hardware from several different locations around the world. Remote operations have previously been discussed at RARAF. The combination of high-speed Internet and telecommunications software has now allowed us to realize this new feature to RARAF experiments.

Reference

1. C. Guardiola, D. Quirion, G. Pellegrini, C. Fleta, S. Esteban, M.A. Cortés-Giraldo, F. Gómez, T. Solberg, A. Carabe and M. Lozano, "Silicon-based three-dimensional microstructures for radiation dosimetry in hadrontherapy," *Applied Physics Letters*, 107 (2), pp. 023505 (2015). ■

DREEBIT Heavy Ion Source at RARAF

Christian Siebenwirth, Andrew D. Harken, Gerhard Randers-Pehrson, and David J. Brenner

Introduction

Carbon ion therapy is becoming more and more popular worldwide. In order to understand the beneficial effect of heavy ion therapy towards protons and x-ray treatment and thus to justify its higher costs, the spectrum of usable ions and thereby the LET at RARAF is going to be expanded. Due to the 5 MV Singletron accelerator at

RARAF, a new ion source was necessary to produce heavy ions like carbon with high charge states up to fully stripped ions. Only highly charged ions gain enough energy in the Singletron accelerator to penetrate cell samples of about 30 μm thickness.

The DREEBIT heavy ion source [1] arrived in the beginning of 2017 and was installed on the test bench to be characterized and optimized for maximum production of C^{6+} ions in particular.

The DREEBIT ion source works on the principle of an electron beam ion trap (Fig. 1). It utilizes a small focused electron beam to ionize the ionization gas. The generated ions are trapped by the voltage potentials of the surrounding drift tubes in axial direction and by the electron beam in radial direction. In this way, the ions can be ionized multiple times to reach high charge states up to fully stripped ions. After a charge and ion specific ionization time, t_{ion} , the trap is opened, and the ions are released.

Bench test of the ion source

A central part of our test setup (Fig. 2) for the analysis of the ion production was a Wien filter, which was generously lent to us by the Columbia Astrophysics group of Daniel Savin. Additional use of a slit system and Faraday cup allowed determination of beam size and, especially, ion current.

The ion production depends on the feeding gas, electron beam intensity and energy, ion trap depth, ionization time, ion beam optics, as well as the vacuum quality and working pressure. Thus, hundreds of spectra were recorded at various conditions. This process was finally automated by controlling the high voltage and the

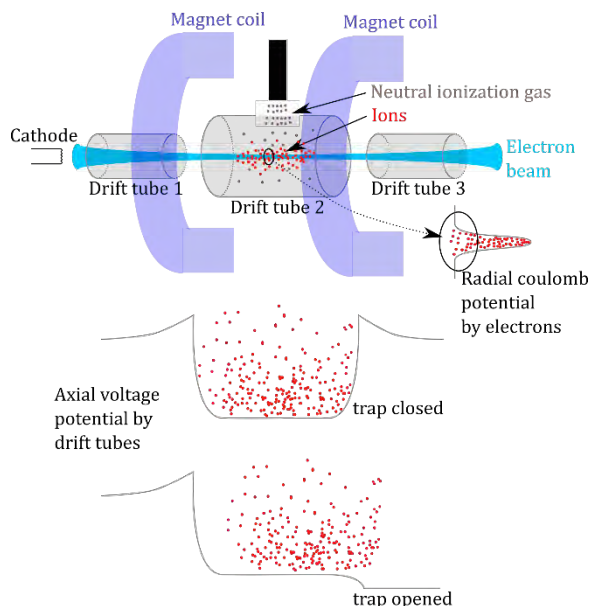


Figure 1. Working principle of an electron beam ion trap. The neutral ionization gas becomes ionized by a focused electron beam. The generated ions are trapped by the voltage potential of the drift tubes and the coulomb potential of the electron beam. Thus, higher ionization states can be reached by multiple ionizations. By lowering the potential of the 3rd drift tube the trap is opened and the ions are released.

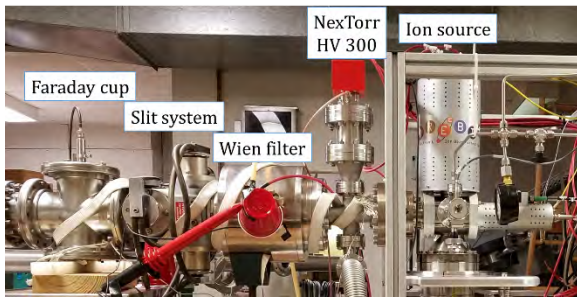


Figure 1. DREEBIT ion source installed at the RARAF test setup.

current measurement with the control computer of the source.

Fig. 3 shows three ion spectra using propane for C6+ production, which were gathered at RARAF. We were able to reproduce the factory tests of DREEBIT and to verify them as optimal conditions of carbon 6+ production. The peaks of the different spectra have a different weighting when t_{ion} is changed. With longer ionization time (e.g. $t_{ion} = 100$ ms), the peak of carbon 6+ is strongly pronounced and we obtained a maximum ion current of 17 pA at the C6+ peak, corresponding to a beam size of about 5.1 mm x 4.5 mm at the slits. Additionally, we characterized the so-called leaky mode ($t_{ion} = \infty$). Here, the ion trap stays closed and occasionally escaping ions are measured. In this way, the maximum current in the C6+ peak reduces to 1 pA. The production of protons is in the same range. Thus, protons can be used as reference irradiation when the ion source is installed in the accelerator. An additional upgrade of the gas feeding system could even allow other types of ions, such as He2+ by changing the feeding gas.

Geometrical integration

Alongside our characterization of the ion source, 3D CAD based planning of its integration in the terminal area of the Singletron accelerator was continued. In this

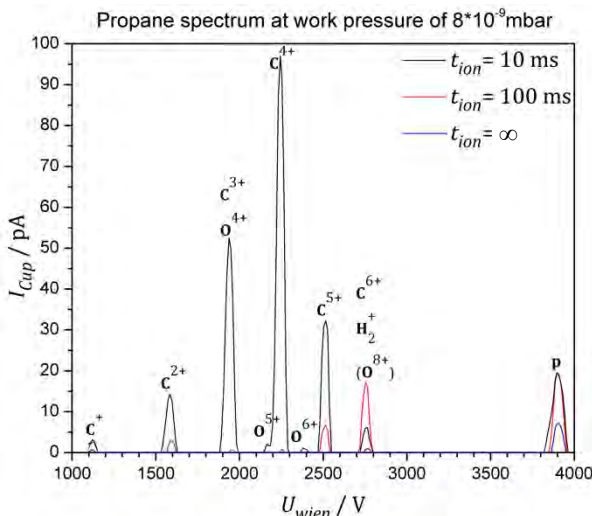


Figure 3. Ion spectra for carbon ion production using propane (C3H8) measured at an ionization time of $t_{ion} = 10$ ms, 100 ms and ∞ (leaky mode).

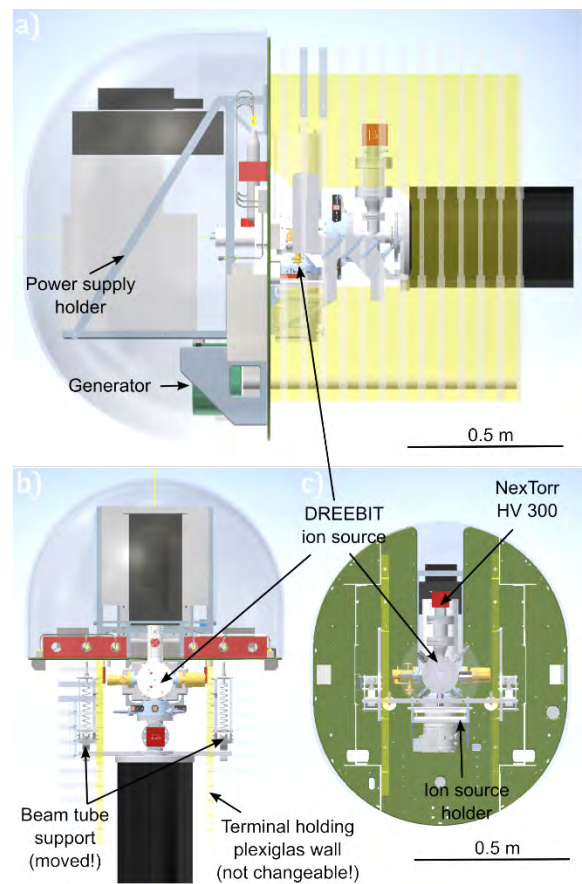


Figure 4. Side (a), top (b) and front (c) view of the 3D CAD model of the terminal area in the RARAF Singletron, where the new DREEBIT ion source is going to be installed. This planning is finished. Additional holding structures for the ion source and power supplies were designed and produced. The CAD modelling pointed out that modifications of the holding mechanism of the beam tube are necessary in order to provide enough space. For these, the vendor of the accelerator (HVEE) was consulted to check for stability and providing instructions for modifications.

process, new holding structures for the added power supplies and the ion source were planned and built. Additionally, we took advantage of accelerator maintenance openings to verify the CAD model, which was mainly based on hardcopy 2D drawings. Fig. 4 shows the current version of the planning. CAD modeling demonstrated that modifications of the holding mechanism of the beam tube are necessary in order to provide enough space. For these the manufacturer of the accelerator, High Voltage Engineering Europe (HVEE), was consulted to check for stability and providing instructions for modifications. Additionally, readjustment procedures of the terminal position were clarified, which are necessary due to the added weight on the terminal.

System integration: Vacuum, optical communication, electronic power and protection

The characterization of the ion source showed that a very high vacuum of 10^{-9} mbar is crucial for the C6+



Figure 5. NexTorr HV 300 vacuum pump. It combines a NEG pump (Non-evaporating-gettter material) with an ion pump. A huge gas capacity is achieved by heating the NEG element to 250°C. This provides the necessary vacuum quality for the ion source for 1-2 months.

production, as fully charged ions like N7+, and O8+ are very hard to separate. Additionally, the breeding efficiency of higher charged ions becomes worse when the number of atoms and ions in the trap is too high. With respect to C6+ production, the vacuum in the beam tube in front of the ion source has to be improved. We found the SAES NexTorr HV 300 pump (Fig. 5) as the only solution of a high vacuum pump, which does not need a roughing vacuum and consumes low power. By heating of its NEG (Non Evaporating Getter material) element to 250°C, the pump has a unique gas capacity to maintain vacuum for 1-2 months.

For communications, the accelerator includes fiber optic channels that can be used. We successfully tested the compatibility of fiber optic communication used in the accelerator, by the ion source and NexTorr HV 300 control.

To verify that the power consumption of the whole ion source setup does not exceed the available power in the accelerator, a motor/generator system was set up, which is identical to the one currently used in the accelerator. This system provides the electric power for a pair of AC/DC converters, which finally supply the control units of the

ion source and the ion pump with 24 V. An additional 5 V power supply is going to heat the NexTorr HV 300 to its working conditions. It was possible to run the ion source using the generator. However, improvements are in progress to provide more functional reliability.

The support of HVEE highlighted the importance of additional electronic protection circuits for protection of power supplies and other electronic components from destruction by heavy arcs, which often occur in the accelerator. The development and testing of these circuits is difficult and time consuming. Additionally, it can only be done by RARAF because it is very specific to the given system. RARAF is in contact with various accelerator labs worldwide to use their knowledge to find the fastest and best solution. At the end, an effective protection can only be proven by its successful application in the accelerator.

Conclusion

The characterization of the DREEBIT ion source for heavy ion production at RARAF is finished and the result of its factory test was verified. The planning of its geometrical integration is completed and new holding structures for additional components were built. Necessary modifications on the accelerator were verified in agreement with HVEE and solutions for vacuum requirements, communication and powering of the ion source were developed and tested. The realization of the protection of electrical components from arcs in the accelerator tank and successful installation of the ion source in the accelerator are the last hurdles for the heavy ion source. We anticipate these will be overcome in the near future, and we will begin offering heavy ion irradiations at RARAF.

References

1. Schmidt M, Zschornack G, Grossmann F, Heller R, Kentsch U, Kreller M, Landgraf S, Ovsyannikov V P and Ullmann F. *Report on the current developments and experiments of the Dresden EBIT System*. Journal of Physics: Conference Series, 2007; 72: DOI:10.1088/1742-6596/72/1/012020. ■



(l to r) Howard Lieberman, Constantinos Broustas, Yi-Fang Wang, and Charles Geard

Ultrahigh Dose-rate Ion Beam Irradiations

Veljko Grilj, Manuela Buonanno, Brian Ponnaiya, and David J. Brenner

Last year we reported on the experimental layout and preliminary results obtained with the ultrahigh dose-rate (Flash) ion irradiator that was assembled as an addition to existing RARAF irradiation platforms. Here we present more details about the dosimetric procedures in use and biological models that were investigated with this platform so far.

Dosimetry

Being able to deliver therapeutically relevant doses (1- 20 Gy) in time intervals as short as one millisecond requires significant ion currents. Precisely, the highest proton dose rate that we have used in experiments was 1000 Gy/s with the particle flux of 7×10^{10} ions/s. Such high ion currents make the accurate dosimetry challenging. The necessary requirement is to have a reliable, dose rate independent dosimeter. In our setup, we use two dosimeters, an ionization chamber and unlaminated EBT3 films. Thin (3 mm) custom-made parallel plate ionization chamber serves as instantaneous beam current monitor. Because the dose rate is directly proportional to the beam current, this device is used to define the dose rate that will be used for irradiations. It comprises of two 6 μm thick aluminized mylar foils which hold the potential difference of 1000 V. Chamber volume is filled with methane based tissue equivalent gas which makes it suitable to be also used as an absolute dosimeter. Even for the maximum dose rate used the chamber enters the plateau region when bias surpasses 700 V, which means that for higher applied voltages the charge recombination inside the chamber is negligible and its output is proportional to the beam current.

The unlaminated version of EBT3 film is used as a primary dosimeter for absolute dose measurement. Composition and density of the active layer are nearly tissue equivalent. That makes the mass stopping powers of film and tissue equal, so the dose delivered to a biological sample of comparable thickness is approximately equal to the dose delivered to the active layer of the film. If the biological sample is much thicker than the sensitive layer of the unlaminated film (14 μm), then after a certain depth in the sample particle's LET changes and the dose equivalency between the film and the sample doesn't hold anymore. In such case it is possible to determine the depth profile of the absorbed dose by multiplying the dose registered with EBT3 film by the ratio of the mass stopping power at a given depth in the sample and the mass stopping power of the film.

The dose rate independence of EBT3 film was confirmed for photons and electrons. To check if it also holds in case of protons, we irradiated several film samples with dose rates ranging from 0.1 Gy/s up to 1000

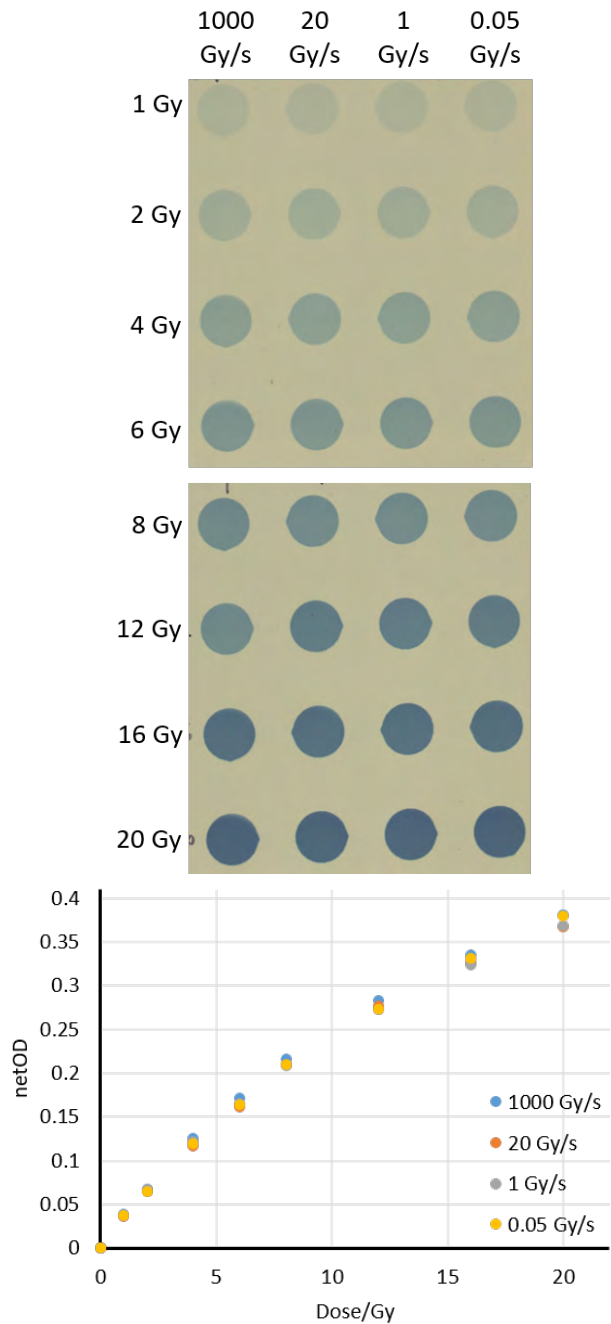


Figure 1. Top: Unlaminated EBT3 film irradiated with 1-20 Gy at 1000, 20, 1 and 0.05 Gy/s. Bottom: Dose response of EBT3 film for different dose rates.

Gy/s. The dose response of the film was quantified in terms of the change in optical density that arises from the polymerization of LiPCDA monomers upon exposure to ionizing radiation. Figure 1 shows dose responses of unlaminated EBT3 films irradiated with various dose

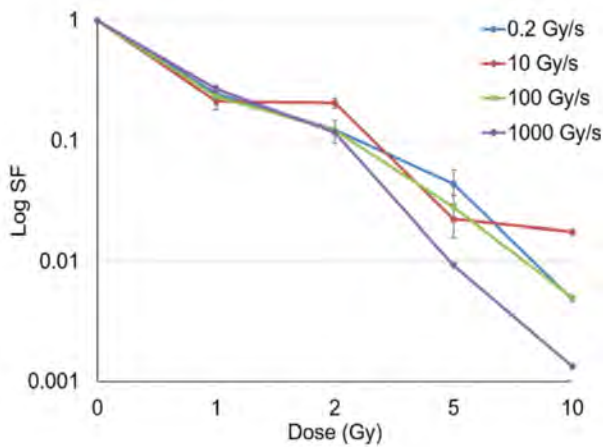


Figure 2. Survival curves for normal lung cells (IMR90) irradiated at various dose rates.

rates of 4.5 MeV protons. It is evident from those measurements that film response depends only on the total dose, regardless of the dose delivery time. Thus, EBT3 films meet our requirement for a dose rate independent dosimeter.

Biological models at the Flash irradiator

The ultrahigh dose-rate (Flash) proton irradiator is compatible with studies on biological models of various complexity. For instance, cell monolayers, 3-D tissue models and mice were all irradiated at this platform. Minimal requirements on size and shape of samples as well as the availability to manufacture custom designed sample holders make the platform easily adjustable to the needs of the researcher.

Cells

Two types of studies were done with normal and cancer human lung cells. In one the influence of the dose

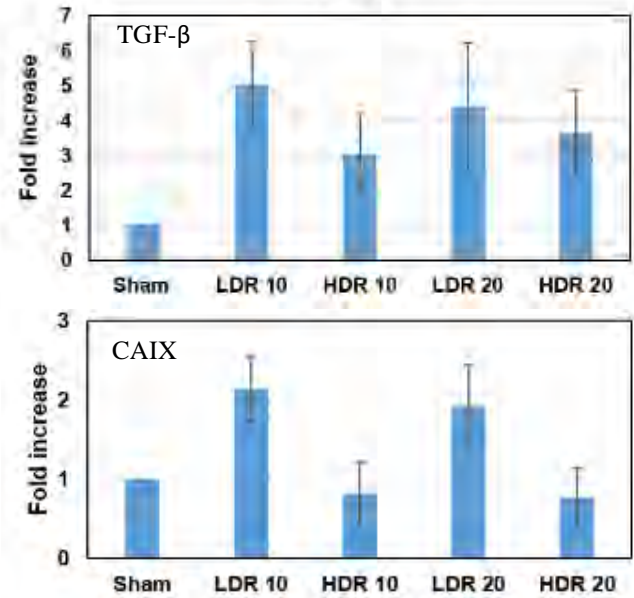


Figure 3. Expression of TGF-β and CAIX in MatTek lung tissue models 3 months after proton irradiations with 10 or 20 Gy delivered at 1000 Gy/s (HDR) or 0.2 Gy/s (LDR).

rates on cell survival was investigated. The obtained survival curves (example for normal lung cells is shown in Figure 2.) show no significant difference in survival fractions for the same absorbed dose. The second type of cell studies was focused on differential cytokine response after low and high dose rate irradiations. Analysis of these experiments is still ongoing.

Tissue models

To address the potential beneficial characteristics of high dose rates on development of radiation stimulated lung fibrosis, we used EpiAirway tissue models from MatTek. These human airway tissue models consist of normal, human-derived tracheal/bronchial epithelial cells co-cultured with normal human stromal fibroblasts. Samples were irradiated with 10 or 20 Gy delivered at high dose rate (HDR, 1000 Gy/s) or low dose rate (LDR, 0.2 Gy/s) and maintained in medium for three months after exposure. Immunohistochemical analysis of markers of fibrosis such as transforming growth factor (TGF) β and carbonic anhydrase IX (CAIX) revealed higher levels of both when radiation was delivered at lower dose rate (Figure 3).

Mice

Ongoing experiments based on intravital imaging techniques will allow for real time observations of exposed mice. Indeed, using a polypropylene skin fold chamber window and a custom made mouse holder (Figure 4), we were able to observe fluorescence-labelled tumor cells that were injected within the skin of the

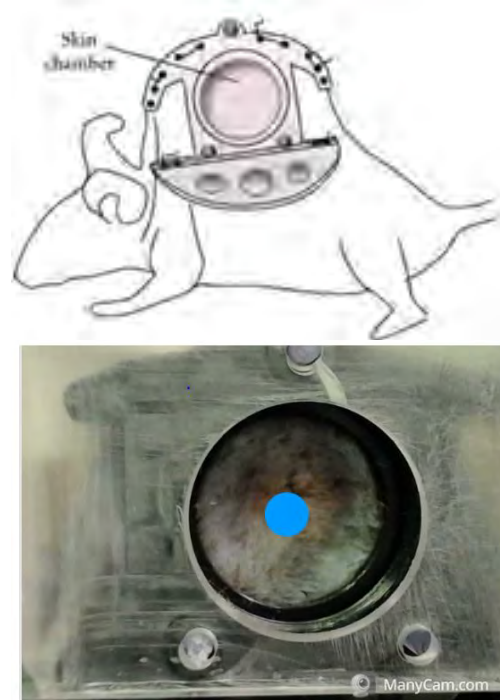


Figure 4. Top: Dorsal skin fold chamber model. Bottom: The polypropylene skin fold chamber window used for irradiation at the ultrahigh dose-rate ion beam irradiator; the superimposed blue dot indicates the irradiated area.

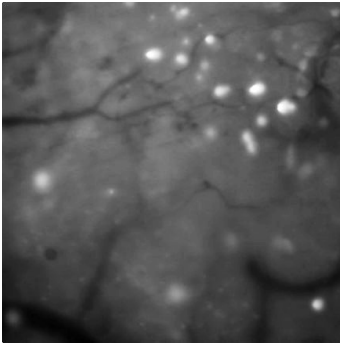


Figure 5. Mouse skin injected with fluorescently labeled tumor cells seen at the microscope through the polypropylene skin fold chamber window. Skin capillaries can also be observed.

mouse (Figure 5). Besides the fluorescent cells that can be followed in real time before and after Flash irradiation, skin capillaries can also be observed. Using this technique, the biological applications of our ultrahigh dose-rate ion beam irradiator for clinical application will be far-reaching. ■

High LET Ion Beam Dosimetry with Unlaminated Radiochromic Films

Veljko Grilj and David J. Brenner

GafChromic radiochromic films (Ashland Specialty Ingredients, Wayne, NJ) are widely used for dosimetry in external beam radiotherapy. They offer several advantages, in particular, high spatial resolution, no need for post-irradiation development, tissue equivalence and energy independence for photons and electrons. However, when it comes to film usability in proton and carbon beam dosimetry, an under-response was observed for protons in the proximity of the Bragg peak and for carbon ions in both, the plateau and Bragg peak regions. This behavior is related with higher linear energy transfer (LET) of such beams. Since our intention is to use radiochromic films for dosimetry in cell experiments with relatively high LET ion beams, we investigated the LET dependent response of GafChromic films to proton, deuteron and helium ions.

Ion beam energies available at RARAF permit the use of standard GafChromic EBT3 film with active region sandwiched between two 125 μm thick clear polyester outer layers. Because of a limited range, ions cannot penetrate the polyester layer. Fortunately, the manufacturer is able to produce the unlaminated version

of GafChromic films. In that case, the active layer that contains crystals of monomers of lithium salt of pentacosanoic acid (LiPCDA) is on the surface of the film, directly exposed to impinging ions. The thickness of the active layer is halved in comparison with standard laminated films and equals 14 μm . When exposed to ionizing radiation, LiPCDA monomers undergo polymerization, which results in the increased light absorbance and optical density of the film. When the density of the ionization generated by the incoming particle is much higher than the density of polymerization sites, a part of the deposited energy becomes wasted in a sense that it is not followed by subsequent polymerization. That reflects in dose response curve as an under-response compared to the same dose delivered by the low LET radiation.

Two types of unlaminated GafChromic films, EBT3 and MD-V3, with the same active component and specified dose ranges of 0.01 cGy -10 Gy and 1 Gy - 100 Gy respectively, were included in the study. Films were irradiated at the RARAF Track Segment facility with various ion species and energies. Data in Table 1 describe the energies and average LETs of the ions used. The values of LETs at the entrance and exit of sensitive layer are also stated and indicate the magnitude of the LET change throughout the sample. Both EBT3 and MD-V3 films were irradiated with doses up to 200 Gy to increase the accuracy of fitting towards the saturation region. Epson Perfection V700 Photo flatbed scanner was used as an optical densitometer and ImageJ software was used to extract the average net optical density for the red channel from scanned films. The manufacturer typically suggests rational functions like $y=a+b/(x-c)$ as appropriate phenomenological models to fit the dose response data.

Table 1. Ion beam energies and LETs used in this study.

Ion (energy/MeV)	LET/keV/ μm (EBT3)	LET/keV/ μm (MD-V3)
protons (4.5)	12	12
protons (3.4)	16	15
protons (2.7)	20	19
deuterium (4.5)	22	21
deuterium (3.5)	28	26
deuterium (2.5)	40	37
helium (11)	80	75
helium (9)	99	93

However, the parameters in such model have no physical meaning, so determining whether one or more of them are dependent on particle's LET is difficult. Instead, we applied the Schumann plate equation [1] that was empirically found in 19th century and derived later from the law of mass action [2]:

$$\frac{netOD}{netOD_{max} - netOD} = \left(\frac{D}{D_{1/2}} \right)^p$$

As indicated in the work of Perles et al. [3], this mathematical formalism, although originally used to describe the reaction between two atoms, can be equally applied to adjacent monomers in a crystal lattice.

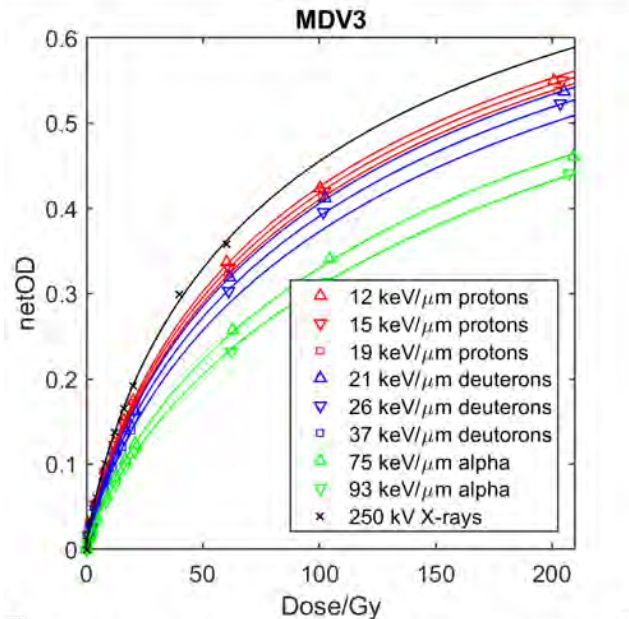
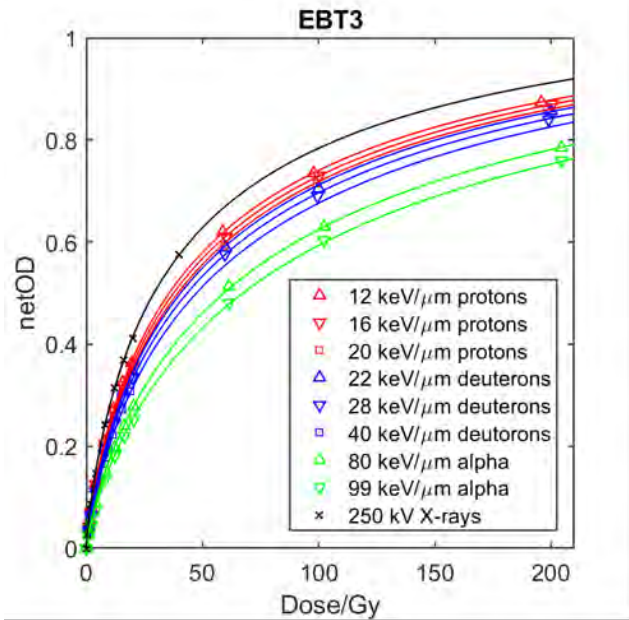


Figure 1. Dose response of EBT3 (top) and MD-V3 (bottom) films for ions with various LET.

Meanings of parameters in the above equation are as follows: $netOD_{max}$ is the maximum net optical density that can be obtained with particular batch of film and densitometer used; $D_{1/2}$ is the dose which results with a film response equal to half of the $netOD_{max}$; and p is a dimensionless parameter known as a reaction order. In

Table 2. $D_{1/2}$ parameters for EBT3 and MD-V3 films

LET/keV/μm EBT – MDV3	$D_{1/2}$ /Gy (EBT3)	$D_{1/2}$ /Gy (MDV3)
12 – 12	50.0 ± 0.3	117.4 ± 0.4
16 – 15	52.7 ± 0.3	122.2 ± 0.5
20 – 19	55.2 ± 0.3	127.3 ± 0.5
22 – 21	56.9 ± 0.3	130.5 ± 0.5
28 – 26	60.9 ± 0.3	141.6 ± 0.6
40 – 37	66.5 ± 0.5	156 ± 1
80 – 75	82.9 ± 0.5	199.2 ± 0.8
99 – 93	94.5 ± 0.5	226 ± 1
Xrays	40.9 ± 0.3	99.9 ± 0.4

order to determine the $netOD_{max}$ values for EBT3 and MD-V3 batches used in this study, pieces of both film types were exposed to very high doses of hundreds of kilograys from proton, deuterium and helium beams. The measured average values are:

$$netOD_{max} (EBT3) = 1.16 \pm 0.03$$

$$netOD_{max} (MD-V3) = 0.91 \pm 0.02$$

and they were used subsequently in fitting procedures. Among the other two parameters in Schumann's equation, only $D_{1/2}$ can depend on the particle's LET. Therefore, data sets for all combinations of ions/energies were fitted with p as a common global parameter and $D_{1/2}$ as a parameter whose value is specific for each data set. Fitting curves are shown together with raw data points in Figure 1. $D_{1/2}$ parameter values obtained by least squares fitting method are given in Table 2.

The proposed bimolecular model provides excellent fit to experimental data. One global and only one ion/energy specific parameters were enough to reproduce the measured film response for all data sets. Optical density data for all ions used indicate a significant under-response in comparison to X-rays. The effect gets stronger for higher LET particles and is reflected in values of $D_{1/2}$.

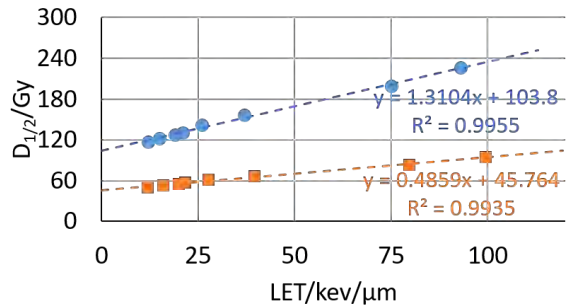


Figure 2. Dependence of $D_{1/2}$ values on particle LET for EBT3 (orange) and MD-V3 (blue) films.

When plotted against the LET, they follow a linear trend (Figure 2) so $D_{1/2}$ value for any LET can be estimated. That, together with known values for $netOD_{max}$ and reaction order p , allows us to unanimously establish the correlation between the measured film optical density and delivered dose regardless of the LET of the particles in case.

References

1. T. Lyman, Victor Schumann *Astrophys. J.* 39 1914
2. C. Candler, The photographic process as a diatomic reaction *Aust. J. Phys.* 13 1960
3. L.A. Perles et al. LET dependence of the response of EBT2 films in proton dosimetry modeled as a bimolecular chemical reaction *Phys. Med. Biol.* 58 2013

Design Study of a Heavy Ion Particle Accelerator

Malek Haj Tahar, David J. Brenner, and Gerhard Randers-Pehrson

Introduction

The main purpose of this study is to design a compact and cheap particle accelerator that can boost the energy of the existing accelerator complex at RARAF from 6 MeV/nucleon (MeV/n) to 100 MeV/n for carbon ions, thus allowing a penetration depth of ~1 cm in mice. A ring is the most cost-effective solution for energies of several 10s of MeV. Thus, several options exist: microtrons, synchrotrons, cyclotrons, synchrocyclotrons or Fixed Field Alternating Gradient (FFAG) accelerators. Microtrons are excluded given that they are weak focusing and have poor transmission for heavy ions, requiring energies of several 100s of MeV/n. Cyclotrons and synchro-cyclotrons are compact, thus compatible with a hospital environment, yet they cannot achieve a variable energy extraction. Therefore, a beam degrader would be required in order to tune the extracted beam energy for various penetration depths in tissue. This has important consequences, such as degrading the quality of the beam, as well as increasing beam losses. In order to remediate all these problems and design a compact, strong focusing and variable energy extraction accelerator, a novel concept of FFAG accelerator is proposed in this study.

Main Idea

In order to achieve a variable energy extraction heavy ion accelerator capable of delivering beams with energies up to 450 MeV/n, the idea is to design a racetrack FFAG with dispersion free straight sections. Strong focusing is usually achieved by increasing the azimuthal field variations, i.e. creating positive and negative curvature fields (alternating the sign of the vertical component of the magnetic field in the median plane of the accelerator). However, for a compact fixed field medical accelerator, this will consequently increase the size. Thus, at the initial phase of this design study, we have opted for a drift space instead of the negative curvature field, which helps increase the focusing and maintain a relatively small size of the accelerator.

Design Approach

The design approach consists of transforming the conventional circular FFAG into a racetrack configuration by replacing the 4-fold symmetry machine with a 2-fold symmetry machine: at first, a configuration with 4 identical radial sector magnets (m1) is privileged since it provides enough space between the magnets to place injection/extraction devices, as well as other elements to be discussed below. Then, a second magnet (m2) is added for each sector and its field profile is optimized in order for the pair (m1+m2) to create a 90-degree bending angle for all energies. The beam dynamics tracking code ZGOUBI is employed for this purpose: a fitting method is employed that consists of tracking particles with different momenta and the same initial coordinates (point A in Figure 1) to the screen where their final coordinates are

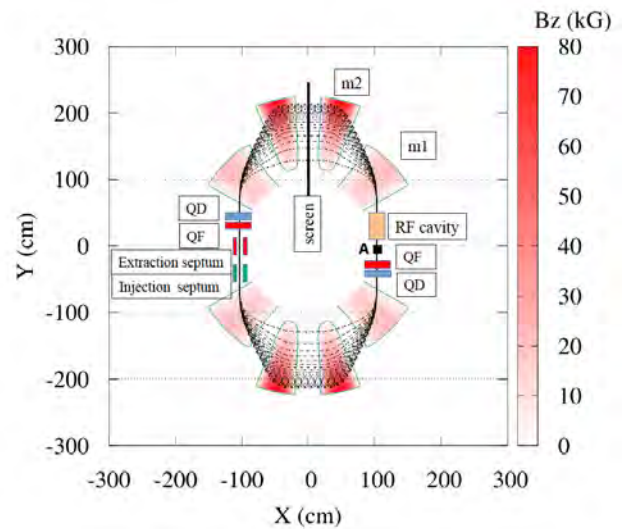


Figure 1. Vertical component of the magnetic field in the median plane of the accelerator with some of the closed orbits between injection and extraction energies (shown in dashed black curves). QF and QD refer to the focusing and defocusing trim quadrupoles respectively.

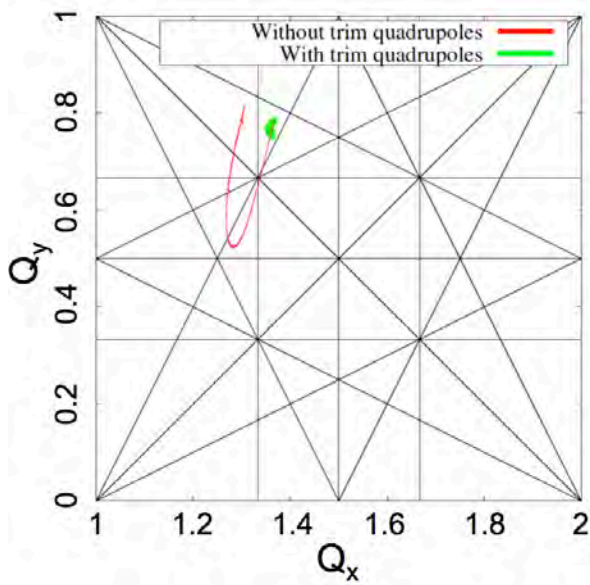


Figure 2. Betatron tunes from 8 to 100 MeV/n (right to left) in red. The solid lines (in black) show the resonance lines up to the 3rd order.

recorded. The field along the radius of magnet m2 is adjusted until all particles exit perpendicular to the screen. Once this is achieved, the ring is completed by creating mirror symmetries with respect to the screen and to the line passing by point A and perpendicular to the screen. A microtron-like racetrack FFAG configuration with dispersion-free straight sections is thus achieved and is illustrated in Figure 1.

The advantages of the dispersion-free straight sections are numerous (manuscripts submitted). The main advantages are simplification of the design of the RF cavity, allowing extraction of the beam at various energies, as well as allowing the dual acceleration of protons and carbon ions.

Betatron resonance crossing is a major issue in circular accelerators. However, the dispersion free straight sections allow placement of time-varying structures that can help reduce the tune excursion in order to avoid the crossing of betatron resonances. A scheme was developed and we have demonstrated (Figure 2) that a fixed tune FFAG can be achieved using this concept by adding time varying trim quadrupoles (QF, QD) in the dispersion free sections as shown in Figure 1. A provisional patent covering this concept was submitted in September of

Table 1. Main parameters of the optimized lattice.

Parameter	Value	Unit
Charge to mass ratio	1/2	NA
Circumference	15	m
Length of field-free straight section	1	m
Kield index k of m1	0.75	NA
Injection/extraction kinetic energy	8/100	MeV/n
Maximum field	8	T

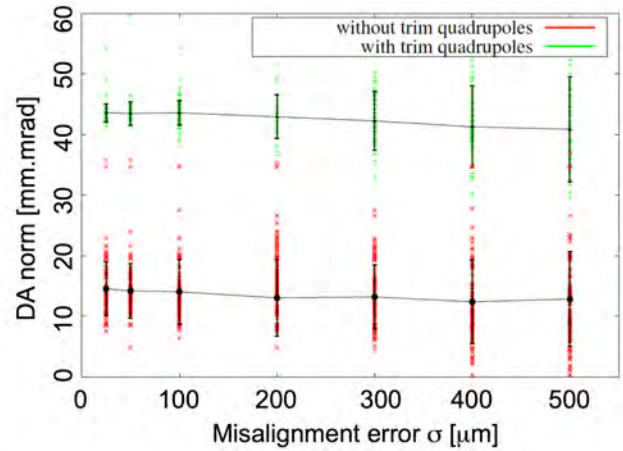


Figure 3. The DA as a function of the horizontal and vertical cell misalignment errors with a Gaussian distribution of width σ .

2017 and a marketing campaign is ongoing. In addition, an invited talk was given at the last FFAG workshop to present this concept [1].

The parameters of the optimized lattice are listed in Table 1. In order to demonstrate the validity of the concept, the Dynamic Aperture (DA) of the accelerator in the presence of misalignment errors must be evaluated. The DA is defined here as the maximum initial horizontal normalized amplitude that the particle can have without any losses due to single particle dynamics effects over 30,000 turns of the entire acceleration cycle. This is a fundamental criterion in order to determine the tolerance of the lattice to imperfections. Each of the 12 magnets is transversely (horizontally and vertically) offset randomly using a Gaussian distribution with a standard deviation σ and a cutoff at 3σ . For each error, 100 different patterns are tested and an initial normalized vertical displacement at 20 mm.mrad is chosen. The effect of the misalignment on the DA is shown in Figure 3, where one can see that with reasonable alignment errors ($\sigma \approx 100 \mu\text{m}$) the DA is essentially unchanged. However, the DA of the lattice with trim quadrupoles is almost 3 times larger than the DA of the bare lattice.

Conclusion

We have developed a novel concept for a racetrack medical accelerator that enables dual acceleration of protons and carbon ions. The proposed machine has a large dynamic acceptance, which makes it suitable for high intensity applications. We have also demonstrated for the first time that it is possible to overcome the problem of resonance crossings by timely variation of the field of the trim quadrupoles during the acceleration cycle.

Reference

[1] M. Haj Tahar, “Novel concept of a Non-Scaling Fixed Field Alternating Gradient Accelerator”, invited talk FFAG’17 workshop (September 8th, 2017). ■

Simultaneous Detection of Multiple Reactive Species

Guy Garty and David J. Brenner

During radiolysis, multiple reactive oxygen and nitrogen species (ROS/RNS) are formed in the cellular environment. These radiation-induced reactive species are thought to contribute to genomic instability and ultimately to cancer [1-3]. In order to understand perturbations of oxidative metabolism, in the context of DNA damage and cellular dysfunction [4-6], it is useful to combine an irradiation platform, such as a microbeam with a method for measuring ROS/RNS yields in single cells.

While generic oxidative stress can be quantified, on a microbeam platform, by incorporating redox-sensitive dyes such as DHR-123 (Dihydrorhodamine) into the cells and following them using fluorescence microscopy, it is extremely difficult to expand this technique to quantify the formation of multiple reactive species. Primarily, most redox-sensitive dyes have very similar emission spectra (cf. Table in [7]).

Previously we have reported on preliminary data obtained using the CE-LIF system at the Sweedler lab [7]; as described below, we have replicated and expanded these results, using our own home-built system integrated into one of the charged particle microbeam endstations at RARAF.

CE-LIF at RARAF

Our CE-LIF system (Fig. 1) is centered on a 70 cm long fused silica capillary (50 μm inner diameter). One end is mounted on a 6 axis manipulator (Fig. 1a), and the other end inserted into a sheath flow assembly [8] (Fig. 1b).

In order to load reagents into the capillary a 5 μl drop containing an analyte mixture is placed on a microscope coverslip on the microbeam endstation stage. The capillary tip is inserted into the droplet and the waste

reservoir is lowered by 30 cm for 10-30 sec. This loads 10-30 nl into the capillary. The capillary tip is then moved into a grounded steel vial containing run buffer (50 mM Borate pH 9, See Fig. 1a insert), the LIF enclosure locked, room lights turned off and acquisition started. About 1 sec later high voltage (-30kV) is applied between the grounded run buffer vial and the waste reservoir, resulting in a field of ~ 425 V/cm along the capillary.

This results in both electroosmotic flow of all reagents along the capillary and electrophoretic separation of analytes by mobility. After a few minutes the analytes arrive at the sheath flow cuvette where they are detected using laser induced fluorescence.

Excitation is provided by a 473 nm 50 mW Solid State laser, coupled via optical fiber (orange fiber on the left of Fig. 1b) to the LIF enclosure. The laser is focused on the sheath flow cuvette, just below the tip of the capillary, using a long working distance 10x objective. Emitted fluorescence light is collected perpendicularly via a 40 mm focal length lens onto a second optical fiber, connected to a high sensitivity spectrometer.

The optical fibers serve a dual role of decoupling the LIF system electrically and mechanically from the laser and spectrometer, allowing the latter to be placed anywhere on the table housing the microbeam endstation.

Fluorescence emission spectra from the spectrometer are collected roughly once per second for 10-20 minutes, depending on the migration times of the analytes.

Separation of ROS and RNS probes

The main goal of this work is to be able to simultaneously quantify more than one reactive species. Figure 2a shows a wavelength resolved electropherogram

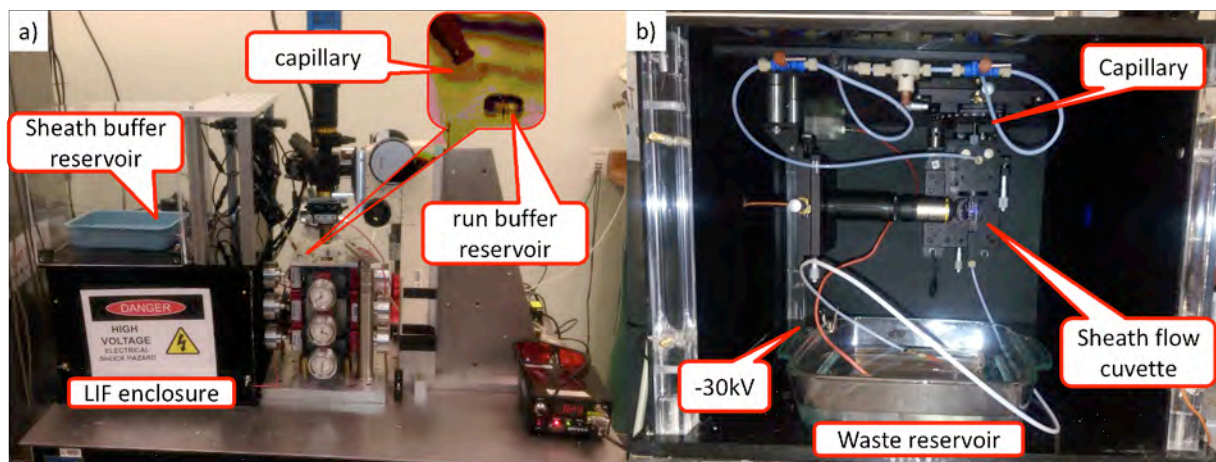


Figure 1. Images of the (a) CE and (b) LIF system constructed at the RARAF microbeam endstation: The insert in (a) shows close-up of the capillary in the run buffer reservoir.

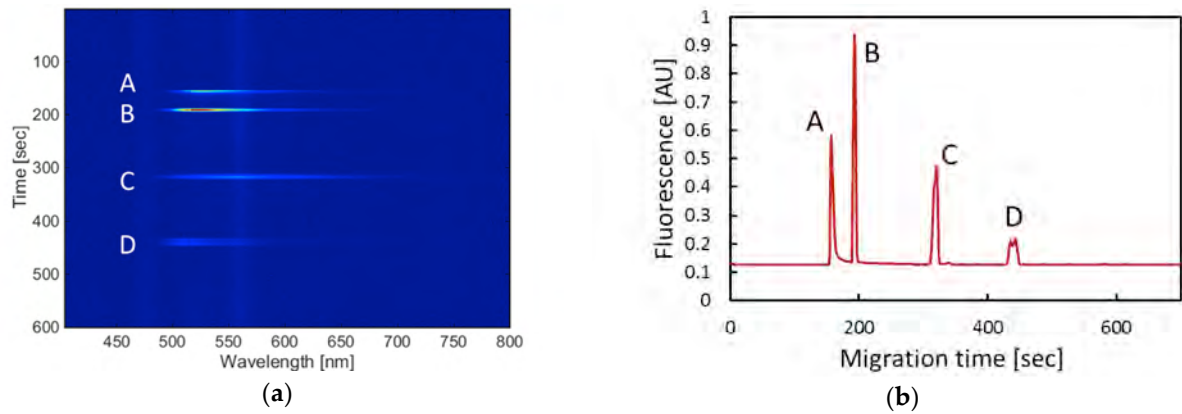


Figure 2. (a) wavelength-resolved electropherogram of Rh-123, NO-activated DAF-2 and GSH-NDA. b) Integrated electropherogram (summing over 500-700 nm).

(brightness vs. migration time and wavelength) of a 10 nL volume of a 1:1:1 mixture of

- Rh-123 (3.3 μM), representing oxidized Rhodamine
- GSH-NDA (made with 5 mM Glutathione and 5 mM NDA)
- NO-activated DAF-2 (5 μM DAF-2 + 0.6 μM Diethylamine NONOate – a NO donor)

Besides the laser scatter line, appearing as a constant vertical line at around 473 nm and a second much dimmer vertical line at 560-570 nm, due to Raman scattering of the laser in water, four peaks are evident at migration

times of 157 sec, 192, 319 and 441 sec. Integrating over wavelengths between 500 and 700 nm, we get the conventional electropherogram shown in Fig. 2b.

Peak identification

Based on migration times of the individual components, we expect that Peak B is Rh-123, Peak C is GSH-NDA and peak D is NO-DAF-2; however the precise migration times are somewhat different than those measured on previous days for the individual reagents.

In order to validate the identities of the peaks, we can use the extra information provided by the emission

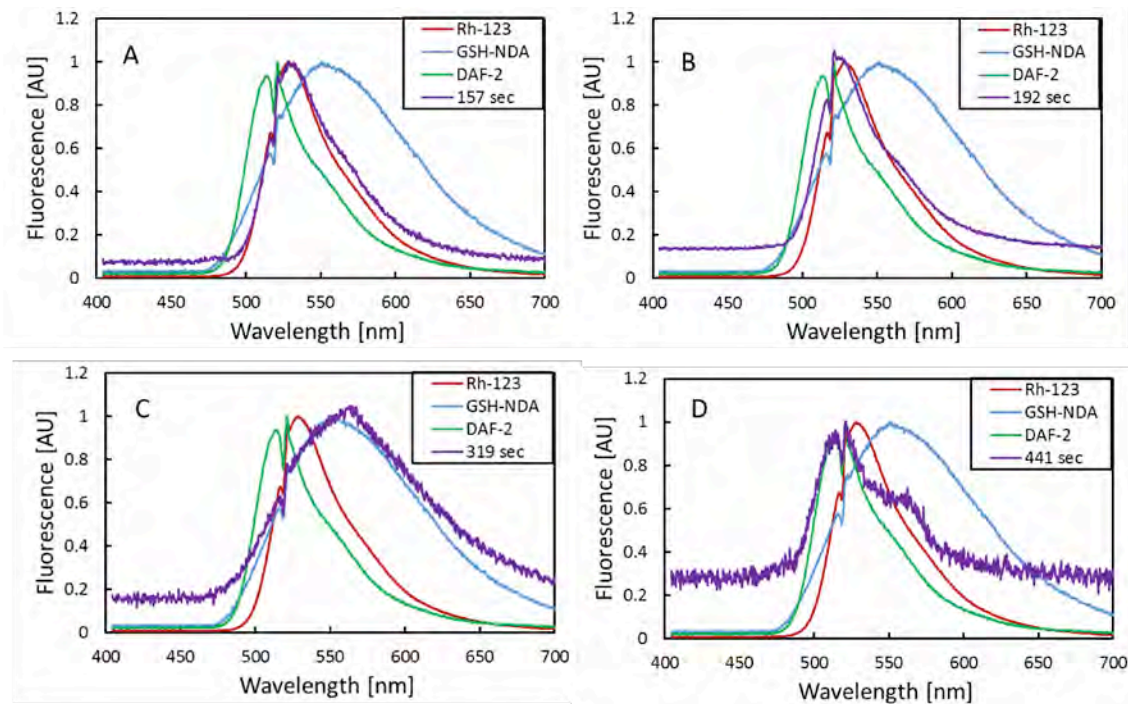


Figure 3. Emission spectra for each of the 4 peaks in Fig. 2b. In each panel, the red, green and blue curves correspond to the emission spectra of Rh-123, GSH-NDA and NO-activated DAF-2. The purple curve corresponds to a row in Fig 2a, roughly corresponding to the center of each peak.

spectrum. Figure 3 shows the emission spectra measured for individual analytes injected into the capillary, overlaid on the spectrum measured for each of the peaks. It is clear from the figure that peaks A and B correspond to Rhodamine-123, peak C corresponds to GSH-NDA and peak D corresponds to NO- activated DAF-2.

Conclusions

We have integrated a wavelength-resolved CE-LIF system into one of the microbeam endstations at the Radiological Research Accelerator Facility with the intent of simultaneously measuring reactive oxygen and nitrogen species in cells shortly following irradiation. The next steps are to extend this system to the detection of superoxide, using DHE as a derivatizing agent, and detection of oxidized glutathione, by incorporating post column derivatization. In parallel to these developments we will develop electrokinetic loading to allow picking single cells from a microbeam dish.

References

1. Dayal, D., et al., Hydrogen peroxide mediates the radiation-induced mutator phenotype in mammalian cells. *Biochem J*, 2008. 413(1): p. 185-91.
2. Dayal, D., et al., Mitochondrial complex II dysfunction can contribute significantly to genomic

- instability after exposure to ionizing radiation. *Radiat Res*, 2009. 172(6): p. 737-45.
3. Ralph, S.J., et al., The causes of cancer revisited: "mitochondrial malignancy" and ROS-induced oncogenic transformation - why mitochondria are targets for cancer therapy. *Mol Aspects Med*, 2010. 31(2): p. 145-70.
4. Park, S.H., et al., Sirt3, Mitochondrial ROS, Ageing, and Carcinogenesis. *Int J Mol Sci*, 2011. 12(9): p. 6226-39.
5. Spitz, D.R., Metabolic oxidative stress and low dose radiation responses: are mitochondria involved. *Health Phys*, 2011. 100(3): p. 295.
6. He, C., et al., Mitochondrial Cu,Zn-superoxide dismutase mediates pulmonary fibrosis by augmenting H₂O₂ generation. *J Biol Chem*, 2011. 286(17): p. 15597-607.
7. Garty, G., et al., Microbeam-coupled Capillary Electrophoresis. *Radiation Protection Dosimetry*, 2015. 166: p. 188-191.
8. Wuttke, K., Müller, W.-U., and Streffer, C., The sensitivity of the in vitro cytokinesis-blocked micronucleus assay in lymphocytes for different and combined radiation qualities. *Strahlentherapie und Onkologie*, 1998. 174(5): p. 262-268. ■

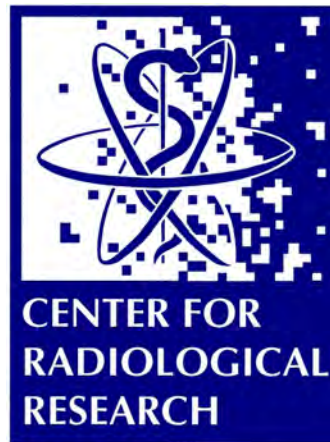


Top: RARAF 50th Anniversary dinner. (l to r): Manuela Buonanno and Christian Siebenwirth welcome guests. Norman Kleiman and David Brenner



Bottom: Hijinks celebrating the Anniversary during the annual RARAF site visit. (l to r) David Brenner, Guy Garty

FAR-UVC STUDIES



222-nm Light Prevents MRSA Infection of Superficial Wounds *in vivo*

Brian Ponnaiya, Manuela Buonanno, David Welch, Igor Shuryak, Gerhard Randers-Pehrson, and David J. Brenner

Introduction

The majority of surgical site infection (SSI) are believed to be caused by airborne transmission of bacteria alighting onto the wound [1, 2]. SSI infections from drug-resistant bacteria such as methicillin resistant *Staphylococcus aureus* (MRSA) currently present a major health care burden.

Surgical wound irradiation with conventional germicidal UV lamps, typically emitting 254-nm light, has shown great promise for infection control. However, the major downside of using conventional germicidal UV lamps during surgery is that exposure to germicidal 254-nm light is a health hazard, causing skin cancer and cataracts [3, 4].

Previously, we have shown that 222-nm light kills bacteria efficiently, but without the skin damaging effects associated with conventional germicidal UV exposure [5]. Based on our earlier studies *in vitro* and *in vivo*, here we hypothesized that exposure to far-UVC light onto the surgical wound area during surgery is a suitable approach to killing bacteria both in the air and as they lay down onto the wound area or settle on the surgeon's hands and instruments, without adverse health hazards for patient or staff.

To mimic the scenario wherein incisions are infected during surgical procedures as bacteria in the room alight on the skin, we developed a mouse protocol in which MRSA was spread on a defined area of the skin and then exposed to UVC light. We measured bactericidal efficacy (CFU/g) and DNA photodamage two and seven days after exposure to different fluences of 222-nm light vs. 254-nm light.

Results

Figure 1 shows bacterial counts (CFU/g) in skin of mice two days (Fig. 1A) or seven days (Fig. 1B) after infection with MRSA and subsequently exposed to 40 or 300 mJ/cm² of 222- or 254-nm light. The results were compared with bacterial counts measured in skin incisions that were uninfected by applying saline prior to exposure to the UV light (sample denoted as Saline) and to those obtained from skin incisions that were infected but not UVC-irradiated (sample denoted as MRSA).

Compared to incisions that were infected but not UVC-irradiated (MRSA), both fluences from either 222- or 254-nm light resulted in a statistically significant reduction of bacteria counts on day 2 day 7 (see Fig. 1 caption for specific p values).

We measured DNA photodamage as percentage of cyclobutane pyrimidine dimers (CPD) induced by 40 or 300 mJ/cm² from the 222-nm lamp or the 254-nm emitting lamp, two or seven days after exposure (Fig. 2). In agreement with our previous studies [5-7], 254-nm light produced high yields of CPD at both fluences that were significantly higher than controls (p < 0.005) and persisted up to seven days after exposure (p < 0.05). In contrast, neither fluence from 222-nm light produced the pre-mutagenic skin lesions.

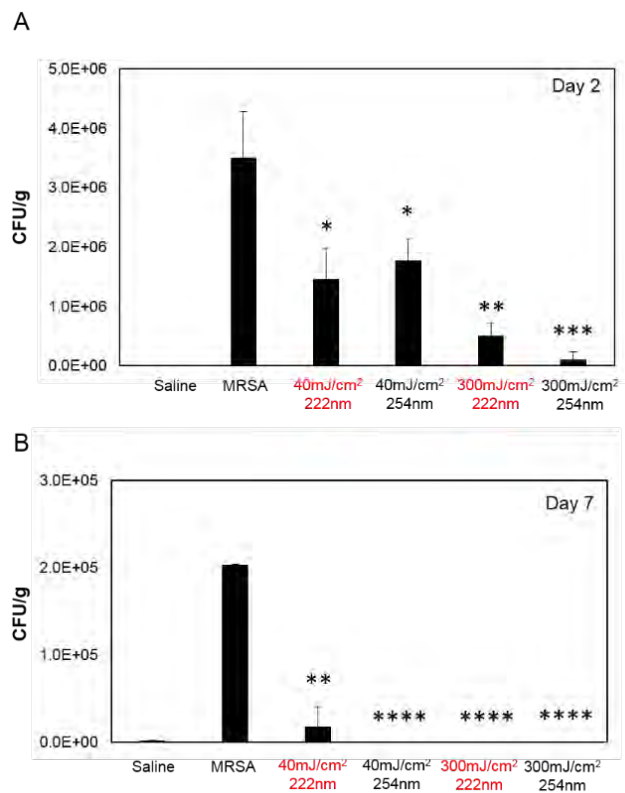


Figure 1. Bactericidal efficacy of UVC light exposure of superficial wounds infected with MRSA. CFU/g of mouse skin where MRSA was spread before exposure to 40 or 300 mJ/cm² delivered by the 222- or 254-nm light, and followed by a superficial incision. Negative controls were obtained from skin incisions that were uninfected by applying saline prior to exposure to either UV lamp (Saline), whereas skin incisions that were infected but not exposed to the UV light (MRSA) represented the positive controls. Tissues were harvested at A) day 2 or B) day 7 after exposure. *p < 0.05, **p < 0.01, ***p < 0.005, ****p < 0.0001 compared to positive controls (MRSA).

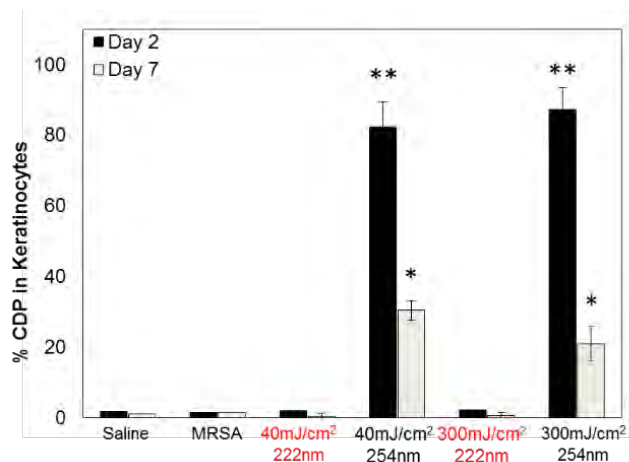


Figure 2. Percentage of pre-mutagenic skin lesion CPD in keratinocytes two or seven days after exposure to 40 or 300 mJ/cm² from the 222-nm or 254-nm light to that of skin incisions that were uninfected by applying saline prior to exposure by either UV lamp (Saline). Skin incisions that were infected but not exposed to the UV light (MRSA) represented the positive controls; values represent the average \pm SD measured in nine randomly selected field of view per mouse. * p < 0.05, ** p < 0.005 compared to positive controls (MRSA).

Conclusions

It has been estimated that up to 90% of pathogenic bacteria detected from surgical wounds in the operating room are airborne. During surgical procedures, bacteria-laden airborne particles may directly enter the surgical site or settle on surgical instruments, resulting in SSI.

Using a protocol to simulate superficial wounds infected with bacteria potentially alighting onto the

surgical wound from the room air or that for instance may be carried by bacteria settling on the clinical staff hands or surgical tools, here we showed that 222-nm light had the same bactericidal properties of 254-nm light, but without causing skin damage.

References

- Ritter, M.A., E.M. Olberding, and R.A. Malinzak, Ultraviolet lighting during orthopaedic surgery and the rate of infection. *J Bone Joint Surg Am*, 2007. 89(9): p. 1935-40.
- Gosden, P.E., A.P. MacGowan, and G.C. Bannister, Importance of air quality and related factors in the prevention of infection in orthopaedic implant surgery. *J Hosp Infect*, 1998. 39(3): p. 173-80.
- Setlow, J.K. and R.B. Setlow, Ultraviolet action spectra of ordered and disordered DNA. *Proc Natl Acad Sci U S A*, 1961. 47: p. 1619-27.
- Balasubramanian, D., Ultraviolet radiation and cataract. *J Ocul Pharmacol Ther*, 2000. 16(3): p. 285-97.
- Buonanno, M., et al., Germicidal Efficacy and Mammalian Skin Safety of 222-nm UV Light. *Radiat Res*, 2017.
- Buonanno, M., et al., 207-nm UV Light - A Promising Tool for Safe Low-Cost Reduction of Surgical Site Infections. I: In Vitro Studies. *PLoS ONE*, DOI: 10.1371/journal.pone.0076968, 2013.
- Buonanno, M., et al., 207-nm UV Light-A Promising Tool for Safe Low-Cost Reduction of Surgical Site Infections. II: In-Vivo Safety Studies. *PLoS One*, 2016. 11(6): p. e0138418. ■



David Brenner presenting at TED2017.
 Photos: Bret Hartman / TED by Creative Commons License CC BY-NC 2.0

Quantification of Killing MRSA with Far-UVC Light Using an Optical Diffuser

David Welch, Manuela Buonanno, Igor Shuryak, Gerhard Randers-Pehrson, Henry M. Spotnitz^a, and David J. Brenner

Wound infections from drug-resistant bacteria such as methicillin-resistant *Staphylococcus aureus* (MRSA) present major health care challenges with over 23,000 cases resulting in death in the United States each year. While significant resources have been applied to combat infection from drug-resistant bacteria, and incremental gains have been reported, effective resolutions remain elusive.

One method of microbial disinfection is using ultraviolet (UV) light, conventionally using low-pressure mercury lamps emitting primarily at 254 nm. UV light at 254 nm can efficiently kill both drug-sensitive and multi-drug-resistant bacteria. However, the widespread use of germicidal ultraviolet light has been very limited because conventional UVC light sources are a human health hazard, being both carcinogenic and cataractogenic. By contrast, it has been shown that far-UVC light generated

by filtered excimer lamps emitting in the 207 to 222 nm wavelength range, efficiently kills drug-resistant bacteria, without apparent harm to exposed mammalian skin [1,2,3].

Adventitious infections due to pathogens such as MRSA are especially prominent within wounds surrounding catheters, drivelines for left ventricular assist devices, and lines for hemodialysis. In these cases, a far-UVC light source such as an excimer lamp would not be sufficient for disinfection because the implanted lines would act as shielding for much of the wound. Additionally, the far-UVC light cannot penetrate the skin to disinfect within the wound. One possible solution to these situations is to direct light around and within complex geometries using fiber optics. Pairing the fiber optic with a diffusing element capable of emitting the light radially from the fiber would allow for application over a large target area within the percutaneous site that would be impossible to expose otherwise.

This study examines the use of far-UVC light generated from a laser source to be delivered via fiber optics to an optical diffuser element for bactericidal applications. These studies are performed *in vitro* as a first step to demonstrate the efficacy of this method.

Test methods

The experimental setup involved positioning a 5 cm long diffusing fiber over a petri dish. A schematic of the test configuration is shown in Figure 1. The distance from the fiber to the agar surface was 1 cm. A deep UV laser, operating at 224 nm, was focused into the proximal end of the diffusing fiber and transmitted to the diffusing tip through approximately 1 meter of fiber optics.

The first test performed with the experimental setup was an area disinfection assay. One 50- μ l aliquot of 10^6 CFU/ml of MRSA was spread evenly across the entire agar surface. The laser was powered for 2 hours to expose the sample and then the dish was incubated overnight to allow bacteria growth.

A second series of tests were performed to generate quantifiable data. The test configuration is shown in Figure 1, with four identical areas of MRSA located directly beneath the diffusing fiber. The exposure times for the four areas were 30, 60, 90, and 120 minutes. The four exposure doses delivered were measured as 4.1, 8.1, 12.2, or 16.3 mJ/cm². Zero dose controls were achieved by not exposing the areas to any far UVC irradiation. Swabs of each MRSA area were taken and the results were quantified with a colony forming assay.

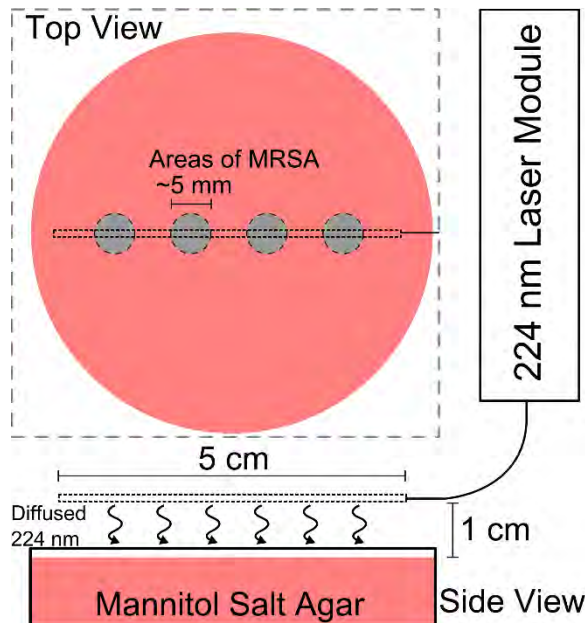


Figure 1. A schematic of the test setup shows the diffusing fiber suspended over the agar dish. The laser light is transmitted through the fiber and then diffuses out of all sides of the diffusing fiber. Some light does not irradiate the MRSA because it is directed away from the dish. We measured the UV exposure amount by placing a UV sensitive film in the exact position as the top of the agar dish. The top view of the figure shows the positions of the MRSA during irradiation.

^aDepartment of Surgery, New York Presbyterian Hospital

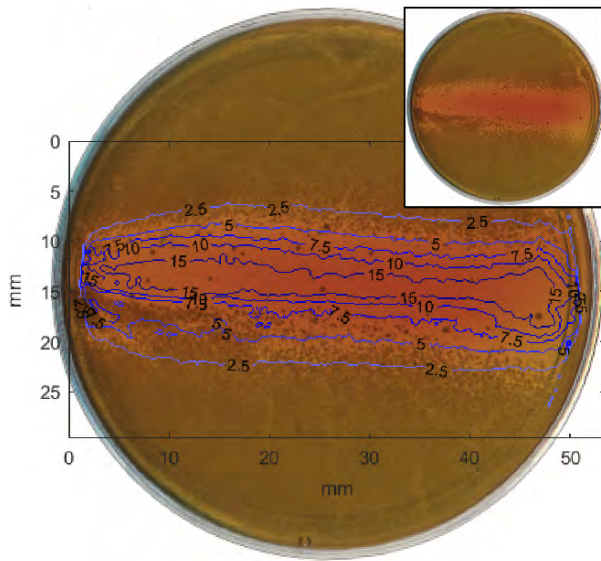


Figure 2. A top-down picture of the MRSA on the agar surface following exposure shows the area of killing. The raw image is shown in the top right. A contour map of the exposure doses is overlaid on the main image.

We used the USA300 strain (multilocus sequence type 8, clonal complex 8, staphylococcal cassette chromosome mec type IV), which was originally encountered in the community, but now is a major cause of invasive nosocomial infections. Fresh colonies of *S. aureus* were inoculated into tryptic soy broth and grown overnight at 37°C. The culture was then resuspended in fresh broth and grown to mid-log phase for 3 h. Bacteria were collected by centrifugation, washed, resuspended in broth, and adjusted to an optical density at 600 nm of 0.5 in order to achieve a density of 10^6 CFU/ml. The area disinfection assay used a 50 μ l aliquot of MRSA spread across the entire dish. The quantified assay used 5 μ l aliquots for each exposure dose.

The UV irradiance experienced by the bacteria on the surface of the agar was quantified using unlaminate Gafchromic EBT3 film. As we have shown [4,5], this film responds to UV irradiance with a color change, which can be quantified to determine the total exposure. We placed a piece of film in the exact position as the dish of bacteria and measured the irradiance upon the surface.

Results

The killing of MRSA across a surface is shown in Figure 2. An unmodified picture of the bacterial plate is shown in the inset of the figure. Dark areas on the figure indicate areas of bacterial growth. The figure includes an overlay of contour lines which indicate the levels of far-UVC exposure in mJ/cm^2 for the two-hour test as calculated using film dosimetry. The area of highest exposure coincides with the area directly beneath the cylindrical diffuser. Less far-UVC exposure to an area on the surface corresponds to an increase in the amount of MRSA growth. Irregularities in the exposure pattern are due to physical variations in the diffuser itself that impacted the uniformity of the diffusion of light.

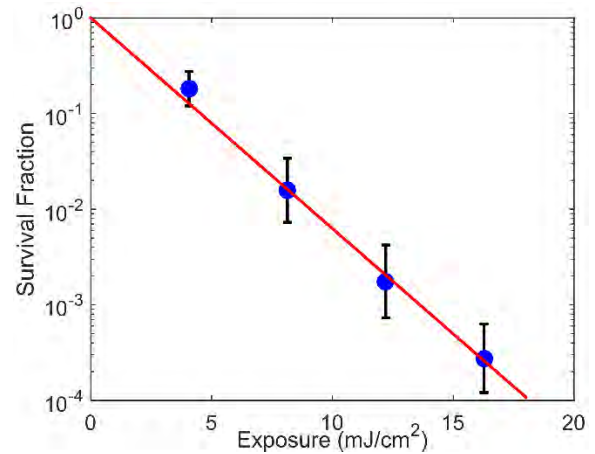


Figure 3. Results for the survival assay for the killing of MRSA on a surface using far-UVC light emitted from a diffuser are plotted as bacterial survival fraction relative to zero-dose controls for the different exposures. The data follow a log-linear decay with a rate constant of $0.51 \text{ cm}^2/\text{mJ}$. The calculated exposure dose required to kill 90% of bacteria is $D_{90} = 4.5 \text{ mJ}/\text{cm}^2$.

Figure 3 shows MRSA killing as a function of exposure to far-UVC light generated by a 224-nm laser and delivered through a diffuser. The reduction of bacterial survival followed a classical log-linear UV disinfection model, with rate constant $k = 0.51 \text{ cm}^2/\text{mJ}$ (standard error = 0.03, $R^2=0.76$), with a 95% bootstrapped confidence interval of $0.44 \text{ cm}^2/\text{mJ}$ to $0.57 \text{ cm}^2/\text{mJ}$. The rate constant corresponds to inactivation cross-sections of $D_{90} = 4.5 \text{ mJ}/\text{cm}^2$. A line plotting best-fit regression of the inactivation rate is included on Figure 3.

Conclusions

This study shows for the first time that far-UVC sterilization delivered using fiber optics is a promising technology in preventing infections caused by bacterial contamination. Delivery of a far-UVC light from a laser, through an optical fiber, and emitted from a diffuser is a unique application of this technology.

The area killing assay results shown in Figure 2 illustrate that this simple setup using only a single far-UVC laser source is capable of killing bacteria in vitro over an area much larger than the original laser beam diameter. The effectiveness of killing MRSA with far-UVC delivered in this manner was quantified through the survival assay. The disinfection rate constant of $0.51 \text{ cm}^2/\text{mJ}$, with $D_{90} = 4.5 \text{ mJ}/\text{cm}^2$, is comparable to surface disinfection studies done on antibiotic-susceptible *S. aureus* with germicidal light at 254 nm emitted from a lamp, which had a rate constant $k = 0.72 \text{ cm}^2/\text{mJ}$ with $D_{90} = 3.2 \text{ mJ}/\text{cm}^2$. Overall, the qualitative area assay results in Figure 2 displayed general agreement with the quantified survival response assay results.

This study demonstrates that far-UVC light emitted from a laser and delivered using an optical diffuser is an effective tool to kill MRSA in vitro. The dose required to kill bacteria on a surface with far-UVC is slightly higher than with conventional UVC at 254 nm; however, given

the lack of harmful biological effects with far-UVC, it is an attractive option for sterilization within wounds. The ability to diffuse the laser output over a large area makes this a viable solution for sterilization of infection prone tissues, such as around a catheter or other skin penetrating medical device.

References

1. Buonanno, M., et al., 207-nm UV Light - A Promising Tool for Safe Low-Cost Reduction of Surgical Site Infections. I: In Vitro Studies. PLOS ONE, 2013. 8(10): p. e76968.
2. Buonanno, M., et al., 207-nm UV Light—A Promising Tool for Safe Low-Cost Reduction of Surgical Site Infections. II: In-Vivo Safety Studies. PLOS ONE, 2016. 11(6): p. e0138418.
3. Buonanno, Manuela, et al. "Germicidal efficacy and mammalian skin safety of 222-nm UV light." Radiation research 187.4 (2017): 493-501.
4. Welch, David, et al. "Unlaminated Gafchromic Ebt3 Film For Ultraviolet Radiation Monitoring." Radiation protection dosimetry 176.4 (2017): 341-346.
5. Welch, D., Spotnitz, H. M. and Brenner, D. J. (2017), Measurement of UV Emission from a Diffusing Optical Fiber Using Radiochromic Film. Photochem Photobiol, 93: 1509–1512. doi:10.1111/php.12798. ■

Efficacy of Far-UVC for Inactivation of Aerosolized Influenza Virus

David Welch, Manuela Buonanno, Veljko Grilj, Igor Shuryak, Connor Crickmore^a, Alan W. Bigelow, Gerhard Randers-Pehrson, Gary W. Johnson, and David J. Brenner

A direct approach to prevent the transmission of airborne-mediated diseases such as influenza is inactivation of the corresponding airborne pathogens. The airborne antimicrobial efficacy of ultraviolet (UV) light has long been established with germicidal UV light (typically at 254 nm) effective against both drug-sensitive and multi-drug-resistant bacteria as well as viruses. However, the widespread use of germicidal ultraviolet light in public settings has been very limited because conventional UVC light sources are a human health hazard, being both carcinogenic and cataractogenic.

By contrast, we have earlier shown that far-UVC light generated by filtered excimer lamps, emitting in the 207 to 222 nm wavelength range, efficiently inactivates drug-resistant bacteria without apparent harm to exposed mammalian skin [1,2,3].

In that a major pathway for the spread of influenza is aerosol transmission, we investigate for the first time the efficacy of far-UVC 222-nm light for inactivating airborne viruses carried by aerosols – with the goal of providing a potentially safe alternative to conventional 254-nm germicidal lamps to inactivate airborne microbes.

Test methods

A one-pass, dynamic aerosol / virus irradiation chamber was constructed in a similar configuration to that used by Ko et al. [4], Lai et al. [5], and McDevitt et al. [6]. An overview of the system is shown in Figure 1.

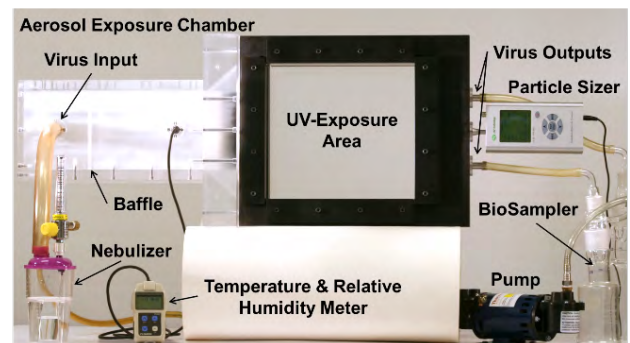


Figure 1. The aerosol exposure chamber is pictured.. Components of the setup include: a nebulizer, baffles, an RH and temperature meter, a particle sizer, far-UVC lamps with band pass filters (not pictured), a far-UVC transmitting plastic window to the exposure area, a reflective aluminum surface at the rear of the exposure area, and a BioSampler. Pumps are used to pressurize the nebulizer for aerosol generation and to control flow through the system. Flow control valves allow adjustments through the system. HEPA filters are included on all air inputs and outputs. The vertically stacked lamps are directed at the window in the side of the chamber to expose the aerosols passing horizontally.

Aerosolized viruses were generated by adding a virus solution into a high-output extended aerosol respiratory therapy (HEART) nebulizer (Westmed, Tucson, AZ) and operated using a dual-head pump (Thermo Fisher 420-2901-00FK, Waltham, MA) with an input flow rate of 11 L/min. The aerosolized virus flowed into the irradiation chamber where it was mixed with independently controlled inputs of humidified and dried air. Humidified

^aREU summer student from St. Edmund Hall, Oxford University, Oxford, UK.

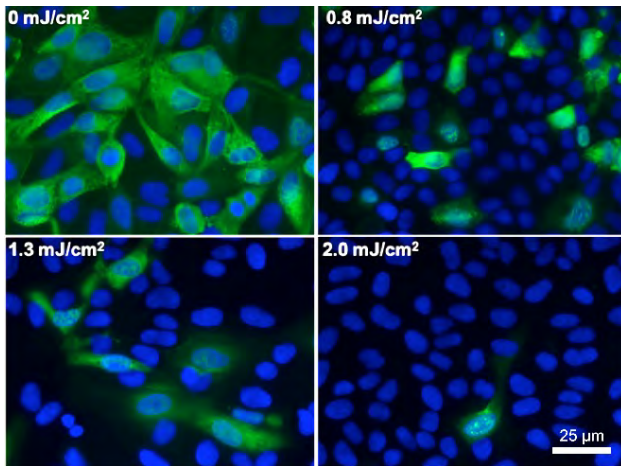


Figure 2. Typical fluorescent images of epithelial cells infected with influenza A virus (H1N1). The viruses were exposed in aerosolized form in the irradiation chamber to doses of 0, 0.8, 1.3 or 2.0 mJ/cm² of 222-nm far-UVC light. Infected cells fluoresce green.

air was produced by bubbling air through water, while dry air was provided by passing air through a desiccant air dryer (X06-02-00, Wilkerson Corp, Richland, MI). Adjusting the ratio of humid and dry air enabled control of the relative humidity (RH) within the irradiation chamber, which, along with the nebulizer settings, determined the aerosol particle size distribution. An optimal RH value of 55% resulted in a distribution of aerosol particle sizes similar to the natural distribution from human coughing and breathing, which has been shown to be distributed around approximately 1 µm, with a significant tail of particles less than 1 µm.

After combining the humidity control inputs with the aerosolized virus, input flow was directed through a series of baffles that promoted droplet drying and mixing to produce an even particle distribution and stable humidity. The RH and temperature inside the irradiation chamber were monitored using an Omega RH32 meter (Omega Engineering Inc., Stamford, CT) immediately following the baffles. A Hal Technologies HAL-HPC300 particle sizer (Fontana, CA) was adjoined to the irradiation chamber to allow for sampling of particle sizes throughout operation.

During UV exposure, the 222-nm lamps were placed 11 cm from the irradiation chamber window. The lamps were directed at the 26 cm × 25.6 cm chamber window, which was constructed of 254-µm thick UV transparent plastic film (Topas 8007X10, Topas Advanced Polymers, Florence, KY), and which had a transmission of ~65% at 222 nm. The wall of the irradiation chamber opposite the transparent window was constructed with polished aluminum in order to reflect a portion of the UVC light back through the exposure region, therefore increasing the overall exposure dose by having photons pass in both directions. The depth of the irradiation chamber between the window and the aluminum panel was 6.3 cm, creating a total exposure volume of 4.2 L.

Flow of the aerosols continues out of the irradiation chamber to a set of three-way valves that could be configured to either pass through a bypass channel (used when no sampling was required), or a BioSampler (SKC Inc, Eighty Four, PA) used to collect the virus. The BioSampler uses sonic flow impingement upon a liquid surface to collect aerosols when operated at an air flow of 12.5 L/min. Finally, flow continued out of the system through a final HEPA filter and to a vacuum pump (WP6111560, EMD Millipore, Billerica, MA). The vacuum pump at the end of the system powered flow through the irradiation chamber. The flow rate through the system was governed by the BioSampler. Given the flow rate and the total exposure volume of the irradiation chamber, 4.2 L, a single aerosol droplet passed through the exposure volume in approximately 20 seconds.

The entire irradiation chamber was set up inside a certified class II type A2 biosafety cabinet (Labconco, Kansas City, MO). All air inputs and outputs were equipped with HEPA filters (GE Healthcare Bio-Sciences, Pittsburgh, PA) to prevent unwanted contamination from entering the chamber, as well as to block any of the virus from releasing into the environment.

During each testing period, which lasted for 30 minutes, the inside of the irradiation chamber was exposed to 222 nm far-UVC light through the UVC semi-transparent plastic window. Variation of the far-UVC dose delivered to aerosol particles was achieved by inserting additional UVC semi-transparent plastic films, identical to the material used as the chamber window, between the lamps and the chamber window. The extra plastic films uniformly reduced the power entering the chamber. The three test doses of 0.8, 1.3 and 2.0 mJ/cm², were achieved by adding two, one, or no additional plastic films, respectively. Zero-dose control studies were conducted with the excimer lamps turned off. Dosimetry was verified using unlaminate EBT3 [7] and an 818-UV/DB low-power UV enhanced silicon photodetector.

Influenza A virus [A/PR/8/34 (H1N1)] was used as the test pathogen. We measured viral infectivity with a focus forming assay that employs standard fluorescent immunostaining techniques to detect infected host cells and infectious virus particles. Images of stained cells were counted to measure the FFU(UV) as the ratio of cells infected with the virus divided by the total number of cells.

The surviving fraction (S) of the virus was calculated by dividing the fraction of cells that yielded positive virus growth at each UV dose (FFU(UV)) by the fraction at zero dose (FFUcontrols): $S = \text{FFU(UV)} / \text{FFUcontrols}$. Data was fit to a log-linear kinetics equation for analysis.

Results

Figure 2 shows representative fluorescent 40x images of mammalian epithelial cells incubated with airborne viruses that had been exposed in aerosolized form to far-

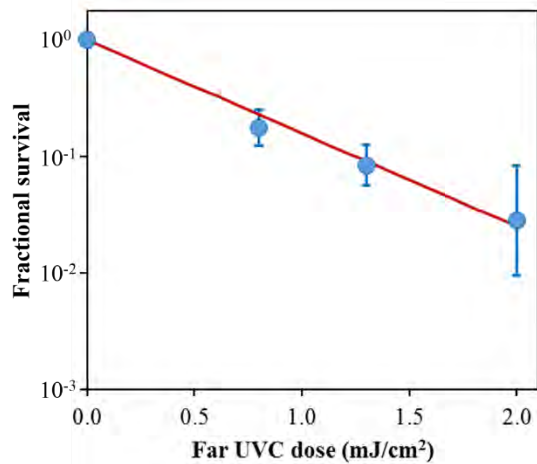


Figure 3. Fractional survival, $FFU(UV) / FFU_{controls}$, is plotted as a function of the 222-nm far-UVC dose. Means and standard deviations refer to triplicate repeat studies and the line represents the best-fit regression to the exponential model.

UVC doses (0, 0.8, 1.3 or 2.0 mJ/cm²) generated by filtered 222-nm excimer lamps. Blue fluorescence was used to identify the total number of cells in a particular field of view, while green fluorescence indicated the integration of live influenza A (H1N1) viruses into the cells.

Figure 3 shows the surviving fraction, as a function of the incident 222-nm far-UVC dose, of exposed H1N1 aerosolized viruses, as measured by the number of focus forming units in incubated epithelial cells relative to unexposed controls. Linear regressions showed that the survival results were consistent with a classical exponential UV disinfection model with rate constant $k=1.8 \text{ cm}^2/\text{mJ}$ (95% confidence intervals 1.5-2.1 cm^2/mJ). The rate constant of 1.8 cm^2/mJ corresponds to an inactivation cross-section (dose required to inactivate 95% of the exposed viruses) of $D_{95} = 1.6 \text{ mJ}/\text{cm}^2$ (95% confidence intervals 1.4-1.9 mJ/cm^2).

Conclusions

We have shown for the first time that very low doses of far-UVC light efficiently inactivate airborne viruses carried by aerosols. For example, a very low dose of 2 mJ/cm² of 222-nm light inactivates >95% of airborne H1N1 virus. Our results indicate that far-UVC light is a powerful and inexpensive approach for prevention and reduction of airborne viral infections without the human health hazards inherent with conventional germicidal UVC lamps.

References

1. Buonanno, M., et al., 207-nm UV Light - A Promising Tool for Safe Low-Cost Reduction of Surgical Site Infections. I: In Vitro Studies. PLOS ONE, 2013. 8(10): p. e76968.
2. Buonanno, M., et al., 207-nm UV Light—A Promising Tool for Safe Low-Cost Reduction of Surgical Site Infections. II: In-Vivo Safety Studies. PLOS ONE, 2016. 11(6): p. e0138418.
3. Buonanno, Manuela, et al. "Germicidal efficacy and mammalian skin safety of 222-nm UV light." Radiation research 187.4 (2017): 493-501.
4. Ko, G., First, M.W. & Burge, H.A. Influence of relative humidity on particle size and UV sensitivity of Serratia marcescens and Mycobacterium bovis BCG aerosols. Tubercle and Lung Disease 80, 217-228 (2000).
5. Lai, K.M., Burge, H.A. & First, M.W. Size and UV Germicidal Irradiation Susceptibility of Serratia marcescens when Aerosolized from Different Suspending Media. Appl. Environ. Microbiol. 70, 2021-2027 (2004).
6. McDevitt, J.J., et al. Characterization of UVC Light Sensitivity of Vaccinia Virus. Appl. Environ. Microbiol. 73, 5760-5766 (2007).
7. Welch, David, et al. "Unlaminated Gafchromic Ebt3 Film For Ultraviolet Radiation Monitoring." Radiation protection dosimetry 176.4 (2017): 341-346. ■



Shanaz Ghandhi and Helen Turner

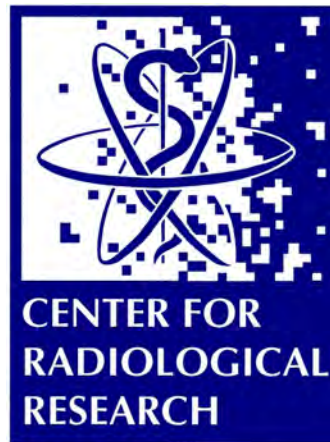


Micaela Cunha, Manuela Buonanno, and Sanjay Mukherjee



Vladimir Ivanov

CELLULAR AND MOLECULAR STUDIES



Cytokine Storm in Human Glioblastoma Cells after Combined Treatment with Gamma-irradiation, ATM Inhibitor and Cannabidiol

Vladimir N. Ivanov, Jinhua Wu, and Tom K. Hei

Glioblastoma (GBM) is the most common primary brain cancer. Despite advances in therapy, outcomes remain poor with a median survival rate of 12-15 months after initial diagnosis [1]. As such, there is an urgent need for new forms of therapy. Traditionally, surgery followed by external beam radiation therapy (EBRT) alone or in combination with chemotherapy (Temozolomide) is the standard of care for primary brain tumors including glioblastoma. However, the majority of GBM eventually relapses and new treatment modalities are desperately needed.

It is estimated that ~25% of GBM patients are using medical marijuana off label primarily for its palliative effects to reduce nausea, emesis and pain associated with chemotherapy [2]. However, the potential effects of cannabinoids (CBs) on glioma growth, and the ways that CBs may influence other (standard) forms of therapy are not well understood. There is evidence from several *in vitro* and *in vivo* studies that CBs at micromolar concentration (4-20 μM) can induce apoptosis and autophagy in glioma cells while having little or no effect on surrounding brain tissues [3, 4]. This range of CB doses is considered safe and even substantially lower than

cannabidiol (CBD) doses (25-64 μM) that are currently used in clinical trials for the treatment of epilepsy in young adults [5]. On the other hand, there is a single report that CBs at submicromolar concentration (0.1-0.3 μM) increased DNA synthesis and cellular proliferation of GBM whereas higher concentrations, such as those proposed in the present study (4-20 μM), resulted in apoptosis and cell death [6]. It should be noted that palliative applications of marijuana through smoking resulted in serum CBs concentration that is less than 1 μM , which is far below the level required for inducing cell death in glioma cells [6].

Several scientific groups, including our laboratory, investigate mechanisms of cell death induced by one of two main marijuana components, CBD without psychogenic activity, alone in combination with γ -irradiation. Recent investigation showed that the combination of both CBD and irradiation was more effective than either treatment alone at enhancing the therapeutic effects of irradiation in cell culture and in an experimental GBM model [7]. Besides the apoptotic type of death, programmed necrosis and inflammation-induced death might possibly be involved. Figure 1A demonstrates

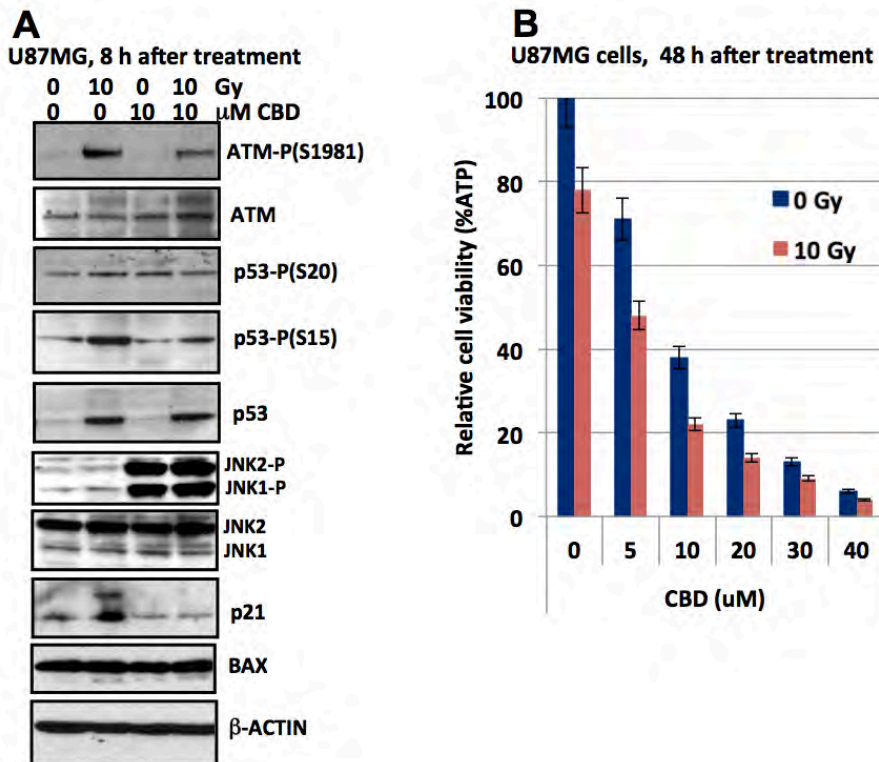


Figure 1. Cannabidiol (CBD) alone or in combination with γ -irradiation effectively kills U87MG human glioblastoma cells. (A) Western blot analysis of indicated signaling proteins 8 h after treatment of U87MG cells using CBD and γ -irradiation, alone or in combination. (B) Dose-dependent effects of CBD (5-40 μM), alone or together with γ -irradiation (10 Gy), on relative U87MG cell viability that was determined through intracellular ATP levels.

characteristic features of U87MG human glioblastoma treatment by γ -irradiation and CBD: activation of the ATM-p53 pathway and dramatic up-regulation of phospho-JNK1/2, respectively. CBD alone or especially in combination with irradiation at 10 Gy initiated dose-dependent glioblastoma cell death. This effect was quite specific for cancer cells in the brain, with substantially less effect for normal astrocytes (data not shown).

As expected, γ -irradiation, especially in combination with ATM inhibitor KU60072, resulted in cell cycle arrest at the G2/M phase and relatively modest levels of apoptotic death (% of pre-G1 cells) (Figure 2).

To evaluate a possible involvement of pro-inflammatory signaling in the regulation of death of human glioblastoma cells in culture, we used quantitative RT-PCR for determination of RNA expression levels of

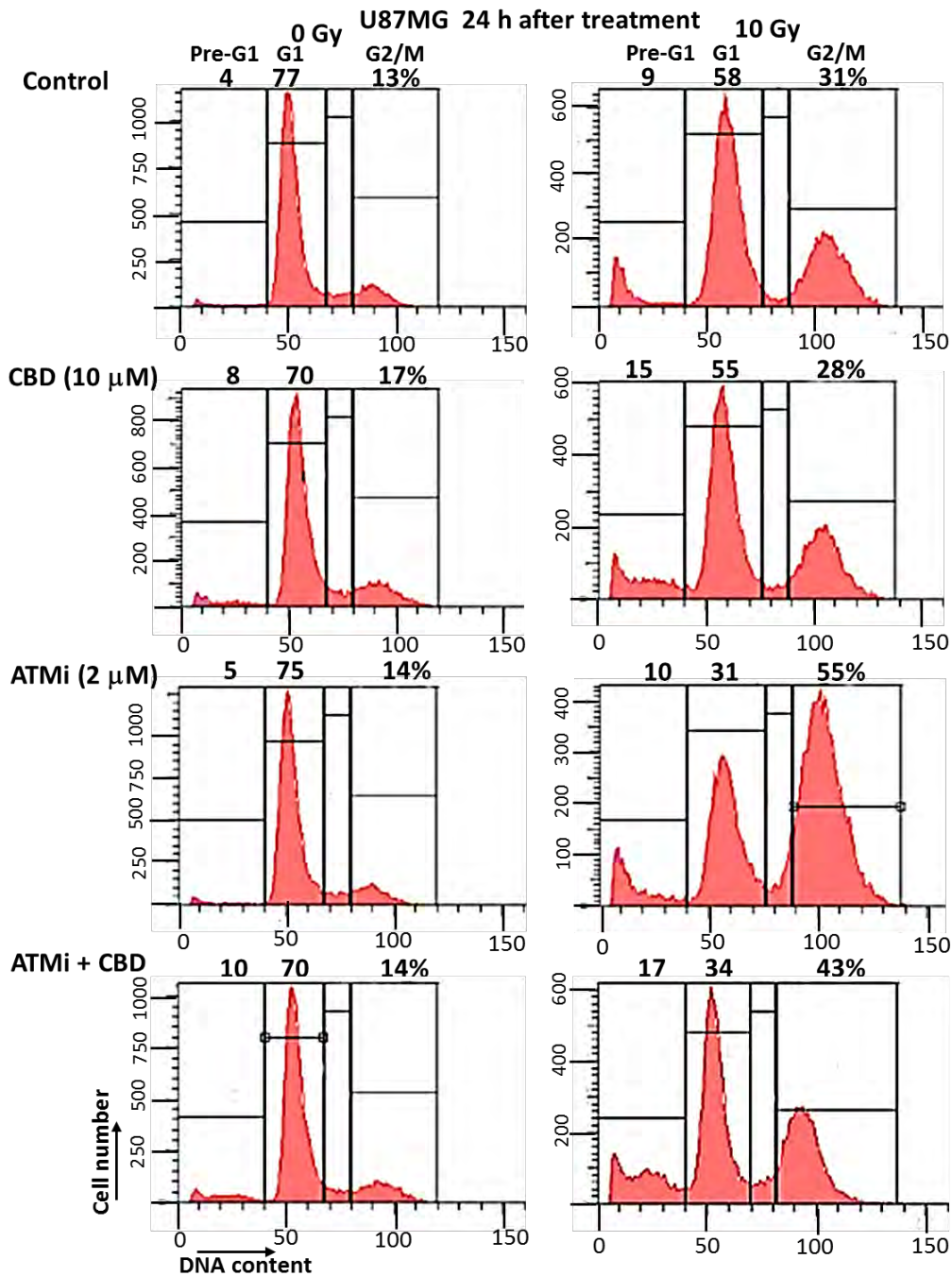


Figure 2. Induction of cell death (via apoptosis and secondary necrosis) in U87MG cells following treatments with CBD (10 μ M), ATM inhibitor KU60072 (2 μ M) alone or in combination, without or with γ -irradiation at 10 Gy. Cell cycle-apoptosis was assayed 24 h after indicated treatments. CBD and ATMi or their combination (diluted in 0.1% DMSO), as well control 0.1% DMSO were added 30 min before irradiation. The nuclei of treated cells were stained with PI for determination of DNA content using flow cytometry. The nuclei of apoptotic cells and secondary necrotic cells were localized in the pre-G1 region.

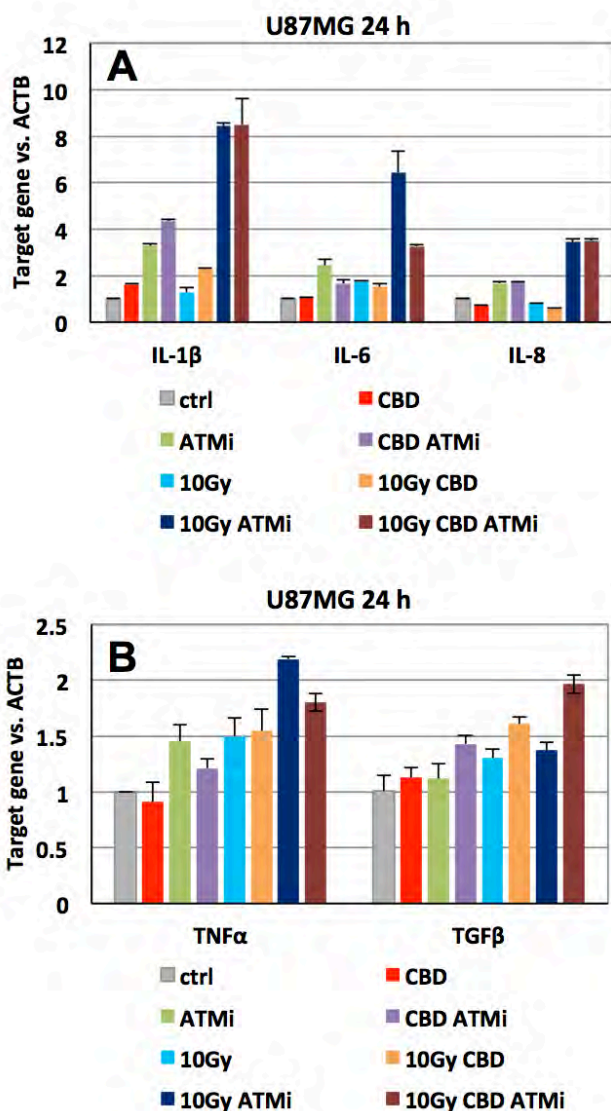


Figure 3. Gene expression pattern of pro-inflammatory cytokines (IL1, IL6, IL8 and TNF) and TGF β in U87MG cells was determined by quantitative real-time PCR. (A-B) mRNA was isolated 24 h after treatment with 0.1% DMSO (control vehicle), CBD (10 μ M), ATMi (2 μ M) and γ -irradiation (10 Gy) alone or in combination. The graphs indicate the fold change of target gene mRNA levels against time-point control after normalization to reference gene (beta-Actin). The pooled results of four independent experiments are presented. Error bars represent means \pm S.D. ($p < 0.05$, Student's *t*-test).

the main pro-inflammatory cytokines, including IL1 β , IL6, IL8, and TNF α . Furthermore, levels of TGF β , active in many signaling pathways, were also determined. The most striking observation was a dramatic upregulation of IL1 β , IL6 and IL8 gene expression 24 – 48 h after treatment with γ -irradiation at 10 Gy in combination with ATM inhibitor, or in triple combination with ATM inhibitor and CBD (Figure 3). The effects of CBD alone or with irradiation significantly increased 48 h after treatment (data not shown). It is well known that γ -irradiation initiates a stress response in both normal and

cancer cells that is accompanied by stable exit from the cell cycle to the state of “senescence”, with many characteristic features including senescence-associated secretory phenotype (SASP) [8]. As a result, dying cancer cells exhibited strong and sometimes negative bystander effects on the normal cells in the brain via production of pro-inflammatory cytokines. It will be very important to consider negative and positive effects of the inflammatory response after combined treatment of glioblastoma.

REFERENCES

- Porter KR, McCarthy BJ, Freels S, Kim Y, Davis FG. Prevalence estimates for primary brain tumors in the United States by age, gender, behavior, and histology. *Neuro-oncology*. 2010;12(6):520-7. Epub 2010/06/01. doi: 10.1093/neuonc/nop066. PubMed PMID: 20511189; PMCID: 2940648.
- Javid FA, Phillips RM, Afshinjavid S, Verde R, Ligresti A. Cannabinoid pharmacology in cancer research: A new hope for cancer patients? *Eur J Pharmacol*. 2016;775:1-14. doi: 10.1016/j.ejphar.2016.02.010. PubMed PMID: 26852955.
- Massi P, Solinas M, Cinquina V, Parolaro D. Cannabidiol as potential anticancer drug. *Br J Clin Pharmacol*. 2013;75(2):303-12. doi: 10.1111/j.1365-2125.2012.04298.x. PubMed PMID: 22506672; PMCID: 3579246.
- Velasco G, Sanchez C, Guzman M. Towards the use of cannabinoids as antitumour agents. *Nat Rev Cancer*. 2012;12(6):436-44. doi: 10.1038/nrc3247. PubMed PMID: 22555283.
- Welty TE, Luebke A, Gidal BE. Cannabidiol: promise and pitfalls. *Epilepsy Curr*. 2014;14(5):250-2. doi: 10.5698/1535-7597-14.5.250. PubMed PMID: 25346628; PMCID: PMC4189631.
- Hart S, Fischer OM, Ullrich A. Cannabinoids induce cancer cell proliferation via tumor necrosis factor alpha-converting enzyme (TACE/ADAM17)-mediated transactivation of the epidermal growth factor receptor. *Cancer Res*. 2004;64(6):1943-50. PubMed PMID: 15026328.
- Scott KA, Dalglish AG, Liu WM. The combination of cannabidiol and Delta9-tetrahydrocannabinol enhances the anticancer effects of radiation in an orthotopic murine glioma model. *Mol Cancer Ther*. 2014;13(12):2955-67. doi: 10.1158/1535-7163.MCT-14-0402. PubMed PMID: 25398831.
- Kuilman T, Peeper DS. Senescence-messaging secretome: SMS-ing cellular stress. *Nat Rev Cancer*. 2009;9(2):81-94. doi: 10.1038/nrc2560. PubMed PMID: 19132009. ■

X-ray Irradiation has a Strong Effect on Human HSC and Progenitor Populations Engrafted in the Immunodeficient Mouse

Monica Pujol Canadell and Lubomir Smilenov

Conventional allogeneic unrelated hematopoietic cell transplantation (HCT) was developed for patients with hematological malignancies. It involves conditioning with high doses of systemic chemo/radiation therapy, which is a high-risk therapy specifically for some patients that are over the age of 50 years. Since the average age of patients with hematological malignancies is in the range of 65-70 years, reduced-intensity regimens have been developed. These regimens usually involve 2Gy of total body radiation (TBI) combined with or without fludarabine, and given postgrafting cyclosporine and mycophenolate mofetil to control the graft-versus-tumor effects. It was shown that this regimen allowed the extension of allografting to older and medically infirm patients ([1, 2]. The hematopoietic stem cell (HSC) counts

in the bone marrow of the patients is an important measure of the radiation effect, but due to treatment restrictions, bone marrow cells from patients are rarely isolated and analyzed. We reasoned that information on these counts can be obtained from irradiated humanized mice, where the cell counts of the HSC and early lineage negative progenitors can be determined very exactly. To test this approach, we irradiated humanized mice with X-rays at a dose of 1, 2 and 3 Gy, and analyzed the bone marrow counts between day 3 and day 5 after irradiation.

Materials and Methods

Mice:

All animal husbandry and experimental procedures were conducted in accordance with applicable federal and

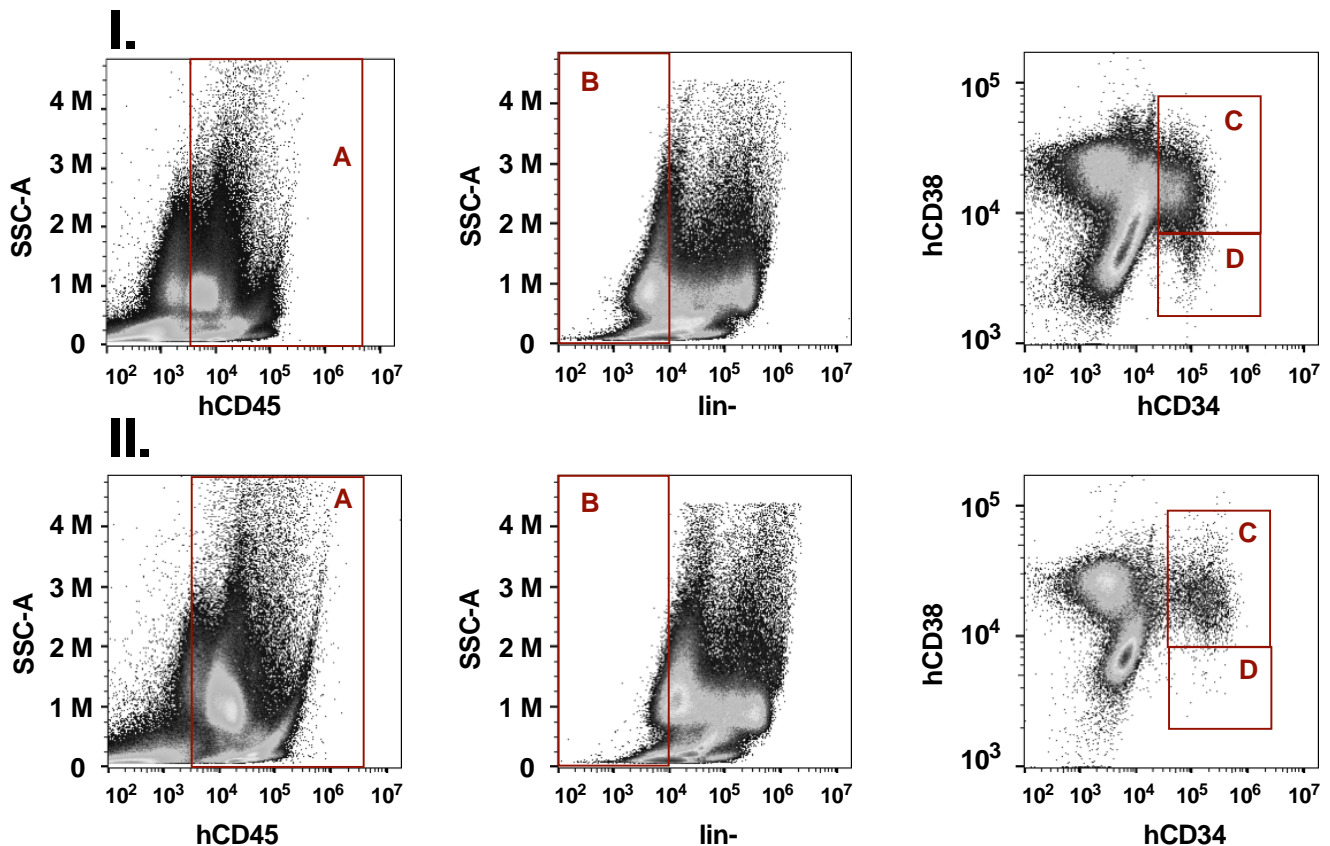


Figure 1. Identification of different cell populations in the bone marrow of control mice (I) and irradiated mice (II). A-cells positive for human CD45, B- lineage negative cells (negative for the lineage markers), C – Early progenitor subpopulation (CD34+/CD38+) and D- HSC/MPP subpopulation (CD34+/CD38-). There is a clear difference in the cell counts between the C and D quadrants of the control and irradiated mice.

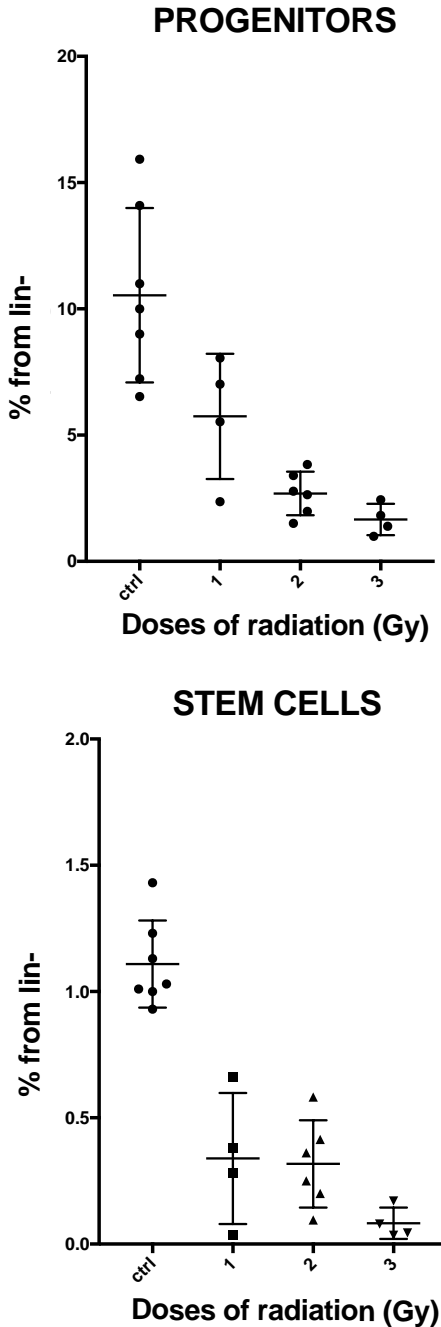


Figure 2. Effect of different doses of radiation on the frequency of the early progenitor and HSC/MPP subpopulation expressed as percentage from the lineage negative subpopulation. A large decrease in the frequencies of both populations can be seen for all irradiation doses.

state guidelines, and approved by the Animal Care and Use Committees of Columbia University.

Immunodeficient NOD.Cg-Prkdc^{scid} Il2rg^{tm1Wjl}/SzJ (NSG) mice (The Jackson Laboratory; Bar Harbor, ME, USA), aged 6 to 8 weeks, were engrafted with commercially available human cord blood CD34+ cells. For the engraftment, the NSG mice were irradiated with 2.0 Gy of gamma rays followed by injection of 200,000

human CD34+ into the tail vein within 24 hours after irradiation.

Twelve weeks later, the engraftment was quantified using antibodies specific to human and mouse cells (listed below). For analysis of the different human cell populations from mouse bone marrow and spleen, the mice were sacrificed and then peripheral blood, spleen, femurs and tibiae were obtained. The femurs and tibiae were flushed with DPBS, 5% BSA for bone marrow cell isolation. Single cell suspensions were made from BM and spleen by passing tissues through a 40µM cell strainer (Fisher Scientific, USA).

Immunophenotyping:

The Immunophenotyping was done by flow cytometry using a 13 color Cytoflex flow cytometer (Beckman Coulter). This flow cytometer has volumetric-based fluidics, allowing exact cell count determination.

Cell types identified:

Human stem and progenitor cell markers used: CD45, Lineage positive cocktail markers (CD2, CD3, CD14, CD16, CD19, CD56 and CD235a), CD34 and CD38.

Mouse cell identification: anti-mouse CD45, CD20 and CD3 antibodies.

Mouse irradiation: The mice were irradiated with doses of 1Gy, 2Gy and 3Gy using X-rad machine at 320kVp/12mA.

Results and Discussion

The main goal of this study was to determine counts of the human hematopoietic stem cells (HSC) and early progenitor cells in the bone marrow of humanized mice after irradiation. These cells give rise to all cells of the hematopoietic system and are characterized by the presence of the CD34 and CD38 markers, as well as the lack of the mature blood cell lineage markers (i.e., therefore, lineage negative cells or “lin-“). Two main subgroups were targeted for identification by immunophenotyping. These are the lin-, CD34+/CD38- cells, which include the HSC and multipotent progenitor (MPP) cells (identified here as “HSC/MPP subpopulation”), and the lin-, CD34+/CD38+ cells, which contain the common myeloid progenitor (CMP), common lymphoid progenitor (CLP), granulocyte-monocyte progenitor (GMPs) and megakaryocyte-erythroid progenitors (MEPs) identified here as “early progenitor subpopulation”. This gating strategy is shown in Fig. 1. A total of 23 humanized mice were used for the experiments, including 7 controls and 16 irradiated animals. The mice were irradiated with doses of 1Gy, 2Gy and 3Gy, and sacrificed between day 3 and day 5 after the irradiation. Around 500,000 bone marrow cells/mouse were analyzed. The results show an unequivocally strong effect of the X-ray irradiation on the cells (Fig. 2). Counts of the HSC/MPP subpopulation were reduced significantly. The range of their frequency

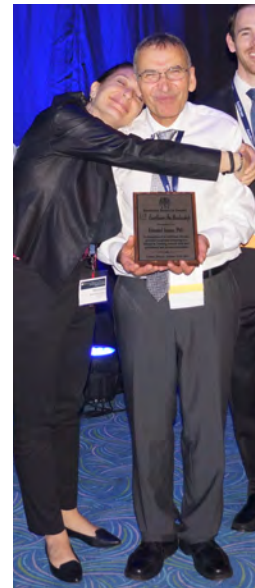
in the lineage negative population was below 0.5% for all doses. The counts of this group of cells in the control mice was in the range of 2,000, with a frequency of 1.2% in the lin- population. More cells survived in the early progenitor subpopulation, where we see a gradual decrease of the cell counts reaching a very low frequency at 3 Gy. The average counts of this group of cells in the control mice were about 4,000, with 11% average frequency in the lin- population.

Overall, these results show that X-ray irradiation reduced the frequency of HSC in the lin- population, around 3-fold for the dose of 1 and 2 Gy, and about 10-fold for the 3Gy dose. For the early progenitor subpopulation, these numbers were ~2-fold for 1Gy, 4-fold for 2Gy and 5-fold for 3Gy, which is a significant effect. However, the results show that some proportion of the cells survived and most probably the same percent of cancer stem cells if present would also survive. This though is acceptable since the goal of this treatment is to condition the bone marrow for HSC transplantation and the subsequent graft-versus-tumor effect mediated by the transplanted cells. This mechanism was confirmed by successful patient treatments. We believe that the results shown here clarify the mechanisms involved in the reduced-intensity regimens for HSC transplantation.

Of note, in this study we used the X-ray machine at the stated energy. In hospitals, patients are irradiated TBI with 0.07 to 0.2 Gy/min from a linear accelerator or by a cobalt-60 source. Most probably the higher energy used for patients can induce greater cell death in the BM of the individuals.

References

1. Hegenbart U, Niederwieser D, Sandmaier BM, Maris MB, Shizuru JA, Greinix H, Cordonnier C, Rio B, Gratwohl A, Lange T *et al*: Treatment for acute myelogenous leukemia by low-dose, total-body, irradiation-based conditioning and hematopoietic cell transplantation from related and unrelated donors. *J Clin Oncol* 2006, **24(3)**:444-453.
2. Niederwieser D, Maris M, Shizuru JA, Petersdorf E, Hegenbart U, Sandmaier BM, Maloney DG, Storer B, Lange T, Chauncey T *et al*: Low-dose total body irradiation (TBI) and fludarabine followed by hematopoietic cell transplantation (HCT) from HLA-matched or mismatched unrelated donors and postgrafting immunosuppression with cyclosporine and mycophenolate mofetil (MMF) can induce durable complete chimerism and sustained remissions in patients with hematological diseases. *Blood* 2003, **101(4)**:1620-1629. ■



Top (l to r): Andrew Harken, Christian Siebenwirth, Guy Garty, Paul Goldhagen, Peter Grabham, Manuela Buonanno, Ed Azzam.

Bottom (l to r): David Brenner, Charles Geard, Mike Joiner, Hale and Gerhard Randers-Person

MEK Downregulation Sensitizes Human Prostate Cancer Cells to Etoposide Treatment

Constantinos G. Broustas, Axel J. Duval, and Howard B. Lieberman

Early-stage prostate cancer can usually be managed with active surveillance, radiation or surgery [1]. Nevertheless, a number of treated patients eventually relapse into an androgen-insensitive state experiencing progression of the disease [2]. Metastatic prostate cancer can be castration-sensitive (mCSPC) or castration-resistant (mCRPC), with the majority of mCSPC cases progressing to mCRPC after developing resistance to hormonal treatment [1, 2]. At that stage, there are very few treatment interventions that at best extend survival for a few months. Pro-survival pathways such as PI3K/Akt and members of the MAPK family, as well as DNA damage response and repair defects are mainly responsible for mCRPC treatment resistance. Therefore, inhibiting these pro-survival pathways alone or in combination with genotoxic drugs may prove beneficial in sensitizing mCRPCs and improving patient survival [3].

The mitogen-activated protein kinase kinase 5 (MAP2K5, MEK5) forms part of the mitogen-activated kinases (MAPK) family, which is activated at Ser311/Thr315 by upstream MAPKKs, being MEKK2 and MEKK3 specific for MEK5. Furthermore, MEK5 activates extracellular signal-regulated kinase 5 (ERK5), by phosphorylating it at Thr218/Thr220 [4, 5].

Activation of the MEK5-ERK5 pathway plays a crucial role in chemoresistance and is a central mediator of anti-apoptotic signaling, cell survival, epithelial-mesenchymal transitions (EMT), and an increase in cell proliferation [5, 6]. Furthermore, preclinical data have shown that targeting ERK5 enhances T-cell infiltration in prostate cancer [7]. MEK5 expression is not only increased in prostate cancer cells compared to benign prostatic tissue, but is also related to metastatic state and poor prognostic value [8, 9].

Etoposide, a topoisomerase II inhibitor that induces DNA double strand breaks, is known to inhibit cell growth of both mCSPC and mCRPC [1]. Specifically, etoposide alone or in combination with carboplatin is used to promote the activation of apoptosis pathways with special significance for metastatic castration-resistant prostate adenocarcinoma and neuroendocrine prostate cancer [3], where it has been shown that tumorigenic and invasion cascades, such as MEK5/ERK5, are highly expressed.

This study proposes the hypothesis that the presence of MEK5 in prostate cancer cells affects the response to chemotherapy, and explores the regulation of MEK5 as an additional therapeutic option.

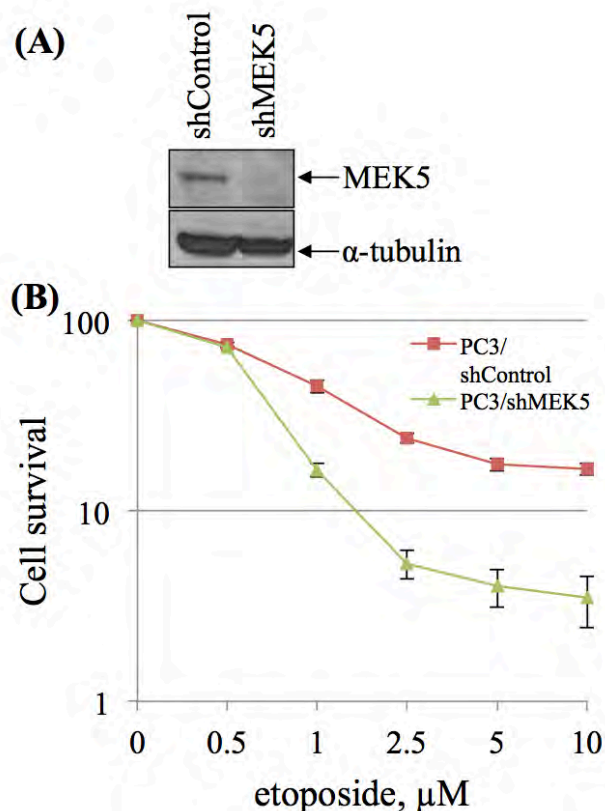


Figure 1. (A) Western blot analysis showing MEK5 knockdown in PC3/shMEK5 cells. α -Tubulin levels were used as loading control. (B) Dose-response curve. PC3/shControl and PC3/shMEK5 cells were plated overnight, treated with increasing concentrations (0, 0.5, 1, 2.5, 5 and 10 μ M) of etoposide, and incubated for 4 days in the presence of the drug, without medium change. Cells were fixed and stained with crystal violet. Color was extracted and absorbance was measured at 595 nm. Shown mean \pm S.D. (n=3).

Results

Castration-resistant PC3 prostate cancer cells were treated with MEK5 short hairpin (sh) RNA in combination with topoisomerase II inhibitor, etoposide. Short-term survival assays were performed to assess the impact of MEK5 depletion on cancer cell chemotherapy sensitization. The presence of MEK5 was detected by using specific antibodies and immunoblotting (Figure 1A). Both PC3/shControl and PC3/shMEK5 cells were treated with increasing doses of etoposide and plated for cell survival assay. The cells were incubated at 37°C for 4 days in the presence of the drug. Both PC3 cell colonies showed decreasing growth rates related to the presence of higher doses of etoposide. However, knockdown of

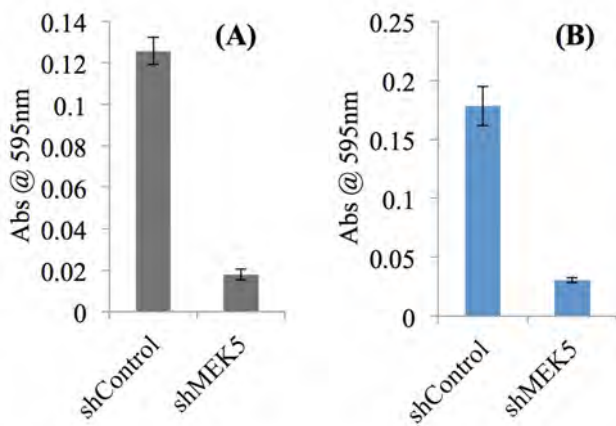


Figure 2. Cell survival assay. PC3/shControl and PC3/shMEK5 cells were incubated for 6 days and treated for either the complete time of incubation (A) or only the first 16 hours, with 1 μ M etoposide (B). Both were preserved in complete medium. Cells were fixed, then stained with crystal violet. Stain was recovered and absorbance was measured at 595 nm. Shown is mean \pm S.D. ($n=3$).

MEK5 sensitized PC3 cells to the action of the drug compared with parental cells, showing a half maximal inhibitory concentration (IC₅₀) value of 0.75 μ M versus 2 μ M for PC3/shControl cells (Figure 1B).

PC3/shControl and PC3/shMEK5 cells were treated with 1 μ M etoposide on the frame of a short-term cell proliferation assay. Both populations were either incubated for 6 days in the presence of the drug (Figure 2A), or treated with etoposide for only 16 hours and incubated for 6 days (Figure 2B). Knocking down MEK5 alone had no effect on cell survival, whereas etoposide treatment alone reduced cell survival by ~45%. In contrast, combining MEK5 silencing with etoposide resulted in a significant effect on the rate of cell survival, related to the PC3/shControl cells, showed a decrease of 85% in survival after 6 days of exposure. Similar results were obtained after both PC3/shControl and PC3/shMEK5 cells were exposed to the same dose of etoposide for only 16 hours and incubated for 6 days (82% decrease in proliferation). The combination index (CI) theorem of Chou-Talalay offers quantitative definition for an additive effect (CI = 1), synergism (CI < 1), and antagonism (CI > 1) in drug combinations [10]. When applied to both treatment protocols, the CI for the combination of MEK5 depletion with 1 μ M etoposide was calculated to be approximately 0.5, which denotes a synergistic effect.

Conclusions

In the present study, we present *in vitro* evidence that MEK5 silencing acts synergistically with the DNA

damaging drug etoposide in sensitizing castration-resistant prostate cancer cells to killing. Future studies will focus on elucidating the mechanistic details of the MEK5 knockdown-etoposide synergism.

References

1. Filson CP, Marks LS, Litwin MS. Expectant management for men with early stage prostate cancer. *CA Cancer J Clin.* 2015;65(4):265-282.
2. McEleny KR, Watson RW, Coffey RN, O'Neill AJ, Fitzpatrick JM (2002). Inhibitors of apoptosis proteins in prostate cancer cell lines. *Prostate* 51: 133–140.
3. Caubet M, Dobi E, Pozet A, Almotlak H, Montcuquet P, Maurina T, Mouillet G, N'guyen T, Stein U, Thierry-Vuillemin A, Fiteni F (2015). Carboplatin-etoposide combination chemotherapy in metastatic castration-resistant prostate cancer: A retrospective study. *Molecular And Clin Oncol* 3 (6): 1208-1212.
4. Nithianandarajah-Jones GN, Wilm B, Goldring C, Müller J, Cross MJ (2012). ERK5: Structure, regulation and function. *Cellular Signaling* 24:2187 – 2196.
5. Hoang VT; Yan TJ; Burow ME; Cavanaugh JE; Flaherty PT; Beckman BS (2017). Oncogenic signaling of MEK5-ERK5. *Cancer Lett.* 392:51-59.
6. Kamakura S, Moriguchi T, Nishida E (1999). Activation of the Protein Kinase ERK5/BMK1 by Receptor Tyrosine Kinases. *J Biol Chem* 274(37):26563-71.
7. Loveridge CJ, Mui EJ, Patel R, Tan EH, Ahmad I, Welsh M, Galbraith J, Hedley A, Nixon C, Blyth K, Sansom O, Leung HY. Increased T-cell Infiltration Elicited by Erk5 Deletion in a Pten-Deficient Mouse Model of Prostate Carcinogenesis. *Cancer Res.* 2017;77(12):3158-3168.
8. Hugh H. Song HH, Keller ET (2005). MEK5 promotes PC-3 prostate cancer cell invasion in vitro. *Cancer Res* 65: 238.
9. Ramsay AK, McCracken SRC, Soofi M, Fleming J, Yu AX, Ahmad I, Morland R, Machesky L, Nixon C, Edwards DR, Nuttall RK, Seywright M, Marquez R, Keller E, Leung HY (2001). ERK5 signalling in prostate cancer promotes an invasive phenotype. *British J. Cancer* 104: 664 – 672.
10. Chou TC. Drug combination studies and their synergy quantification using the Chou-Talalay method. *Cancer Res.* 2010;70(2):440-446. ■

RAD9 Silencing Impairs Anchorage-independent Growth through the Suppression of AGR2

Constantinos G. Broustas, Kevin M. Hopkins, Li Wang, Sunil K. Panigrahi, and Howard B. Lieberman

RAD9 displays pleiotropic functions [1, 2]. As part of the RAD9-HUS1-RAD1 complex, it acts as a sensor of DNA damage that enables ATR kinase to phosphorylate and activate its downstream effector CHK1. In addition, RAD9 participates in multiple DNA repair pathways, such as base excision repair, nucleotide excision repair, mismatch repair, and homologous recombination. Moreover, human RAD9 can function as a sequence-specific transcription factor. RAD9 can bind to p53 DNA-binding consensus sequences in the promoter region of p21^{Waf1/Cip1} [3] and *NEIL1* [4], and enhance transcription of these genes.

Aberrant RAD9 expression has been associated with breast, lung, skin, thyroid, and gastric cancers [1]. In addition, we have shown previously that RAD9 is overexpressed in human prostate cancer specimens as well as prostate cancer cell lines [5], and down-regulation of RAD9 in human tumor cell line xenografts impairs growth in nude mice [5]. Furthermore, immunohistochemical analysis of non-cancer and tumor prostate specimens showed that RAD9 expression increased along with cancer progression stages, suggesting a role for RAD9 in prostate malignant progression [5].

AGR2 protein is a member of the oxidoreductase family of protein disulphide isomerases (PDIs) [6]. The protein is localized in various cellular compartments, including the endoplasmic reticulum, the cytosol, the plasma membrane, and the nucleus, as well as the

extracellular matrix. AGR2 is involved in numerous biological processes including cell transformation, cell migration and invasion, cell adhesion, as well as regulation of p53 in response to genotoxic stress [6]. Moreover, increased levels of AGR2 in various tumors have been associated with increased tumor growth, metastasis, and drug resistance. AGR2 protein levels are elevated in prostate cancer and downregulation of AGR2 decreases metastatic behavior [7]. We have shown previously that RAD9 can act as a transcriptional activator of *AGR2* mRNA, by directly binding the *AGR2* promoter.

Given the link between RAD9 and AGR2, as well as their increased expression in metastatic prostate cancer, we addressed whether the two proteins cooperate in the induction of cell migration and anchorage-independent growth.

Results

We have shown that knockdown of RAD9 in PC-3 cells impairs cell migration and invasion. Moreover, AGR2 depletion compromises migration of numerous tumor cell lines. To examine the effect of ectopically expressed AGR2 on PC-3 cells expressing reduced levels of endogenous RAD9, we carried out a wound-healing assay. We first generated PC-3 cells with reduced levels of RAD9 using the CRISPR/Cas9 technology (PG13; Figure 1A). Endogenous levels of AGR2 protein were undetectable in PG13 cells (Figure 1A). In agreement with our previous results using RAD9 shRNA [8], PG13

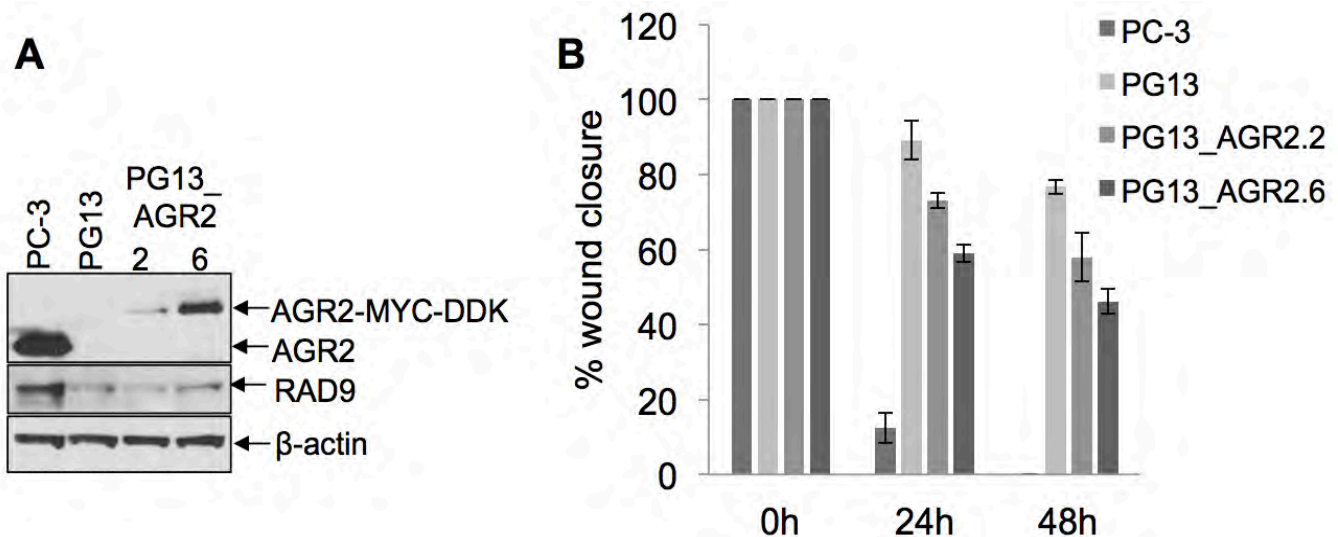


Figure 1. Wound closure assay. **A**, PG13 (RAD9 targeted using the CRISPR/Cas9 technology), and two clones of PG13 cells stably expressing ectopic AGR2-MYC-DDK (PG13.2, PG13.6). **B**, wound closure assay of parental (PC-3), PC-3/RAD9 knockdown (PG13), PG13_AGR2.2, and PG13_AGR2.6) measured at times 0 h, 24 h, and 48 h. Data shown are mean \pm SD (n=3).

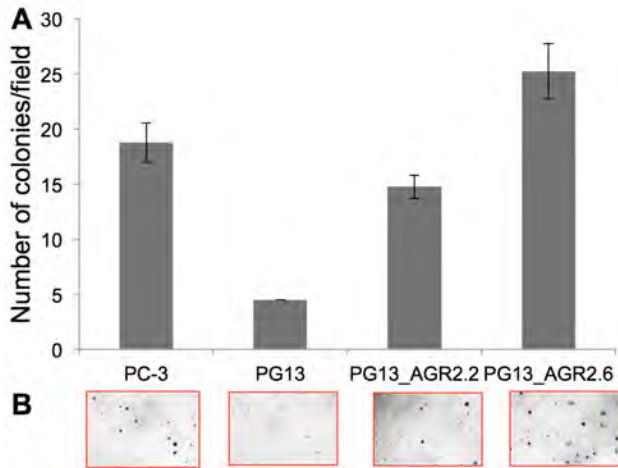


Figure 2. Anchorage-independent growth. **A**, an equal number of PC-3 cells from different groups was assayed for colony formation in soft agarose. The numbers of colonies with a diameter greater than 20 μm were quantified 3 weeks later. Shown is one representative experiment of three independent experiments, each performed in triplicate. **B**, representative images of colonies in soft agarose.

cells displayed impaired wound closure, with only ~25% gap closure after 48 h (Figure 1B). In contrast, PG13 cells stably expressing a DDK-MYC-tagged *AGR2* construct (two clones denoted PG13_AGR2.2 and PG13_AGR2.6), accelerated wound closure, with ~45% gap closure for PG13_AGR2.6 after 48 h (Figure 1B); however, the closure was partial and did not reach the rate of the parental PC-3 cells. We conclude that *AGR2* only partially rescues the migration defect of PG13 cells and *RAD9* affects cell migration by *AGR2*-dependent and independent pathways.

In vitro anchorage-independent growth of cancer cells correlates with their ability to produce experimental metastasis *in vivo* [9]. We have shown previously that *RAD9* depletion in DU145 cells impairs anchorage-independent growth, whereas ectopic expression of mouse *RAD9* in DU145 with depleted endogenous *RAD9* is able to restore growth in soft-agarose [8]. *AGR2* is considered a metastatic gene, and, like *RAD9*, downregulation of *AGR2* using siRNA impairs anchorage-independent growth in various cancer cell lines. In agreement with these results, we were able to show that *RAD9* downregulation in PC-3 could no longer support anchorage-independent growth as assessed by colony formation in soft agarose. However, ectopic expression of *AGR2* in PG13 cells allowed the cells to regain their ability to grow in soft-agarose (Figure 2A and 2B).

These results support the model that *AGR2* may be an effector of *RAD9* in the metastatic process.

Conclusions

We show that *RAD9* acts upstream of *AGR2* in supporting PC-3 prostate cancer cell migration and anchorage-independent growth. Future studies will focus on determining the contribution of *AGR2* to the *RAD9*-induced pro-metastatic phenotype *in vivo*.

References

1. Lieberman HB, Bernstock JD, Broustas CG, Hopkins KM, Leloup C, Zhu A. (2011) The role of *RAD9* in tumorigenesis. *J. Mol. Cell Biol.* 3;39–43.
2. Broustas CG, Lieberman HB. (2012) Contributions of *RAD9* to tumorigenesis. *J. Cell Biochem.* 113;742–751.
3. Yin Y, Zhu A, Jin YJ, Liu YX, Zhang X, Hopkins KM, Lieberman HB. (2004) Human *RAD9* checkpoint control/proapoptotic protein can activate transcription of p21. *Proc. Natl. Acad. Sci. U.S.A.* 101;8864–8869.
4. Panigrahi SK, Hopkins KM, Lieberman HB. (2015). Regulation of NEIL1 protein abundance by *RAD9* is important for efficient base excision repair. *Nucleic Acids Res.* 43(9):4531-4546.
5. Zhu A., Zhang C. X., Lieberman H. B. (2008) *RAD9* has a functional role in human prostate carcinogenesis. *Cancer Res.* 68, 1267–1274.
6. Chevet E, Fessart D, Delom F, Mulot A, Vojtesek B, Hrstka R, Murray E, Gray T, Hupp T. (2013). Emerging roles for the pro-oncogenic anterior gradient-2 in cancer development. *Oncogene.* 32(20):2499-2509.
7. Zhang Y, Ali TZ, Zhou H, D'Souza DR, Lu Y, Jaffe J, Liu Z, Passaniti A, Hamburger AW. (2010). ErbB3 binding protein 1 represses metastasis-promoting gene anterior gradient protein 2 in prostate cancer. *Cancer Res.* 70(1):240-248.
8. Broustas CG, Zhu A, Lieberman HB. (2012). *Rad9* protein contributes to prostate tumor progression by promoting cell migration and anoikis resistance. *J Biol Chem.* 287(49):41324-41333.
9. Cifone M. A., Fidler I. J. Correlation of patterns of anchorage-independent growth with *in vivo* behavior of cells from a murine fibrosarcoma. *Proc. Natl. Acad. Sci. U.S.A.* 1980;77, 1039–1043. ■

NBS1 and H2AX Complement Each Other in the DNA Damage Response

Yuan-Cho Lee, Junjie Chen^a, and Jingsong Yuan

Introduction

Cells are continuously challenged by genotoxic agents from endogenous and exogenous sources. DNA double-strand breaks (DSBs) represent one of the most lethal forms of DNA lesions that must be appropriately repaired

for cell survival. In response to DSBs, phosphorylation of histone variant H2AX at serine 139 creates γ H2AX, which is a key event in the DNA damage response (DDR). However, we and others showed that the MRE11-RAD50-NBS1 (MRN) complex can act independently of the H2AX-mediated DDR cascade to promote DNA end

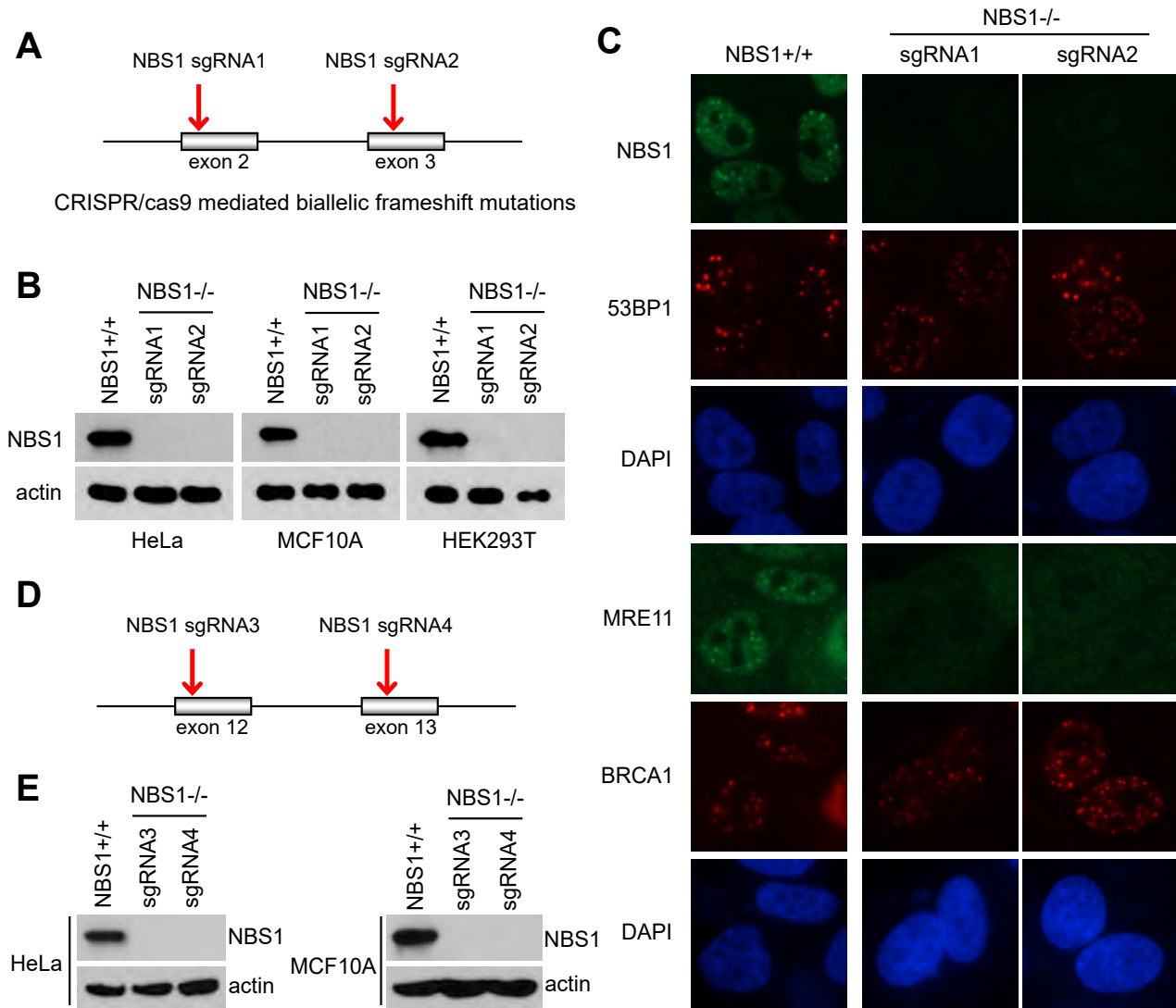


Figure 1. NBS1-null human somatic cells are viable. (A) Two sgRNAs targeting exon 2 and 3 respectively were used in CRISPR/cas9 mediated NBS1 knockout. (B) NBS1 knockout in HeLa, MCF10A and HEK293T cells was confirmed by immunoblotting. (C) NBS1 knockout in MCF10A was confirmed by immunostaining. Cells were irradiated (10 Gy) and allowed to recover for one hour. (D and E) Another two sgRNAs targeting exon 12 and 13, respectively, were used in NBS1 knockout in HeLa and MCF10A cells.

^aDepartment of Experimental Radiation Oncology, the University of Texas M. D. Anderson Cancer Center, Houston, TX 77030, USA

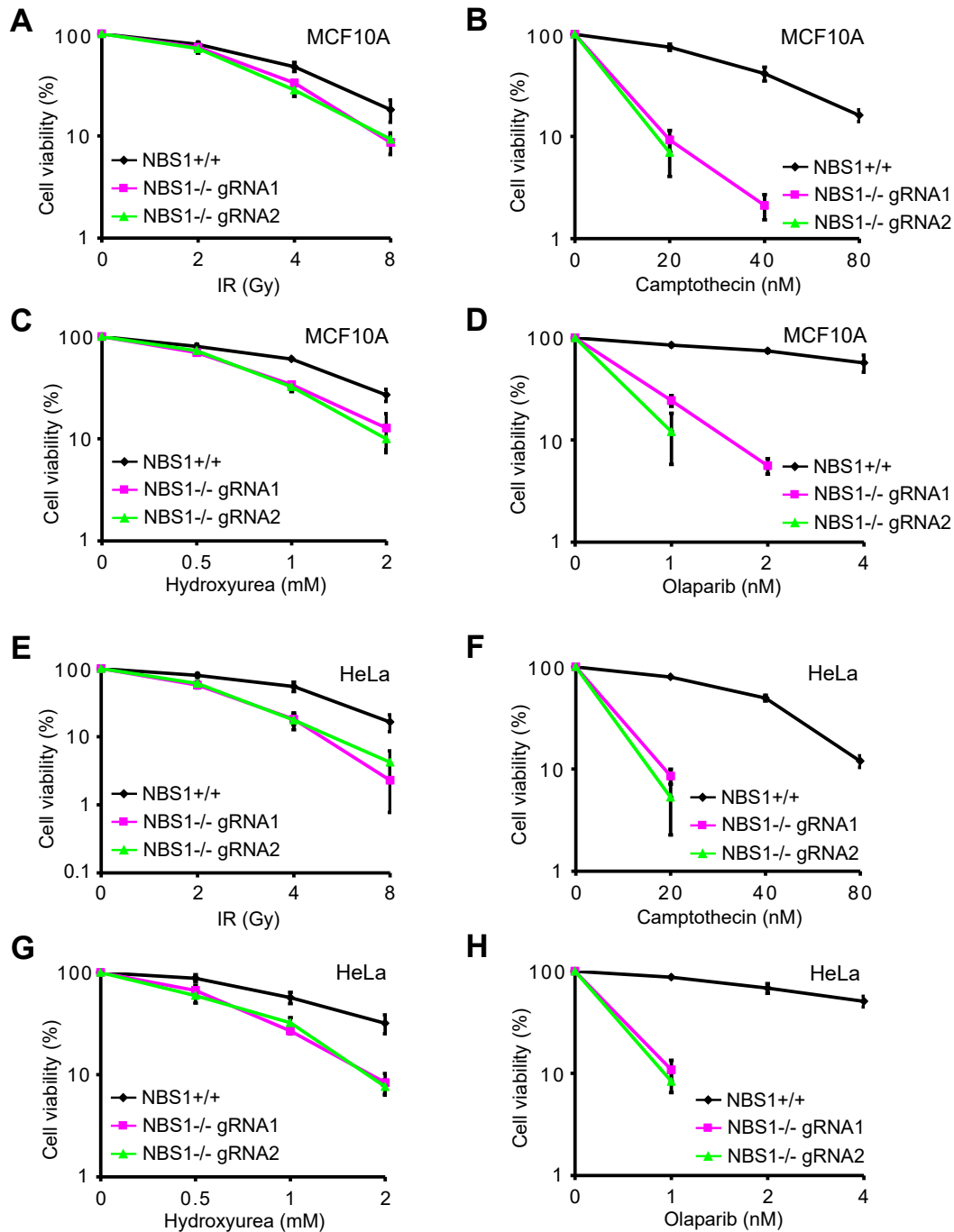


Figure 2. *NBS1* is required for cell survival when cells encounter *S* phase-specific double-strand breaks.

(A-D) Survival curves in response to increasing doses of IR (A), Camptothecin (B), Hydroxyurea (C) and Olaparib (D) for indicated wild-type and *NBS1* knockout MCF10A cells are presented. (E-H) Survival curves in response to increasing doses of IR (E), Camptothecin (F), Hydroxyurea (G) and Olaparib (H) for indicated wild-type and *NBS1* knockout HeLa cells are presented. Data are presented as mean \pm s.d. from three different experiments.

resection, which is critical for homologous recombination (HR) repair (1). Here, we show unexpectedly that *NBS1*-null human somatic cells are viable. We further demonstrate that *NBS1* is required for cell survival when cells encounter *S* phase-specific DSBs. More interestingly, using an inducible reconstitution system we conclude that double knockout of *NBS1* and *H2AX* is synthetic lethal in human cells. We therefore propose that the *NBS1*-dependent initial recruitment and *H2AX*-

dependent stable accumulation of DDR signalling components complement each other and are required for DNA repair and cell survival.

Results

NBS1-null human somatic cells are viable

The conversion of DNA DSB ends to ssDNA regions is considered as a key step that controls not only HR

repair but also DNA damage checkpoints (2). The MRN complex has been implicated in the detection of DSBs and DNA end resection. In an attempt to test whether the DNA end resection pathway is essential for mammalian cell survival, we utilized the CRISPR/cas9 genome editing system to generate cell lines with deficiency in DNA end resection. Two single guide RNAs (sgRNA) were designed to target exon 2 and 3 of *NBS1*, respectively (Fig. 1A). To our surprise, *NBS1* knockout was successfully achieved in all human cell lines tested so far (HeLa, MCF10A and HEK293T; Fig. 1B). The *NBS1* knockout cell lines were confirmed by immunoblotting (Fig. 1B) and genomic DNA sequencing to make sure that there were biallelic frameshift mutations in these modified cell lines (Fig. 1A). Furthermore, the *NBS1* knockout in MCF10A cells was also confirmed by immunostaining (Fig. 1C). As shown in Figure 1C, *NBS1* is required for nuclear localization and foci formation of MRE11 following ionizing radiation (IR), which is consistent with previous reports (3, 4). However, *NBS1* knockout has a minor effect on the stable recruitment of DNA repair proteins 53BP1 and BRCA1 to DSB sites (Fig. 1C).

Mutations in *NBS1* gene are responsible for the Nijmegen breakage syndrome (NBS), which display elevated risk to develop several types of malignant tumours, especially breast, prostate and colorectal cancers, lymphoblastic leukaemia, and non-Hodgkin's lymphoma (NHL). The 657del5 mutation in exon 6 of *NBS1* gene accounts for more than 90% of all mutant alleles in NBS and contributes significantly to cancer incidence. This mutation results in the synthesis of two truncated proteins of 26 kDa (p26) and 70 kDa (p70). The p70 protein is produced by an alternative initiation of translation upstream the 5 base pair deletion, and therefore has the identical sequence as the wild-type *NBS1* from the amino acid 221 to the end, and contains the BRCT2 domain and the C-terminal region of *NBS1* (5, 6). The *NBS1* knockout via the sgRNAs targeting exon 2 and 3 may potentially generate a truncated *NBS1* protein by an alternative initiation, similar to the situation of the 657del5 mutation. To rule out this possibility, we first performed immunoblotting using an antibody recognizing the C-terminal region of human *NBS1* (Fig. 1B), and we did not detect any band lower than full-length *NBS1* (data not shown). In order to draw a reliable conclusion, we introduced two additional sgRNAs targeting exon 12 and 13 of *NBS1*, respectively (Fig. 1D). In this case, biallelic frameshift mutations were generated right before the coding sequence for the MRE11-binding domain of *NBS1*. As shown in Figure 1E, the *NBS1* knockout via sgRNA3 and 4 in both HeLa and MCF10A cells was confirmed by immunoblotting.

Together these results demonstrate that although *Nbs1*-null mice are embryonic lethal, the *NBS1*-null human somatic cells are viable.

NBS1 is required for cell survival when cells encounter S phase-specific double-strand breaks.

The choice between NHEJ and HR for repair of DSBs is tightly cell cycle regulated. NHEJ is active throughout the cell cycle, but is most efficient during G1 phase when no homologous template for recombination is available. HR, instead, requires an undamaged template for faithful DSB repair, usually the sister chromatid, and is therefore restricted to S/G2 phase, in which HR is initiated by MRN/CtIP dependent DSB end resection to form 3'-ssDNA overhangs. We examined the effect of *NBS1* knockout on cell survival following various DNA-damaging events. We found that while *NBS1*-null MCF10A and HeLa cells showed moderate sensitivity to IR and hydroxyurea treatment (Fig. 2A, C, E and G), they were extremely sensitive to camptothecin and olaparib (Fig. 2B, D, F and H). Hydroxyurea treatment reduces the production of deoxyribonucleotides via inhibition of ribonucleotide reductase, therefore causing replication stress. IR exposure produces a variety of DNA damages in cells, including DSBs that are mostly repaired via NHEJ pathway. Camptothecin is a topoisomerase I inhibitor, and the toxicity of Camptothecin is primarily a result of conversion of single-strand breaks into DSBs during S-phase (7). Olaparib is a PARP inhibitor, inhibiting poly ADP ribose polymerase, which is important for repairing single-strand breaks. PARP inhibition will result in persistent unrepaired single-strand breaks, which will eventually be converted to DSBs during DNA replication in S-phase (8). Thus, our data suggested that *NBS1* is specifically required for survival when cells encounter S phase-specific DSBs, which is consistent with the essential role of *NBS1* in DSB end resection prior to HR repair in late S/G2 phase.

Inducible reconstitution of wild-type H2AX and NBS1 in H2AX and NBS1-null human somatic cells, respectively.

Although extensive studies have demonstrated that the histone variant H2AX is a central regulator of IRIF formation, surprisingly H2AX seems to be dispensable for the initial recognition of DNA breaks since transient localization of several DNA damage repair proteins were observed in the absence of H2AX (9). Our previous study showed that the MRN complex can function in DSBs recognition and end resection independently of the H2AX-mediated DDR cascade (1). We propose that the MRN complex is responsible for initial recognition of DSBs and works together with both CtIP and the H2AX-dependent DDR cascade to facilitate repair by HR and regulate DNA damage checkpoints. To test this hypothesis, the best way is to generate a cell model with the disruption of both MRN and H2AX signaling. A recent study reported the generation and characterization of a human H2AX knockout cell line, which was obtained by zinc finger nuclease (ZFN)-mediated deletion. In this study, we took advantage of the CRISPR/cas9 system, which is more efficient than other genome editing tools.

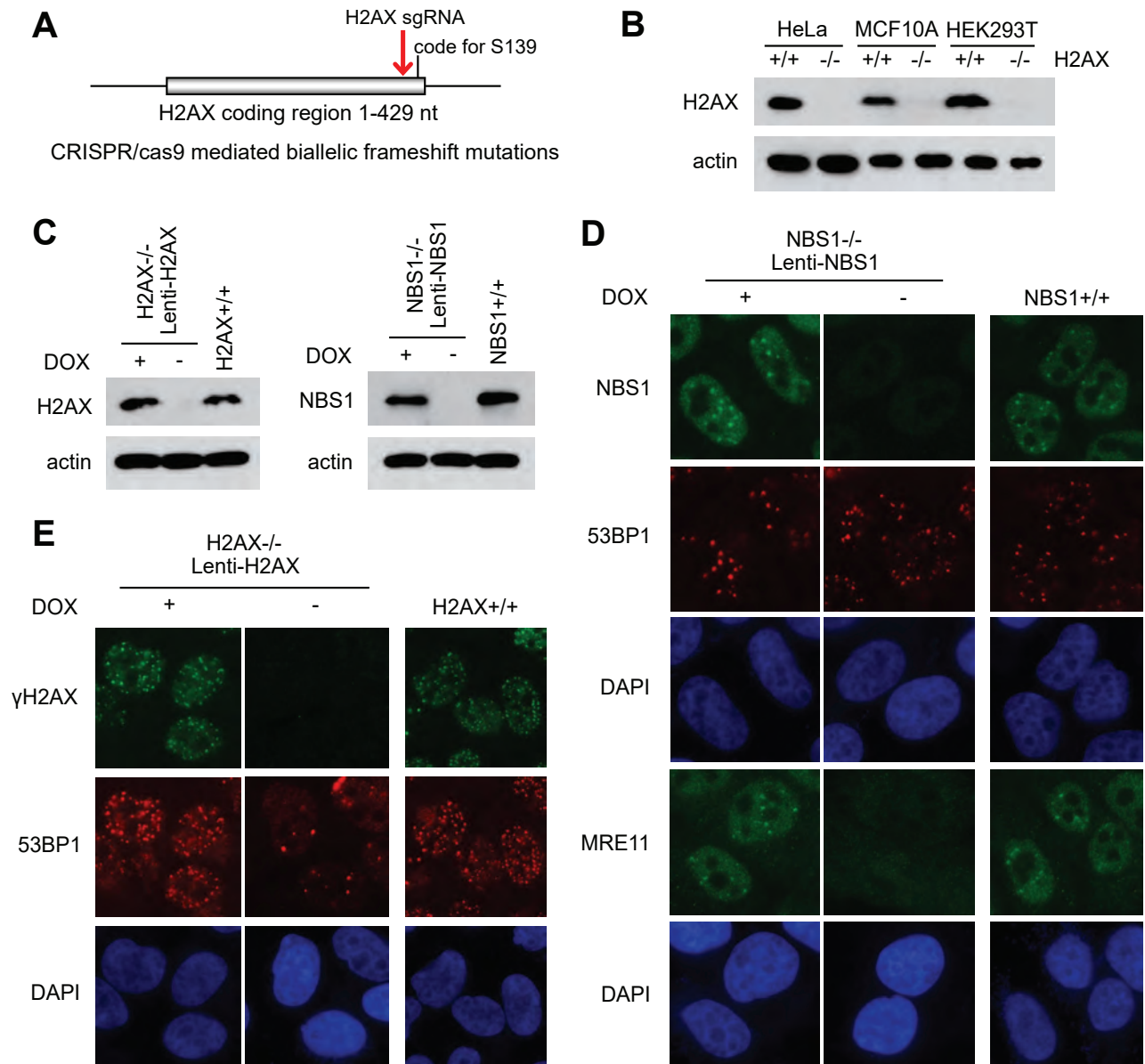


Figure 3. Inducible reconstitution of wild-type H2AX and NBS1 in, respectively, H2AX and NBS1-null human somatic cells. (A) The sgRNA used in CRISPR/cas9 mediated H2AX knockout. (B) H2AX knockout in HeLa, MCF10A and HEK293T was confirmed by immunoblotting. (C) The Tet-On expression of exogenous H2AX and NBS1 was delivered by the lentiviral system and was confirmed by immunoblotting. One $\mu\text{g/ml}$ doxycycline was added to the cells for at least 24 hours to induce H2AX and NBS1 expression. (D and E) The inducible expression of H2AX and NBS1 in H2AX and NBS1 knockout cells was also confirmed by immunostaining. Cells were irradiated (10 Gy) and allowed to recover for one hour before fixation and immunostaining.

Human H2AX has a highly conserved nucleotide coding region compared with H2A, and the only available region for specific CRISPR/cas9 targeting is at the 3' end of H2AX coding sequence. We designed an sgRNA specifically targeting a region nearer the 3' end and right before the code for serine 139 (Fig. 3A), so we can make sure that the CRISPR/cas9 mediated genome editing will be able to remove serine 139, therefore disrupting the γH2AX mediated DDR signaling. As shown in Figure 3B, we successfully generated H2AX knockout in a number of human somatic cells. So far, we successfully generated NBS1-null and H2AX-null cell lines, respectively, and we

also had efficient sgRNAs targeting at both NBS1 and H2AX. However, we failed multiple times to obtain viable cell lines with disrupted NBS1 and H2AX, regardless of whether we tried to generate the double knockout sequentially or simultaneously. We realized that blocking both pathways might result in synthetic lethality in human somatic cells. To test that, we reconstituted NBS1-null and H2AX-null HeLa cell lines, respectively, with wild-type NBS1 and H2AX delivered by lentiviral infection (Fig. 3C). The expression of wild-type NBS1 and H2AX was controlled by tetracycline response element (TRE), which can be transactivated with the

addition of doxycycline, a derivative of tetracycline, in the culture media. As shown in Figure 3C, the induced expression level of NBS1 and H2AX was comparable to the endogenous level in parental HeLa cells. We further checked the DNA damage response signaling in NBS1 and H2AX reconstituted cells. As expected, the reconstituted NBS1 formed clear DNA damage foci, and reconstituting the expression of NBS1 in NBS1-null HeLa cells totally restored the proper localization and recruitment of MRE11 to DSBs, following IR treatment (Fig. 3D). Similarly, reconstituted H2AX in H2AX-null cells was phosphorylated at DNA damage sites, and restored the IRIF of the downstream response protein 53BP1 (Fig. 3E). Thus, we successfully generated the inducible reconstitution of wild-type H2AX and NBS1 in H2AX and NBS1-null HeLa cells, respectively.

Double knockout of NBS1 and H2AX is synthetic lethal in human cells

Given that the NBS1 and H2AX double knockout cells may not be viable, an inducible reconstitution system in the NBS1 and H2AX-null cells yielded the possibility to eventually generate cell lines with the disruption of both NBS1 and H2AX dependent DDR signaling pathways. To achieve this goal, we maintained the reconstituted H2AX and NBS1-null HeLa cells in doxycycline-containing medium, and generated NBS1 and H2AX knockout respectively in the reconstituted H2AX and NBS1-null cells. As shown in Figure 4A, withdrawal of doxycycline successfully resulted in NBS1 and H2AX double knockout in both reconstituted cell lines. Further cell survival assays showed that withdrawal of doxycycline in the reconstituted NBS1 and H2AX double knockout cells resulted in dramatically reduced colony formation (Fig. 4B and C), while withdrawal of doxycycline in wild-type cells actually improved cell survival most likely because of the release of the selection pressure from doxycycline (Fig. 4B and C). These results

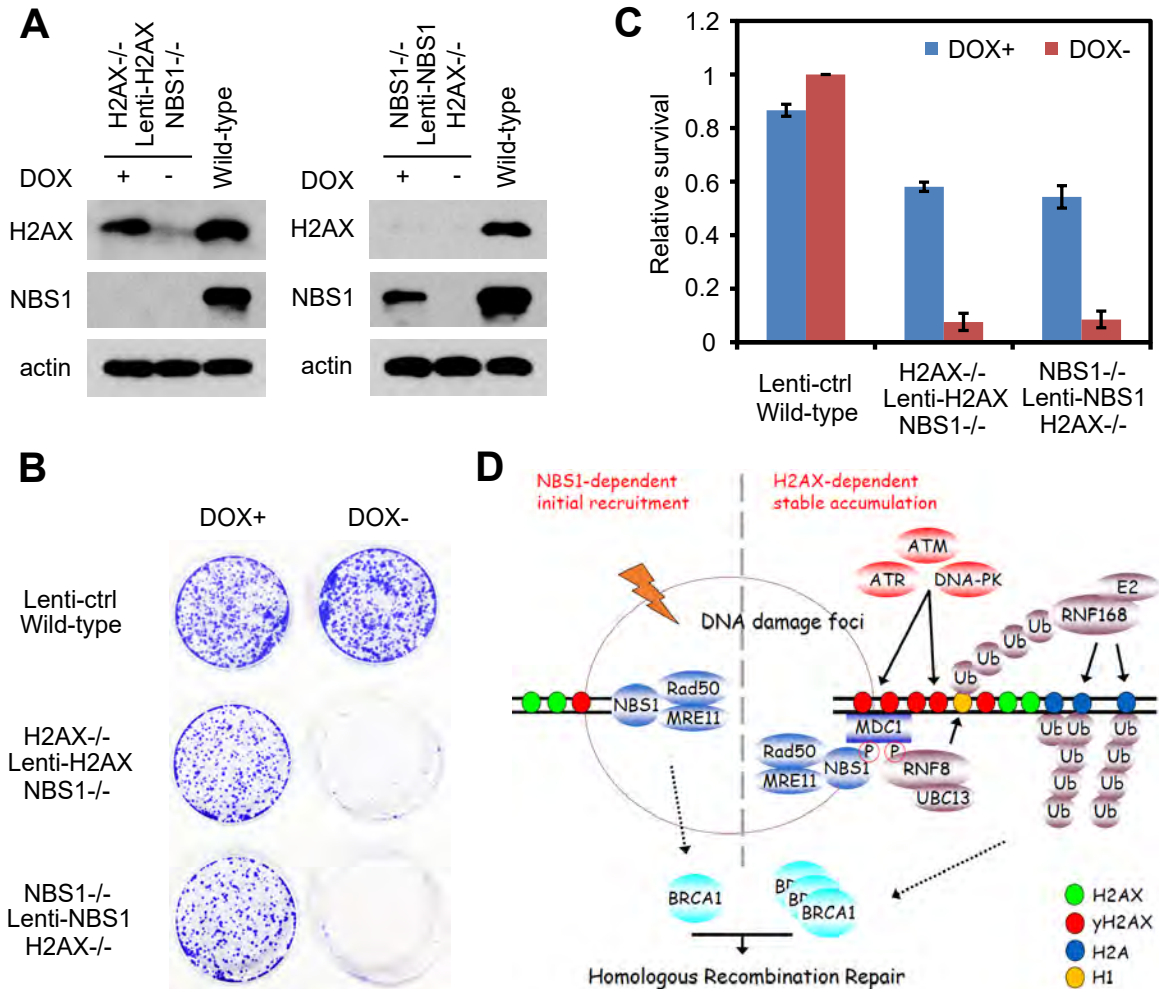


Figure 4. Double knockout of NBS1 and H2AX is synthetic lethal in human cells.

(A) H2AX and NBS1 double knockout cells were generated by the CRISPR/cas9 system. The selection for exogenous expression of H2AX and NBS1 was removed by doxycycline withdrawal. The expression of H2AX and NBS1 was confirmed by immunoblotting. (B) A total of 1×10^3 cells were seeded onto 60-mm dishes and incubated for two weeks. Resulting colonies were fixed and stained with Coomassie blue. (C) Numbers of colonies from B were counted and the data were normalized to those obtained from wild-type cells with doxycycline withdrawal (set as 1.0). Data are presented as mean \pm s.d. from three different experiments. (D) A proposed revised model of the mammalian DNA damage response.

strongly suggest that while NBS1-null and H2AX-null cells can survive endogenous DSBs, double knockout cells have a severe survival disadvantage, most likely due to the removal of two mutually complementary DSBs response and repair pathways.

Conclusion

In this study, we started with the successful generation of a number of NBS1-null human somatic cell lines, which indicate that NBS1 is dispensable for the survival of human somatic cells. Using an inducible reconstitution system in NBS1-null and H2AX-null cell lines, we were further able to generate cellular models with double knockout of NBS1 and H2AX. We conclude that double knockout of NBS1 and H2AX is synthetic lethal in human cells, which strongly supports our hypothesis that cells are equipped with two distinct, however related, DNA damage response pathways: the MRN-dependent initial recruitment and the H2AX-dependent stable accumulation pathways (Fig. 4D).

Synthetic lethality, a situation in which the combination of two independently viable mutations leads to death, has been exploited for cancer therapy. Targeting a gene that is synthetic lethal to a cancer-relevant mutation should kill only cancer cells and spare normal cells (10). The identification of NBS1 and H2AX as a novel pair of synthetic lethal genes will help shed light on not only research in the field of DNA damage repair but also new directions for cancer therapy. We anticipate that this synthetic lethality paradigm can be potentially expanded from NBS1 and H2AX to the MRN complex and H2AX/MDC1 signaling axis.

Acknowledgments

This work was supported in part by a Susan G. Komen CCR Grant and an NCI Transition Career Development Award (K22) to Jingsong Yuan.

References

1. Yuan J & Chen J (2010) MRE11-RAD50-NBS1 complex dictates DNA repair independent of H2AX. *J Biol Chem* 285(2):1097-1104.
2. Zou L & Elledge SJ (2003) Sensing DNA damage through ATRIP recognition of RPA-ssDNA complexes. *Science* 300(5625):1542-1548.
3. Desai-Mehta A, Cerosaletti KM, & Concannon P (2001) Distinct functional domains of nibrin mediate Mre11 binding, focus formation, and nuclear localization. *Mol Cell Biol* 21(6):2184-2191.
4. Cerosaletti KM, et al. (2000) Retroviral expression of the NBS1 gene in cultured Nijmegen breakage syndrome cells restores normal radiation sensitivity & nuclear focus formation. *Mutagenesis* 15(3):281-6.
5. Williams BR, et al. (2002) A murine model of Nijmegen breakage syndrome. *Curr Biol* 12(8):648-653.
6. Becker E, Meyer V, Madaoui H, & Guerois R (2006) Detection of a tandem BRCT in Nbs1 and Xrs2 with functional implications in the DNA damage response. *Bioinformatics* 22(11):1289-1292.
7. Pommier Y, et al. (2003) Repair of and checkpoint response to topoisomerase I-mediated DNA damage. *Mutat Res* 532(1-2):173-203.
8. McGlynn P & Lloyd RG (2002) Recombinational repair and restart of damaged replication forks. *Nat Rev Mol Cell Biol* 3(11):859-870.
9. Celeste A, et al. (2003) Histone H2AX phosphorylation is dispensable for the initial recognition of DNA breaks. *Nat Cell Biol* 5(7):675-679.
10. Kaelin WG, Jr. (2005) The concept of synthetic lethality in the context of anticancer therapy. *Nat Rev Cancer* 5(9):689-698. ■



Constantinos Broustas, Qi Wang, Monica Pujol, Manuela Buonanno, Rob Morton

Mitochondrial Fission Protein DRP1 Regulates Tumor Immunogenicity through PD-L1 Expression

Jinhua Wu and Tom K. Hei

The recent success of combining radiation therapy with immunotherapy in cancer treatment has demonstrated a powerful role of local radiation therapy. Growing evidence suggested that radiation therapy targeted to a tumor can convert it into an *in situ* tumor vaccine by recruiting anti-tumor T cells. In the current study, we investigated the connection between energy metabolism and tumor immunogenicity in response to radiation therapy. We reported that radiation leads to mitochondrial fission protein DRP1 inactivation, which is required for induction of immune-suppressor PD-L1 in various cancer cell lines. CRISPR knockdown of DRP1 increased basal levels of PD-L1 as well as the radiation-induced PD-L1 level. Our study is the first to connect mitochondrial function with radiation induced immune responses, hence providing alternative targets in radiation-immunotherapy to potentially enhance the

synergistic effect.

Using three cancer cell lines representing three different cancer types: lung cancer cell line A549, breast cancer cell line MDA-MB-231, and neuroblastoma cell line SH-SY5Y, we tested whether radiation induces PD-L1 expression. Using 2 Gy and 10 Gy γ -radiation, PD-L1 induction was detected at both the mRNA (Fig. 1A) and protein (Fig. 1B) levels. Although the induction of mRNA was less than 2-fold in all three cell lines 48 hour after irradiation, the increase in protein expression level was much more significant. More interestingly, this induction of PD-L1 was only observed in cancer cell lines while no change was observed in immortalized human small airway epithelial cells (SAECs) (Fig. 1C). Hence, we conclude that radiation induces PD-L1 expression only in cancer cells, which is consistent with previous reports in the literature.

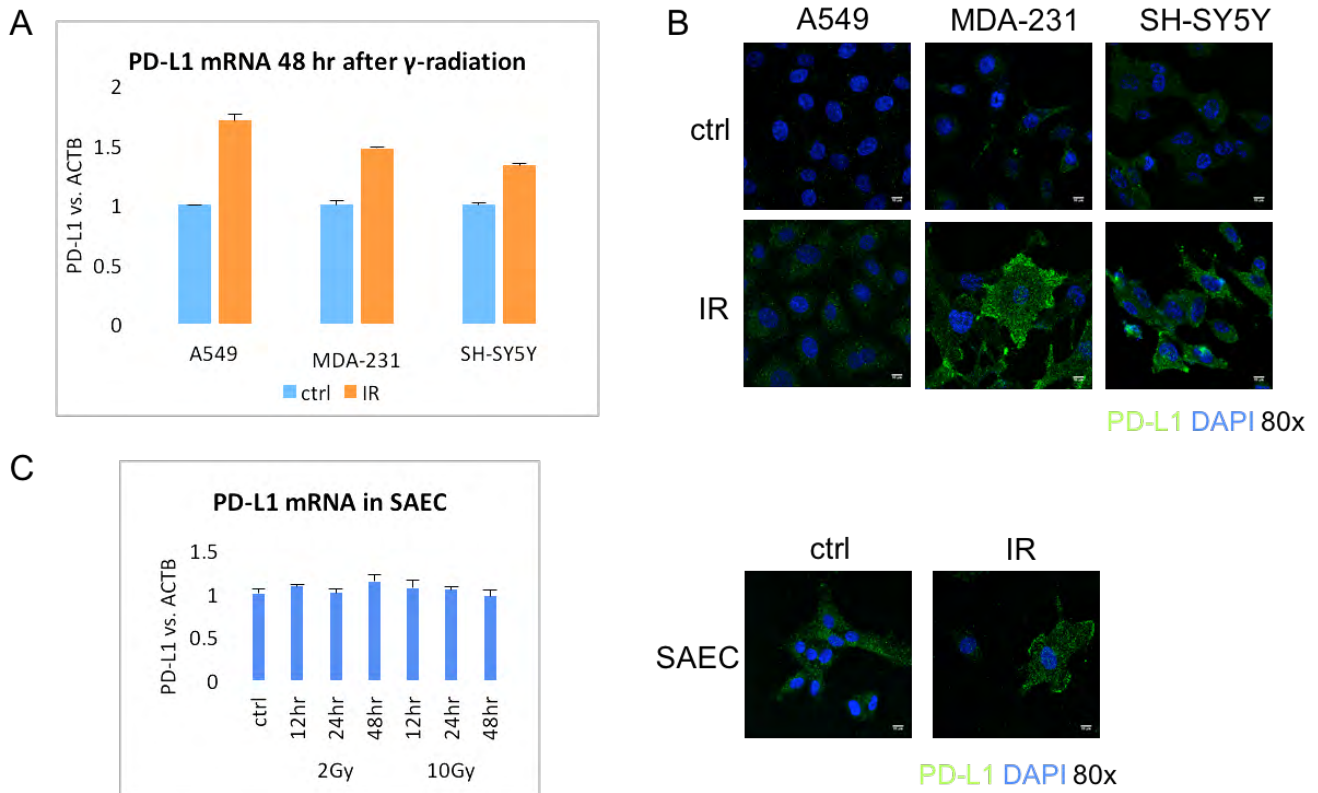


Figure 1. Radiation induces PD-L1 expression in cancer cell lines. A. Cancer cell lines were irradiated with 10 Gy γ -rays and cells were lysed using Trizol 48 hours after radiation exposure. RT-QPCR was used to evaluate PD-L1 mRNA level. β -actin was used as a reference gene. B. Cancer cell lines were irradiated with 10 Gy γ -rays and cells were fixed 48 hours after irradiation. Immunofluorescence was used to detect PD-L1 protein levels. DAPI was used to visualize the nucleus. C. RT-QPCR and immunofluorescence were performed as described in A and B in small airway epithelial cells (SAECs).

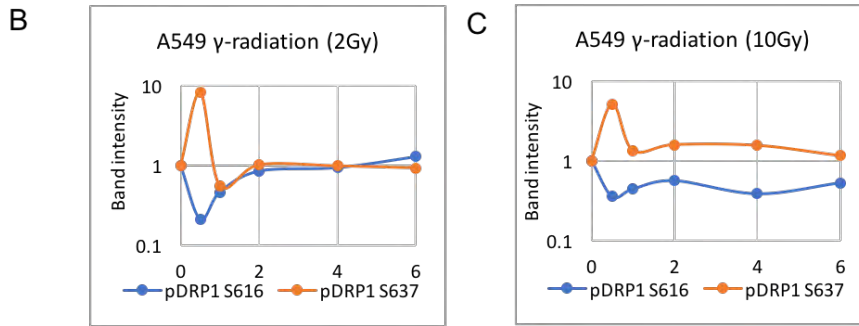
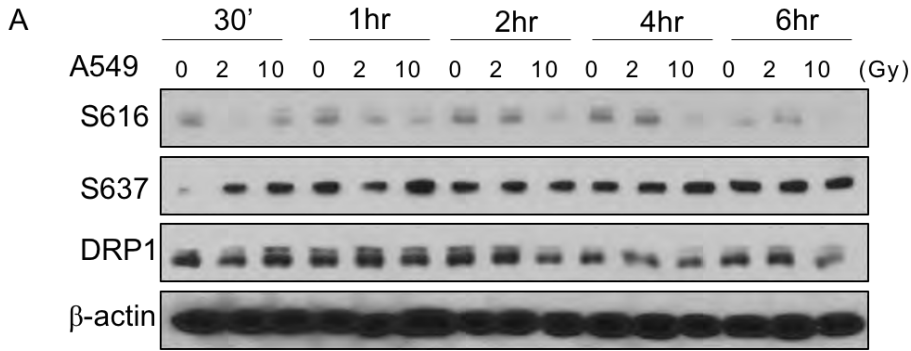


Figure 2. Radiation inactivates DRP1 in a time-dependent manner. **A.** Lung cancer cell line A549 was irradiated using γ -rays at 2 Gy and 10 Gy. Cells were harvested at indicated time points and lysates were used for western blotting. β -actin was used as a loading control. **B** and **C** phosphorylation status of S637 and S616 residues was quantified based on band intensity in **A** using ImageJ.

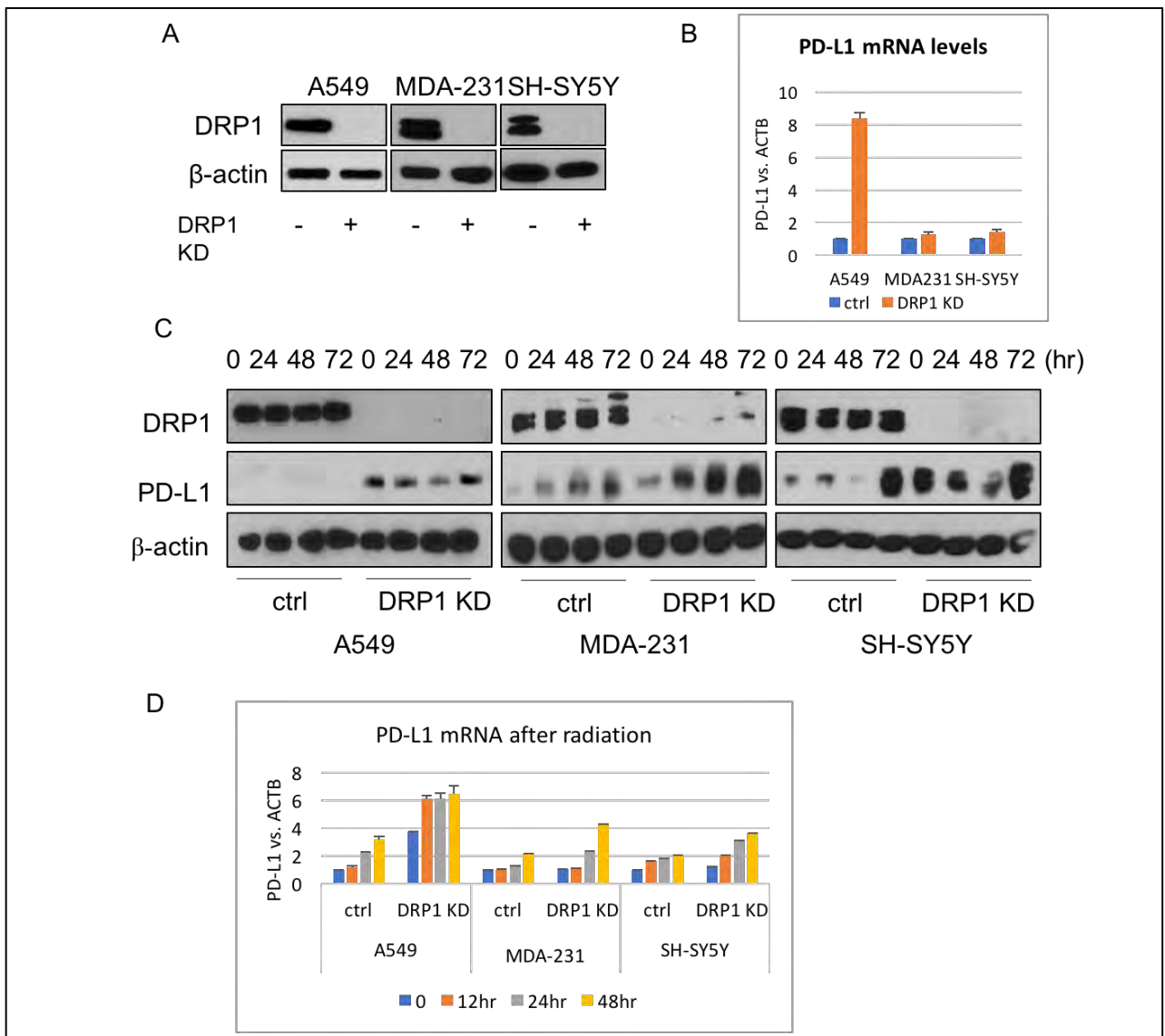


Figure 3. (Previous page) PD-L1 level increased in DRP1 knockdown cells. A. DRP1 knockdown efficiency was verified using western blotting. B. PD-L1 mRNA levels in DRP1 knockdown cells were examined using QPCR against β -actin. C & D. Cells were irradiated with 10Gy γ -radiation and samples were lysed at indicated time points. Western blotting (C) and QPCR (D) were performed to evaluate protein and mRNA level of PD-L1, respectively, after irradiation.

In an effort to understand how radiation induces PD-L1, we investigated mitochondrial changes in a time-dependent manner. We found that the activity of one of the proteins important for mitochondrial biogenesis, DRP1, changed activity shortly after irradiation. As shown in Fig. 2A, two different phosphorylation sites on DRP1 were tested using western blotting on lung cancer cell line A549; phosphorylation at serine residue 616 (S616) indicates the activation of DRP1 while phosphorylation at serine residue 637 (S637) suggests inactivation of the protein. Quantification of band intensity separated by different radiation doses is shown in Fig. 2B and 2C. Shortly after radiation, a significant increase of S637 and a decrease in S616 was observed after both 2Gy (Fig. 2B) and 10 Gy (Fig. 2C) irradiation.

Restoration of DRP1 activity was seen around 2 hours after 2 Gy radiation and not until 6 hours after 10 Gy radiation.

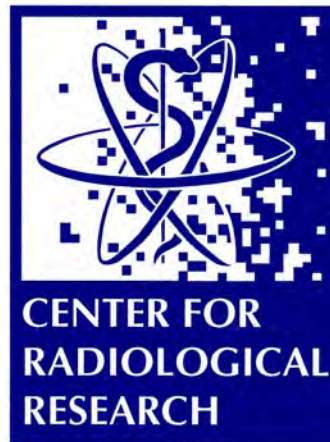
Our next goal was to figure out whether the inactivation of DRP1 by radiation is related to the induction of PD-L1. To answer this question, we generated DRP1 knockdown cells using CRISPR gRNAs in the three cancer cell lines used in Fig. 1. The knockdown efficiency was first evaluated using western blotting (Fig. 3A). A more than 70% knockdown was achieved in all three cell lines. The knockdown efficiency was further confirmed using RT-QPCR (data not shown). Using these knockdown cell lines, we tested if impaired DRP1 played a role in PD-L1 expression. Using RT-QPCR, we were able to detect increased levels of basal PD-L1 mRNA in all three cell lines with knockdown of DRP1 (Fig. 3B). Furthermore, in response to radiation, more significant increases of PD-L1 were found in DRP-1 knockdown cell lines (Fig. 3C & D).

In conclusion, our study indicates mitochondrial fusion protein DRP1 plays an important role in radiation enhanced immunosurveillance by regulating PD-L1 expression levels. These findings provide vital targets to improve the effect of radiation therapy in cancer immunotherapy. ■



Picnic at Nevis

POPULATION AND CLINICAL STUDIES



Dose Dependence of Accelerated Repopulation in Head and Neck Cancer: Supporting Evidence and Clinical Implications

Igor Shuryak, Eric J. Hall, and David J. Brenner

Cancer treatment with any cell-killing agent, including radiation, typically stimulates the remaining surviving cells to divide faster than before [1, 2]. In the radiotherapeutic context, there is strong clinical evidence for such phenomena in human tumors: For example, Withers and colleagues [3, 4] surveyed the literature for the radiotherapy of head and neck cancers (HNC) and concluded that the tumor clonogens in this rapidly growing cancer start accelerated repopulation (AR) around 28 days after the initiation of fractionated radiotherapy. In that AR is most likely a compensatory proliferative response to cell killing or dead cell removal [5-7], it is likely that the onset and rate of AR will depend on the level of cell killing at any given time during treatment.

Following Tucker et al. [8] and Fowler [9], AR is now a standard component of the linear-quadratic model, which is routinely used to compare fractionation protocols, or to design new protocols [10]. In this standard model, tumor cell killing is described by the linear-quadratic model, and AR is assumed to begin at a fixed onset time after the beginning of the treatment, often referred to as the “kickoff” time. At all later times, AR is assumed to progress at a rate characterized by a fixed exponential growth parameter. Both of these parameters are assumed to be independent of dose or fractionation.

Such a model appears inconsistent with the notion that AR is a proliferative response to cell killing and removal. In such a case, both the onset and the rate of AR would be expected to depend on the level of cell killing at the time, and thus on the dose and dose-fractionation delivered up to that time. Such mechanisms have been discussed in the context of normal tissue response [11, 12], and we propose here an alternative model of tumor AR in which the onset time and rate of AR are both modulated by the rate of tumor cell killing. Thus, for example, when a tumor is subjected to a more intense dose fractionation regimen where larger numbers of tumor cells are killed per day, surviving clonogens respond by increased AR.

To test this hypothesis, we developed a model of the potential dose and dose-fractionation dependences of AR. We compared the performance of this dose-dependent (DD) model with the dose-independent (DI) model, using a data set of published tumor control probability (TCP) data from 16 randomized clinical trials for HNC (7,283 patients), which used a wide range of doses, treatment times, and fractionation schemes. We then explored the

potential clinical implications by using best-fit predictions to identify potentially improved radiotherapy protocols for HNC.

Our results showed that the alternative DD model of AR provides significantly-improved descriptions of the clinical data, relative to the DI model. Importantly, the two models differ substantially in their predictions (Fig. 1). The DD model predicts that, for currently-used HNC fractionation schemes, the last 5 fractions do not increase TCP, but simply compensate for increased accelerated repopulation (Fig. 1).

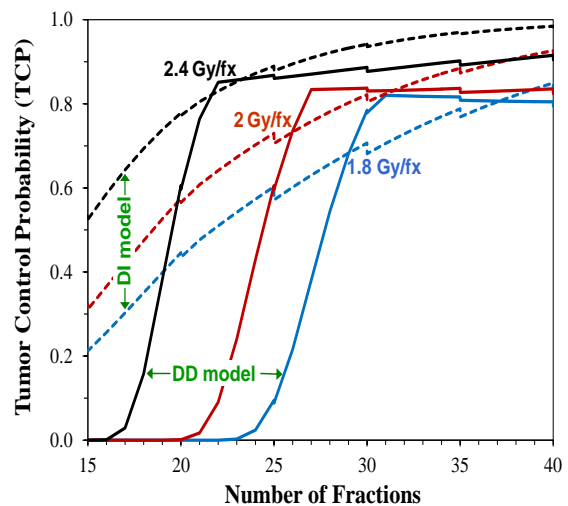


Figure 1. Predicted TCP values for stages T1/2 HNC as a function of number of fractions delivered. Predictions by the standard dose-independent DI model (dashed curves) and the dose-dependent DD model (solid curves) for regimens using doses per fraction (fx) of 1.8 Gy (blue), 2 Gy (red) and 2.4 Gy (black), administered daily on weekdays. The jagged behavior of the curves is due to repopulation of tumor clonogens on weekends. The curves show that the tumor control as predicted by the DI model grows steadily with increasing numbers of radiotherapy fractions - AR can slow the increase in TCP, but does not stop it at these doses per fraction. By contrast, the DD model predicts that in the later stages of treatment, intense AR may completely stop any increase in tumor control.

In summary, we describe an alternative quantitative model of AR in which both the onset and the rate of AR depend on the level of clonogen killing, which in turn depends on the dose and fractionation scheme. The notion that AR is quantitatively related to cell killing has been

discussed for normal tissue response [11, 12], but we suspect that this work is the first time the concept has been quantitatively applied to radiotherapy-induced tumor kinetics.

We compared this dose-dependent (DD) model of AR, and also the standard dose-independent (DI) model of AR, with a large body of clinical data (16 clinical trials, 35 protocols, 7,283 patients) which used a broad range of doses, overall times and fractionation schemes, and which together are therefore particularly sensitive to the effects of AR. We also applied both models to an earlier data set compiled by Withers et al. [3]. The results show that the more mechanistically-motivated dose dependent (DD) model is in better agreement with the large body of clinical data analyzed, than the standard dose-independent (DI) model.

While this conclusion in terms of the mechanisms of AR is of interest, we suggest that it has considerable implications for standard radiotherapeutic treatments of tumors that do undergo significant AR during radiotherapy, such as HNC. Specifically, in contrast to the prediction of the standard DI model, the dose-dependent AR model predicts that, for conventionally fractionated treatments for HNC (e.g. $35 \times 2\text{Gy}$ fractions or $40 \times 1.8\text{Gy}$), AR becomes so active towards the end of the treatment that, during the last week of treatment, the TCP may actually stop increasing or even decrease (Fig. 1). In other words, during the last few days of a conventional treatment with 1.8 or 2.0 Gy/fraction, cell killing by the radiotherapy is unable to overcome the effects of AR, and, thus, it is not contributing to improved tumor control.

It follows that reducing the number of fractions for these standard protocols by 5, i.e., eliminating the last week of radiotherapy but not otherwise changing the protocol, does not reduce (and may even slightly increase) the TCP predicted by the DD model. However, the decreased overall dose associated with eliminating the last week of treatment would significantly reduce late sequelae (Fig. 2). For example abbreviating the standard $35 \times 2\text{Gy}$ HNC protocol to $30 \times 2\text{Gy}$ is predicted to maintain TCP (estimated here as ~84% for T1/2 HNC) but, due to the lower total dose, is predicted to markedly reduce late normal tissue complication probability (NTCP, e.g. grade 3–5 late toxicity at 5 years) from ~13.1% to less than 1%. Comparable benefits may be expected by reducing the standard $40 \times 1.8\text{Gy}$ to $35 \times 1.8\text{Gy}$ (Fig. 2). Considering a slightly higher dose per fraction, which, from the perspective of TCP is desirable but would normally be associated with a higher NTCP, abbreviating a protocol from $30 \times 2.4\text{Gy}$ to $25 \times 2.4\text{Gy}$ is predicted to almost maintain TCP (estimated here as ~89% and ~87%, respectively for T1/2 HNC), but to markedly reduce NTCP from about 37% to about 2% (Fig. 2).

While a major decrease in late sequelae is predicted with these abbreviated protocols due to the decreased overall dose, a decrease in early sequelae is less likely – and thus there is probably limited scope for dose

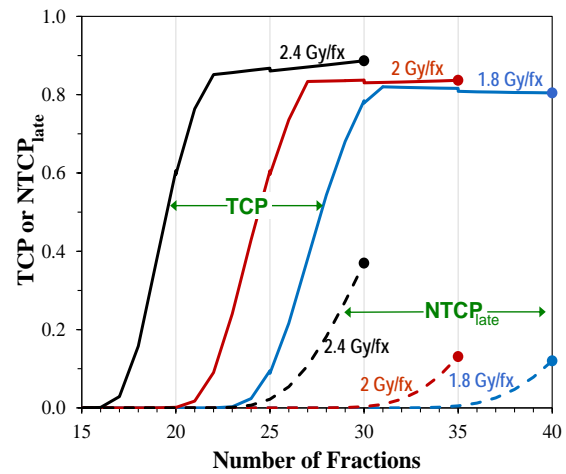


Figure 2. Predicted TCP values (solid curves) as a function of number of fractions delivered, for stages T1/2 HNC, predicted by the preferred DD model; doses per fraction (fx) 1.8 Gy (blue), 2.0 Gy (red) or 2.4 Gy (black), administered daily on weekdays. $\text{NTCP}_{\text{late}}$ predictions for late toxicity (dashed curves with same color coding as above) were made with the standard linear-quadratic model normalized (see text) to a 13.1% value (grade 3–5 late toxicity at 5 years) for $35 \times 2\text{Gy}$ fractions. The solid circles represent current standard treatment regimens. It can be seen that a 5-fraction (1 week) reduction in these standard regimens is predicted to not appreciably change the predicted TCP, but to markedly reduce the late toxicity ($\text{NTCP}_{\text{late}}$).

escalation. Rather we expect no major changes in early sequelae because early effects such as mucositis are likely to be associated with the same cellular repopulation kinetics as for the adjacent head and neck tumors.

In summary, if the arguments presented here should prove realistic, there is the potential for a major decrease in late sequelae after head and neck radiotherapy, without loss of tumor control, simply by eliminating the last week of current standard protocols. In addition, the abbreviated HNC protocols proposed here, involving a one week decrease in overall treatment time, should be advantageous both logistically and for patient convenience. That said, there are of course caveats in terms of the analyses performed here: In that the baseline factors and treatment results for individual patients were not available from the literature, this analysis contains a number of simplifications, such as not accounting for the effects of individual tumor location, patient age and sex, calendar year and institution-specific factors, as well as more recently developed prognostic factors, such as the HPV16 status in oropharyngeal tumors. In addition, it is of course well established that the standard linear quadratic model used here (as well as in most contemporary mechanistic radiotherapeutic analyses), while mechanistically motivated, does not take into account a number of phenomena such as reoxygenation and possible changes in the alpha/beta ratio during treatment.

Despite these caveats, we suggest that the comparisons described here provide insight into how well each of the two models captures the major effects of radiotherapy on tumor repopulation – and if the conclusions reached here prove realistic, a significant decrease in late normal tissue complications after head and neck radiotherapy is a real possibility.

References

1. Roti JL, Dethlefsen LA. Matrix simulation of duodenal crypt cell kinetics. II. Cell kinetics following hydroxyurea. *Cell Tissue Kinet* 1975;8:335-53.
2. Hermens AF, Barendsen GW. Changes of cell proliferation characteristics in a rat rhabdomyosarcoma before and after x-irradiation. *Eur J Cancer* 1969;5:173-89.
3. Withers HR, Taylor JM, Maciejewski B. The hazard of accelerated tumor clonogen repopulation during radiotherapy. *Acta Oncol* 1988;27:131-46.
4. Roberts SA, Hendry JH. The delay before onset of accelerated tumour cell repopulation during radiotherapy: a direct maximum-likelihood analysis of a collection of worldwide tumour-control data. *Radiother Oncol* 1993;29:69-74.
5. Pang LY, Hurst EA, Argyle DJ. Cyclooxygenase-2: A role in cancer stem cell survival and repopulation of cancer cells during therapy. *Stem Cell Internat* 2016;2016:2048731.
6. Wilson GD, Thibodeau BJ, Fortier LE, Pruetz BL, Galoforo S, Marples B, et al. Cancer stem cell signaling during repopulation in head and neck cancer. *Stem Cell Internat* 2016;2016:1894782.
7. Huang Q, Li F, Liu X, Li W, Shi W, Liu F-F, et al. Caspase 3-mediated stimulation of tumor cell repopulation during cancer radiotherapy. *Nature Med* 2011;17:860-66.
8. Travis EL, Tucker SL. Iso-effect models and fractionated radiotherapy. *Int J Radiat Oncol Biol Phys* 1987;13:283-87.
9. Fowler JF. Rapid repopulation in radiotherapy: a debate on mechanism. The phantom of tumor treatment--continually rapid proliferation unmasked. *Radiother Oncol* 1991;22:156-8.
10. Brenner DJ. Accelerated repopulation during radiotherapy: Quantitative evidence for delayed onset. *Radiat Oncol Invest* 1993;1:167-72.
11. Morris GM, Hopewell JW. Changes in the cell kinetics of pig epidermis after single doses of X rays. *Br J Radiol* 1988;61:205-11.
12. Trott K-R. Biological basis for skin and mucosal toxicity. In: Dunst J, Sauer R, editors. *Late Sequelae in Oncology*. Berlin, Heidelberg: Springer. 1995; 89-91. ■

Association between Non-melanoma and Melanoma Skin Cancer Rates, Vitamin D and Latitude

Miguel Rivas^a, Elisa Rojas^a, and Gloria M. Calaf^{b,c}

The major role of vitamin D in vertebrate animals and humans is to increase calcium and phosphate absorption for the mineralization of the skeleton. The most important source of this vitamin for individuals living at mid and low latitudes is vitamin D synthesis induced by solar ultraviolet-B (UVB) radiation [1]. The recommended daily allowance (RDA) for vitamin D in the United States is 200 IU (5.0 µg), which is reasonable for adults who receive some sun exposure; however, in the absence of sun exposure, this RDA may be 2 to 3 times lower than that actually required to satisfy what the body requires [2]. Vitamin D₃ is efficiently produced via pre-vitamin

D₃ from the precursor 7-dehydrocholesterol when human skin is exposed to solar UVB [3, 4].

The total volume of atmospheric ozone and cloudiness are also important factors that control UVB radiation, and the area of exposed skin and skin type is relevant to the amount of vitamin D synthesis [5]. At subtropical latitudes, there is no alteration of vitamin D production during winter. At low latitudes, vitamin D synthesis continues throughout the winter at reduced capacity, and at high latitudes, there is no production for 4-6 months of the year [6]. Vitamin D synthesis originates from two sources, firstly from solar or artificial UVB exposure, and secondly from dietary products and supplements in individuals who live at higher latitudes where solar UVB radiation is weak in winter [3,4].

Vitamin D deficiency is commonly found in risk groups such as postmenopausal women and individuals suffering from rickets, osteomalacia and osteoporosis, since vitamin D is vital for normal calcium metabolism

^aDepartment of Physics, Faculty of Science, Tarapaca University, Arica, Chile

^bCenter for Radiological Research

^cInstitute of Advanced Research, Tarapaca University, Arica, Chile

and the maintenance of bone density [7]. Vitamin D deficiency is also associated with an increased cardiovascular risk and arterial stiffness [8]. Furthermore, it is associated with epidemic influenza, as solar radiation produces a seasonal variation that profoundly affects the pathogenesis of the disease [9, 10].

Non-melanoma skin cancer (NMSC) is the most commonly occurring cancer type in the Caucasian population. The non-melanoma tumors may originate from squamous or basal cells. These cells in the skin occasionally change and do not behave normally, resulting in precancerous conditions. As a consequence, there is a high chance that these abnormal cells will become cancerous [11]. Melanoma skin cancer (MSC) is a result of the transformation of skin melanocytes. At present, MSC is the most common tumor diagnosed in the United States and numerous other countries, and NMSC and MSC cases have each markedly increased in number over the last few decades. Melanomas represent <10% of all skin cancers, but they are responsible for the majority of skin cancer-related mortalities due to a high metastatic potential and therapeutic resistance [9,12,13]. Previous studies demonstrated that risk factors for cutaneous melanoma depended upon the anatomical site and the clinicopathological variant [14], and that there was an inverse association between vitamin D blood levels and cutaneous thickness of the melanoma at diagnosis [15].

The associations among skin type IV, the time to induce solar erythema (T_{Ery}) and the time required to produce 1,000 IU vitamin D (T_{vitD}) have previously been studied in Arica, a city located in the northern region of Chile, close to the equator and surrounded by desert and ocean [16,17]. The association between skin cancer rates per 100,000 inhabitants and the solar UV index (UVI) was previously studied between 2001 and 2006 in this city [18], and between 2007 and 2011 with latitude variation [19]. The most common skin types in Chile have been found to be type III for women and type IV for men [20]. The skin type is expressed as the number of standard erythema doses (SED) according to the Fitzpatrick skin type classification; skin type III for women (3-5 SED) induced erythema type III in Caucasian skin, whereas skin type IV for men (4.5-6 SED) induced type IV in Mediterranean skin [21]. Vitamin D is formed mainly in the skin upon exposure to UVB and it is taken orally with food or through supplements [14, 22-24]. Since sun exposure is a known factor for skin cancer development, the aim of the present study was to analyze the association between NMSC and MSC rates, and solar UVI data obtained from 6 different cities in Chile ranging from latitude 18 to 53°S.

Measurements. Solar UVI measurements were obtained using a YES-UVB-1 UV biometer (Yankee Environmental Systems, Inc., Turners Falls, MA, USA), according to the manufacturer's instructions [25], in the Solar Ultraviolet Laboratory of Tarapaca University in Arica, Chile. The data provided by this instrument

included the latitude, longitude and altitude, as well as the ozone layer and cloudiness for each location. This laboratory is run in agreement with and as part of the Chilean Meteorological Organization network. This instrument is calibrated in accordance with their recommendations. It is accepted that solar UVI fluctuates from 1 to 11 according to the World Meteorological Organization. An algorithm developed by McKenzie, *et al* [26] was used to calculate the T_{vitD} from experimental measurements of solar UVI in different cities. The minimal erythema dose (MED) is the minimum amount of UV that produces redness 24 h after exposure, where one MED is equal to 240 J/m² of UV doses required to induce erythema [27], according to the Fitzpatrick skin type classification [21]. The T_{ery} in unprotected skin (only hands and face, i.e., 10% of the body) was calculated using the following equation:

$$T_{ery} = \frac{MED(\text{skin}_{type})}{UV_{ery}}$$

The amount of UV solar radiation to induce erythema (UV_{ery}) was directly obtained from the following equation [where the unit for UV_{ery} is milliwatt (mW) divided by square meters (m²)]:

$$UV_{ery} = \frac{UVI}{40} \left(\frac{mW}{m^2} \right)$$

Population data. The NMSC ratio was calculated in males and females for each city in comparison to Punta Arenas. NMSC and MSC rates were considered for each location and the data for skin cancer rate normalized by patient age was obtained between 2005 and 2007 from the Ministerio de Salud (Ministry of Health) of Chile, where open access to cancer population data has been established by Resolution number 23.01.2002, therefore Ethics/guidelines must be considered in each hospital of Chile.

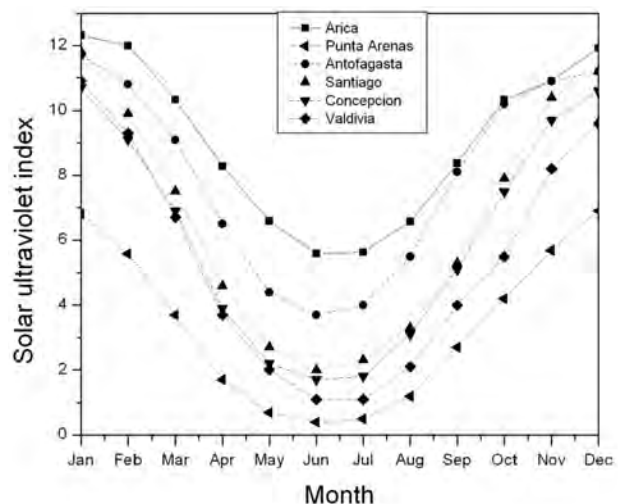


Figure 1. Solar ultraviolet index per month obtained in several cities of Chile between January and December.

Table I. Latitude, longitude, altitude and solar UVI data per year in different geographical locations of Chile.

City	Latitude	Longitude	Alt. (m)	Solar UVI data (Year)
Arica	18°18'S	70°18'W	25	2006 - 2013
Antofagasta	23°38'S	70°24'W	40	1997 - 2005
Santiago	33°23'S	70°47'W	475	2004 - 2009
Concepción	36°46'S	73°03'W	8	2003 - 2007
Valdivia	39°48'S	73°14'W	9	2001 - 2004
Punta Arenas	53°00'S	70°51'W	37	2001 - 2005

Atl. = altitude. UVI = Ultra-violet Index

Statistical analysis. Statistical analysis was performed using standard statistical criteria, and correlations were assessed by evaluating the quotient between covariance and standard deviation for each variable. Pearson's linear correlation was used for statistical purposes. Statistical analysis was performed using StatDisk software (version 12.0.2; Pearson plc, London, UK). $P < 0.05$ was considered to indicate a statistically significant difference.

The present study considered solar UVI measurements, NMSC and MSC rates, mortality rates per 100,000 inhabitants and the association with the time required to synthesize adequate levels of vitamin D in different geographical locations of Chile. T_{vitD} was calculated to explain the association between NMSC and MSC rates in 6 cities in Chile between latitude 18 and 53°S. The monthly averages of the T_{vitD} were calculated from the maximum UVI daily values obtained from Arica, Antofagasta, Santiago, Concepción, Valdivia and Punta Arenas, with latitudes of 18, 23, 33, 36, 39 and 53°S, respectively.

Fig. 1 shows the mean solar UVI per month considering the maximum value for each day (at noon) and the latitude of these cities between January and December. Solar UVI values fluctuated from a minimum in winter (June) to a maximum in summer (January), recorded as 5.6-12.3 in Arica, 3.7-11.7 in Antofagasta, 2.0-11.8 in Santiago, 1.7-10.7 in Concepción, 1.1-10.9 in Valdivia and 0.4-6.9 in Punta Arenas.

Table II. NMSC and MSC mortality rates per 100,000 individuals between 1990 and 2005 [28]

City	NMSC	MSC
Arica	1.07	0.54
Antofagasta	1.89	0.75
Santiago	0.75	1.00
Concepción	0.84	1.07
Valdivia	0.57	0.82
Punta Arenas	0.89	1.21

MSC = melanoma skin cancer; NMSC = non-MSC.

Table III. NMSC and MSC rates per 100,000 individuals in males and females between 2003 and 2007 [28]

City	NMSC		MSC	
	M	F	M	F
Arica	69.7	52.4	3.7	1.2
Antofagasta	55.5	46.7	2.1	2.1
Santiago	24.7	16.5	2.9	2.5
Concepción	20.9	19.5	3.4	2.5
Valdivia	19.7	21.4	3.6	2.5
Punta Arenas	22.8	29.4	0.8	0.9

MSC = melanoma skin cancer; NMSC = non-MSC.
M=male; F=female.

Tables I-III show solar UVI data, and NMSC and MSC rates from different geographical locations in Chile. Table I presents latitude, longitude and altitude, and solar UVI data per year, from the following geographical locations in Chile: Arica, Antofagasta, Santiago, Concepción, Valdivia and Punta Arenas. Table II presents NMSC and MSC mortality rates per 100,000 inhabitants in the same locations as aforementioned between 1990 and 2005, while Table III presents NMSC and MSC rates in males and females in these cities between 2003 and 2007 [28]. Data from Table III is also shown in Fig. 2A and B. The results indicated that the NMSC rates in males and females were greater in the northern cities of Chile, such as Arica and Antofagasta, compared with the rate in cities located farther south, such as Concepción and Valdivia (Fig. 2A). Fig. 2B shows MSC rates in males and females from Arica to Punta Arenas; the data indicated that the rate of MSC was lower in females than males in Arica and in cities located farther south, such as Santiago, Concepción and Valdivia. An inverse association was observed between NMSC and latitude in males and females, as observed at 18°S in Arica and 36°S in Concepción (Fig. 2C); thus rates decreased as latitude increased. Fig. 2D shows that the MSC rates in males and females increased as latitude increased (23 and 40°S), with the exception of Punta Arenas (53°S), in which the MSC rates in males and females decreased.

In Chile, the most common skin types are type III for women that tan moderately and uniformly, with an MED of 0.30-0.50 kJ/m², and skin type IV for men with corresponding light brown skin that tans minimally, moderately and easily with an MED of 0.40-0.60 kJ/m² [27]. Fig. 3 shows the T_{vitD} in 6 cities of Chile every month. The maximum values were observed in June (winter) and varied from 18-700 min in Arica and Punta Arenas, respectively.

Fig. 4A-B shows NMSC and MSC mortality rates with regard to latitude and T_{vitD} accumulated over 1 year. Fig. 4A shows that there was a negative correlation between NMSC mortality rates and latitude ($r = -0.53$), and no correlation between NMSC mortality rate and T_{vitD} accumulated in 1 year ($r = -0.25$). A strong correlation was also found between MSC mortality rates and latitude ($r = 0.88$), and between MSC and T_{vitD} accumulated over 1

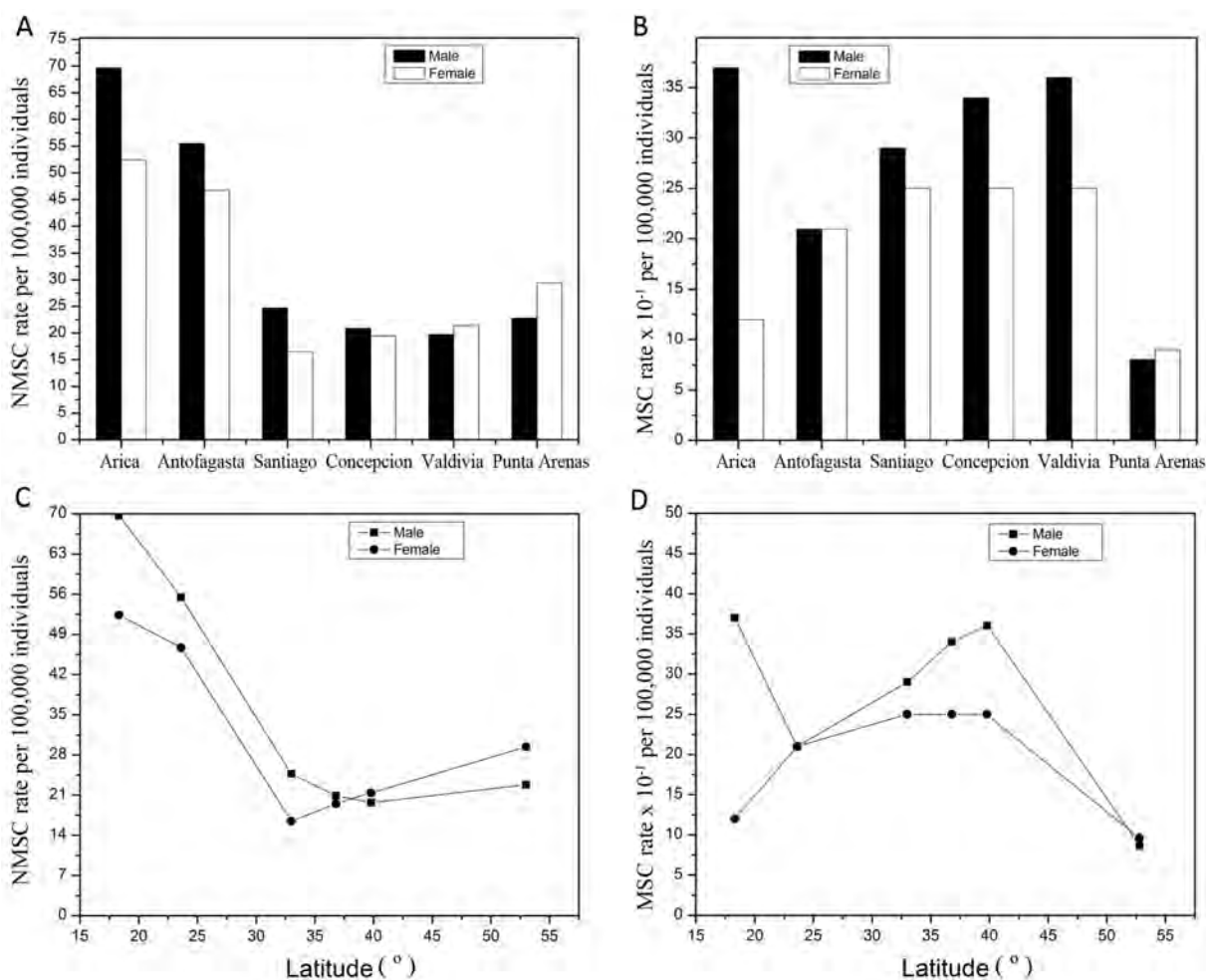


Figure 2. (A) NMSC and (B) MSC rates in 6 cities, and (C) NMSC and (D) MSC rates at different latitudes in males and females in Chile. MSC, melanoma skin cancer; NMSC, non-MSC.

year ($r=0.72$), as shown in Fig. 4B. The NMSC ratio was calculated in males and females for each city in comparison to Punta Arenas. This was found to be 3.1 and 1.8 in Arica, 2.4 and 1.6 in Antofagasta, 1.1 and 0.6 in Santiago, 0.9 and 0.7 in Concepción, and 0.9 and 0.7 in Valdivia, respectively. This was probably due to the low solar UVB radiation levels in the southern cities of Chile in winter (June 21 to September 20). The MSC ratio was calculated for each city in comparison to Punta Arenas in males and females. This was found to be 4.6 and 1.3 in Arica, 2.6 and 2.3 in Antofagasta, 3.6 and 2.8 in Santiago, 4.3 and 2.8 in Concepción, and 4.5 and 2.8 in Valdivia, respectively.

The dose-response associations between vitamin D and cancer risk reduction have been previously estimated, and data has indicated that it takes 1,500 IU vitamin D3 per day to obtain a 29% cancer risk reduction for male cancer mortality rates in the United States [29]. The present study provides an analysis of solar UVI levels reported in 6 cities from the north to the south of Chile in different months. The results showed that the solar UVI ratio of monthly mean values was 1.8 times higher in Arica than in Punta Arenas in January (summer in Chile),

whereas it was 14 times higher in June (winter in Chile). This factor is an important consideration since vitamin D synthesis is directly associated with the exposure of individuals to solar UVB radiation. A similar trend was

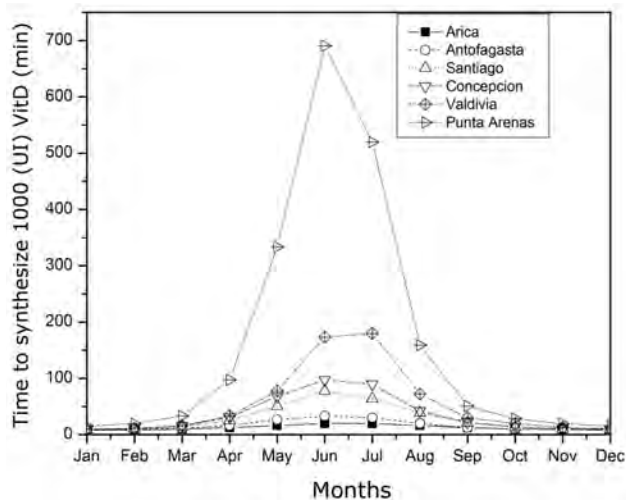


Figure 3. Exposure time to synthesize 1,000 IU vitamin D (min) in 6 cities of Chile per month.

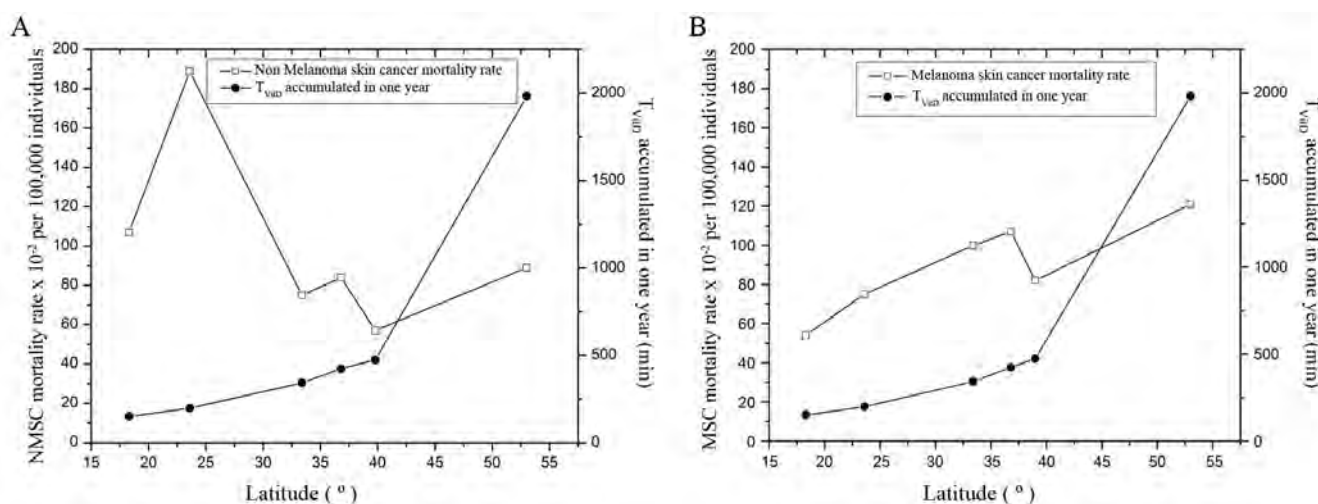


Figure 4. (A) NMSC and (B) MSC mortality rate and mean TV_{vitD} accumulated over 1 year with respect to latitude. MSC, melanoma skin cancer; NMSC, non-MSC; TV_{vitD}, exposure time to synthesize 1,000 IU vitamin D.

observed in Antofagasta, Santiago, Concepcion, Valdivia and Punta Arenas.

Therefore, high solar UVB radiation levels imply a great capability to synthesize vitamin D in the northern regions of Chile. A recent analysis determined that the diagnosis of NMSC was associated with a reduced risk of several vitamin D-sensitive cancers [30, 31]. This was in accordance with low solar UVB radiation levels in the southern cities of Chile in winter. Therefore, high solar UVB radiation levels imply a lower capability to synthesize vitamin D in the southern regions of Chile than in the northern regions. Melanoma is another cancer that has been linked to solar UV irradiance. However, it has been associated with sun burning, limited solar UV irradiance [32], solar UVA irradiance [24, 33, 34], low dietary vitamin D intake [35] and a lack of chronic solar UVB irradiation at higher latitudes [36, 37].

An inverse correlation was found between NMSC rates in males and females, and different latitudes of 18°S in Arica and 36°S in Concepción. NMSC rates decreased as latitude increased, which was in accordance with the low UVI values measured in those cities. There was a strong inverse correlation coefficient between NMSC rate and latitude ($r=-0.84$) among males, whereas there was a weak inverse correlation in females ($r=-0.65$). The NMSC rate in males in Punta Arenas was similar to the rates in Santiago and Concepcion, however, this rate was higher in females. NMSC appears to be directly associated with the Caucasian type of skin, that is, types II and III. It is notable that the population from Punta Arenas has a Croatian origin, with skin types II and III (50% of the population according to the Republic of Croatia State Office for Croats Abroad) [38]. NMSC is the most common malignant neoplasm in fair-skinned people, and in a number of sunny countries this frequency exceeds the total number of all other neoplasms. The incidence of basal cell carcinoma is always greater than that of squamous cell carcinoma, varying by latitude from 10:1

to 2.5:1 [39]. Studies have also indicated that NMSC has been increasing by 2-3% per year, at least in the United States, which is most likely caused by greater outdoor exposure for leisure and social reasons.

The results of the present study indicated that MSC decreased between latitude 18°S (Arica) and 23°S (Antofagasta) in males. MSC rates increased between latitude 23°S (Antofagasta) and 40°S (Valdivia) in males and females. However, MSC rates decreased at higher latitudes in each gender; this trend is consistent with the reported annual doses of UVA radiation, which decreased with increasing latitude [24].

There was a weak inverse coefficient correlation between MSC rate and latitude ($r=-0.56$) among males, and none ($r=-0.12$) in females. TV_{vitD} was similar in Arica, Antofagasta, Santiago and Concepción, with maximum values that varied from 175 to 700 min in Valdivia and Punta Arenas in winter, and where TV_{vitD} was 39 times higher in Punta Arenas than in Arica.

There was a weak inverse correlation coefficient between NMSC mortality rates and latitude ($r=-0.53$). However, there was a strong correlation between MSC mortality rates and latitude ($r=0.88$). Mortality rate and TV_{vitD} accumulated in 1 year were analyzed. Results showed that there was no correlation between NMSC and TV_{vitD} accumulated in 1 year. However, there was a strong correlation between MSC mortality rates and TV_{vitD} accumulated over the same period ($r=0.72$). In Punta Arenas, the MSC mortality rate was higher despite a lower MSC incidence.

When explaining the lack of correlation between different skin cancers and sunny cities, such as Arica, and less sunny cities, such as Punta Arenas, there are several aspects to take into consideration; for example, less body exposure to solar UVB, which thereby reduces the amount of vitamin D production [23, 40], and lower UVB doses. The low risk for skin cancers in dark-skinned

individuals is partly attributable to the photo-protection provided by the epidermal melanin barrier, which halves the penetration of UVB through the epidermis in black people compared with that in those of individuals of white European ethnicity (Caucasians, corresponding to type I and type II skin classification) [41]. One study previously reported a comprehensive bibliographic search of the literature that identified studies on cutaneous malignant melanomas and non-melanomas, vitamin D receptor polymorphisms, vitamin D intake and 25(OH) D serum levels. An association was found for two types of polymorphisms and melanoma [42].

It can be concluded from these studies that there is a direct correlation between NMSC rates and mortality with UVB radiation, meaning that this type of cancer would not depend on vitamin D synthesis and therefore on calcium uptake; by contrast, MSC rates increased with decreased levels of vitamin D and thus calcium uptake in all cities, with the only exception being Punta Arenas.

Grant support: UTA-Mayor #4728-2016 (MR and ER) and MINEDUC-UTA #UTA1117 (GMC)

References

- Engelsen O. The relationship between ultraviolet radiation exposure and vitamin D status. *Nutrients* 2: 482-495, 2010.
- Holick MF. The use and interpretation of assays for vitamin D and its metabolites. *J Nutr* 120 (Suppl 11): S1464-S1469, 1990.
- Matsuoka LY, Wortsman J, Haddad JG, Kolm P and Hollis BW. Racial pigmentation and the cutaneous synthesis of vitamin D. *Arch Dermatol* 127: 536-538, 1991.
- Porojnicu AC, Lagunova Z, Robsahm TE, Berg JP, Dahlback A and Moan J. Changes in risk of death from breast cancer with season and latitude: Sun exposure and breast cancer survival in Norway. *Breast Cancer Res Treat* 102: 323-328, 2007.
- Matsuoka LY, Wortsman J, Dannenberg MJ, Hollis BW, Lu Z and Holick MF. Clothing prevents ultraviolet-B radiation-dependent photosynthesis of vitamin D₃. *J Clin Endocrinol Metab* 75: 1099-1103, 1992.
- McKenna MJ. Differences in vitamin D status between countries in young adults and the elderly. *Am J Med* 93: 69-77, 1992.
- Edvardsen K, Brustad M, Engelsen O and Aksnes L. The solar UV radiation level needed for cutaneous production of vitamin D₃ in the face. A study conducted among subjects living at high latitude (68 degrees N). *Photochem Photobiol Sci* 6: 57-62, 2007.
- Casado J, Parra P, Vega L and Suárez C. Relación entre hormona paratiroidea y riesgo cardiovascular en pacientes con insuficiencia de vitamina D. *Med Clin* 141: 292-294, 2013.
- Miller DL and Weinstock MA. Non-melanoma skin cancer in the United States: Incidence. *J Am Acad Dermatol* 30: 774-778, 1994.
- Cannell JJ, Vieth R, Umhau JC, Holick MF, Grant WB, Madronich S, Garland CF and Giovannucci E. Epidemic influenza and vitamin D. *Epidemiol Infect* 134: 1129-1140, 2006.
- Lucena SR, Salazar N, Gracia-Cazaña T, Zamarrón A, González S, Juarranz A and Gilaberte Y. Combined treatments with photodynamic therapy for non-melanoma skin cancer. *Int J Mol Sci* 16: 25912-25933, 2015.
- Houghton AN and Polsky D. Focus on melanoma. *Cancer Cell* 2: 275-278, 2002.
- Donaldson MR and Coldiron BM. No end in sight: The skin cancer epidemic continues. *Semin Cutan Med Surg* 30: 3-5, 2011.
- Caini S, Gandini S, Sera F, Raimondi S, Fagnoli MC, Boniol M and Armstrong BK. Meta-analysis of risk factors for cutaneous melanoma according to anatomical site and clinic-pathological variant. *Eur J Cancer* 45: 3054-3063, 2009.
- Caini S, Boniol M, Bazolli E, Tosti G, Bazolli B, Russel-Edu W, Giusti F, Testori A and Gandini S. The risk of developing a secondary primary cancer in melanoma patients: A comprehensive review of the literature and meta-analysis. *J Dermatol Sci* 75: 3-9, 2014.
- Rivas M, Rojas E and Calaf GM. Prediction of skin cancer occurrence by ultraviolet solar index. *Oncol Lett* 3: 893-896, 2012.
- Rivas M, Rojas E, Araya MC and Calaf GM. Ultraviolet light exposure, skin cancer risk and vitamin D production. *Oncol Lett* 10: 2259-2264, 2015.
- Rivas M, Araya MC, Durán V, Rojas E, Cortes J and Calaf GM. Ultraviolet light exposure and skin cancer in the city of Arica, Chile. *Mol Med Rep* 2: 567-572, 2009.
- Rivas M, Araya MC, Caba F, Rojas E and Calaf GM. Ultraviolet light exposure influences skin cancer in association with latitude. *Oncol Rep* 25: 1153-1159, 2011.
- Zemelman V, Alvarado O, Von Beck P and Valenzuela C. Assessment of skin type, eye and hair color, freckles tendency in Chilean adolescents. *J Eur Acad Dermatol Venereol* 12: 321, 1990.
- Fitzpatrick TB. The validity and practicality of sun-reactive skin types I through VI. *Arch Dermatol* 124: 869-871, 1988.

22. Grant WB. An ecologic study of cancer mortality rates in Spain with respect to indices of solar UVB irradiance and smoking. *Int J Cancer* 120: 1123-1128, 2007.
23. Grant WB. The effect of solar UVB doses and vitamin D production, skin cancer action spectra, and smoking in explaining links between skin cancers and solid tumours. *Eur J Cancer* 44: 12-15, 2008.
24. Grigalavicius M, Moan J, Dahlback A and Juzeniene A. Daily, seasonal, and latitudinal variations in solar ultraviolet A and B radiation in relation to vitamin D production and risk for skin cancer. *Int J Dermatol* 55: e23-e28, 2016.
25. Systems YES. Operation manual calibrated high range YES-Biometer. Yankee Environmental Systems, Inc, Turners Falls, OK, USA, 2006. <http://www.yesinc.com/> (Accessed September 5, 2016).
26. McKenzie RL, Liley JB and Björn LO. UV radiation: Balancing risks and benefits. *Photochem Photobiol* 85: 88-98, 2009.
27. Holick MF. Biologic effects of light: Historical and new perspectives. In: Holick MF, Jung EG, eds. *Biologic effects of light 1998*. Proceedings of a symposium Basel, Switzerland November 1-3, 1998. Boston: Kluwer Academic Publishers 11-32, 1999.
28. Vallebuono C. Primer informe de registros poblacionales de cáncer de Chile, quinquenio 2003-2007, unidad de vigilancia de enfermedades no transmisibles y estudios. Ministry of Health of Chile. Epidemiology Section, 2012.
29. Giovannucci E, Liu Y, Rimm EB, Hollis BW, Fuchs CS, Stampfer MJ and Willett WC. Prospective study of predictors of vitamin D status and cancer incidence and mortality in men. *J Natl Cancer Inst* 98: 451-459, 2006.
30. De Hertog SA, Wensveen CA, Bastiaens MT, Kielich CJ, Berkhout MJ, Westendorp RG, Vermeer BJ and Bouwes Bavinck JN. Leiden Skin Cancer Study: Relation between smoking and skin cancer. *J Clin Oncol* 19: 231-238, 2001.
31. Milán T, Verkasalo PK, Kaprio J and Koskenvuo M. Lifestyle differences in twin pairs discordant for basal cell carcinoma of the skin. *Br J Dermatol* 149: 115-123, 2003.
32. Garland FC, White MR, Garland CF, Shaw E and Gorham ED. Occupational sunlight exposure and melanoma in the U.S. Navy. *Arch Environ Health* 45: 261-267, 1990.
33. Moan J, Dahlback A and Setlow RB. Epidemiological support for an hypothesis for melanoma induction indicating a role for UVA radiation. *Photochem Photobiol* 70: 243-247, 1999.
34. Garland CF, Garland FC and Gorham ED. Epidemiologic evidence for different roles of ultraviolet A and B radiation in melanoma mortality rates. *Ann Epidemiol* 13: 395-404, 2003.
35. Millen AE, Tucker MA, Hartge P, Halpern A, Elder DE, Guerry D VI, Holly EA, Sagebiel RW and Potischman N. Diet and melanoma in a case-control study. *Cancer Epidemiol Biomarkers Prev* 13: 1042-1051, 2004.
36. Berwick M, Armstrong BK, Ben-Porat L, Fine J, Krickler A, Eberle C and Barnhill R. Sun exposure and mortality from melanoma. *J Natl Cancer Inst* 97: 195-199, 2005.
37. Gandini S, Sera F, Cattaruzza MS, Pasquini P, Picconi O, Boyle P and Melchi CF. Meta-analysis of risk factors for cutaneous melanoma: II. Sun exposure. *Eur J Cancer* 41: 45-60, 2005.
38. Republic of Croatia State Office for Croats Abroad. 2013-2016. <http://www.hrvatiizvanrh.hr/en/hmiu/croatian-diaspora-in-chile/22>. Accessed, 5 September, 2016.
39. Urbach F. Incidence of nonmelanoma skin cancer. *Dermatol Clin* 9: 751-755, 1991.
40. Webb AR and Engelsen O. Calculated ultraviolet exposure levels for a healthy vitamin D status. *Photochem Photobiol* 82: 1697-1703, 2006.
41. Brenner M and Hearing VJ. The protective role of melanin against UV damage in human skin. *Photochem Photobiol* 84: 539-549, 2008.
42. Gandini S, Raimondi S, Gnagnarella P, Doré JF, Maisonneuve P and Testori A. Vitamin D and skin cancer: A meta-analysis. *Eur J Cancer* 45: 634-641, 2009. ■

Edith Quimby; A Pioneer in Nuclear Medicine as well as Medical Physics

Eric J. Hall, David J. Brenner, and Sally A. Amundson

The Early Years

Edith was born in Rockford, Illinois, the daughter of Arthur Hinkley, an architect and farmer, and Harriet Hinkley. As a child Edith moved with her family from Illinois to Alabama and then to Boise, Idaho, where she attended high school. At Whitman College in Walla Walla, Washington, she was the first woman to enroll for a physics/mathematics major, and received a BS in 1912. She then taught high school science in Nyssa, Oregon for two years and in 1914 received a fellowship for the graduate physics program at the University of California at Berkeley. In 1915, she married her fellow student, Shirley Quimby, and in 1916 received her MA in physics. In 1919 Shirley Quimby was appointed as an Instructor in the physics department of Columbia University, so they moved to New York together. However, the \$1,200 annual stipend that Shirley received was not enough for both to live on in the big City and so Edith went looking for a job.

The Years at Memorial Hospital

The Center for Radiological Research traces its roots to the Biophysics Laboratory set up by Dr. Gino Failla at Memorial Hospital, in New York City, in 1915. In looking for a job, Edith Quimby landed an interview with Dr. Failla for a position as assistant physicist. According to Edith he said "I don't mind trying you for 6 months." She stayed for over 60 years, eventually retiring as Emeritus Professor of Radiology in 1978. During their years at Memorial Hospital, Failla and Quimby worked closely together on the development of radium needles and radon seeds for the treatment of cancer. Edith Quimby became well known as a result of the "Quimby Rules." (1) These rules governed the pattern of the placement of radium needles to give a uniform dose to the tumor volume, made it possible to determine the activity of the radium needed together with a set of tables to allow the calculation of the time that the implant should be left in place to achieve the desired dose. This was quite an achievement in the 1920's and 1930's, long before the availability of computers, since it allowed physicians to apply radium implants safely and accurately and in a reproducible manner.

1942; The Move to Columbia University Medical Center

In 1942, Dr. Failla moved his entire laboratory to the College of Physicians and Surgeons at Columbia University Medical Center. He did so with funding from the Atomic Energy Commission, with whom he had become familiar during the time that he worked on the



Figure 1. Dr. Edith Quimby in the radioisotope laboratory that she had set up in Columbia University Medical Center. Photograph from around 1950.

Manhattan District Project. His plan was to devote his time to basic research, freed from the service needs of a busy medical physics group. From this time on Failla and Quimby went their separate ways to a large extent. At this time, radioactive isotopes were just becoming available for medical use. This was Edith Quimby's new challenge and second career. She is recognized by the American Society for Nuclear Medicine and Molecular Imaging as one of the pioneers in the field.

Nuclear Medicine at Columbia Presbyterian

She formed a partnership with physicians from Presbyterian Hospital and set up a busy radioisotope laboratory. Fig 1 shows Dr. Quimby in her laboratory circa 1950. The Columbia-Presbyterian group was not the first to use radioactive iodine in humans. In 1939, Hamilton and Soley, working at the Berkeley cyclotron in California, were able to make a mixture of Iodine-130 (half-life 12.6 hours) and Iodine-131 (half-life 8days) and were the first to give these radioisotopes to humans to study iodine physiology (2). In the early 1940's, the group at the Massachusetts General Hospital (MGH) used the same mixture of Iodine-130 and Iodine-131, produced at the Massachusetts Institute of Technology (MIT) cyclotron, to treat a small number of patients with hyperthyroidism; their early results were not reported until after World War 2 (3, 4).

The Columbia Presbyterian group was the first to publish the results of a large group of patients (more than 80) including tracer studies of iodine uptake in normal and disordered thyroid glands, as well as the treatment of 40 cases of toxic goiter (5). They had the big advantage

BULLETIN OF
THE NEW YORK ACADEMY
OF MEDICINE



SEPTEMBER 1948

THE CLINICAL USE
OF RADIOACTIVE IODINE *

SIDNEY C. WERNER, EDITH H. QUIMBY, Sc.D.
and CHARLOTTE SCHMIDT, B.A.

Figure 2. The first detailed report, with good dosimetry, of the clinical use of radioactive iodine.

of much more accurate and improved dosimetry because by the time their study was initiated, in October 1946, reliable and repeatable supplies of Iodine-131 (not contaminated with the short-lived Iodine-130) were available from the nuclear reactors at Oak Ridge National Laboratory, Tennessee. Their pioneering study was published in September 1948 (Fig. 2). This study paved the way for the widespread use of radioactive iodine on both sides of the Atlantic. In collaboration with a different physician, Edith Quimby was also a pioneer in the use of radioactive sodium as a tracer in the study of peripheral vascular disease. Their early paper was published in 1945 (6).

Forever the Educator

Edith Quimby was forever the accomplished educator. Just as she had been a co-author of “Physical Foundations of Radiology”, the first physics textbook for radiologists (7), she now produced a handbook entitled “Safe Handling of Radioactive Isotopes in Medical Practice” (8). One of her early students was Rosalyn Yalow, who volunteered to work in the Quimby Laboratory to learn about radioactive isotopes and went on to win the Nobel Prize in Physiology or Medicine in 1977 for the development of the Radioimmunoassay technique.



Figure 3. Edith Quimby teaching in the course set up to prepare physicians for licensure by the Atomic Energy Commission.



Figure 4. Edith Quimby with her husband of more than 60 years Shirley Quimby, who was professor emeritus of physics at Columbia University. The photograph dates from the 1970's when they were both in their eighties.

During these pioneering days in Nuclear Medicine, the Atomic Energy Commission (AEC) was responsible for the regulation of radioactive materials (before the NRC was created) and so there was a great need of a course to help physicians who wanted to enter the field but needed the licensure of the AEC to be allowed to administer radioactive isotopes to humans. Together with her clinical colleagues, Drs. Feitelberg and Silver, Edith Quimby set up the required course and over the next two decades more than 600 students completed the course successfully. Figure 3 is a photograph of Edith teaching in this course; she had the reputation as a strong disciplinarian and a hard task master!

Honors and Awards.

Dr. Quimby received many honors and awards to recognize her outstanding contributions to the development of radiological physics and nuclear medicine. She received two honorary D.Sc. degrees, one of which was from her Alma Mater, Whitman College. She was awarded the Gold Medals of the Radiological Society of North America, the American College of Radiology and The Indian Radiological Association. She also received the Ewing Medal, the Medal of the American Cancer Society as well as the Katherine Berkan Judd Award for cancer research. The American Radium Society specifically changed their rules in 1954 so that Edith, with a D.Sc. rather than an MD, could be President.

Dr. Quimby's summary of her life at the time of her retirement

“My professional life placed me in a field full of fascinating problems. I have always had good health and the ability to work at a high pace. Any success I have achieved I owe to the help and encouragement of others. Dr. Gino Failla, plus my physics and medical colleagues. Above all, an understanding and encouraging husband,

always proud of any accomplishment.” Figure 4 is a photograph of Edith Quimby with her husband of more than 60 years, Shirley Quimby, who was Professor of physics at Columbia University.

Conclusion.

Edith Quimby had a long and distinguished career; indeed, at 80 years of age she was still commuting to Columbia by subway from her apartment in Greenwich Village. As outlined above she actually had two careers, either of which alone would have been sufficient to make her an outstanding scientist. First as a medical physicist in the field of radium therapy, and second as a pioneer in nuclear medicine. In each of these fields she combined three things...innovative experimental research, teaching of the subject to the next generation, and publication of a book or manual that has stood the test of time. She was a remarkable woman who was admired by all who knew her.

References.

(1) Quimby, E.H. The grouping of radium tubes in packs or plaques to produce the desired distribution of radiation. Am. J. Roentgenol. Radium Therapy. 27; 18; 1932

(2) Sawin, C.T., and Becker, D.V. Radioiodine and the Treatment of Hypothyroidism: The Early History. Thyroid; 7 ;163-176; 1997

(3) Chapman, E.M. and Evans, R.D. The Treatment of Hypothyroidism with Radioactive Iodine. J.A.M.A. 131; 86-92; 1946.

(4) Hertz, S., and Roberts, A. Radioactive Iodine in the Study of Thyroid Physiology. J.A.M.A., 131, 81-86; 11946

(5) Werner, S.C., Quimby, E.H., and Schmidt, C. The Clinical use of Radioactive Iodine. Bulletin of the New York Academy of Medicine. 549-560; September 1948.

(6) Smith, B. C. and Quimby, E. The use of Radioactive Sodium as a Tracer in the Study of Peripheral Vascular Disease. RTadiology, 45; 335-346; 1945.

(7) Glasser, o., Quimby, E.H., Taylor, L.S., and Weatherwax, J.L. Physical Foundations of Radiology. New York and London. Paul B Hoeber Inc. 1944

(8) Quimby, E.H. Safe Handling of Radioactive isotopes in Medical Practice. The Macmillan Company. 60 Fifth Ave. New York 11



Steve Marino



Above, scenes from the cookout with staff and students of the Microbeam Training Course



David Welch



David Brenner

Guidelines for Moderate Hypofractionation in Prostate Cancer Radiotherapy

David J. Brenner and Eric J. Hall

It is now more than 18 years since Brenner and Hall (1) and, in the same year, Duchesne and Peters (2), independently suggested that there was a strong radiobiological rationale, specific to prostate cancer, for hypofractionating prostate cancer radiotherapy. In short, this was because the slow growing nature of most prostate

cancers results in their response to changes in fractionation being similar to those of the surrounding late-responding normal tissues. Consequently, as compared with standard 40 to 45 fraction treatment protocols for prostate cancer radiotherapy, smaller numbers of higher-dose fractions (with an appropriately

Table 1. Summarized results from randomized trials of moderately hypofractionated radiation therapy for prostate cancer. The four larger more recent trials are shown in the lower half of the Table. Both groups of trials are listed by increasing $BED_{2.5Gy}$

Trial Number of patients; Risk groups	Hypofractionated total dose; dose per fraction	BED (Gy _{1.5})	BED (Gy _{2.5})	BED (Gy ₅)	Toxicity	Tumor control
Yeoh <i>et al</i> 2011 (4) 217 patients Mixed risk patients	55 Gy; 2.75 Gy	156	116	85	Similar toxicity	Hypofractionation superior
Arcangeli <i>et al</i> 2017 (5) 168 patients Predominantly high risk patients	62 Gy; 3.1 Gy	190	139	100	Similar toxicity, increased macroscopic hematuria	Hypofractionation non superior
Hoffman <i>et al</i> 2014 (6) 203 patients Intermediate risk patients	72 Gy; 2.4 Gy	187	141	107	Non-significant increase in late GI toxicity associated with dosimetric factors	Hypofractionation non superior
Pollack <i>et al</i> 2013 (7) 303 patients Predominantly high risk patients	70.2 Gy; 2.7 Gy	197	146	108	Increased toxicity associated with preexisting urinary symptoms	Hypofractionation non superior
Dearnaley <i>et al</i> 2016, CHHiP Trial (8) 3,216 patients Intermediate risk patients	57 Gy, 60 Gy; 3 Gy	171, 180	125, 132	91,96	No significant difference in late toxicity	Hypofractionation (60 Gy) non-inferior
Catton <i>et al</i>, 2017, PROFIT Trial (9) 1,206 patients Intermediate risk groups	60 Gy; 3 Gy	180	132	96	No significant difference in late toxicity	Hypofractionation non-inferior
Lee <i>et al</i> 2016, RTOG-0415 (10) 1,092 patients Low risk patients	70 Gy; 2.5 Gy	186	140	105	Increased grade 2+ late GI and GU toxicity	Hypofractionation non-inferior
Incrocci <i>et al</i>; Aluwini <i>et al</i> 2015, 2016 HYPRO Trial (11-13). 820 patients Intermediate / high risk patients	64.6 Gy; 3.4 Gy 3 fractions/week	211	152	108	Higher grade 2+ GI but not GU acute toxicity; Higher grade 3+ GU but not GI late toxicity	Hypofractionation non superior

reduced total dose) would be expected to be as clinically effective, but would potentially have advantages in terms of economics, logistics, and patient convenience.

After much initial debate – quite appropriate in light of some poor results after hypofractionation in other sites (3) – a number of non randomized and then randomized clinical trials of prostate cancer hypofractionation were initiated. These randomized trials, with the more recent studies involving up to 3,000 patients, are now mature, with median follow up times of 5 to 9 years, and their results for tumor control (largely based on 5-year biochemical failure), as well as early and late toxicity, have been documented (4-13). In concert, several excellent reviews have recently been published (14-16).

The results for the randomized trials for moderate hypofractionation (which we define here as between 2.5 and 3.4 Gy per fraction) are summarized in Table 1. In brief summary, and we particularly focus on the larger more recent trials, tumor control is non inferior (and probably non superior) to conventional fractionation, and there is evidence in some of the randomized trials of significantly increased late effects, with estimated hazard ratios from 1.2 to 1.6 (10,13). Further details can of course be found in the original reports (4-13).

In assessing these various studies, there has been rather less attention paid to the comparative radiation doses and, particularly, the Biologically Effective Doses (BED (17)), used in the various protocols – interestingly almost every trial used a different dose / fractionation scheme. Hence we include in Table 1 the BEDs associated with the various trials. We show BEDs based on α/β values of 1.5 Gy and 2.5 Gy, which is a range that is probably typical for prostate tumor control. We include a range of α/β ratios because these values are likely to vary from patient to patient based on stage, length of ADT, and other individual factors. In that a typical α/β ratio characterizing late rectal toxicity may be slightly larger - possibly around 5 Gy, we also include BED values based on this α/β value. We emphasize that choosing somewhat different α/β values would not alter our conclusions.

What becomes immediately obvious from Table 1 is that the studies, which used the highest BEDs are the studies in which the most significant late effects were reported. In particular 64.6 Gy in 3.4 Gy fractions as used in the HYPRO study (11-13), was associated with the highest BEDs and the most late effects. Again focusing on the four later (larger) studies, the study with the next highest BED (RTOG-0415, 70 Gy in 2.5 Gy fractions) reported less but still significant late effects (10), while the two studies (8,9) using the lowest BEDs reported no significant late effects, while maintaining non-inferiority in tumor control.

We conclude from the randomized trials summarized in Table 1 that BEDs for moderately hypofractionated radiotherapy should not exceed approximately a $BED_{1.5Gy}$

Table 2. Moderately hypofractionated protocols for prostate radiotherapy, all with $BED_{1.5Gy}$ values of 180 $Gy_{1.5}$, and which all have $BED_{2.5Gy}$ values less than 136 $Gy_{2.5}$ and BED_{5Gy} values less than 102 Gy_5 .

Dose per fraction (Gy)	Number of fractions	Total dose (Gy)
2.5	27	67.5
2.75	23	63.25
3	20	60.0
3.2	18	57.6
3.3	17	56.1

of 183 $Gy_{1.5}$, or a $BED_{2.5Gy}$ of 136 $Gy_{2.5}$, or a BED_{5Gy} of 102 Gy_5 .

Using these guidelines, therefore, Table 2 shows a number of different moderately hypofractionated protocols, all of which have a $BED_{1.5Gy}$ of 180 $Gy_{1.5}$, and have $BED_{2.5Gy}$ values less than 136 $Gy_{2.5}$, and BED_{5Gy} values less than 102 Gy_5 . The protocols in Table 2 are of course guidelines, but are based firmly on the recent large randomized clinical trials, and we emphasize again that

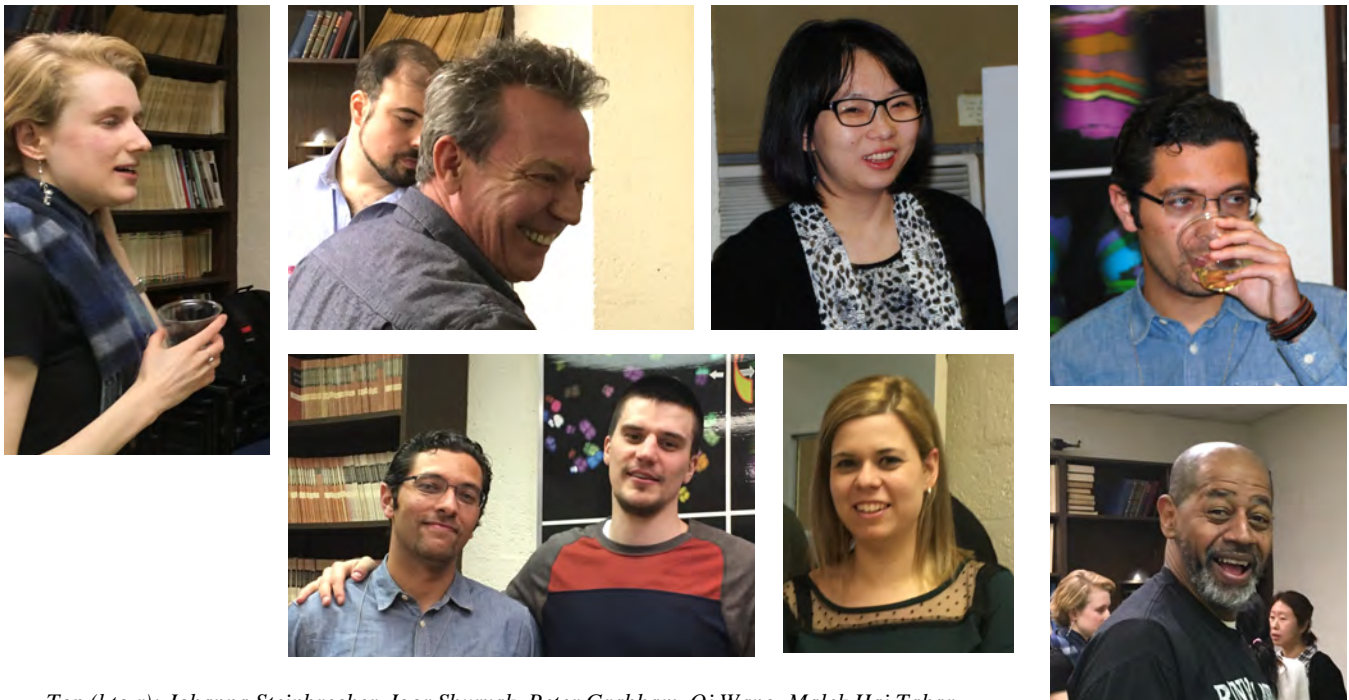
they do not depend on any specific choice of α/β value within the range of 1.5 to 5 Gy.

For example the newly proposed ASTRO recommendation for moderate hypofractionation for prostate cancer, 70 Gy in 28 2.5-Gy fractions, somewhat exceeds our suggested guideline for $BED_{1.5Gy}$ ($BED_{1.5Gy}=187 Gy_{1.5}$), and also for $BED_{2.5Gy}$ ($BED_{2.5Gy}=140 Gy_{2.5}$), as well as for BED_{5Gy} ($BED_{5Gy}=105 Gy_5$). Our guidelines (Table 2) would suggest one less fraction (i.e., $27 \times 2.5 Gy$).

References

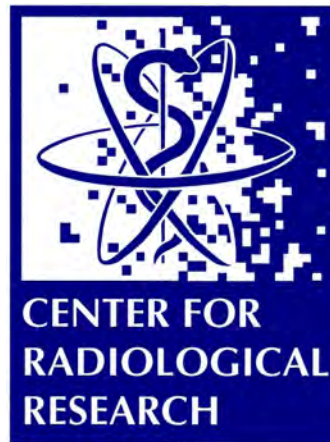
1. Brenner DJ, Hall EJ. Fractionation and protraction for radiotherapy of prostate carcinoma. *Int J Radiat Oncol Biol Phys* 1999;43:1095-1101.
2. Duchesne GM, Peters LJ. What is the α/β ratio for prostate cancer? Rationale for hypofractionated high-dose-rate brachytherapy. *Int J Radiat Oncol Biol Phys* 1999;44:747-748.
3. Peters LJ, Withers HR. Morbidity from large dose fractions in radiotherapy. *Br J Radiol* 1980;53:170-171.
4. Yeoh EE, Botten RJ, Butters J, et al. Hypofractionated versus conventionally fractionated radiotherapy for prostate carcinoma: final results of phase III randomized trial. *Int J Radiat Oncol Biol Phys* 2011;81:1271-1278.
5. Arcangeli G, Saracino B, Arcangeli S, et al. Moderate Hypofractionation in High-Risk, Organ-Confined

- Prostate Cancer: Final Results of a Phase III Randomized Trial. *J Clin Oncol* 2017;35:1891-1897.
6. Hoffman KE, Voong KR, Pugh TJ, et al. Risk of late toxicity in men receiving dose-escalated hypofractionated intensity modulated prostate radiation therapy: results from a randomized trial. *Int J Radiat Oncol Biol Phys* 2014;88:1074-1084.
 7. Pollack A, Walker G, Horwitz EM, et al. Randomized trial of hypofractionated external-beam radiotherapy for prostate cancer. *J Clin Oncol* 2013;31:3860-3868.
 8. Dearnaley D, Syndikus I, Mossop H, et al. Conventional versus hypofractionated high-dose intensity-modulated radiotherapy for prostate cancer: 5-year outcomes of the randomised, non-inferiority, phase 3 CHHiP trial. *Lancet Oncol* 2016;17:1047-1060.
 9. Catton CN, Lukka H, Gu CS, et al. Randomized Trial of a Hypofractionated Radiation Regimen for the Treatment of Localized Prostate Cancer. *J Clin Oncol* 2017;35:1884-1890.
 10. Lee WR, Dignam JJ, Amin MB, et al. Randomized Phase III Noninferiority Study Comparing Two Radiotherapy Fractionation Schedules in Patients With Low-Risk Prostate Cancer. *J Clin Oncol* 2016;34:2325-2332.
 11. Incrocci L, Wortel RC, Alemayehu WG, et al. Hypofractionated versus conventionally fractionated radiotherapy for patients with localised prostate cancer (HYPRO): final efficacy results from a randomised, multicentre, open-label, phase 3 trial. *Lancet Oncol* 2016;17:1061-1069.
 12. Aluwini S, Pos F, Schimmel E, et al. Hypofractionated versus conventionally fractionated radiotherapy for patients with prostate cancer (HYPRO): acute toxicity results from a randomised non-inferiority phase 3 trial. *Lancet Oncol* 2015;16:274-283.
 13. Aluwini S, Pos F, Schimmel E, et al. Hypofractionated versus conventionally fractionated radiotherapy for patients with prostate cancer (HYPRO): late toxicity results from a randomised, non-inferiority, phase 3 trial. *Lancet Oncol* 2016;17:464-474.
 14. Hocht S, Aebbersold DM, Albrecht C, et al. Hypofractionated radiotherapy for localized prostate cancer. *Strahlenther Onkol* 2017;193:1-12.
 15. Lee WR. Hypofractionation for prostate cancer: tested and proven. *Lancet Oncol* 2016;17:1020-1022.
 16. Yu JB. Hypofractionated Radiotherapy for Prostate Cancer: Further Evidence to Tip the Scales. *J Clin Oncol* 2017;35:1867-1869.
 17. Fowler JF. 21 years of biologically effective dose. *Br J Radiol* 2010;83:554-568. ■



Top (l to r): Johanna Steinbrecher. Igor Shuryak, Peter Grabham. Qi Wang. Malek Haj Tahar. Bottom (l to r): Malek Haj Tahar, Veljko Grilj. Monica Pujol. Rob Motron.

RADIATION BIODOSIMETRY



VADER: a Variable Dose rate External irradiator for Internal Emitter and Low Dose Rate Studies

Guy Garty, Yanping Xu, Lubomir Smilenov, Gary Johnson, and David J. Brenner

Beyond prompt irradiation, ^{137}Cs is likely to be the most biologically important agent released in many accidental (or malicious) radiation exposure scenarios [1, 2]. Cs can either enter the food chain and be consumed or if present in the environment (e.g. fallout) provide external irradiation. In either case, due to the high penetration of the 662keV γ rays emitted by ^{137}Cs , the individual will be exposed to a uniform, whole body, irradiation typically at low dose rates.

Thus, further research regarding the effects of ^{137}Cs , both from internal or external exposure, is much needed [6]. In order to model this in animal studies, we and others have previously used an injection of soluble $^{137}\text{CsCl}$ [7-9]. In these studies, the amount of activity of the solution can be varied to produce a specific absorbed cumulative dose by specific time points with the time dependence of the dose determined by the biokinetics of Cs within the animal under study (Fig. 1). This type of experiment is complicated to do – resulting in radioactive excreta and biofluids, which require dedicated “hot” equipment for analysis and, secondly, are expensive to dispose of.

The VADER provides a solution to both problems; making use of discarded ^{137}Cs brachytherapy seeds, the VADER can provide arbitrarily, varying low dose rate irradiations to mice.

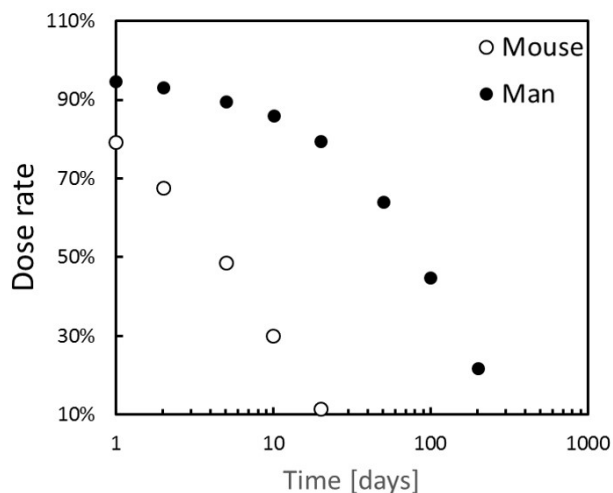


Figure 1. Biokinetics of Cesium in mouse and man. The full circles represent the time dependent dose rate from ingested ^{137}Cs , as per the model described in [3]. Open circles are from our own data based on total body counting in mice [4, 5].

VADER structure

Shown in figure 2, the VADER consists of a mouse cage, designed to allow long term residency of up to 15 mice. Two source platters containing ~250mCi each of discarded brachytherapy seeds are mounted above and below the cage, and can be moved under computer control to provide constant low dose rate or a varying dose rate mimicking ^{137}Cs biokinetics.

VADER mouse cage

In order to support long term irradiations of mice, a custom mouse cage (Fig. 3) has been developed for the VADER. The cage includes an integrated temperature and humidity monitor, integrated LED lighting and an integrated camera. Temperature and humidity controlled medical grade air is piped into the cage and vented through HEPA filters into the VADER volume, providing the required number of air changes. Sufficient food and water for up to a week of residency for 15 mice is also provided. Tests of the cage indicated that mice are not stressed when residing in the cage for over a week.

A feature of the VADER is that there are no fixed active components within the VADER enclosure. All

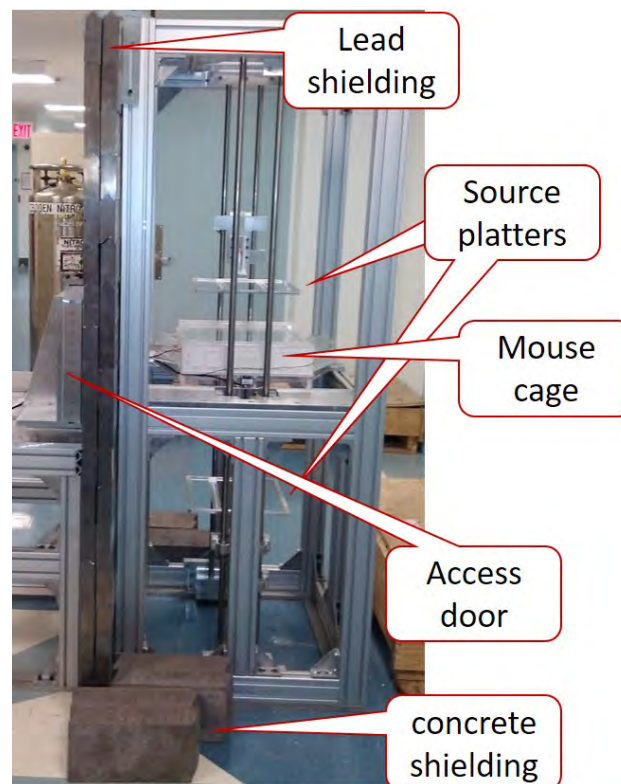


Figure 2. The VADER

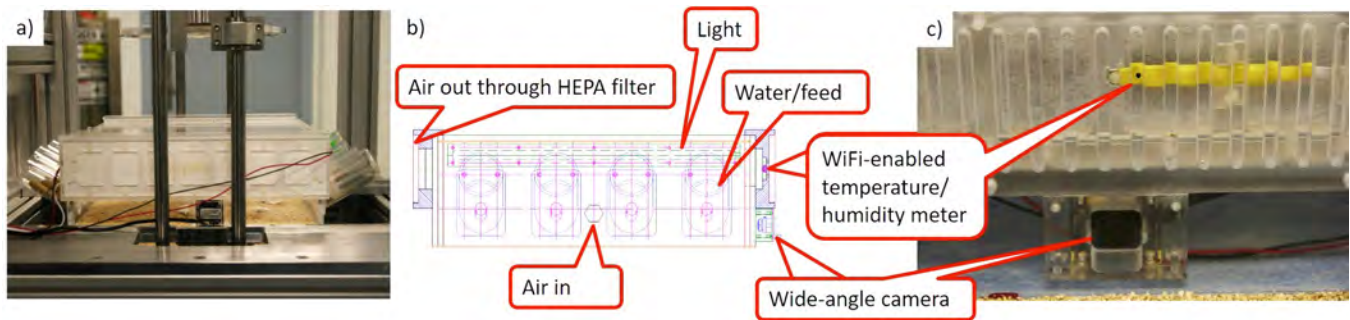


Figure 3. a) Photo and b) design drawing of the mouse cage. Air inlet and outlet, feeders, illumination, temperature/humidity sensor and camera are indicated. The latter two are shown in close up in panel c).

environmental controls and monitoring are integrated into the cage so that they can be easily removed and replaced in case of damage by the radiation. This is significantly cheaper than using radiation hardened sensors and electronics. Similarly, the motors driving the source holders are placed outside the shielding and the platters moved using cables.

Irradiation Geometry

Ideally, the dose rate across the mouse cage should be as uniform as possible. We are, however, limited in that we want to use available discarded sources, which vary greatly in intensity (Sources of 5-50 mCi were made

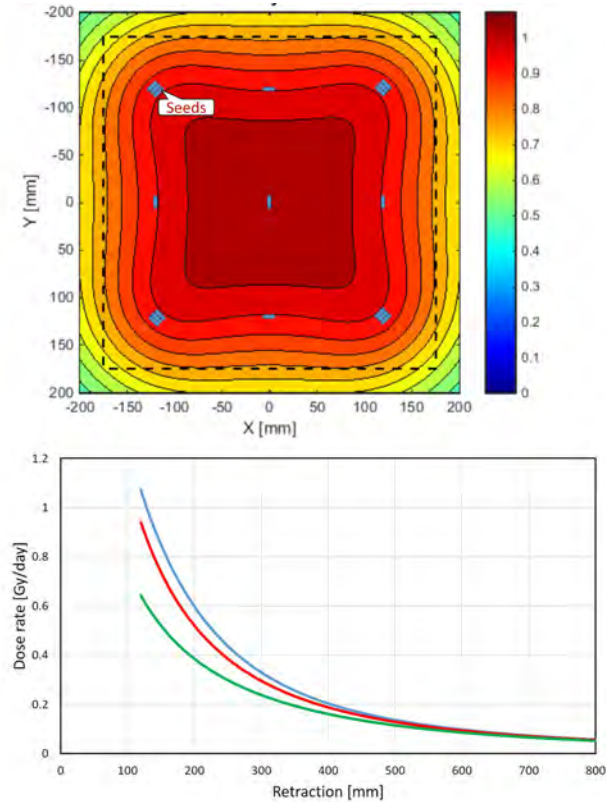


Figure 4. (Top) Calculated dose distribution within the mouse cage (dashed square) at the highest dose rate setting. The color bar corresponds to dose rate in Gy/day. (Bottom) maximum (red), minimum (blue) and average (green) dose rate vs source retraction.

available to us). We thus designed the source holder platters to position 2-3 seeds totaling 50 mCi above the corners of the mouse cage and single ~10-15 mCi seeds at the centers of the edges and at the center of the cage. Using this geometry the dose rate within the mouse cage varies between 0.6 and 1 Gy/day when the sources are closest to the mice (Fig. 4 Top). As the sources are retracted, the dose rate becomes lower and more uniform across the cage (Fig 4. bottom).

Shielding

Operator safety is a prime concern in the design of ^{137}Cs based irradiators. In consultation with Columbia University's Radiation Safety Officer, we have determined the required shielding to be 3" of lead or 12" of high density concrete (HDC). We have therefore decided to build the side walls out of HDC interlocking bricks (Fig 2). The front and top faces of the VADER, however, require penetrations for inserting/removing the mouse cage as well as for control cables and were therefore made of lead which is easier to machine. A custom sliding door made of lead was designed and built that allows access to the mouse cage. The VADER is enclosed in sufficient shielding to reduce the dose rate outside the VADER below 5mSv/year.

References

1. Simon, S.L., Bouville, A., and Beck, H.L., The geographic distribution of radionuclide deposition across the continental US from atmospheric nuclear testing. *J Environ Radioact*, 2004. **74**(1-3): p. 91-105.
2. Homeland Security Council, National planning scenarios (final version 21.3). 2006.
3. Leggett, R.W., Biokinetic models for radiocaesium and its progeny. *J Radiol Prot*, 2013. **33**(1): p. 123-40.
4. Goudarzi, M., et al., The effect of low dose rate on metabolomic response to radiation in mice. *Radiation and environmental biophysics*, 2014. **53**(4): p. 645-657.
5. Yasunari, T.J., et al., Cesium-137 deposition and contamination of Japanese soils due to the Fukushima

nuclear accident. Proceedings of the National Academy of Sciences, 2011. **108**(49): p. 19530-19534.

6. Jeong, H., et al., Radiological risk assessment caused by RDD terrorism in an urban area. *Appl Radiat Isot*, 2013. **79**: p. 1-4.

7. Goudarzi, M., et al., Development of Urinary Biomarkers for Internal Exposure by Cesium-137

Using a Metabolomics Approach in Mice. *Radiation Research*, 2014. **181**(1): p. 54-64.

8. Paul, S., et al., Gene Expression Response of Mice after a Single Dose of (137)Cs as an Internal Emitter. *Radiat Res*, 2014. **182**(4): p. 380-9.

9. Nikula, K.J., et al., Biological effects of 137CsCl injected in beagle dogs. *Radiat Res*, 1995. **142**(3): p. 347-61. ■

RABiT-II: Development of Accelerated High-throughput Micronucleus Biodosimetry Assay

Mikhail Repin, Sergey Pampou^a, Charles Karan^a, David J. Brenner, and Guy Garty

The Columbia Center for High Throughput Minimally Invasive Radiation Biodosimetry has developed Rapid Automated Biodosimetry Tools (RABiT) based on custom-built robotic platforms [1-6], and the next generation RABiT II approach based on commercial, automated HTS/HCS systems for performing high throughput biodosimetry [7].

Recently, we demonstrated a complete automation for the miniaturized (20 µl of blood per sample) cytokinesis-block micronucleus (CBMN) assay using commercial robotic systems, consisting of a PerkinElmer cell::explorer and General Electric IN Cell Analyzer 2000 (Fig. 1), both located at the Columbia Genome Center [8]. However, one of the limitations of the CBMN assay is the requirement of a 72-hour culture period to complete the

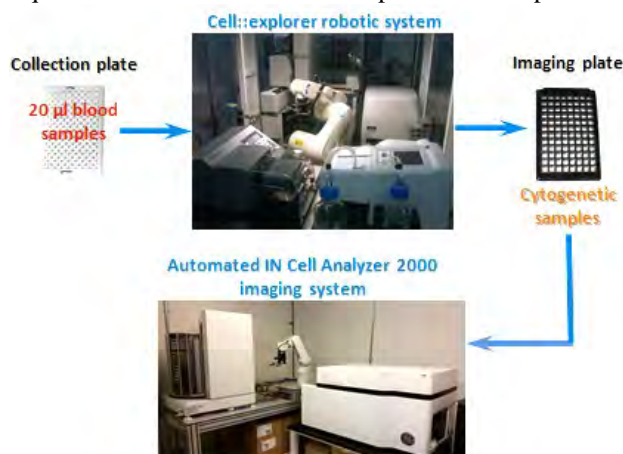


Figure 1. General scheme of the automated CBMN assay of peripheral human blood lymphocytes at the Columbia Genome Center.

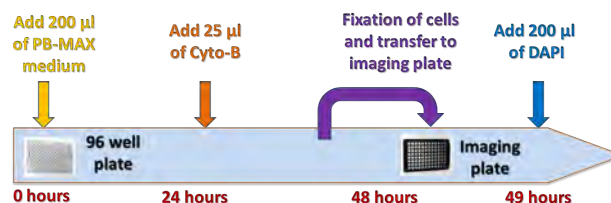


Figure 2. The time-line scheme of 20 µl peripheral human blood lymphocyte sample preparation for accelerated automated high-throughput CBMN assay.

assay. The CBMN assay with shortened protocol will allow receive the results of biodosimetric screening of multiple human samples faster. That is especially critical after radiological incidents.

Here, we demonstrate that the RABiT-II system can be used for accelerated CBMN assay, with only 48 hours of cell culturing instead of the recommended 72 hours.

The time-line workflow of the sample preparation for the accelerated CBMN assay in cell::explorer system is shown in Fig. 2: 10-25 µl of blood samples are cultured during 48 h in 96-well plates with complete cytogenetic PB-MAX medium and addition of Cyto-B at 24 h. Cells are fixed after culturing, transferred to imaging plate and stained with DAPI. Imaging plates are automatically scanned on the IN Cell Analyzer 2000 system with 81 frames per well (or per sample), using a 20x objective lens. Image analysis was performed using home-made FluorQuantMN software [9].

Typical captured images are shown in Fig. 3. Binucleated cells can be found on cytogenetic preparations already after 48 h of cell culturing in control samples as well as in irradiated samples.

^aColumbia Genome Center High Throughput Screening Facility

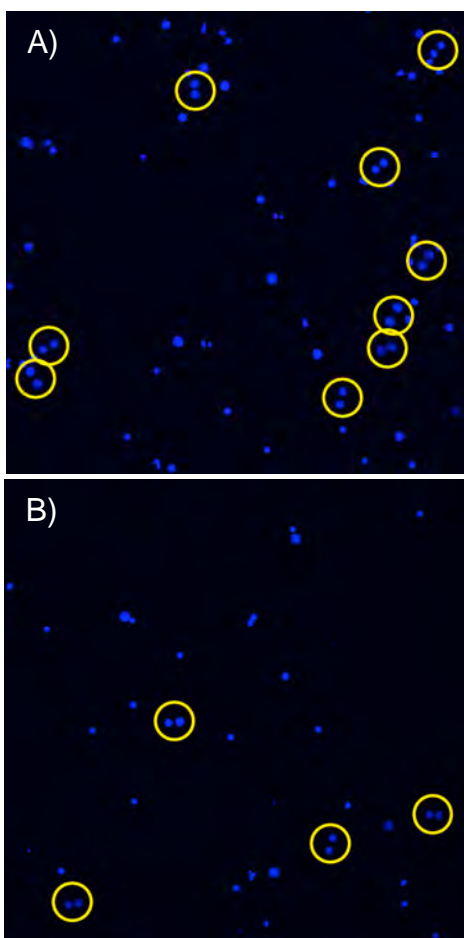


Figure 3. Fixed and DAPI-stained samples of human lymphocytes after 48 hours of cell culturing: A) control sample; B) sample after irradiation with 4.0 Gy of γ -rays. Images were captured by IN CELL Analyzer using 20x objective lens. Binucleated cells are outlined with yellow circles.

More than 100 binucleated cells (recommended minimum for the CBMN assay) were identified by FluorQuantMN software in all 20 μ l and 25 μ l blood samples including samples after irradiation with the

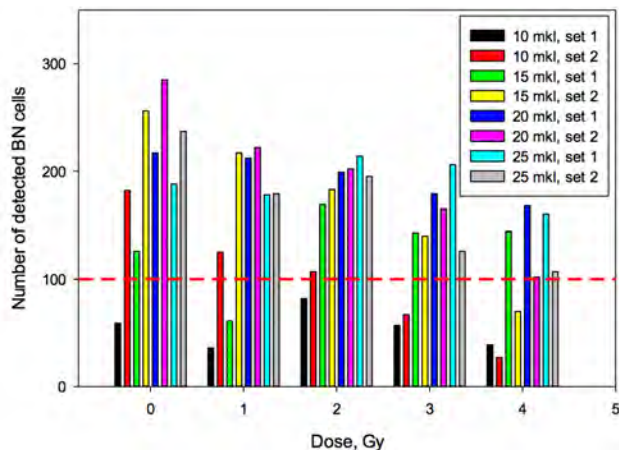


Figure 4. The number of binucleated cells detected by the FluorQuantMN software at doses up to 4.0 Gy for volumes of blood per sample from 10 μ l to 25 μ l. “mkl” = μ l

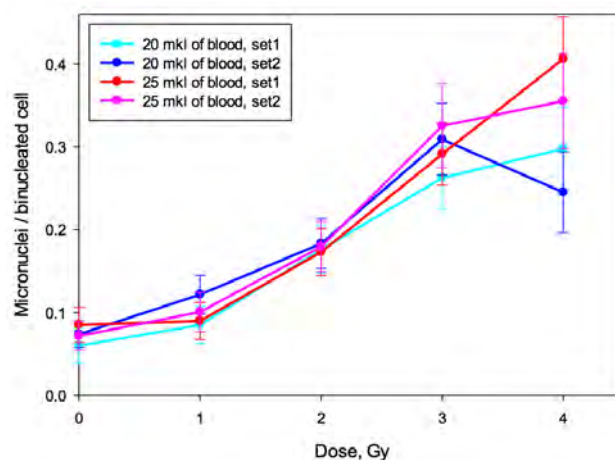


Figure 5. Dose-response curves of the MN yields induced in human lymphocytes by γ -rays produced using the automated RABiT II approach after 48 hours of cell culturing. The error bars represent the upper and lower 95% confidence intervals. “mkl” = μ l

maximum used 4.0 Gy of γ -rays (Fig. 4). We were able to increase the number of detectable binucleated cells by updating the FluorQuantMN software in such a way that the program can detect binucleated cells surrounded by mononucleated cells. This is very important for the miniaturized high-throughput CBMN assay due to the limited surface of the bottom of wells of imaging plates, in comparison with the surface of microscopical slides.

The linear-quadratic dose-response curves for 20 μ l and 25 μ l of blood samples are shown in Fig. 5.

In summary, we demonstrated that an accelerated fully automated micronucleus assay can be performed on a commercial HTS/HCS platform. This approach reduces the total time of CBMN assay from three days to two days. The study described here demonstrates that high-throughput radiation biodosimetry based on accelerated CBMN assay is practical using current commercial robotic HTS and imaging systems.

References

1. Garty, G., et al., THE DECADE OF THE RABiT (2005-15). Radiat Prot Dosimetry, 2016. 172(1-3): p. 201-206.
2. Garty, G., P.A. Karam, and D.J. Brenner, Infrastructure to Support Ultra High Throughput Biodosimetry Screening after a Radiological Event. International Journal of Radiation Biology, 2011. 87(8): p. 754-765.
3. Garty, G., et al., The RABiT: a rapid automated biodosimetry tool for radiological triage. Health Phys, 2010. 98(2): p. 209-17.
4. Turner, H.C., et al., Adapting the γ -H2AX assay for Automated Processing in Human Lymphocytes. 1. Technological Aspects. Radiation Research, 2011. 175(3): p. 282-290.

5. Turner, H.C., et al., The RABiT: high-throughput technology for assessing global DSB repair. *Radiation and Environmental Biophysics*, 2014. 53(2): p. 265-272.
6. Garty, G., et al., The RABiT: A Rapid Automated Biodosimetry Tool For Radiological Triage II. Technological Developments International Journal of Radiation Biology, 2011. 87(8): p. 776-790.
7. Repin, M., et al., Next generation platforms for high-throughput biodosimetry. *Radiation Protection Dosimetry*, 2014. 159(1-4): p. 105-110.
8. Repin, M., et al., RABiT-II: Implementation of a High-Throughput Micronucleus Biodosimetry Assay on Commercial Biotech Robotic Systems. *Radiat Res*, 2017.
9. Garty, G., FluorQuant 6.0: Software for scoring Micronuclei and Immunofluorescence. CRR annual report, 2016. ■

Chromosomal DNA Damage in Human Lymphocytes from Humanized Mice Exposed to Neutrons and X rays

Helen C. Turner, Qi Wang, Younghyun Lee, Igor Shuryak, Monica Pujol Canadell, Jay R. Perrier, Lubomir B. Smilenov, Andrew Harken, Brian Ponnaiya, Guy Garty, and David J. Brenner

Introduction

In the event of an improvised nuclear device (IND) scenario, prompt radiation exposure would consist of a mixture of photons and Me-V range neutrons [1 2]. Based on Monte Carlo calculations of radiation transport in an urban environment, it is expected that the neutron dose at a survivable distance from an IND detonation would be on the order of 10-20% of the total dose [3]. The relative biological effectiveness (RBE) of neutrons has been reported to be as low as 1 and perhaps higher than 10, depending on the tissue type, neutron energy and the biological endpoint being measured [4 5]. Neutrons have been shown to be 2-6 times more effective than photons in inducing cytogenetic damage. Roughly half of the biological effect observed will be due to neutrons, with the other half due to photons [6-8].

It is generally accepted that DNA double-strand breaks (DSB) play an important role in the formation of chromosome aberrations. These mechanisms of formation will be strongly dependent on LET as DSB induced by high-LET radiation are more clustered and possess a high structural complexity, compared with those induced by low-LET radiation. The latter damage is mainly dispersed simple DSB. As a result, the rejoining of high-LET DSB will be less efficient and the DSB will rejoin more slowly, allowing more opportunity for interactions leading to exchanges [9-11]. The focus of the present work was to compare the level of cytogenetic damage *in vivo* in human lymphocytes from hematopoietically humanized mice [12 13] after exposure to 0.3 Gy neutrons (1.55 Gy/h + 0.4 Gy/h γ rays) and 1 Gy x rays (1.23 Gy/min). Chromosomal DNA damage in human T-cells from the

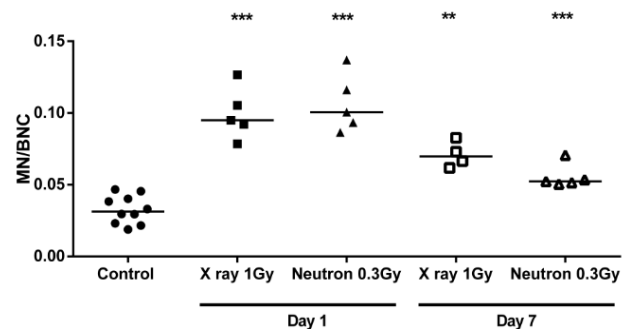


Figure 1. Micronucleus frequency/binucleate cell in human T-lymphocytes, 1 and 7 days after exposure to x-rays and neutron exposure.

mouse spleen was measured using the *in vitro* cytokinesis-block micronucleus (CBMN) assay, 1 and 7 days after exposure [14] and p53 protein expression levels in human CD45+ cells were quantified using ImageStream[®]X imaging flow cytometry (IFC) and associated analysis by IDEAS[®] software.

Results

Human hematopoietic cell counts in the blood and spleen measured by flow cytometry before irradiation showed that engraftment efficiency was ~85%, based on the frequency of mice with more than 50% human CD45+ cells. Radiation-induced loss of human T-cells in the blood at 1 and 7 days was significantly ($p < 0.05$) larger for the x-ray dose compared to the neutron dose; human T-cell counts in the spleen were not significantly different. At Day 1, there was no significant difference in micronucleus yields per binucleate cell (MNi/BNi)

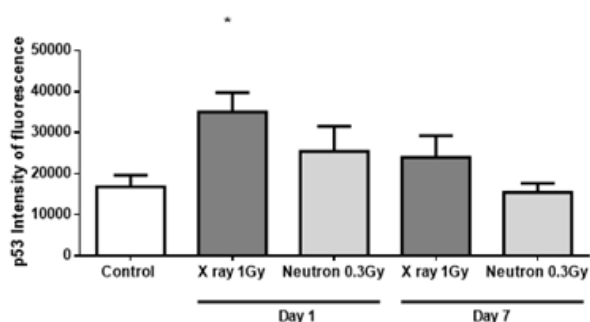


Figure 2. Phosphorylated-p53 (Ser37) expression in human CD45+ lymphocytes by image flow cytometry analysis.

between the two radiation types, whereas MNi/BN values at day 7 were significantly lower ($p < 0.05$) after neutron exposure (Fig. 1). The horizontal line indicates the median values. The Kruskal-Wallis test was first performed to compare the data among the five study groups ($p < 0.05$). Comparison between the control and irradiated groups was performed by the Mann-Whitney U test (** $p < 0.01$ and *** $p < 0.001$).

Phosphorylated-p53 (Ser37) expression in human CD45+ lymphocytes at day 1 was significantly ($p < 0.05$) elevated above control, baseline levels after exposure to x rays but not for neutrons. By day 7, elevated p53 protein expression was not detectable above control levels (Fig. 2). Data are expressed as the mean \pm SEM. The Kruskal-Wallis test was performed to compare the data among the three study groups ($p < 0.05$). Comparison between the control and irradiated groups was performed by the Mann-Whitney U test (* $p < 0.05$).

Summary

In practice, neutrons from an IND will be a relatively small component by dose, but potentially a relatively large component by biological effect. The neutron-induced chromosomal DNA damage *in vivo* measured here using the CBMN assay indicates that neutrons were more biologically effective. The results also suggest that lymphocyte DNA damage repair kinetics may be different for neutron and x-ray exposures. The availability of the hematopoietically humanized mouse model represents a potentially valuable resource for radiation biodosimetry studies.

References

- Garty G, Xu Y, Elliston C, Marino SA, Randers-Pehrson G, Brenner DJ. Mice and the A-Bomb: Irradiation Systems for Realistic Exposure Scenarios. *Radiation research* 2017;187(4):465-75.
- Egbert SD, Kerr GD, Cullings HM. DS02 fluence spectra for neutrons and gamma rays at Hiroshima and Nagasaki with fluence-to-kerma coefficients and transmission factors for sample measurements. *Radiat Environ Biophys* 2007;46(4):311-25
- Kramer K, Li A, Madrigal J, Sanchez B, Millage K. Monte Carlo Modeling of the Initial Radiation

Emitted by an Improvised Nuclear Device in the National Capital Region (Revision 1), 2016.

- Seth I, Schwartz JL, Stewart RD, Emery R, Joiner MC, Tucker JD. Neutron exposures in human cells: bystander effect and relative biological effectiveness. *PLoS one* 2014;9(6):e98947
- Ryan LA, Wilkins RC, et al. Relative biological effectiveness of 280 keV neutrons for apoptosis in human lymphocytes. *Health physics* 2006;91(1):68-75.
- Xu Y, Randers-Pehrson G, Turner HC, et al. Accelerator-Based Biological Irradiation Facility Simulating Neutron Exposure from an Improvised Nuclear Device. *Rad. Res.* 2015;184(4):404-10.
- Wuttke K, Müller W-U, Streffer C. The sensitivity of the *in vitro* cytokinesis-blocked micronucleus assay in lymphocytes for different and combined radiation qualities. *Strahlentherapie und Onkologie* 1998;174(5):262-68.
- Huber R, et al. Dose-response relationships of micronuclei in human lymphocytes induced by fission neutrons and by low LET radiations. *Mutation Research/Fundamental and Molecular Mechanisms of Mutagenesis* 1994;306(2):135-41
- Vral A, Thierens H, Baeyens A, De Ridder L. Induction and disappearance of G2 chromatid breaks in lymphocytes after low doses of low-LET gamma-rays and high-LET fast neutrons. *International journal of radiation biology* 2002;78(4):249-57.
- Sachs RK, Brenner DJ. Effect of LET on chromosomal aberration yields. I. Do long-lived, exchange-prone double strand breaks play a role? *International journal of radiation biology* 1993;64(6):677-88.
- Kysela BP, Arrand JE, Michael BD. Relative contributions of levels of initial damage and repair of double-strand breaks to the ionizing radiation-sensitive phenotype of the Chinese hamster cell mutant, XR-V15B. Part II. Neutrons. *International journal of radiation biology* 1993;64(5):531-8.
- Shultz LD, Lyons BL, Burzenski LM, et al. Human lymphoid and myeloid cell development in NOD/LtSz-scid IL2R gamma null mice engrafted with mobilized human hemopoietic stem cells. *Journal of immunology* 2005;174(10):6477-89
- Shultz LD, Brehm MA, Garcia-Martinez JV, Greiner DL. Humanized mice for immune system investigation: progress, promise and challenges. *Nature reviews. Immunology* 2012;12(11):786-98.
- Fenech M. The lymphocyte cytokinesis-block micronucleus cytome assay and its application in radiation biodosimetry. *Health physics* 2010;98(2):234-43. ■

Combination of Imaging Flow Cytometry with High-throughput Automated Robotic Systems for Cytokinesis-block Micronucleus Assay

Qi Wang, Mikhail Repin, Matthew Rodrigues^a, Sergey Pampou^b, Jay Perrier, Lindsay A. Beaton-Green^c, Ruth C. Wilkins^c, David J. Brenner, and Helen C. Turner

Introduction

Biodosimetry is a determination of the dose of ionizing radiation that an individual may have received based on the evaluation of biological damage. In the case of a large-scale radiological/nuclear event, hundreds of thousands of people could be exposed to a wide range of radiation doses. The availability of automated high throughput biodosimetry methods will be important for rapid dose assessment and early triage decision [1, 2].

The cytokinesis-block micronucleus (CBMN) assay is a widely accepted method for radiation biodosimetry. It is traditionally performed using microscope-based scoring, which can be labour-intensive, time consuming and subject to inter-scorer variability [3]. Recently, imaging flow cytometry technology has been developed for CBMN assay that combines the statistical power of traditional flow cytometry with the sensitivity and specificity of microscopy [4]. The technology is

potentially capable of automated sample acquisition and batch analysis. As such, this technology is well suited for the adaptation into a fully automated imaging cytometry method for high-throughput screening.

The Center for High-Throughput Minimally-Invasive Radiation Biodosimetry at Columbia University has developed Rapid Automated Biodosimetry Technology (RABiT-II), a fully automated, high-throughput processing system, which can be used for the preparation of samples for the CBMN assay [5]. We have made progress on integrating imaging flow cytometer ImageStream®X (ISX) into the RABiT-II for the CBMN assays.

Experimental overview and results

The goal of this work is to develop the CBMN assay for high-throughput, automated imaging flow cytometry analysis for emergency response biodosimetry by: 1) developing small volume methodology; and 2) optimizing data acquisition and analysis.

Samples were prepared and analyzed according to the workflow shown in Figure 1. Briefly, human peripheral whole blood samples from healthy donors were irradiated *ex vivo* with γ -rays, cultured for 24 hours before cytochalasin-B was added, and harvested after another 44 hours culturing. Samples in solution were stained with DRAQ5 and imaged on the imaging flow cytometer ISX.

To decide the best whole blood culture methods, the ratio of blood and culture media was tested. Result showed that micronuclei (MNi)/binucleate cells (BNCs) yields were not significantly different in culture condition with blood to culture media ratio of 1:2, 1:3 and 1:4. For cell harvesting, methods of hypotonization, lysing and fixation were tested to minimize cell loss during processing and improved image detection of BNCs and MNi. We determined that combination of 75mM potassium chloride hypotonization with FACS lysing solution serve as the best method to harvest the cells. In addition, different concentration of DNA dye DRAQ5 was tested to improve the quality of the nuclear staining. Comparison of the DRAQ5 dye concentration of 2.5 μ M, 10 μ M, 20 μ M, 50 μ M demonstrated that 20 μ M is the best concentration to obtain nuclear images with the maximum signal to noise ratio.

To combine the assay with the RABiT-II system, cell culturing volume and harvesting reagent volume were

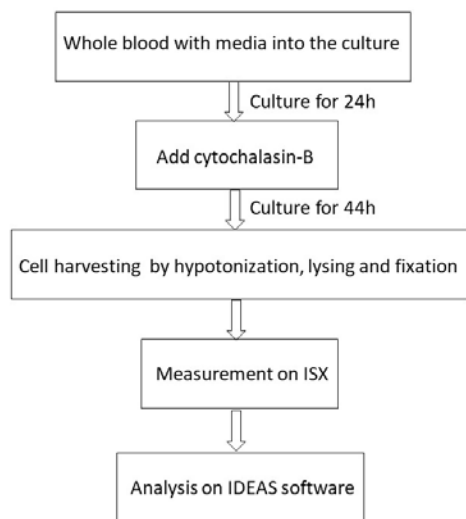


Figure 1. Schematic illustration of experimental procedures.

^aMilliporeSigma, Seattle, WA

^bColumbia Genome Center High Throughput Screening Facility, CUMC

^cConsumer and Clinical Radiation Protection Bureau, Health Canada, Ottawa, ON, Canada

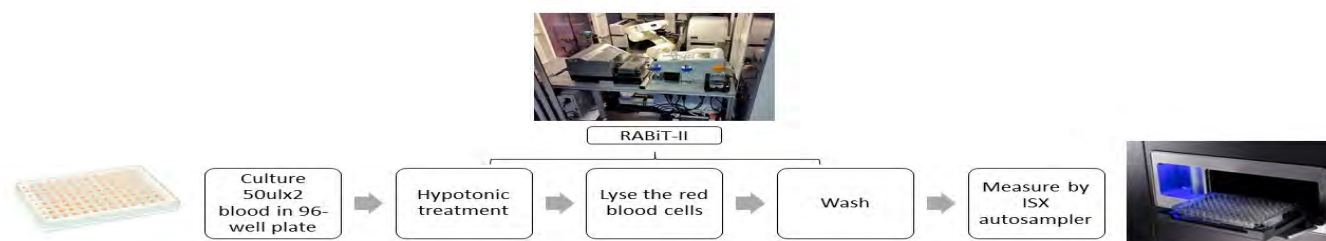


Figure 2. Schematic illustration with RABiT-II processing procedures.

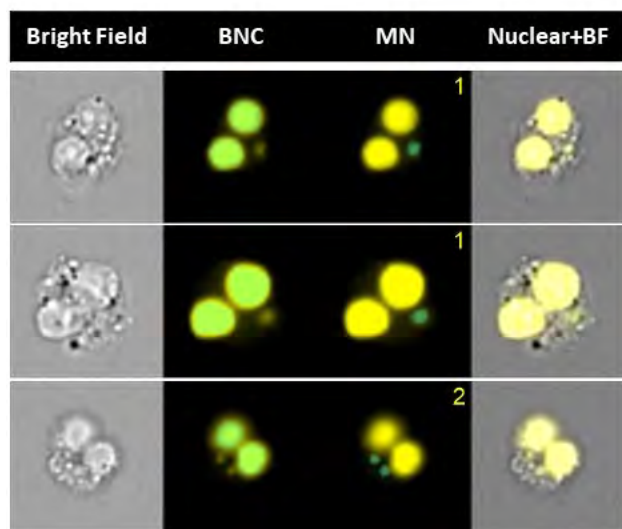


Figure 3. Representative BNC and MN analyzed by IDEAS software. BNC, bi-nucleated cells. MN, micronuclei. BF, bright field. Number of MN (1 or 2) indicated in panel.

modified to fit in the 96-well plate format. Human peripheral whole blood samples were irradiated *ex vivo* with γ -rays at doses of 1Gy, 2Gy, 3Gy, 4Gy and 5Gy at a dose rate of 0.67 Gy/min. 50 μ l blood samples with 200 μ l of PB-MAX[™] karyotyping media were loaded in the 96-well plate. After culturing for 68 hours, cells were harvested using the RABiT-II Perkin Elmer cell::explorer sample preparation work station (Figure 2). After the harvesting, sample was stained with 20 μ M DRAQ5, and

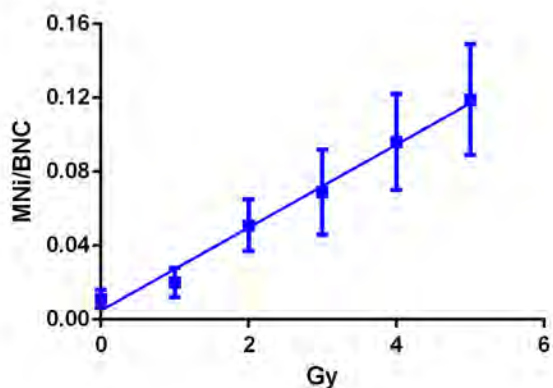


Figure 4. Dose-response curves of the MNi yields induced by γ -rays in human lymphocytes using the RABiT-II approach. The error bars represent standard error.

imaged on the ISX integrated with an autosampler. Modifications to the ISX acquisition had been made to minimize the data file size.

MNi and BNCs yields were identified and quantified using IDEAS[®] software. IDEAS[®] data analysis template has been optimized to increase the specificity and sensitivity for detection of MNi and BNC (Figure 3) [6]. MNi/BNC yields demonstrated a linear-quadratic function of dose after γ -ray exposures up to 5 Gy (Figure 4).

Conclusion

Approaches for evaluation of MNi yields combining the imaging flow cytometry system and biotech robotic systems increased the throughput of the measurement and allowed for a reduction in the volume of blood requirement compared with traditional protocols [7]. These results indicate that a novel, imaging flow cytometry autosampler system can be integrated into our RABiT-II automated system and provide high-throughput biodosimetric screening possibility for use in large-scale radiological incidents. Further efforts can be made to shorten the whole blood culture time and extending the γ -ray application radiation dose range.

References

1. Flood, A. B., et al. (2014). Advances in a framework to compare bio-dosimetry methods for triage in large-scale radiation events. *Radiation protection dosimetry*, **159**(1-4), 77-86.
2. Sproull, M., & Camphausen, K. (2016). State-of-the-art advances in radiation biodosimetry for mass casualty events involving radiation exposure. *Radiation research*, **186**(5), 423-435.
3. Fenech, M., et al. (2013). HUMN project initiative and review of validation, quality control and prospects for further development of automated micronucleus assays using image cytometry systems. *International journal of hygiene and environmental health*, **216**(5), 541-552.
4. Rodrigues, M. A., et al. (2014). Automated analysis of the cytokinesis-block micronucleus assay for radiation biodosimetry using imaging flow cytometry. *Radiation and environmental biophysics*, **53**(2), 273-282.
5. Repin, M., et al. (2017). RABiT-II: Implementation of a High-Throughput Micronucleus Biodosimetry Assay

on Commercial Biotech Robotic Systems. *Radiation research*, **187**(4), 502-508.

6. Rodrigues, M. A., et al. (2016). The effect of an optimized imaging flow cytometry analysis template on sample throughput in the reduced culture cytokinesis-block micronucleus assay. *Radiation*

protection dosimetry, **172**(1-3), 223-229.

7. Rodrigues, M. A., et al. (2016). Validation of the cytokinesis-block micronucleus assay using imaging flow cytometry for high throughput radiation biodosimetry. *Health physics*, **110**(1), 29-36. ■

In Vivo Blood Cell Sub-type Changes after Irradiation via Deconvolution of the Gene Expression Response using CIBERSORT

Shanaz A. Ghandhi, Shad R. Morton, Nils Rudqvist, and Sally A. Amundson

The Non-Human Primate (NHP) is a large animal model that is suited for studies pertaining to human health and physiological response [1, 2]; and in the context of radiation biology used for assessing the effects of mitigators [3-7] of acute radiation syndrome and organ damage after different types and modes of exposure. NHPs are physiologically more similar to humans than small animals such as mice, and the advantage of using NHP biofluids for radiation studies is in the ability to follow animals over longer periods of time with greater abundance of biological material. We studied the effects of radiation on the species *Macaca mulatta*, also called Rhesus macaque, Chinese strain. The genome of this species is ~93% similar to the human genome, with many common structurally and functionally related genes, enriched in biological functions related to immune response and signaling [8].

We performed two independent studies, both involving Total Body Irradiation (TBI, doses of 4.0 Gy and 7.4 Gy) of *M. mulatta*; in which blood was collected pre-irradiation and at different days post irradiation. In

Study 1, NHPs were TBI irradiated with 4.0 Gy and samples were collected at 3 days before irradiation and then at 1, 3, 5 and 7 days after irradiation. In Study 2, NHPs were TBI irradiated with ~7.4 Gy and samples were collected at 1 day before irradiation and then at 1, 2 and 3 days after irradiation. We collected whole blood, from which we extracted RNA, performed relevant QC tests (evaluating A260/230 ratios and RINs using the Agilent Bioanalyzer) and performed microarray analysis on total RNA. We collected the whole genome gene expression data following well-established methods [9, 10]. We show here analysis of the data from blood samples collected at pre- and 3 days after irradiation, because this was the only time point in both studies for which we had the complete whole genome data sets. Between 4 and 20 animals for each time point were used for the analysis shown here.

Analysis of gene expression using Gene Ontology and pathways revealed that immune function and inflammation is a top biological process across all time points in these two studies. We have also shown this

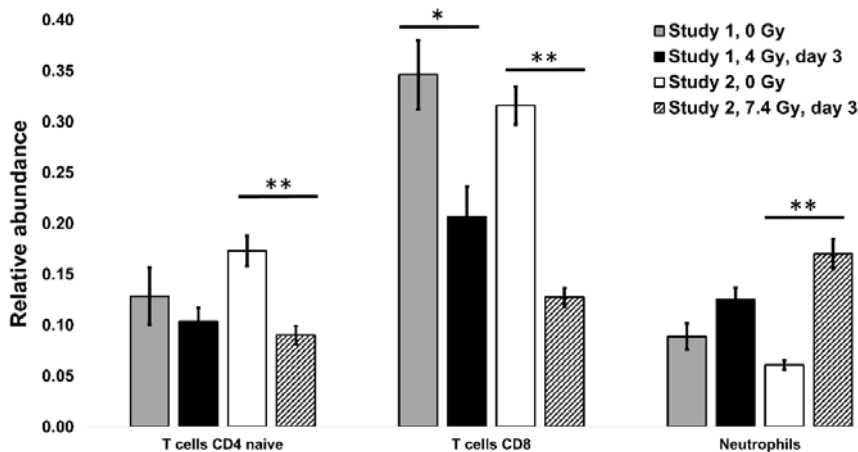


Figure 1. CIBERSORT generated relative abundance of T cells (CD4 and CD8) and neutrophils at 3 days after TBI, from two different studies. Study 1 used a TBI dose of 4 Gy, and Study 2, a TBI dose of ~7.4 Gy. We used a two-tailed student's t-test for statistical significance, * is p-value < 0.05, ** is p-value < 0.005.

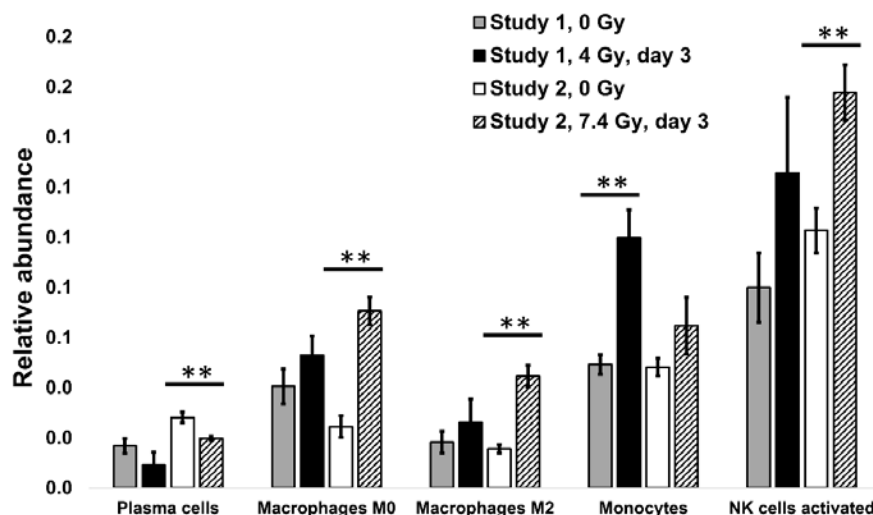


Figure 2. CIBERSORT generated relative abundance of other blood cell subtypes that showed significant differences in relative abundance after irradiation (in at least one study/one dose) at 3 days after TBI, from two different studies. Study 1 used a TBI dose of 4 Gy, and Study 2, a TBI dose of ~7.4 Gy. We used a two-tailed student's *t*-test for statistical significance, * is p -value < 0.05, ** is p -value < 0.005.

response to persist up to 1 month after irradiation in another independent study on partial body irradiated NHPs [9]. These immune processes may reflect corresponding changes in the relative abundance of blood cells over the course of the study, which in turn reflect changes in physiology of the animal after irradiation, especially with regards to response to stress, infection and recovery. Information regarding such changes in blood cell sub-populations after irradiation were not available in our two studies. Therefore, we applied a recently developed method called CIBERSORT that deconvolutes whole genome gene expression data to predict the fractions of 22 blood cell types based on a gene expression signature defined for each cell type [11]. We applied this method to our NHP gene expression data to predict fractions of cell subsets and compared the results of our two studies, looking for differences in cell types and also trends based on the two doses 4 Gy and 7.4 Gy (LD50/60).

In the data shown in Figures 1 and 2, we compared the two irradiated groups to their matching controls, and found that the higher 7.4 Gy dose significantly altered the levels of both T cells and neutrophils by day 3 in these studies, while the lower 4 Gy dose significantly changed only the CD8 cell fraction. Although we could not make statistical comparisons across the two studies, there is a trend of increased change with the higher dose (for CD8 cells compared to control 40% decrease after 4 Gy and 60% decrease after 7.4 Gy; Neutrophils, compared to control, 40% increase after 4 Gy and 180% increase after 7.4 Gy). Other cell types such as monocytes did not show this trend in response to TBI (Figure 2). The cell subtypes shown in Figure 2 were mostly significantly different at the higher dose, with the exception of monocytes, and may indicate that a higher dose is required to significantly alter the levels of these cells. These predictions of change in blood cell subtype fractions after irradiation with ~7.4 Gy correlate with hematology measurements of absolute

lymphocyte and neutrophils counts after a similar TBI dose reported in other studies [4, 7].

Immune reconstitution after irradiation following a radiological event, therapy or transplant is important for the recovery of an individual, in preventing infection and further damage to organs. Therefore, establishment of immune parameters after irradiation are critical to understand this process. This study shows that it may be possible to investigate changes in blood cell subtypes after irradiation of NHPs using a gene signature and also a potential dose response at a given time after irradiation. The best way is to experimentally determine changes in blood subtypes by flow cytometry; however, this method may also be useful in corroborating changes where sample is limited and gene expression data is available.

References

1. Grow DA, McCarrey JR, Navara CS. Advantages of nonhuman primates as preclinical models for evaluating stem cell-based therapies for Parkinson's disease. *Stem cell research*. 2016;17(2):352-66. Epub 2016/10/26. doi: 10.1016/j.scr.2016.08.013.
2. Hong SG, Lin Y, Dunbar CE, Zou J. The Role of Nonhuman Primate Animal Models in the Clinical Development of Pluripotent Stem Cell Therapies. *Molecular therapy : the journal of the American Society of Gene Therapy*. 2016;24(7):1165-9. Epub 2016/08/11. doi: 10.1038/mt.2016.131.
3. Williams JP, Brown SL, Georges GE, Hauer-Jensen M, Hill RP, Huser AK, et al. Animal models for medical countermeasures to radiation exposure. *Radiat Res*. 2010;173(4):557-78. Epub 2010/03/26. doi: 10.1667/rr1880.1.
4. Thrall KD, Love R, O'Donnell KC, Farese AM, Manning R, MacVittie TJ. An Interlaboratory Validation of the Radiation Dose Response Relationship (DRR) for H-ARS in the Rhesus

- Macaque. *Health Phys.* 2015;109(5):502-10. doi: 10.1097/HP.0000000000000339.
5. MacVittie TJ, Farese AM, Jackson W, 3rd. The Hematopoietic Syndrome of the Acute Radiation Syndrome in Rhesus Macaques: A Systematic Review of the Lethal Dose Response Relationship. *Health Phys.* 2015;109(5):342-66. doi: 10.1097/HP.0000000000000352.
 6. MacVittie TJ. The MCART Consortium Animal Model Series: MCART Animal Model Refinement and MCM Development: Defining organ dose, organ-specific tissue imaging, model validation and the natural history between the acute radiation syndrome (ARS) and the delayed effects of acute radiation exposure (DEARE). *Health Phys.* 2015;109(5):335-41. Epub 2015/10/02. doi: 10.1097/hp.0000000000000318.
 7. Farese AM, Cohen MV, Katz BP, Smith CP, Jackson W, 3rd, Cohen DM, et al. A nonhuman primate model of the hematopoietic acute radiation syndrome plus medical management. *Health Phys.* 2012;103(4):367-82. doi: 10.1097/HP.0b013e31825f75a7.
 8. Gibbs RA, Rogers J, Katze MG, Bumgarner R, Weinstock GM, Mardis ER, et al. Evolutionary and biomedical insights from the rhesus macaque genome. *Science.* 2007;316(5822):222-34. Epub 2007/04/14. doi: 10.1126/science.1139247.
 9. Ghandhi SA, Turner HC, Shuryak I, Dugan GO, Bourland JD, Olson JD, et al. Whole thorax irradiation of non-human primates induces persistent nuclear damage and gene expression changes in peripheral blood cells. *PLoS One.* 2018;13(1):e0191402. Epub 2018/01/20. doi: 10.1371/journal.pone.0191402.
 10. Ghandhi SA, Smilenov LB, Elliston CD, Chowdhury M, Amundson SA. Radiation dose-rate effects on gene expression for human biodosimetry. *BMC Med Genomics.* 2015;8:22. Epub 2015/05/13. doi: 10.1186/s12920-015-0097-x.
 11. Newman AM, Liu CL, Green MR, Gentles AJ, Feng W, Xu Y, et al. Robust enumeration of cell subsets from tissue expression profiles. *Nat Methods.* 2015;12(5):453-7. Epub 2015/03/31. doi: 10.1038/nmeth.3337. ■

Protein Markers for Radiation Exposure in in-vivo Irradiated Humanized Mouse Model

Younghyun Lee, Monica Pujol Canadell, Igor Shuryak, Jay R. Perrier, Purvi Patel^a, Antonius Koller^a, Lubomir B. Smilenov, David J. Brenner, Emily I. Chen^a, and Helen C. Turner

Introduction

In large-scale radiological accidents or incidents, many people can be exposed to a wide range of radiation dose. It would be crucial to screen them as soon as possible to predict their received dose for rapid triage. Therefore, potential biomarkers to predict accurate dose and the high-throughput assay system for measuring them are required. Moreover, it would be impossible to collect blood from all potentially exposed populations within 24 h of a large-scale accident, so the identification of radiation responsive biomarkers that are detectable days after a radiological exposure will be valuable for dose assessment and triage after radiation exposure.

To date, few studies have evaluated the long-lived protein markers for radiation biodosimetry in any of the human biofluids because it is not feasible to obtain specimens from humans days after radiation exposure.

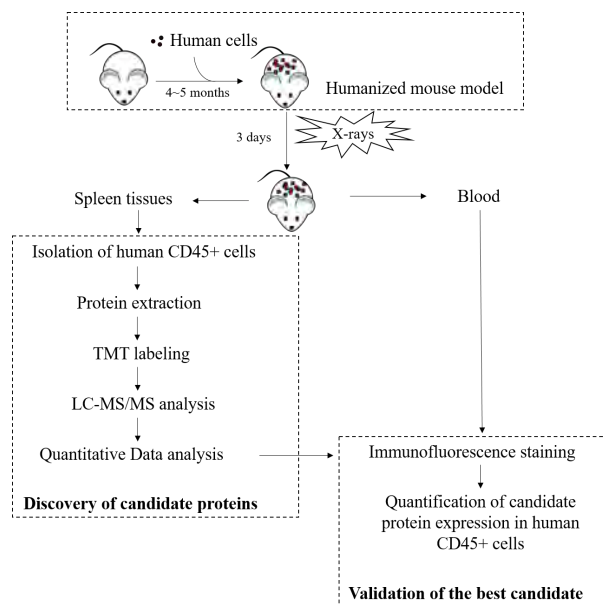


Figure 1. Workflow of the study to find candidate protein markers for radiation exposure in a humanized mouse model.

^aProteomics Shared Resource, Herbert Irving Comprehensive Cancer Center

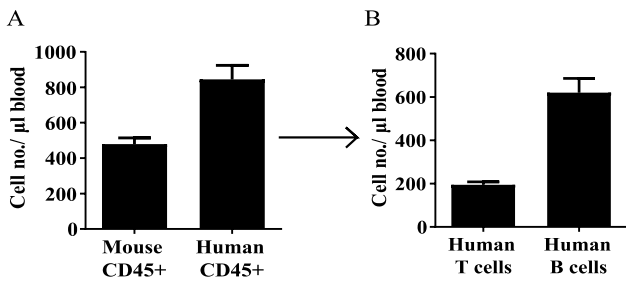


Figure 3. Engraftment of human cells in a humanized mouse model (A) Number of human and mouse cells in humanized mouse blood before irradiation (B) Number of human B and T cells in humanized mouse blood before irradiation.

Although human *in vivo* studies can provide the most predictable information, there is no perfect *in vivo* model for developing radiation biomarkers.

Advanced proteomics technology and bioinformatics tools have allowed researchers to gain valuable insights into radiation-induced biological and physiological changes and discover radiation responsive markers (1-3). The advantage of proteomic profiling is to measure the levels of thousands of proteins at one time without any information for protein identity and to provide information on biological pathway and interaction.

The goal of this study is to investigate long-lived radiation responsive protein biomarkers in human lymphocytes *in vivo* using a humanized mouse model. Using a proteomic-based approach, we identified radiation responsive protein markers days after radiation exposure.

Experimental overview and results

We evaluated the proteome changes in human lymphocytes from Hu-NSG mice 3 days after X-ray

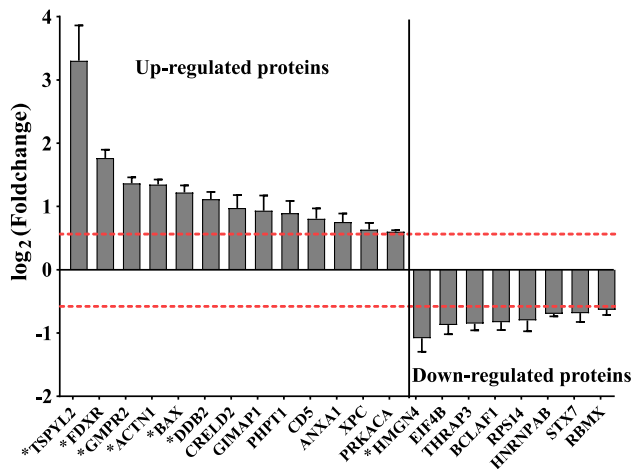


Figure 4. Radiation-induced changes in protein abundance in *in vivo* irradiated human cells. Fold changes of protein abundance, quantified by TMT labeling, were calculated and proteins with more than a 1.5-fold change in 2 Gy irradiated cells were listed. Proteins with more than 2-fold change were marked with an asterisk (*). Red dot line indicates 1.5-fold change increased/ decreased level. Left/right panel in the figure shows up-/down-regulated proteins.

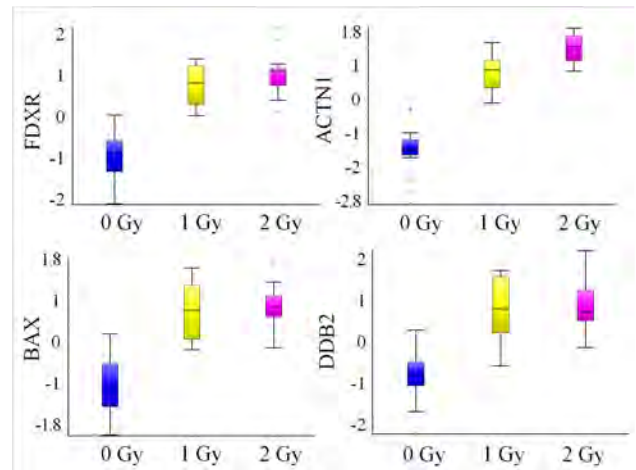


Figure 2. Dose response relationship of the best candidate markers (FDXR, ACTN1, BAX, and DDB2). Bar graph indicates log-transformed TMT ratio, measured as quantitative value of protein abundance in proteomic analysis.

exposure (Figure 1): humanized mice were generated by injecting HSCs to NSG mice, and proteome profiling of isolated human lymphocytes from humanized mice 3 days after X-irradiation were analyzed.

Four-five months after injection of human stem cells, 97% of recipient NSG mice showed successful engraftment of human cells. The humanized mice (n=33) used in this study had 61.3 ± 17.9 % human CD45+ cells including human B and T cells. Figure 2 shows number of human cells and distribution of human hematopoietic reconstitution with human B and T cells in non-irradiated humanized mice.

We identified 3,376 proteins from human lymphocytes of humanized mice, and compared protein expression of each dose groups to identify protein signatures in X-irradiated human lymphocytes 3 days after radiation exposure. We found significantly different proteins between the control and irradiated group in each setting: 18 proteins from 0 vs. 1 Gy comparison (0.0099% FDR), 20 proteins from 0 vs. 2 Gy comparison (0.023% FDR) and 34 proteins from comparison among three different dose groups (0.001% FDR). Several proteins were shared by different groups, and a total of 46 proteins were found to be differentially expressed in response to radiation exposure.

Of the proteins identified, 24 were up-/down-regulated more than 1.5 fold in the 2 Gy irradiated group compared to control. Especially, 8 up-regulated proteins (TSPYL2, FDXR, GMPR2, ACTN1, BAX, DDB2, GIMAP1 and CRELD2) and 1 down-regulated protein (HMGN4) had a fold change greater than 2, which are considered proteins with a high response to radiation in this study (Figure 3).

Dose dependent response of each protein after radiation exposure was assessed by correlation analysis. PRKACA, ACTN1, GMPR2, FDXR, CRELD2, SF3A3,

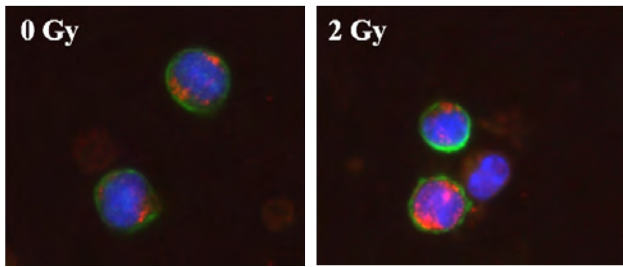


Figure 5. Representative images of FDXR stained human cells in non-irradiated and irradiated humanized mice. Cells isolated from blood of humanized mice were stained with Human CD45 (green) and FDXR (red) antibodies. Nuclei were counter-stained with DAPI.

DDX21, HNRPU, RNASET2, BCLAF1, BAX, XPC, HNRNPAB, PRPF40A, RBM14, TSPYL2, PDLIM5, and GIMAP1 protein expression were found to be significantly correlated with irradiated dose ($|\text{correlation coefficient}| > 0.7$, $p\text{-value} < 0.05$). Of them, HNRNPAB, ACTN1, FDXR, HNRPU, BAX, SF3A3, DDB2, RBM14, and BCLAF1 showed a consistent dose dependent response in more than 3 different donor groups. Taken together, ACTN1, FDXR, BAX, and DDB2 were found to have a relatively high response to radiation and a consistent dose dependent response. Figure 4 shows changes in protein abundance of the best candidate markers after radiation exposure.

Radiation-induced response of FDXR protein, one of the best candidates, was verified by the immunofluorescence method. FDXR protein expression was increased more than 1.5-fold at day 3 after 2Gy X-irradiation (Figure 5).

Conclusion

Distinct protein signatures of radiation exposure were identified in human lymphocytes 3 days after *in vivo* irradiation. We found 46 differentially expressed proteins by radiation exposure in the humanized mice model. Of them, 4 proteins (FDXR, BAX, DDB2 and ACTN1) were suggested as best candidate markers for radiation biodosimetry.

References

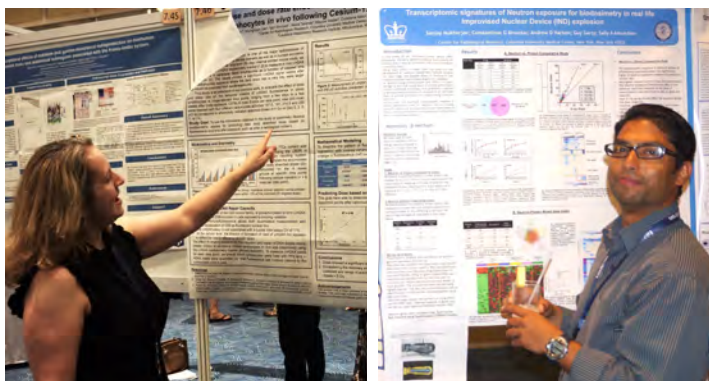
1. Azimzadeh O, Atkinson MJ, Tapio S (2014) Proteomics in radiation research: present status and future perspectives. *Radiat Environ Biophys* **53**:31-38.
2. Guipaud O, Benderitter M (2009) Protein biomarkers for radiation exposure: towards a proteomic approach as a new investigation tool. *Ann Ist Super Sanita* **45**:278-286.
3. Van Riper SK, de Jong EP, Carlis JV, Griffin TJ (2013) Mass spectrometry-based proteomics: basic principles and emerging technologies and directions. *Adv Exp Med Biol* **990**:1-35. ■



(l to r): Guy Garty, Younghyun Lee, Monica Pujol, Sanjay Mukherjee Veljko Grilj, Helen Turner



(l to r): Helen Turner, Tom Hei



(l to r): Helen Turner, Sanjay Mukherjee



(l to r): Manuela Buonanno, Guy Garty, Adrian Treverton

RABiT-II DCA: Optimization of the Fluorescent-based Dicentric Chromosome Assay for High-throughput Radiation Biodosimetry

Ekaterina Royba, Mikhail Repin, Sergey Pampou^a, Charles Karan^a, David J. Brenner, and Guy Garty

RABiT-II DCA

Dicentric chromosomes are an established cytogenetic end-point and a direct marker of severe DNA damage. They are formed in interphase cells through the fusion of two unrepaired/misrepaired segments of broken chromosomes. It is generally accepted that the process of dicentric formation is triggered by the action of ionizing radiation but not by factors of non-radiation nature (e.g. gender and lifestyle). Hence, their frequency accurately reflects an absorbed dose and cytological consequences of radiation damage.

Currently, the dicentric chromosome assay (DCA) is the gold standard for radiation biodosimetry [1]. The DCA is an efficient and validated screening technique.

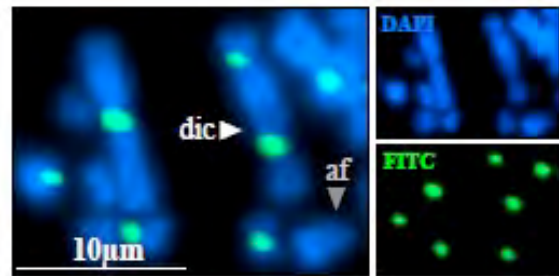


Figure 1. RABiT-II DCA staining. Dicentric (dic) with an accompanied acentric fragment (af) are indicated by white and grey arrows, respectively. Centromeres emitting green fluorescence. 20x, BioTek.

A

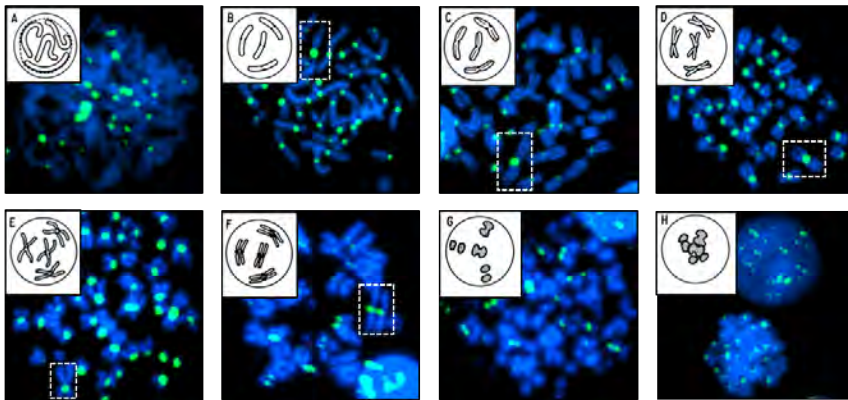
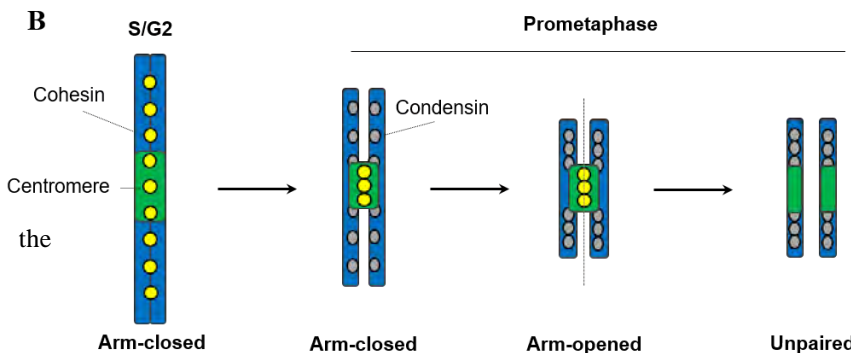


Figure 2. A. Observed chromosomal configurations: A. Strands are weakly condensed. B. Long; arms are closed. C. Arms began to open. D. Progressive dissociation of arms; shortening in length. E. Short; arms are opened; “X-shape” form. F. Sister chromatids are unpaired. G. Relaxation of condensation. H. Decondensed. **B. A model illustrating disjunction of sister chromatids.** Cells enter metaphase with chromatids tightly locked together by cohesin. Then, cohesin rings will proceed to cleavage (except centromeric regions). Dissociation of cleaved cohesin results in progressive separation of chromosomal arms. At the same time, DNA strands will twist by condensin and lead to shortening of chromosomes. After kinetochores will be properly attached to the mitotic spindle, the remaining centromeric cohesin will be cleaved by the enzyme separase, and chromatids become unpaired.

However,



^aColumbia Genome Center High Throughput Screening Facility

conventional DCA approach is a highly labor-intensive and time-consuming procedure. Moreover, scoring of dicentrics remains subjective and leads to significant inter-scorer variability. Thus, it is difficult to perform

manual / semi-automated DCA biomonitoring of large human populations (e.g. in case of radiation disaster) even using cooperative efforts involving several large cytogenetic networks.

Following up on our success in implementation of various radiation biodosimetry assays using a commercial High Throughput/High Content Screening system, we begun work on development, assessment, and validation of the DCA for fully-automated radiation screening of whole-blood using a Perkin Elmer cell::explorer system [2, 3]. Similar to previously reported RABiT-based bioassays, the RABiT-II DCA is designed as a minimally-invasive technique (analysis requires 30µl of whole blood); all manipulations are robotic-optimized and automated.

Centromeres visualized using non-classical FISH hybridization protocol

To visualize dicentrics in cells undergoing mitosis, we implemented labelling of centromeres on condensed chromosomes using fluorescent probes (Fluorescence in situ hybridization (FISH)) [4]. Traditional protocol requires multiple hours incubation of samples at different temperatures. To give spatial access of the probes to the centromeres, the double DNA helix has to be heat denatured first [5]. Recently, Genet et.al. reported that heat is not a critical factor and formamide can be used as an effective denaturant instead [6]. Based on this discovery, we developed a non-classical staining protocol which takes place in a 96 well-plate format.

Visual outcome of staining in the RABiT-II DCA is not different from the classical protocol but, compared to the laborious multistep procedure, sufficient for detection of fluorescent signals from centromeres observed after 3-hour incubation at 37°C degree (Fig.1). Further, sample analysis is possible at low magnification (20x or 10x), depending on the imager used (we have tested the BioTek Cytation 1 and GE InCell analyzer 2000). Monocentric and dicentric chromosomes are scored using custom-designed software [7].

Shapes of chromosomes depend on their association with cohesin

Our preliminary analysis revealed considerable metaphase-to-metaphase

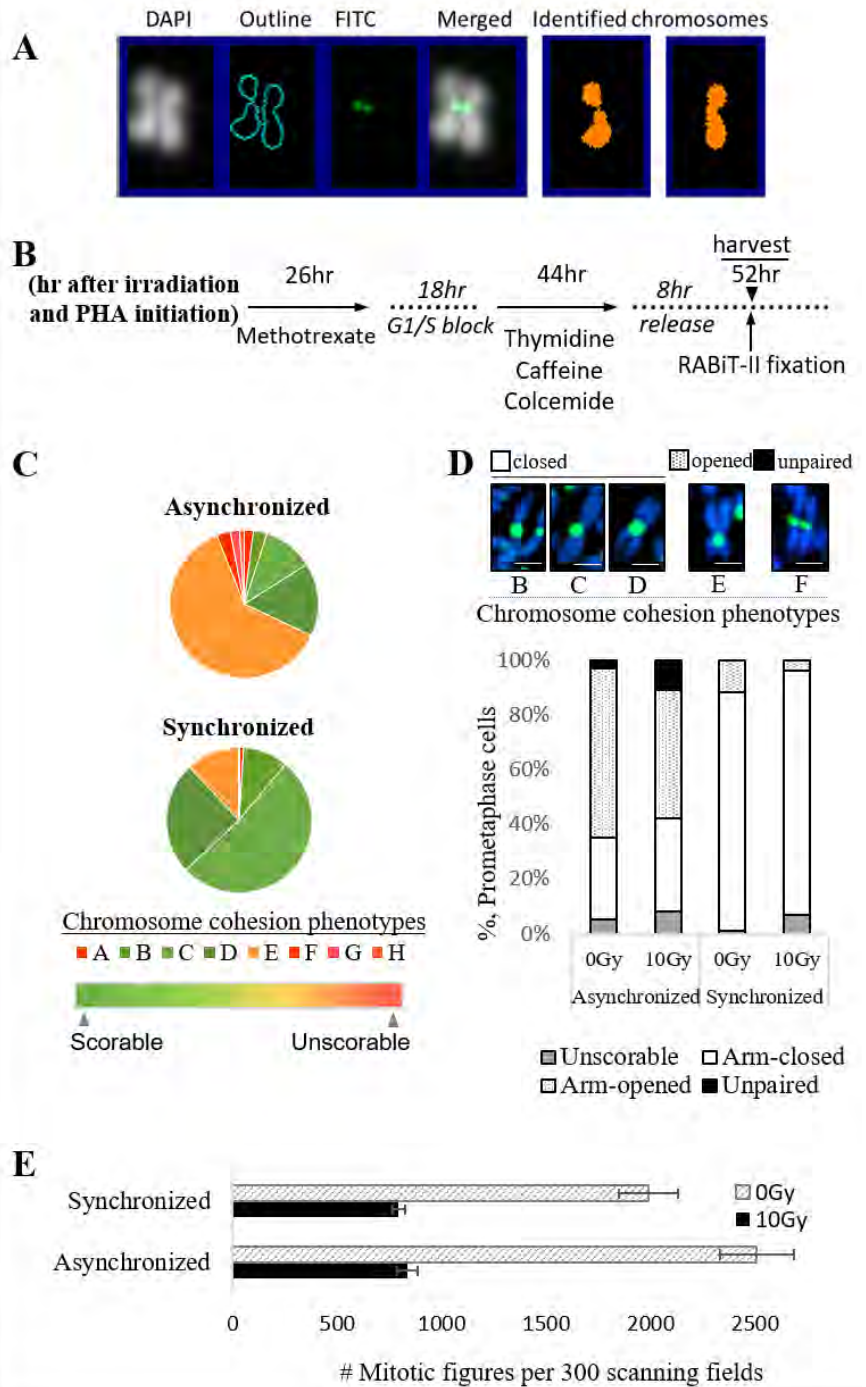


Figure 3. Effects of synchronization with methotrexate and thymidine on human lymphocyte culture. A. E type chromosome incorrectly classified as two B type chromosomes. B. Experimental design using synchronization with methotrexate, thymidine, and caffeine. C. Distribution of scorable and unscorable chromosomes before and after synchronization. 8hrs colcemide treatment used to accumulate mitotic cells. D. Representative images of chromosomes in the presence (left panel, closed) and absence (middle, opened) of arm cohesion. Chromosomes with unpaired sister chromatids are shown on the right. All images were magnified from Fig. 2A. Quantification results for distribution of each chromosomal configuration before and after synchronization calculated for 100 prometaphase cells (0Gy and 10Gy-irradiated samples) and summarized in histogram. White and dashed populations represent cells with closed and open arms, respectively. Dark-grey and black bars referred to unclassified/unscorable populations. E. Quantification data of mitotic figures per 300 scanning fields before and after synchronization. Data, standard deviations, and standard errors were calculated based on 3 independent experiments.

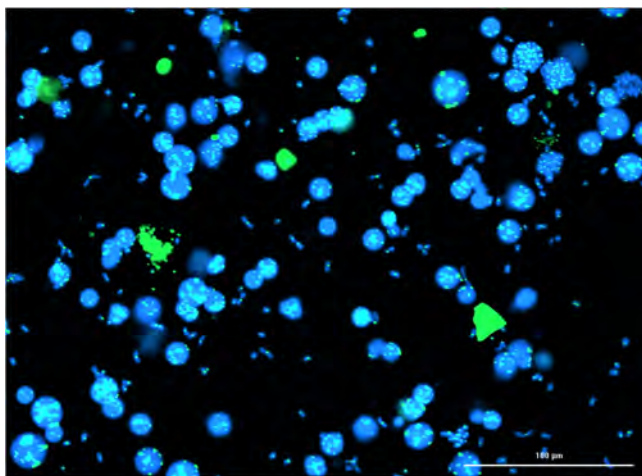


Figure 4. Distribution of chromosomes in synchronized culture per 1 scanning image (0Gy).

variation in chromosomal shape (Fig.2A). These morphological changes are caused by a precisely regulated cell process: stepwise loss of cohesion between chromosomal arms (Fig.2B) [8, 9]. These variations are common for populations of T-lymphocytes growing asynchronously because the cells entering mitosis and, hence, proceeding to chromatid separation, occur at the different times [10, 11].

Due to the aforementioned differences in chromosomal shapes and configurations, the RABiT-II algorithm, which has been programmed to select only chromosomes with particular shape, encountered several minor difficulties due to i) misrecognition of chromosomal types (Fig. 3A), ii) insufficient yield of chromosomes after high-dose rate irradiation caused by arrest of the cell cycle in damaged cells, and iii) significant shortage of chromosomal length after prolonged incubation with colcemide.

Synchronization controls variability of chromosome cohesion phenotypes

To collect long (mildly condensed) prometaphase chromosomes with more or less uniform shapes, we synchronized cell populations with methotrexate, thymidine, and caffeine in a 96 well-plate format [12, 13]. Methotrexate interferes with biosynthesis of pyrimidines. In the absence of building blocks, the replication machinery is unable to multiply DNA strands and resulted in temporary arrest of cells in S-phase. Addition of thymidine allows complete DNA duplication and cells proceed to the next phase of the cell cycle (Fig.3B).

Synchronization resulted in several notable effects. First, the amount of chromosomes with uniform shape (types B, C, and D on Fig. 2A) increased (Fig. 3C). Specifically, the number of long chromosomes with closed-arms increased from 30% to 87%; in contrast, the amount of unscorable or unpaired chromosomes decreased from 8% to only 1% (Fig. 3D). Second, even the proportion of mitotic cells in synchronized cultures was 1.26 times lower (Fig. 3E), and average length of

chromosomes after synchronization was about 2 times longer (7.1 μ m) than before (3.6 μ m) (based on length of largest human chromosome 1 (249.8Mbp, centromere position: metacentric; data not shown). An example of chromosomal distribution shown on Fig. 4.

To answer the main question as to whether or not synchronization is necessary and can improve dicentric analysis in the RABiT-II system, currently we evaluated both protocols (asynchronized and synchronized) by comparison of frequencies of dicentrics in irradiated samples and reproducibility of dose-response curves.

References:

1. Zeegers, D. et al. Biomarkers of Ionizing Radiation Exposure: A Multiparametric Approach. *Genome Integr.* 8, 6 (2017).
2. Garty, G. et al. The decade of the RABiT (2005-15). *Radiat. Prot. Dosimetry* 172, 201–206 (2016).
3. Repin, M., Pampou, S., Karan, C., Brenner, D. J. & Garty, G. RABiT-II: Implementation of a High-Throughput Micronucleus Biodosimetry Assay on Commercial Biotech Robotic Systems. *Radiat. Res.* 187, 492–498 (2017).
4. Ricoul, M., et al.. in 189–208 (2017). doi:10.1007/978-1-4939-6703-2_17
5. Kaddour, A. et al. Transmission of Induced Chromosomal Aberrations through Successive Mitotic Divisions in Human Lymphocytes after In Vitro and In Vivo Radiation. *Sci. Rep.* 7, 3291 (2017).
6. Genet, M. D., et al. Direct DNA and PNA probe binding to telomeric regions without classical in situ hybridization. *Mol. Cytogenet.* 6, 42 (2013).
7. Garty, G. et al. An automated imaging system for radiation biodosimetry. *Microsc. Res. Tech.* 78, 587–98 (2015).
8. Nakajima, M. et al. The complete removal of cohesin from chromosome arms depends on separase. *J. Cell Sci.* 120, 4188–96 (2007).
9. Haarhuis, J. H. I., Elbatsh, A. M. O. & Rowland, B. D. Cohesin and Its Regulation: On the Logic of X-Shaped Chromosomes. *Dev. Cell* 31, 7–18 (2014).
10. Vignon, C. et al. Flow Cytometric Quantification of All Phases of the Cell Cycle and Apoptosis in a Two-Color Fluorescence Plot. *PLoS One* 8, e68425 (2013).
11. Rieder, C. L. & Palazzo, R. E. Colcemid and the mitotic cycle. *J. Cell Sci.* 102 (Pt 3, 387–92 (1992).
12. Bangs, C. D. & Donlon, T. A. in *Current Protocols in Human Genetics* (John Wiley & Sons, Inc., 2005). doi:10.1002/0471142905.hg0401s45
13. Pujol, M. et al. A New Model of Biodosimetry to Integrate Low and High Doses. *PLoS One* 9, e114137 (2014). ■

Assessment of Mouse Pulmonary Function through Whole-body Plethysmography for the Study of Radiation-induced Late Pulmonary Injury

Sanjay Mukherjee, Lubomir Smilenov, Evangelia C. Laiakis^a, Albert J. Fornace^a, and Sally A. Amundson

Radiation induced pulmonary injury is one of the dose-limiting factors in patients undergoing radiotherapy [1]. Lung being a late radiosensitive tissue, it also presents itself as a major concern in the aftermath of an intentional or accidental nuclear event [2,3]. To investigate further and to aid in the development of potential non-invasive methods for detecting radiation induced late lung injury, we studied pulmonary functions in irradiated mice using whole body plethysmography [4,5]-

There are reports of variation in individual sensitivity to radiation induced lung injury in laboratory animals [6]. For this study, we used C57L/J mice, which have sensitivity and progression similar to humans to develop pulmonary pneumonitis post radiation exposure [6,7]. The animals were exposed to whole thorax irradiation (WTI) to the published LD_{50/180} dose of 11.35 Gy of X-rays. A group of sham-irradiated C57L/J mice were used as controls. The mice were monitored for 5 months post irradiation, and their breathing rate and pulmonary functions were assessed using a total-body plethysmograph (Emka Technologies, Falls Church, VA) (Figure 1).

The plethysmograph consists of a commercial differential air pressure sensor (dps) to monitor air pressure changes in the animal chamber in comparison with a calibrated (atmospheric pressure) reference chamber (Figure 1A-C). The signal from the sensor is then sent to an amplifier, filtered further, analyzed and recorded using IOX2 software (Emka Technologies) (Figure 1D). The system gives precise information about volume and breathing rate based pulmonary functions from a freely-moving live animal inside the chamber (Figure 1).

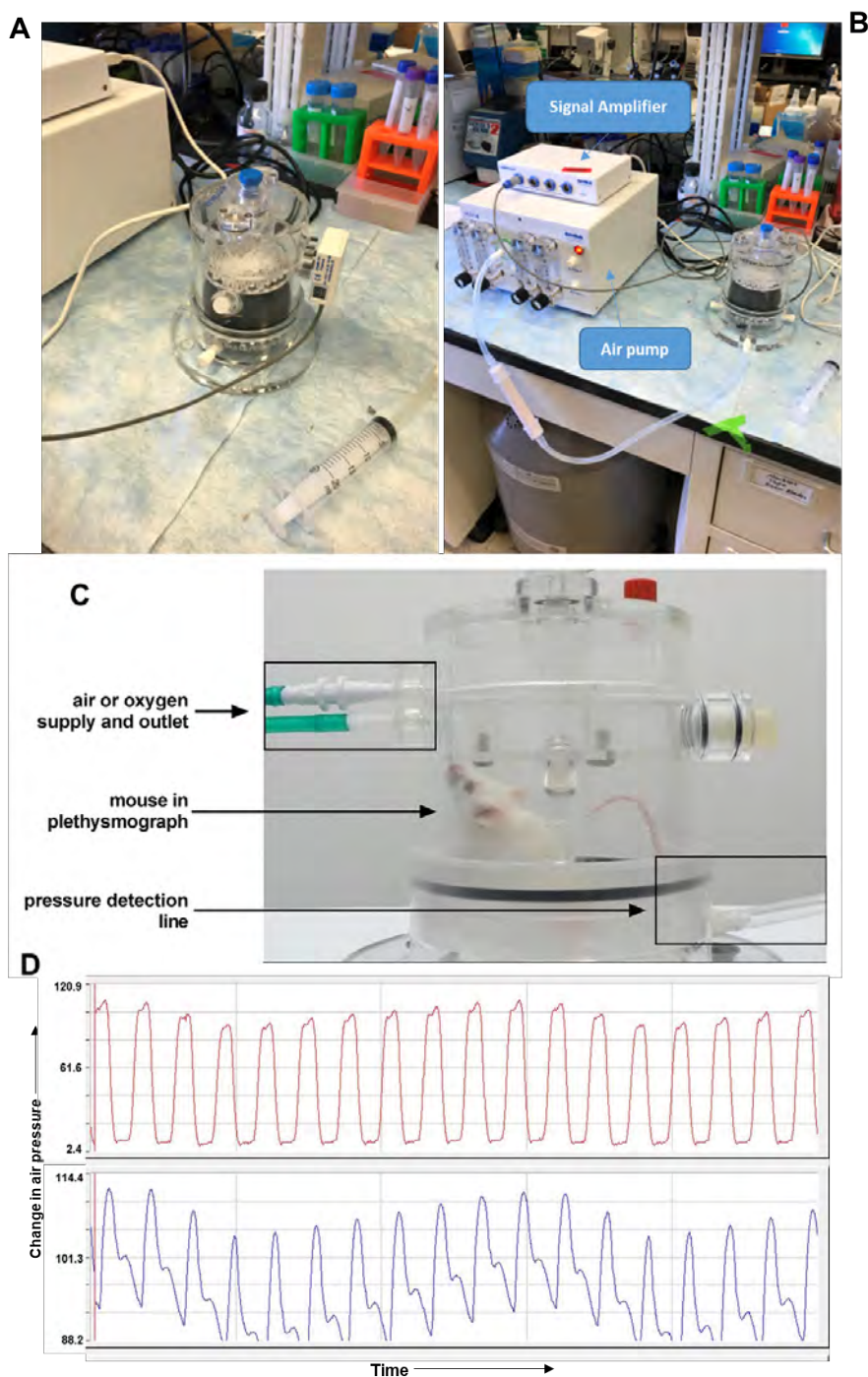


Figure 1. Emka whole-body Plethysmograph. A. The Plethysmographic chamber B. The pump (VENT4) to main air supply at a rate of 0.5mL/s C. Different components of Plethysmograph D. A typical output from plethysmograph.

^aDepartment of Biochemistry and Molecular & Cell Biology, Georgetown University, Washington DC

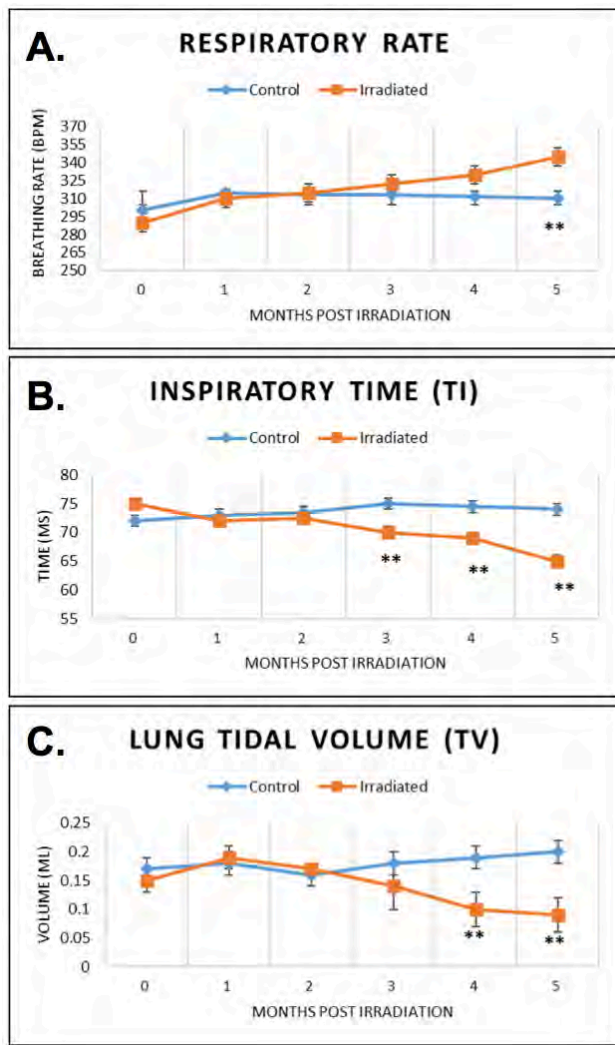


Figure 2. Analysis of different Lung functions in control and irradiated C57L/J mice. A. Respiratory rate (breaths per minute) B. Inspiratory time (Ti) C. Tidal Volume (TV). Blue line indicates Controls; Orange line indicates irradiated mice data. Statistical significance $**P<0.001$.

We collected different breathing rate-based lung parameters from the control (n=5) and irradiated (n=12) mice for the course of 5 months post irradiation (Figure 2). We observed increased breathing rates in irradiated animals beginning 3 months after radiation exposure compared to controls, where the breathing rate remained steady (Figure 2A). At the same time, we also observed decreases in inspiratory time (Ti) and Lung Tidal volume (TV) in irradiated mice compared to controls (Figure 2B and C). Inspiratory time (Ti) is the amount of time the animal takes to breathe in air. The observed decreases in Ti clearly indicate that irradiated animals were having breathing difficulty. Tidal volume (TV) provides information about the amount of air in the lung with every breath. A decrease in this parameter is an indication of lung damage in irradiated mice. The decrease in Ti and

TV values corresponded with the increase in respiratory rate in irradiated animals, which started developing after 3 months post irradiation compared to controls. This method is also better than the closed chamber methods used previously for quiet breathing rate measurements in irradiated mice, where we have found closed chambers to increase the chances of carbon-dioxide (CO₂) accumulation [5].

The plethysmographic measurements can be correlated with lung damage visualized through microCT or in terminal pathology, and can then be used to guide long-term biomarker studies where microCT is not possible and biopsies are not available. In future long-term studies, we will use plethysmographic measurements to guide the time for biofluid collection for development of gene expression or metabolomic biomarkers of injury and disease progression.

References

- Williams JP, Johnston CJ, Finkelstein JN (2010) Treatment for Radiation-Induced Pulmonary Late Effects: Spoiled for Choice or Looking in the Wrong Direction? *Curr Drug Targets*. 11(11): 1386–1394.
- Yu C, Ye G (2005) Multi-organ failure in a radiation accident: The Chinese experience of 1990. *Br. J. Radiol. Supplement_27*, 47–54.
- Uozaki, H., Fukayama, M., Nakagawa, K., Ishikawa, T., Misawa, S., Doi, M., and Maekawa, K. (2005). The pathology of multi-organ involvement: two autopsy cases from the Tokai-mura criticality accident. *Br. J. Radiol. Supplement_27*, 13–16.
- Travis EL, Vojnovic B, Davies EE, Hirst DG (1974) A plethysmographic method for measuring function in locally irradiated mouse lung. *The British Journal of Radiology* 52:67-74.
- Lockhart SP, Hill D, King S, Down JD (1991) A semi-automated method for breathing rate measurement in the mouse. *Radiotherapy and oncology: Journal of the European Society for Therapeutic Radiology and Oncology*. 22:68-70.
- Jackson IL, Vujaskovic Z, Down JD (2010) Revisiting strain-related differences in radiation sensitivity of the mouse lung: recognizing and avoiding the confounding effects of pleural effusions. *Radiation research* 173:10-20.
- Jackson IL, Xu P, Nguyen G, Down JD, Johnson CS, Katz BP, Hadley CC, Vujaskovic Z (2014) Characterization of the dose response relationship for lung injury following acute radiation exposure in three well-established murine strains: Developing an interspecies bridge to link animal models with human lung. *Health Phys*. 106(1):48-55. ■

Comparison of Radiation Biodosimetry Studies Based on Microarray Analyses from the Transcriptomics Group of the Columbia CMCR

Shad R. Morton, Shanaz A. Gandhi, and Sally A. Amundson

With the proliferation of nuclear weaponry and concerns for nuclear terrorism, there is a growing need for methods that can detect exposure levels in individuals within a large population, for proper triage and medical management after a radiological event. Efforts to develop tools and optimize protocols towards this goal come under the field of Radiation Biodosimetry, which has been rapidly advancing, proceeding from classical measurements of chromosome and nuclear damage to the building of molecular tools and methods of assessing radiation exposure. Gene expression in readily available biofluids is a potential source of information to assess exposure levels and predict injury. Gene expression profiles are currently investigated mostly in animal models and human *ex vivo* studies. Our group has contributed to the knowledge base of gene expression after radiation exposure, focusing on blood as the source of biological material. In this summary, we present an overview of the data available from studies from our

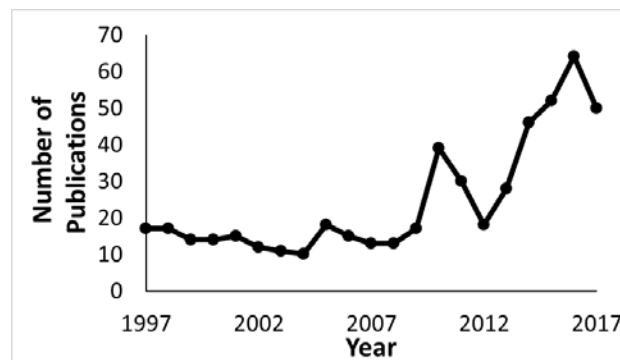


Figure 1. Result of a PubMed search (<https://www.ncbi.nlm.nih.gov/pubmed>) for keywords "Radiation Biodosimetry".

Table 1. Summary of studies across three species (GSE: Gene Expression Omnibus Series accession number; Hs: *Homo sapiens*, Mm: *Mus musculus*, Rh: *Macaca mulatta*).

Study[ref]	GSE	Species	In vivo v ex vivo	Radiation type	Dose rate (Gy/min)	Dose(Gy)	Time Point (hr/Day)
Paul et al (2008)[2]	8917	Hs	Ex vivo	Gamma	0.82	0.5, 2, 5 & 8	6 & 24 hr
Templin et al (2010)[3]	23393	Hs	In vivo	X-ray	0.1	1.25	4 hr
Paul et al (2011)[4]	32515	Hs	Ex vivo	Gamma	0.82	0.1, 0.5 & 2	6 hr
Paul et al (2011)[5]	20162	Hs	In vivo	X-ray	0.1	1.25 & 3.75	4 or 20-24 hr
Paul et al (2013)[6]	44201	Hs	Ex vivo	Gamma	0.82	0.5, 2, 5 & 8	48 hr
Paul et al (2014)[7]	52690	Mm	In vivo	Internal emitter (¹³⁷ Cs)	0.67, 0.52, 0.5, 0.25 & 0.03 (Gy/min)	8.0 MBq ¹³⁷ CsCl	2, 3, 5, 20 & 30 Day
Gandhi et al (2015)[8]	65292	Hs	Ex vivo	X-ray	1.03, 0.0031	0.5, 2 & 4	24 hr
Gandhi et al (2015)[9]	64775	Mm	In vivo	Internal emitter (⁹⁰ Sr)	0.3, 0.2, 0.17, 0.15 & 0.1 Gy/day	200 kBq ^{85/90} SrCl ₂	4, 7, 9, 25 & 30 Day
Paul et al (2015)[10]	62623	Mm	In vivo	X-ray	1.03 & 0.00309	2.2 & 4.4	24 hr
Broustas et al (2017)[11]	85323	Mm	In vivo	X-ray & Neutron	1.23, 0.026 & 0.007	0.25, 1 & 4	1 & 7 Day
Park et al (2017)[12]	102971	Hs & Rh	Ex vivo	Gamma	0.8	2, 6 & 7	24 hr
Broustas et al (2017)[13]	90909	Hs	Ex vivo	X-ray & Neutron	1.23 & 0.025	0.1, 0.3, 0.5, 1, 2 & 4	24 hr
Gandhi et al (2018)[14]	84898	Rh	In vivo	X-ray	6	10	2, 5 & 30 Day
Rudqvist et al (2018)[15]	99176	Mm	In vivo	Gamma	1.45	3, 4 & 8	24 hr

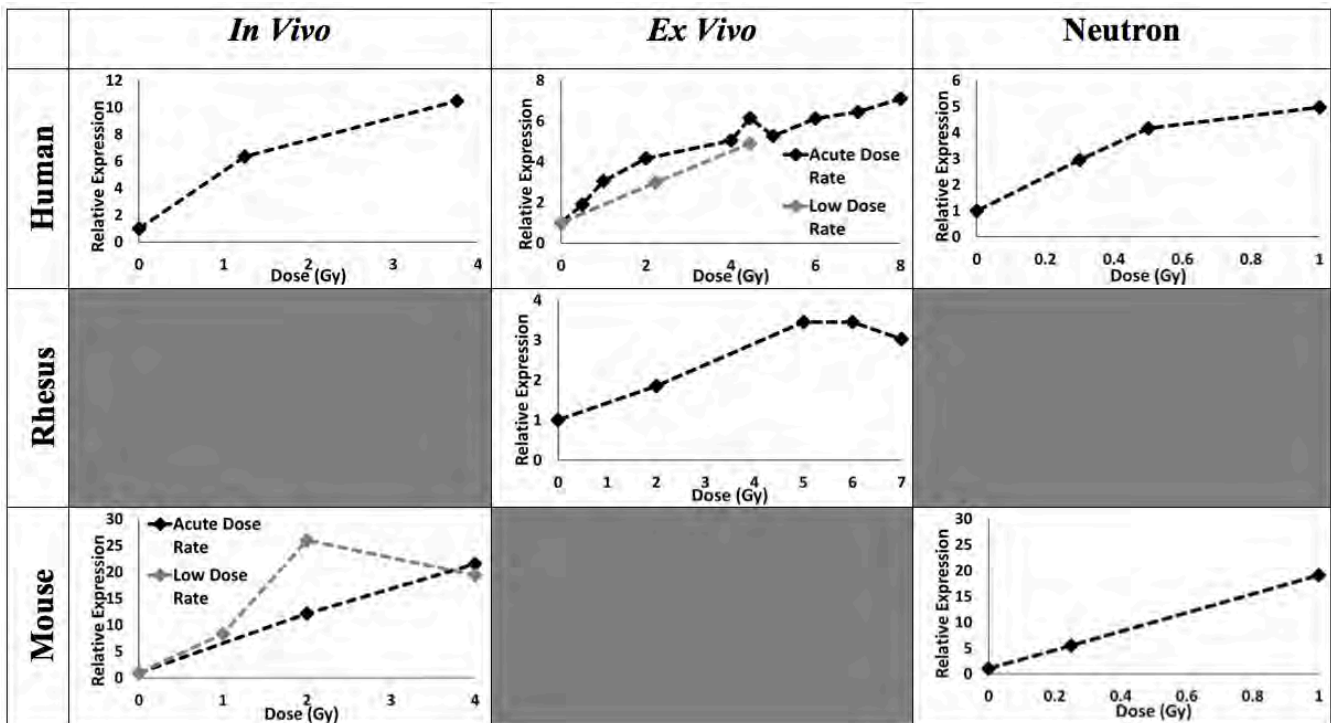


Figure 2. Tracking CDKN1A mRNA changes across all doses at 24 hr. Graphs have been optimized, and the scale varies for relative expression and dose. Relative expression was not significant for Rhesus in vivo and Mouse in vivo.

group and a sampling of common radiation target genes across species, doses, times and dose-rates.

With new publications rapidly emerging in the field of Radiation Biodosimetry since 2001, Figure 1 [1] the process of compiling and cross-referencing the data within will be beneficial for a deeper understanding of responses across species, doses and times after irradiation. In this article it is our goal to create a database comprised of results from studies on gene expression for radiation biodosimetry conducted by the Transcriptomics group of the Columbia CMCR (Center for Medical Countermeasures against Radiation) at the Center for Radiological Research.

Table 1 summarizes the studies that have been published from our group in chronological order. All study results were from gene expression analyses using BRB ArrayTools software and a standard workflow for identifying differentially expressed genes and predictions of class (with the exception of Park et al (2017)).

As our projects have expanded to include the NHP model, we discovered a need to have all data across the three species easily accessible. To address this, we compiled a spreadsheet database of genes (linked to the corresponding raw data and BRB-ArrayTools projects) that were identified as differentially expressed using a low false discovery rate cut-off. Each gene identified in a study as significantly changed after irradiation and its corresponding fold change and p-value at a specified time and dose are included in this database. Operators can search the database and cross-reference between studies (different species, radiation type, exposure modality, dose and time, dose-rate) to get an overview of the response of

the genes. We show here the results of one such common radiation target, CDKN1A, also called p21/CIP1/WAF1, Figure 2. Using the database, we cross-referenced CDKN1A mRNA level changes across all studies to obtain an overview of the response at different doses at 24 hours, shown in Figure 2.

Below, in Figure 3, we graphed CDKN1A relative expression side-by-side across species/studies, and we show that the response of this gene is higher in in vivo studies when compared to ex vivo, and that the radiation response of mouse Cdkn1a is higher compared with primates (both human and NHP (Non-Human Primates)).

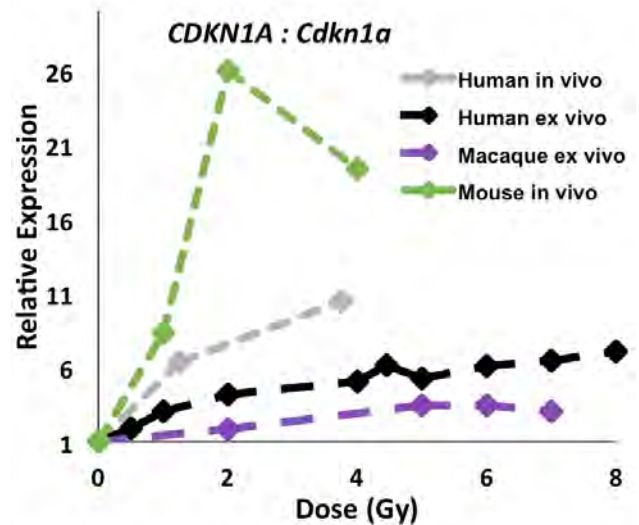


Figure 3. CDKN1A (Cdkn1a in mouse) mRNA changes in blood cells across a range of doses, in human, NHP and mouse at 24 hours.

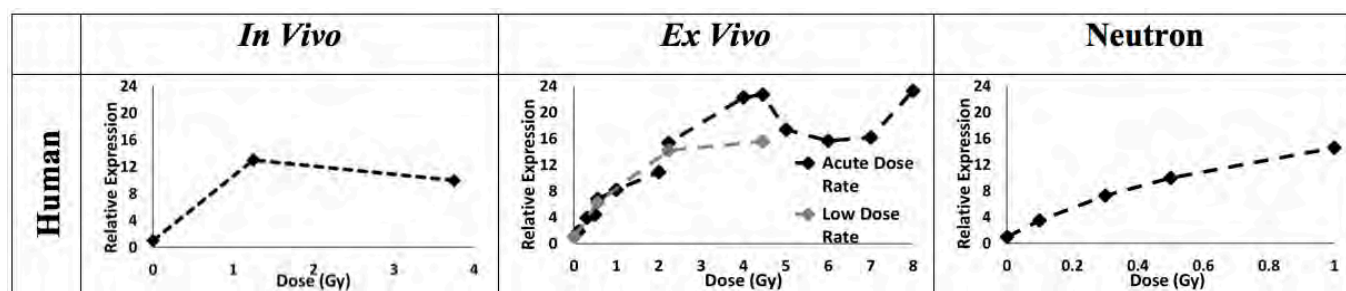


Figure 4. Tracking FDXR expression across varying doses at 24 hr.

This may reflect a difference in p53 response and potentially DNA double strand break repair signaling between mouse and human/rhesus after radiation exposure.

Another gene of interest as a radiation biomarker is *FDXR* (ferredoxin reductase) which is regulated by p53 [16], and which shows significant induction in humans, shown below in Figure 4. Mouse and NHPs did not show significant change in this gene in our microarray results.

As our studies extend to more complicated scenarios, including internal v external irradiation, combined neutron-x ray exposures and different dose rates, more data will be collected and this database will expand. It will be possible to identify and compare known and novel genes at-a-glance using data retrieval methods and macros that may have potential as markers for radiation exposure. The data listed here is not exhaustive and is a subset of the manifold studies on radiation dosimetry available for compilation; however, this is the first step for our group towards providing an overview of radiation responses across species, doses and dose-rates.

References

- [1] NCBI Resource Coordinators, "Database Resources of the National Center for Biotechnology Information," *Nucleic Acids Res.*, vol. 45, no. D1, pp. D12–D17, Jan. 2017.
- [2] S. Paul and S. A. Amundson, "Development of gene expression signatures for practical radiation biodosimetry," *Int. J. Radiat. Oncol. Biol. Phys.*, vol. 71, no. 4, pp. 1236–1244, Jul. 2008.
- [3] T. Templin et al., "Radiation-induced micro-RNA expression changes in peripheral blood cells of radiotherapy patients," *Int. J. Radiat. Oncol. Biol. Phys.*, vol. 80, no. 2, pp. 549–557, Jun. 2011.
- [4] S. Paul and S. A. Amundson, "Gene expression signatures of radiation exposure in peripheral white blood cells of smokers and non-smokers," *Int. J. Radiat. Biol.*, vol. 87, no. 8, pp. 791–801, Aug. 2011.
- [5] S. Paul, C. A. Barker, H. C. Turner, A. McLane, S. L. Wolden, and S. A. Amundson, "Prediction of in vivo radiation dose status in radiotherapy patients using ex vivo and in vivo gene expression signatures," *Radiat. Res.*, vol. 175, no. 3, pp. 257–265, Mar. 2011.
- [6] S. Paul, L. B. Smilenov, and S. A. Amundson, "Widespread decreased expression of immune function genes in human peripheral blood following radiation exposure," *Radiat. Res.*, vol. 180, no. 6, pp. 575–583, Dec. 2013.
- [7] S. Paul et al., "Gene expression response of mice after a single dose of ¹³⁷CS as an internal emitter," *Radiat. Res.*, vol. 182, no. 4, pp. 380–389, Oct. 2014.
- [8] S. A. Gandhi, L. B. Smilenov, C. D. Elliston, M. Chowdhury, and S. A. Amundson, "Radiation dose-rate effects on gene expression for human biodosimetry," *BMC Med. Genomics*, vol. 8, p. 22, May 2015.
- [9] S. A. Gandhi et al., "Effect of ⁹⁰Sr internal emitter on gene expression in mouse blood," *BMC Genomics*, vol. 16, p. 586, Aug. 2015.
- [10] S. Paul, L. B. Smilenov, C. D. Elliston, and S. A. Amundson, "Radiation Dose-Rate Effects on Gene Expression in a Mouse Biodosimetry Model," *Radiat. Res.*, vol. 184, no. 1, pp. 24–32, Jul. 2015.
- [11] C. G. Broustas, Y. Xu, A. D. Harken, G. Garty, and S. A. Amundson, "Comparison of gene expression response to neutron and x-ray irradiation using mouse blood," *BMC Genomics*, vol. 18, no. 1, p. 2, 03 2017.
- [12] J. G. Park et al., "Developing Human Radiation Biodosimetry Models: Testing Cross-Species Conversion Approaches Using an Ex Vivo Model System," *Radiat. Res.*, vol. 187, no. 6, pp. 708–721, 2017.
- [13] C. G. Broustas, Y. Xu, A. D. Harken, M. Chowdhury, G. Garty, and S. A. Amundson, "Impact of Neutron Exposure on Global Gene Expression in a Human Peripheral Blood Model," *Radiat. Res.*, vol. 187, no. 4, pp. 433–440, 2017.
- [14] S. A. Gandhi et al., "Whole thorax irradiation of non-human primates induces persistent nuclear damage and gene expression changes in peripheral

blood cells,” PloS One, vol. 13, no. 1, p. e0191402, 2018.

Deficiency after Gamma Irradiation,” Radiat. Res., Jan. 2018.

[15] N. Rudqvist et al., “Global Gene Expression Response in Mouse Models of DNA Repair

[16] G. O’Brien et al., “FDXR is a biomarker of radiation exposure in vivo,” Sci. Rep., vol. 8, no. 1, p. 684, Jan. 2018. ■

Identification of Differentially Expressed Genes and Pathways in Mice Exposed to Mixed Field Neutron/X-ray Radiation

Constantinos G. Broustas, Andrew D. Harken, Guy Garty, and Sally A. Amundson

Radiation exposure due to the detonation of an improvised nuclear device (IND) poses a growing threat to human health. In such a scenario, large populations will be exposed to various doses of radiation with a number of fatalities occurring immediately after the incident, while a large number of individuals will experience long-term effects such as higher incidence of cancer, infections and other diseases. On the other hand, many people near the affected area will receive radiation that poses no immediate health risk. The goal of radiation biodosimetry is to quickly and accurately evaluate radiation dose as a means to assess radiological injury. Unbiased transcriptomic profiling can serve as a sensitive and accurate assay identify genes that can be used to assess individual exposure to radiation, and we and others have conducted DNA microarray analyses using peripheral blood cells. Global gene expression signatures have been derived from human or mouse blood exposed mainly to photons (x-rays, γ -rays). These studies have identified gene expression changes with radiation dose, time, and dose rate [2-4]. Although radiation quality is expected to play an important role in driving gene expression, and different signaling pathways may be triggered in response to the different types of irradiation, a limited number of radiation quality studies have been performed, focusing

Table 1. Significantly differentially expressed genes in mouse blood after x-ray, neutron, or mixed field neutron/x-ray treatment relative to unirradiated controls ($p < 0.001$).

neutron	up	down	total	%up	%down
0%	1373	2477	3850	35.7	64.3
5%	829	2959	3788	21.9	78.1
15%	1417	3284	4701	30.1	69.9
25%	1052	1807	2859	36.8	63.2
83%	1390	4317	5707	24.4	75.6

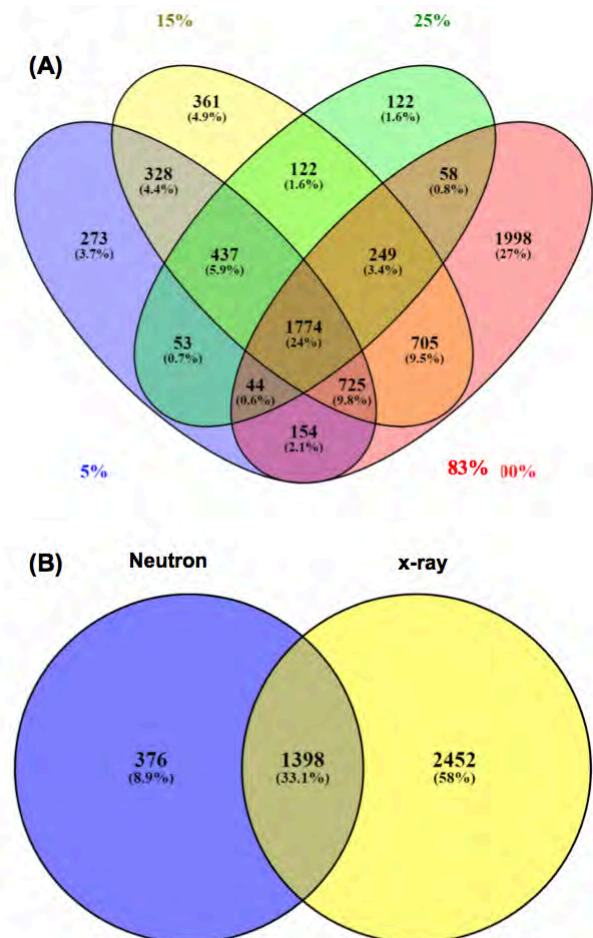


Figure 1. Differentially expressed genes in neutron exposures. (A) overlapping patterns of genes differentially expressed in response to 0.75 Gy neutron (83%), or 3 Gy mixed-field neutron/x-ray (indicated by neutron percent). (B) Differentially expressed genes in x-ray versus neutron or neutron/x-ray exposures.

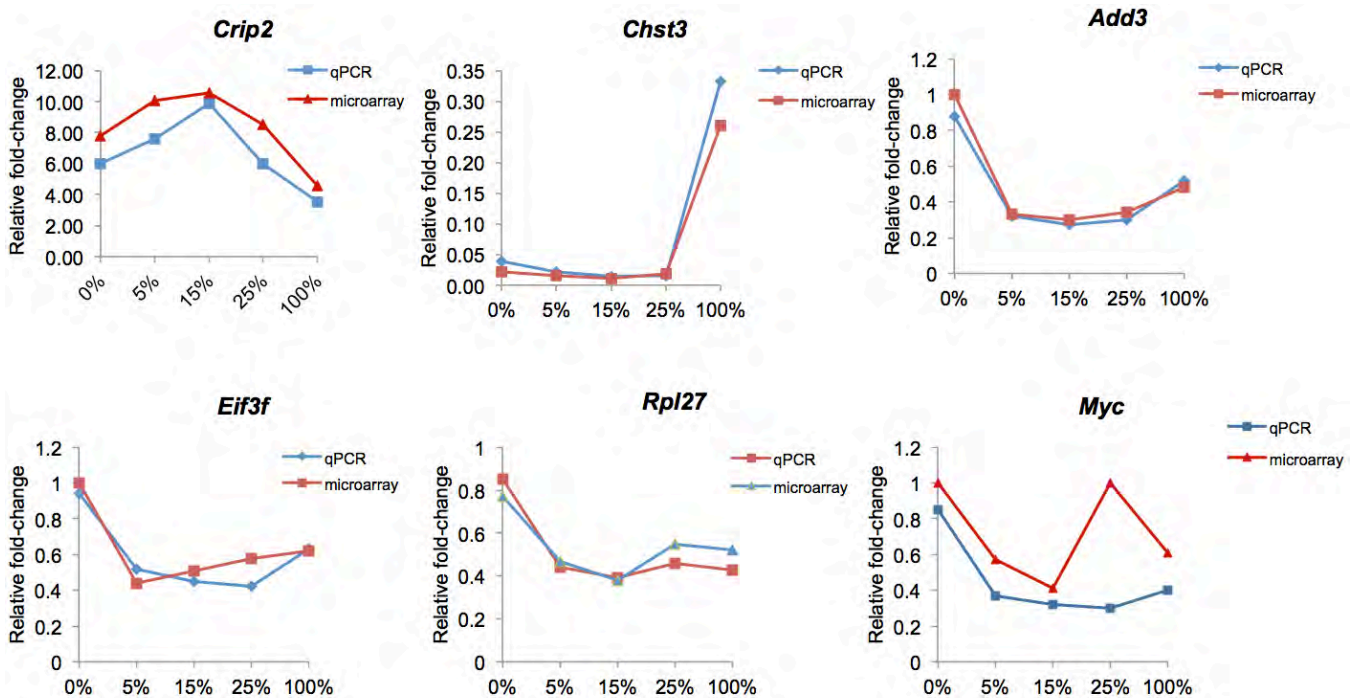


Figure 2. Expression of six genes (*Crip2*, *Chst3*, *Add3*, *Eif3f*, *Rpl27*, and *c-Myc*), shown by microarray analysis to be differentially expressed, was analyzed by quantitative RT-PCR and compared with DNA microarray data. Relative gene expression was normalized against *Actb* expression.

primarily on heavy ions or α -particles, which may be relevant in a radiological dispersal device [5, 6].

The detonation of an IND could expose individuals to a mixture of photon and neutron irradiation. Although most of the radiation dose will come from photons, a small part of it will be due to neutrons. However, neutron’s potential to cause radiological injury will be disproportionately large, since neutrons have high relative biological effectiveness (RBE), as they are able to generate DNA damage that is irreparable or difficult to repair [1]. We previously compared the gene expression signatures in blood of mice exposed separately to either x-rays or neutrons and analyzed 1 and 7 days post-irradiation [7]. Our analysis showed differential gene expression effects of neutrons versus photons. Gene ontology analysis revealed that genes involved in nucleic acid metabolism processes were downregulated in neutron-irradiated mice, whereas genes involved in lipid metabolism were upregulated in x-ray irradiated animals.

In the present study, we analyzed transcriptomic changes over a range of mixed neutron/photon radiation doses with the neutron component contributing 5%, 15%, or 25% of the total dose of 3 Gy.

Results

Mice were either sham-irradiated or exposed to 3 Gy of mixed x-ray/neutron radiation that contained 5%, 15%, or 25% of a neutron component. For comparison, mice were also exposed to 3 Gy x-rays or 0.75 Gy of neutrons. The neutron-only exposure contains a small percentage (~17%) of photons, as well, and represented the

maximum neutron dose used in the combined exposures. All animals remained in apparent good health, with no adverse events noted during the course of the study.

Global gene expression was measured in the blood of mice sacrificed 7 days post-irradiation using Agilent Whole Mouse Genome Microarrays. Class comparison using BRB-ArrayTools identified a total of 3850, 3788, 4701, 2859, and 5707 genes differentially expressed ($p < 0.001$, false discovery rate (FDR) $< 5\%$) between unirradiated controls and x-ray, 5%, 15%, and 25% mixed field x-ray/neutron, and 83% neutron exposed samples, respectively (Table 1). Among all the exposures that contained a neutron component, 1774 significantly differentially expressed genes were identified (Figure 1A). Of these, 376 (or 8.9%) genes were uniquely differentially expressed only following exposures including in neutron, but not after x-rays alone (Figure 1B). The overall number of genes for the 25% neutron/x-ray exposure was significantly lower than other percentages, reflecting mainly the lower number of downregulated genes. Finally, a dose-response effect of the neutron component was not evident among the differentially exposed genes in the neutron exposures.

We confirmed the expression pattern of some of the differentially expressed genes derived from the DNA microarray experiment, by quantitative real-time PCR (Figure 2). Analysis of gene expression of *Crip2*, *Chst3*, *Add3*, *Eif3f*, *Rpl27*, and *c-Myc* by qRT-PCR confirmed that these genes are regulated by radiation. *Crip2* and *Chst3* genes were upregulated in all radiation modalities, while *Add3*, *Eif3f*, *Rpl27*, and *Myc* were downregulated in

the neutron exposures. The fold-change for these genes in response to radiation was in good agreement with the fold-change calculated by the microarray experiment (Figure 2).

Conclusions

Our experiments identified 376 genes that significantly change expression in the blood of mice after exposure to radiation that contains a neutron component, and suggest that they could potentially be used to detect the neutron component in a mixed field radiation exposure, such that would be generated by an IND detonation.

References

1. Hall EJ, Giaccia AJ. Radiobiology for the radiologist. 7th ed. Philadelphia: Wolters Kluwer Health/Lippincott Williams & Wilkins; 2012.
2. Paul S, Amundson SA. Development of gene expression signatures for practical radiation biodosimetry. Int J Radiat Oncol Biol Phys. 2008;71(4):1236-1244.

3. Paul S, Smilenov LB, Elliston CD, Amundson SA. Radiation Dose-Rate Effects on Gene Expression in a Mouse Biodosimetry Model. Radiat Res. 2015;184(1):24-32.
4. Ghandhi SA, Smilenov LB, Elliston CD, Chowdhury M, Amundson SA. Radiation dose-rate effects on gene expression for human biodosimetry. BMC Med Genomics. 2015;8:22.
5. Chauhan V, Howland M, Wilkins R. Identification of gene-based responses in human blood cells exposed to alpha particle radiation. BMC Med Genomics. 2014;7:43.
6. Riquier H, Wera AC, Heuskin AC, Feron O, Lucas S, Michiels C. Comparison of X-ray and alpha particle effects on a human cancer and endothelial cells: survival curves and gene expression profiles. Radiother Oncol. 2013;106(3):397-403.
7. Broustas CG, Xu Y, Harken AD, Garty G, Amundson SA. Comparison of gene expression response to neutron and x-ray irradiation using mouse blood. BMC Genomics. 2017;18(1):2. ■



l to r: Manuela Buonanno, Younghyun Lee, Steve Marino, Guy Garty, Shanaz Ghandhi, Tom Hei, Helen Turner, Monica Pujol, Sanjay Mukherjee, and Veljko Grilj at the 2017 RRS meeting.



David Brenner at the TED2017 Conference in Vancouver, BC



Participants at the 2017 Radiation Oncology retreat.



David Brenner and Charles Geard cutting the cake at the CRR celebration of the RARAF 50th Anniversary

The Influence of Inflammation on Transcriptomic Signatures of Radiation Exposure: Mouse Model of Inflammatory Bowel Syndrome

Sanjay Mukherjee, Evangelia C. Laiakis^a, Albert J. Fornace^a, and Sally A. Amundson

Approximately 5-7% of the human population has underlying inflammatory diseases, and with modern life styles these conditions are on the rise worldwide [1, 2]. Ionizing Radiation (IR) is a known pro-inflammatory agent [3, 4] and in the process of development of

biomarkers for radiation biodosimetry chronic inflammatory conditions need to be considered as a potential confounding factor. An individual with an underlying inflammatory condition could show heightened immune responses to radiation exposure,

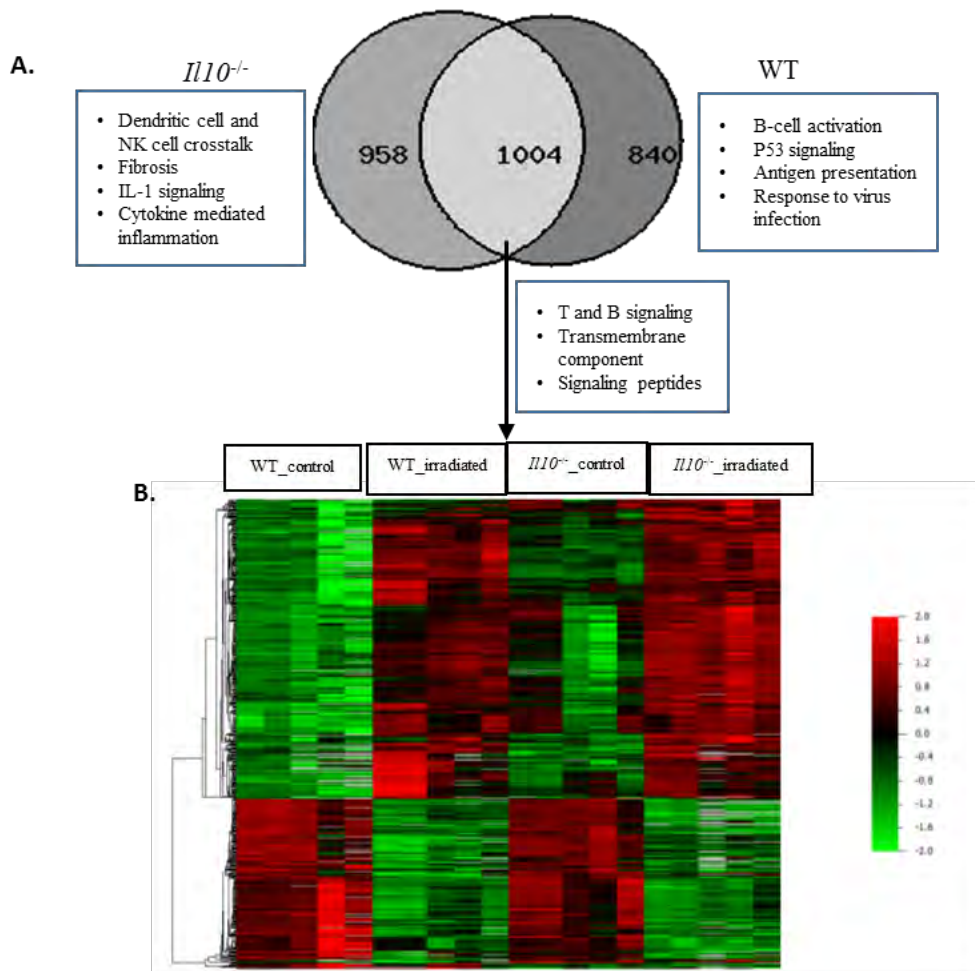


Figure 1. Differentially expressed genes in WT and *Il10^{-/-}* mice. **A.** Venn diagram showing overlap of differentially expressed genes between the two genotypes. Significantly enriched biological processes (Benjamini corrected P -value < 0.05) associated with differentially expressed genes after radiation exposure specific to a particular genotype as well as common between them are shown in blue boxes. **B.** Heat map illustrating expression levels of the 1,005 genes responding in both WT and *Il10^{-/-}* mice. Red indicates high expression, green indicates low expression as shown in the color key. Each row represents one gene and each column represents an individual mouse, ordered by radiation exposure and genotype as labeled.

^aDepartment of Biochemistry and Molecular & Cell Biology, Georgetown University, Washington DC

possibly resulting in false positive tests for IR exposure or altered dose detection. Hence, it is important to develop radiation biodosimetry that can distinguish between IR-induced proinflammatory responses and pre-existing disease.

In this study, we addressed this issue using a genetically engineered mouse model of human inflammatory bowel disease ($Il10^{-/-}$), and compared its transcriptomic responses to radiation with those of normal wild-type (WT) mice. IL10 is an anti-inflammatory cytokine. In the absence of this cytokine, the $Il10^{-/-}$ mice become susceptible to enteric bacterial pathogens, and show a heightened inflammatory response to infection [5].

Wild-type and $Il10^{-/-}$ mice were exposed to whole body irradiation of 7 Gy x-rays (LD_{50/30} for $Il10^{-/-}$). Twenty-four hours after exposure, the mice were sacrificed, and blood was collected through cardiac puncture. The blood was stabilized in PAXgene Blood RNA stabilization and lysis solution. Total cellular RNA was isolated from blood using the PAXgene RNA kit (Qiagen). The RNA was globin cleared and used further for Cy3 labeling, using the Low Input QuickAmp labeling kit (Agilent Genomics). The labeled RNA from control and irradiated samples were hybridized onto Agilent Whole Mouse Genome Microarrays (4x44K v2). The scanned data from microarrays was filtered and normalized using BRB-ArrayTools, and used further for the identification of radiation responsive differentially expressed genes (statistical significance using F-test at $P < 0.001$, False Discovery Rate (FDR) $< 10\%$).

Analysis resulted in identification of 1,962 and 1,844 genes differentially expressed ($p < 0.001$, FDR $< 10\%$) after radiation exposure in $Il10^{-/-}$ and WT mice respectively (Figure 1A). Venn diagram analysis revealed 1,004 radiation responsive genes (35%) in common between the two genotypes (Figure 1A). Heat map analysis of the expression levels of these 1,004 common genes showed a higher level of expression in $Il10^{-/-}$ mice compared to WT mice after radiation exposure (Figure 1B). Functional gene ontology (GO) analysis using DAVID (<http://david.abcc.ncifcrf.gov/>) [6] revealed that genes responsive to radiation exclusively in WT mice were mainly involved in B-cell activation; p53 signaling; antigen presentation and response to virus infection (top GO terms significant at Benjamini corrected $P < 0.05$), while $Il10^{-/-}$ specific differentially expressed genes were associated with Dendritic cell and NK cell crosstalk; Fibrosis; IL-1 signaling and Cytokine mediated inflammation. Analysis of the 1,005 differentially expressed genes common between the genotypes revealed many cytokine genes, which were involved in both T and B cell signaling. We further verified the expression of several candidate genes using qRT-PCR and confirmed higher radiation induced expression of inflammatory cytokines in $Il10^{-/-}$ compared to WT mice. In contrast, the relative expression of Trp53-responsive genes was found to be higher in WT mice compared to $Il10^{-/-}$ mice (Figure 2).

Overall, this study clearly signifies the importance of inflammatory immune responses as a modifying factor in radiation responses. Inflammatory pathways may impair the performance of dosimetric signatures developed using

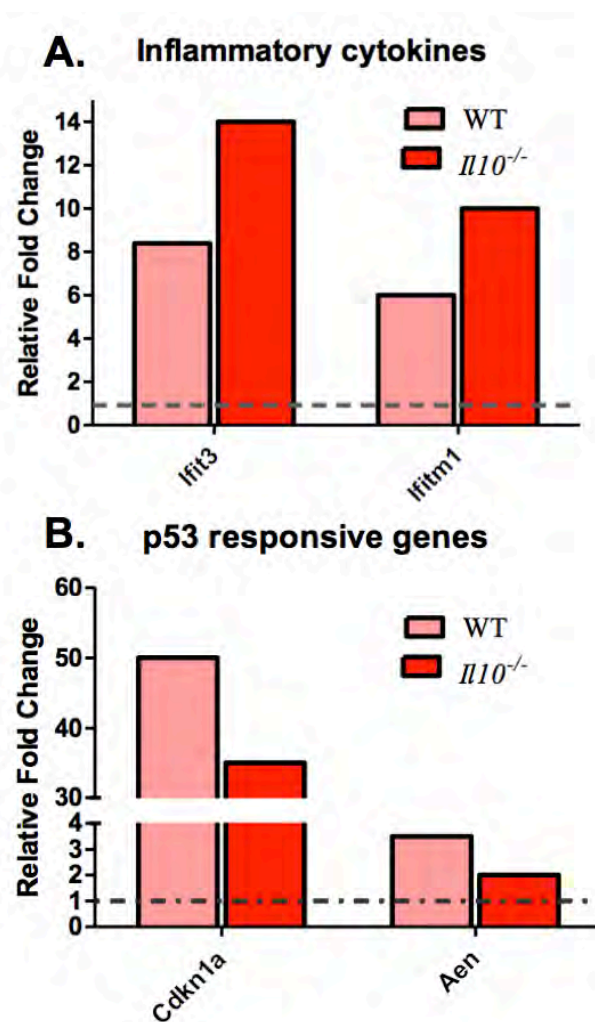


Figure 2. Gene expression measured by qRT-PCR. Expression levels of A. Inflammatory genes (*Ifit3*; *Ifitm1*) and B. *Trp53* responsive genes (*Cdkn1a*; *Aen*) that were shown by microarray analysis to be differentially regulated in $Il10^{-/-}$ mice are depicted. Data represent the mean (fold change compared to unexposed animals of respective genotype) response of 5 animals. The expression was normalized against beta-Actin gene expression.

only individuals of average sensitivity. Inclusion of sensitive subpopulations during gene selection has previously been suggested to assist in producing biosimetric classifiers that are robust to variations in DNA repair responses and radiation sensitivity [7], and such an approach may also be useful in hardening biological signatures against underlying chronic inflammation. Studies are ongoing to further understand the inflammatory component of radiation responses for better development of transcriptomics based biosimetry markers.

References

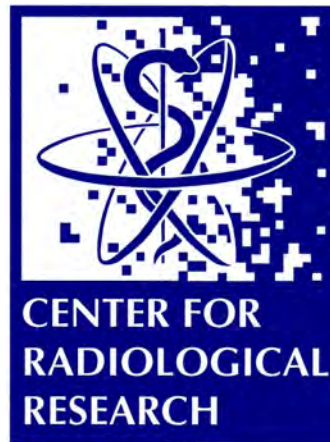
1. El-Gabalawy H, Guenther LC, and Bernstein CN (2010) Epidemiology of Immune-Mediated Inflammatory Diseases: Incidence, Prevalence,

- Natural History, and Comorbidities. *J Rheumatol* 85:2-10.
2. Okin D and Medzhitov R (2012) Evolution of Inflammatory Diseases. *Curr Biol.* 22(17): R733–R740.
 3. Lorimore SA, Coates PJ, Scobie GE, Milne G, and Wright EG (2001) Inflammatory-type responses after exposure to ionizing radiation in vivo: a mechanism for radiation-induced bystander effects? *Oncogene* 20: 7085-7095.
 4. Mukherjee D, Coates PJ, Lorimore SA, and Wright EG (2014) Responses to ionizing radiation mediated by inflammatory mechanisms. *J Pathol* 232: 289-299.
 5. Kennedy RJ, Hoper M, Deodhar K, Erwin PJ, Kirk SJ, and Gardiner KR (2000) Interleukin 10-deficient colitis: new similarities to human inflammatory bowel disease. *Br J Surg* 87: 1346-1351.
 6. Huang DW, Sherman BT, and Lempicki RA (2009) Systematic and integrative analysis of large gene lists using DAVID bioinformatics resources. *Nat Protoc.* 4(1): p. 44-57.
 7. Rudqvist N, Laiakis EC, Ghandhi SA, Kumar S, Knotts JD, Chowdhury M, Fornace AJ Jr, and Amundson SA. (2018) Global Gene Expression Response in Mouse Models of DNA Repair Deficiency after Gamma Irradiation. *Radiat Res.* 189: 337-344. ■



Top (l to r): Jay Perrier, Andrew Harken, Veljko Grilj, David Cuniberti, Constantin Broustas
 Middle (l to r): Younghyun Lee, Monica Pujol, Helen Turner, Margaret German, Annerys Rodriguez, Shanaz Ghandhi
 Bottom (l to r): David Brenner, Carl Elliston, Rob Morton, Peter Grabham, Manuela Buonanno, Malek Haj Tahar

RARAF



THE RADIOLOGICAL RESEARCH ACCELERATOR FACILITY

An NIH-Supported Resource Center

WWW.RARAF.ORG

Director: David J. Brenner, Ph.D., D.Sc.

Associate Directors: Gerhard Randers-Pehrson, Ph.D. and Guy Garty, Ph.D

Research Using RARAF

Both the Microbeam and the Track Segment Facilities continue to be utilized in various investigations of the response to radiation exposure. This year the number of biological experiments has declined somewhat, with newer technological developments on the Super Microbeam displacing machine availability for users. The track segment facility and our neutron capabilities remain in operation providing users averaged particle irradiation for population studies. We also have the new development of a “FLASH” irradiation system delivering high doses in fractions of a second.

Experiments

Listed in Table I are the experiments performed using the RARAF Singletron between January 1 and December 31, 2017 and the number of shifts each was run during this period. Half shifts are assigned when experimental

time is shared among several users (e.g., track segment experiments) or when experiments run for significantly more or less than an 8-hour shift. Use of the accelerator for experiments was 47% of the regularly scheduled time (40 hours per week). Nine different user experiments were run during this period. Three experiments were undertaken by members of the CRR, supported by grants from the National Institutes of Health (NIH), specifically the National Cancer Institute (NCI), the National Institute of Allergies and Infectious Diseases (NIAID) and the National Institute of Biomedical Imaging and Bioengineering (NIBIB). Six experiments were performed by external users, supported by grants and awards from the Department of Energy (DoE), the Department of Defense (DoD), the NIH, the National Aeronautics and Space Administration (NASA), the National Science Foundation (NSF), the National Cancer Institute (NCI), and internal funding from Cornell

Table I. Experiments Run at RARAF January 1 - December 31, 2017

Exp No.	Experimenter	Institution	Exp. Type	Title of Experiment	Shifts Run
113	Alexandra Miller	AFRRI	Biol.	Role of alpha particle radiation in depleted uranium-induced cellular effects	3.5
162	Lubomir Smilenov	CRR	Biol.	Mouse irradiation using IND spectrum neutrons	4
165	Helen Turner	CRR	Biol.	Mouse/blood irradiation using IND spectrum neutrons	2
172	Susan Bailey	Colorado State University	Biol.	Targeted telomeric damage and the persistent DNA damage response	0.5
173	Ekaterina Dadachova	Albert Einstein College of Medicine	Biol.	Comparison of fungal cell susceptibility to external alpha particle beam radiation versus alpha particles delivered by ²¹³ Bi-labeled antibody	4
174	Gordana Vunjak-Novakovic	Columbia University	Biol.	Micro proton induced x-ray emission of bone/cartilage grown on artificial scaffolds	0.5
175	Constantinos Broustas/ Sanjay Mukherjee	CRR	Biol.	Mouse/blood irradiation using IND spectrum neutrons	2
178	Alejandro Carabe-Fernandez	University of Pennsylvania	Phys.	Microdosimetric and radiobiological characterization of new Si-based microdosimeters using particle microbeams	4
179	John Ng	Cornell University	Biol.	Effect of LET on immunotoxicity	26.5
180	Francesco d'Errico	Yale University	Phys.	Neutron bubble spectrometry	5
181	Joel Greenberger	Univ. of Pittsburgh	Biol.	Mouse irradiation using IND spectrum neutrons for radiation mitigator effectiveness studies	3

University. One of these experiments was a collaboration between RARAF/CRR staff and an outside user. Brief descriptions of these experiments follow.

Dr. Alexandra Miller of the Armed Forces Radiobiological Research Institute (AFRRI) continued studies using the Track Segment Facility to evaluate depleted uranium (DU) radiation-induced carcinogenesis and other late effects employing *in vitro* models and to test safe and efficacious medical countermeasures (Exp. 113). One objective of this study has been to determine if phenylbutyrate (PB), a histone deacetylase inhibitor and epigenetic effector, can mitigate neoplastic cell transformation induced by different qualities of radiation, and if so, to identify which adverse epigenetic mechanisms are involved and potentially reversed by PB. This also would be of interest for Space missions and alpha particle exposures from accidental releases. Track segment irradiations with ^4He ions were performed on human small airway epithelial cells (SAECs) and growth rate, transformation, and genomic instability were quantified. Irradiation of SAECs overcame contact inhibition and caused an increase in transformation frequency and induction of gene amplification, i.e., genomic instability. Treatment with PB following irradiation resulted in a significant suppression of transformation frequency and gene amplification. Studies are ongoing to evaluate the impact of PB treatment on changes in DNA methylation caused by irradiation with ^4He ions.

Dr. Miller also instituted a study using her SAEC line in a comparison study of the Columbia IND-spectrum Neutron Facility (CINF) at RARAF and the reactor neutron spectrum irradiator at AFRRI. This intercomparison work is being supported by AFRRI for their systems analysis by comparison to other facilities. Results of this work will be shared with RARAF and the broader community to further understanding of the effects of differing neutron energy spectra.

Drs. Helen Turner, Constantinos Broustas, and Sanjay Mukherjee made use of CINF to study the effects of the spectrum irradiation of human blood samples and mice. This work is supported by the U19 Columbia CMCR for the development of biodosimetry tools for a radiologic event. Mice were irradiated with up to 2 Gy of neutrons and comparison mice were given up to 4 Gy of x-rays using the Westinghouse orthovoltage x-ray system. Blood samples were given up to 2 Gy of neutron spectrum dose and 4 Gy of x-rays. There were also mice given up to 1 Gy of neutrons and then a secondary dose of x-rays to simulate a mixed field. The mice were sacrificed and blood was collected and subjected to whole genome gene expression analysis. Blood samples were also scored for micronucleus and γH2AX foci to determine dose response. Some animals were also held in metabolic cages for collection of urine and feces, for metabolomics analysis.

Dr. Susan Bailey from Colorado State University works on telomere length and damage effects on the health and viability of cells. She uses the RARAF microbeam to target and irradiate telomeres in cells. The work performed this year focused on telomere degradation following targeted nuclear irradiation. The experiment was used also by the RARAF staff as a baseline imaging test for the imaging of telomeres, using labels of interest to Dr. Bailey, with the new super resolution microscope as that facility will become available early next year.

Dr. Ekaterina Dadachova at the Albert Einstein College of Medicine, working with Igor Shuryak of the CRR, has been developing radioimmunotherapy (RIT) for treatment of *Cryptococcus neoformans* infections using ^{213}Bi -labeled antibodies specific to the cryptococcal capsule. She is performing a comparison of fungal cell susceptibility to external α -particle beam radiation versus α particles delivered by the bismuth-labeled antibodies (Exp. 173). Fungi grown to stationary phase in defined minimal medium were suspended in solution. As for other experiments, the solution was formed into a thin layer with a known uniform thickness under a cover slip. The fungi were irradiated with doses of 1 to 80 Gy of 125 keV/ μm ^4He ions. Results so far indicate that: a) *C. neoformans* is more sensitive to external beam α particles than to external γ rays; b) α particles delivered by the capsule-binding antibodies may be more cytotoxic to the *C. neoformans* cells than external beam α particles. This work has expanded in the past year to include proteomic, transcriptomic and metabolomic research into the radioresistance observed in these fungi.

Dr. Gordana Vunjak-Novakovic uses our charged particle microbeam facilities for PIXE analysis of cartilage-bone interfaces looking at chemical composition of the two materials as they interface and progress through the life cycle. The change in calcium concentration in both materials through the development of arthritis is of high interest in arthritis care and prevention. This past year, the neutron microbeam line has been modified to allow higher beam currents on target for more rapid data acquisition, enabling the performance of this work at the neutron microbeam endstation. Samples from both sacrificed animals and laboratory constructs on artificial scaffolds are being measured. The design of the artificial scaffolds could lead to the ability to grow bone and cartilage replacements in the laboratory from a patient's own stem cells for joint reconstruction and repair.

Dr. Carabe-Fernandez of the University of Pennsylvania is developing silicon 3D radiation microsensor arrays, capable of quantifying deposited energies within micron-sized targets. Compared to traditional tissue equivalent proportional counters, these detectors do not require a gas supply, operate at low voltages, are light and easily portable, and have a fast response. The goal of this project is to use the targeting

ability of the microbeam to characterize individual microsensors within the microdosimeter array. Different microdosimeters of different dimensions (diameter, depth and pitch) representing different cell types, will be exposed and the derived relative biological effectiveness (RBE) from mechanistic biophysical models (e.g. MKM and LEM) will be calculated. The experimental RBE obtained from clonogenic assays of individual cells exposed to the microbeam will also be obtained and compared to that obtained from the microsensors. This will allow: 1) characterization of the microdosimetric properties of each individual microsensor as well as study crosstalk between the sensors in an array; 2) validation of the microsensors as viable instruments to calculate RBE; 3) determination of new features required to develop current microsensor technology to a new generation that allows more precise RBE measurements.

Dr. John Ng has expanded his work significantly with the help of the RARAF staff. Building on his significant experience in clinical cancer treatment, he is heading a project looking for immune response signals from cells after irradiation using particles of different LET. The hope is to determine effects of targeted radiotherapy with specifically chosen particle energies that can be combined with immunotherapy to increase the efficacy of both for the treatment of many types of cancers. This study has focused on a mammary tumor cell line that was developed at Cornell University for the study of the immune response. The study monitors the relocation of calreticulin from the ER to the cell membrane and the release of HMGB-1 and ATP into the intercellular matrix/media. These three responses are indicative of immunogenic cell death – a radiation-induced response that activates the immune system. The experiment makes use of the RARAF track segment irradiator as a source for particles of different LETs (from 10 to 160 keV/μm). Studies this year explored the higher end of the LET range (65-160 keV/μm). The results are promising in that they show a peaked response in all three assays at ~110 keV/μm. We are in the process of confirming these results, and we look forward to further exploring low LETs (10, 25 and 40 keV/μm), and expanding these studies to other cancer as well as normal tissue cell lines.

Dr. Francesco d'Errico from the Dept. of Physics at Yale University has developed a technique for neutron spectroscopy based on measurements of bubble formation in superheated emulsions. Dr. d'Errico performed extensive studies of the response of these detectors as a function of emulsion temperature and neutron energy. The preliminary data obtained was used in several applications for further funding and Dr. d'Errico expects to return in 2018.

Dr. Joel Greenberger from the University of Pittsburgh has initiated mouse irradiation studies with our IND spectrum irradiator to test radiation injury mitigator drugs he has developed through their U19 CMCR project. This is a long-term project in collaboration with the Columbia

CMCR, which will run through the next year looking at LD_{50/30} changes with respect to drug application.

Development of Facilities

Development continued on a number of our irradiation facilities and capabilities for imaging and irradiating biological specimens:

- Focused particle microbeams
- CINF
- FLASH irradiation platform
- Advanced imaging systems
- Targeting and manipulation of cells
- New cell analysis tools
- Small animal systems

Focused particle microbeams

The Super Microbeam Phase 1 construction was completed last year. The current beam size is 3.5 μm with further alignment optimization underway. While not the ultimate beam size for the Phase 1 (250 nm), this beam spot size has allowed the recommencement of microbeam operations at the Super Microbeam endstation. The ultimate size of the beam for Phase 1 will be 250 nm, which we hope to achieve early in 2018. Phase 2 will be undertaken in the fall of 2018 with the reinstallation of the electrostatic double lens as the first focusing element.

During the redevelopment of our electrostatic/Super Microbeam system, the permanent magnet microbeam (PMM) was used as our primary charged particle microbeam. This system is also the microbeam endstation for the development of our Flow and Shoot (FAST) microfluidics irradiation system, the capillary electrophoresis (CE) system, and the automated cell picking system. The PMM has all of the irradiation capabilities of the electrostatic microbeam except the sub-micron beam spot size. The PMM also does not have the electrical breakdown potential from failures of the vacuum window making it an ideal initial testbed for all our new technologies.

Columbia IND-Spectrum Neutron Facility (CINF)

CINF was completed in 2014 and has been extensively used since. This year saw the irradiation of mice, fresh whole blood samples, and plated cell lines

The fast neutron irradiation source was designed to generate the neutron spectrum observed from the “Little Boy” atomic bomb at Hiroshima at 1.5 km from ground zero. This field is generated through the reactions ${}^9\text{Be}(d,n){}^{10}\text{B}$ and ${}^9\text{Be}(p,n){}^9\text{B}$ using a mixed beam of monoatomic, diatomic and triatomic protons and deuterons. The RARAF Singletron uses a gas mixture of hydrogen to deuterium of 1:2, which feeds into the RF plasma ion source. This irradiator is on the 0° beam line, as any bending of the beam to get to a target would separate the 6 different beams and prevent spectrum generation.

The neutron spectrum was verified using two proton recoil detection systems, 2"-diameter 2"-thick liquid scintillator for energies >1 MeV and a 1.5"-diameter spherical gas proportional counter with 3 atmospheres of hydrogen gas for <1 MeV. Using MCNPX-PoliMi Monte Carlo simulations to calculate the exact response functions of the detectors, it is possible to reconstruct the spectrum from the readout of the detectors in the neutron field.

The base irradiation dose rate has been calibrated to deliver a dose rate of up to 2 Gy/h (with an additional gamma-ray contribution of 18%).

FLASH irradiation platform

The FLASH irradiation platform is designed for ultra-high dose rate particle irradiations. The proton beam from the accelerator is rapidly switched on and off by sweeping it across the beam window aperture. By precise control of the beam current and timing of the beam sweep, we have tested dose rates from 2 Gy/min up to more than 1000 Gy/sec, delivering a full range of therapeutically relevant doses to samples confirmed through film dosimetry measurements.

This year we verified the dosimetry, cellular survival curves demonstrating delivered dose effects, and conducted preliminary work for tissue models and live animal (mouse) models.

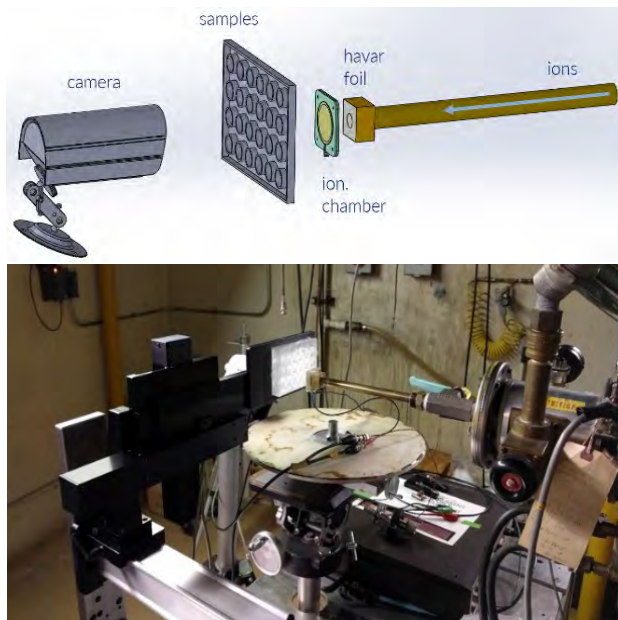


Figure 1. Schematic layout of the FLASH irradiator (top) and photo of the end station on the "cave" beamline with the FLASH setup (bottom).

Advanced imaging systems

We continue to develop new techniques to obtain two- and three-dimensional images of cells, reduce UV exposure and improve resolution.

Real-time imaging

Short-term biological effects that happen within seconds to the first few minutes after irradiation set the stage for later effects. Real-time imaging and observation of the short-term effects will give experimenters insight into their endpoints. Techniques have been developed using our EMCCD camera and our fast switching SOLA LED light source to acquire images with several frames per second to observe the short-term effects of irradiation on a timescale of minutes to hours following irradiation.

Multi-photon microscope with the UV microspot

The multi-photon microscope was developed several years ago and integrated with the charged particle microbeam irradiator. This microscope, through the long wavelength incident laser, allows in depth imaging of 3D tissues and small animals, such as *C. elegans* and zebrafish embryos. This is achieved using the sectioning capability of the multi-photon effect where the photon density increases to generate constructive interference producing a 3D voxel of half the wavelength, twice the energy photons that can locally excite fluorophores and/or other fluorescent effects (e.g. auto fluorescence and second-harmonic generation). This 3D voxel is then scanned through a single layer and stepped through the sample using the nanoprecision z-stage, generating a stack of 3D slices of the sample that are reconstructed into 3D images.

If the intensity of the laser is increased, at the area of constructive interference, there can be a 3-photon interference resulting in a voxel with 1/3 of the wavelength (three times the energy) typically generating a voxel of UV light—the UV microspot. The UV microspot can be used to induce damage within a 3D target.

STED

We are developing a Stimulated Emission Depletion (STED) super resolution microscope system with optical resolution of 75 nm in combination with our super microbeam to achieve compatible imaging resolution and beam spot size. The STED system at RARAF builds on the multi-photon microscope, using it as the primary excitation laser. A second continuous wave laser is added in parallel with the multi-photon laser. Using polarization optics, the second laser projects a donut shaped point spread function around the excitation spot of the multi-photon system. With proper selection of the second laser wavelength and with sufficient intensity, the second laser will deplete the fluorescent states around the excitation spot, allowing fluorescence from the center of the donut, which will be reduced to nanometer sizes.

The STED development continues on the microbeam endstation. We are upgrading the microbeam endstation with new custom control software in preparation for the heavy ion microbeam upgrade. This upgrade includes new control software for the multi-photon microscope with integrated fast timing for the gSTED development.

This work is ongoing and we expect gSTED imaging coming soon in 2018.

Targeting and manipulation of cells

We have the capability to fabricate microfluidic devices in hard plastics, such as acrylic, and soft plastics, such as polydimethylsiloxane (PDMS). The micro-milling machine installed at RARAF has software to produce parts designed using the Solid Works computer-aided design (CAD) program. This system has been used to manufacture the single-cell dispenser and the microfluidics chips for the cell sorter and microFACS systems (described below). Several new microfluidic systems are being developed to target, manipulate and analyze cells.

Cell picker

Picking individual cells that are adhered to a microbeam irradiation dish is one of the methods to isolate and subsequently load a cell into one of the microfluidic analysis chips being developed in the P41 grant. Previously, this capability was incorporated into the Permanent Magnet Microbeam endstation as a semi-automated device, which is part of the microbeam control software and includes joystick control of robotic movements. In the past year, we have worked to improve the workflow of the cell picker. We optimized the picking conditions, including the amount of liquid on the cells, staining method, and imaging setup, as well as the general technique of locating a cell, dispensing trypsin and then aspirating a single cell. We are currently working on improving our picking speed and the efficiency of picking a single cell.

Cell dispenser

Development of the single cell dispenser has continued with a focus on improving electrical signal quality and testing a complete system with cells. We have improved the electrical signal quality, which is used to detect when a cell is passing over the microelectrodes within the device, by making the connection to the electrode more mechanically robust. This robust connection reduces the noise and makes triggering off of a cell detection event easier. Testing of the dispenser system has moved from using beads to using cells in suspension. To extend the period we could test cells without them losing shape (due to their death since they are out of an incubator), we began work with chemically fixed suspended cells. We also applied a crystal violet dye to the fixed cells to enable us to view them easily both within the microfluidic device and within a dispensed droplet. We continue testing the complete system and are evaluating the ability of the system to eject a single cell autonomously.

MicroFACS

We have continued development of the microfluidic Fluorescence-Activated Cells Sorting (microFACS) system to combine flow cytometry and sorting with our

other microfluidic irradiation and dispensing technologies.

The microFACS system uses Dean vortex drift flow focusing to entrain the samples into a sheath flow focused column for flow cytometry detection in the main channel. The sample is illuminated with a laser through fiber optic coupling with the fluorescent output also detected through fiber optic coupling. The combination of fiber optics and microfluidics will allow the microFACS to be coupled to the other microfluidic systems, in close proximity to the microbeam endstations.

AMOEBa

The Automated Microbeam Observation Environment for Biological Analysis (AMOEBa) system allows for long term experiments where cells can be exposed using the microbeam and continuously observed for over 36 hours. The system, which typically monitors and controls temperature, pH, and humidity on a microbeam endstation, is a modular configuration that can be adjusted for any number of experimental conditions. The system is run through custom software that can monitor multiple inputs simultaneously and make appropriate changes to control the environment. Investigators who wish to use the AMOEBa for their microbeam experiments can work with the RARAF team to configure the AMOEBa for their needs.

The microAMOEBa is similar to the AMOEBa, which has been designed to work around the existing microbeam irradiation protocol, because it also has the goal of carefully controlling the environment during a microbeam experiment. The microAMOEBa is unique because it aims to specifically control the microenvironment around cells with the added goal of enabling faster changes of controlled parameters than would be possible with the AMOEBa, because of the significantly reduced control volume. The microAMOEBa is designed to operate using the same control software and modules as the AMOEBa system, while the sensors and actuators for the system are made within a microfluidic system. We construct the microAMOEBa using a silicon substrate, which can contain all necessary electrical connections and a thin window to allow the microbeam to reach the cells, and an attached microfluidic structure made of PDMS. The PDMS not only acts as the cell culture chamber but it also allows for control of the dissolved oxygen through controlled diffusive transport.

New cell analysis tools

CE-LIF

We have finished construction and begun testing of our Capillary Electrophoresis – Laser Induced Fluorescence (CE-LIF) system to provide our users with the capability of measuring reactive oxygen species within individual cells immediately after irradiation. The nanoliter input volumes makes this system ideal for single-cell, small-scale biochemical analysis.

The CE-LIF system at RARAF: The grounded end of a 50 μm bore capillary is brought to the cell using the semi-automated cell picker. Once a cell is aspirated into the capillary, 20-30 kV is applied between the grounded end of the capillary and the Laser Induced Fluorescence (LIF) system, enclosed in a light tight insulating box. This results in two superimposed flow modalities experienced by the analytes: (1) Electrophoretic flow, responsible for separating the analytes by charge and Stokes radius; (2) Electroosmotic flow, which drives the buffer and analytes (regardless of polarity) toward the detector. The electroosmotic flow is much stronger than the electrophoretic flow, ensuring that all analytes will reach the detector. In the LIF system, the analytes are hydrodynamically focused into the path of a laser, with the light collected perpendicularly and detected by a high-sensitivity spectrometer. We have recently acquired a deep cooled Bayspec spectrometer, providing highly sensitive detection of fluorescent molecules.

Small animal systems

Mouse Ear Irradiation

Investigations of radiation-induced bystander effects have been conducted in cell cultures and 3-D systems *in vitro*. The next logical step was to develop and implement microbeam irradiation protocols to study effects in living organisms. We have developed a mouse ear model for *in vivo* bystander studies. With an average thickness of 250-300 μm , this model can be used to investigate radiation-induced bystander effects with a 3-MeV proton microbeam having a range of 134 μm .

Using gentle suction, the ear of an anesthetized mouse is flattened onto the underside of a flat plate of a custom-made holder. The flattened mouse ear is then placed over the microbeam port and cells along a line of the ear are irradiated with the proton microbeam. At chosen times after irradiation, mice are sacrificed and a punch of the ear is collected. Tissues are then fixed, paraffin-embedded and cut in 5- μm sections perpendicularly to the direction of the line of irradiation. The sections are then analyzed for biological endpoints (i.e., formation of repair protein foci, apoptosis) as a function of the distance from the irradiated line.

Mouse Phantom

The anatomically accurate mouse phantoms continue to be used in various capacities around the CRR. A crucial development in the past year has been comparison of the mouse phantom performance in a sample irradiation with a computer model of the same radiation. Two common irradiation protocols performed in the CRR, both using the Small Animal Radiation Research Platform (SARRP), were used to compare modeling with the physical phantom: a lung irradiation using the 3 mm square collimator and an abdominal irradiation using a 5 mm square collimator. The physical models were tested using radiochromic film strategically placed within the phantoms. The computer simulation was performed in MCNP and included the phantom as well as the SARRP.

A comparison of the resulting radiation dose map, specifically in regions of very low dose outside of the target region, showed very good agreement between the physical models and the simulation. These results confirmed that this unique phantom is a good tool to accurately assess dose distribution.

The mouse phantoms were also used to help assess neutron dosimetry for projects in our Center for Medical Countermeasures against Radiation (CMCR). The phantoms were loaded into the exact positions used to irradiate mice in this experiment, thus allowing us to confirm that a uniform dose was received through the body of each mouse while it was rotated around the neutron source.

Singletron Utilization and Operation

Table II summarizes accelerator usage for the past year. The nominal Singletron availability is one 8-hour shift per weekday (~248 days per year); however, the accelerator is frequently run well into the evening, often on weekends, and occasionally 24 hours a day for experiments or development. Accelerator usage for online experiments and development was 51% of nominal day shifts. The off-line development, which did not require the accelerator while occupying the facility operations, used 83% of the nominal facility time. Combined with our maintenance and safety system operations, 151% of effective day shifts were utilized in 2017.

Accelerator use for radiobiology and associated dosimetry was about 85% that for last year and slightly below the average of the last 5 years. About 76% of the use for all experiments was for track segment irradiations, 5% for charged particle microbeam irradiations, and 19% for neutron irradiations. Approximately 84% of the experiment time was for studies proposed by external users, and 16% was for internal users.

On-line facility development and testing was about 24.5% of the available time, primarily for development and testing of the Super Microbeam solenoid focusing system, development of the FLASH irradiation platform, and dosimetry calibration amongst our different

Table II. Accelerator Use, January 1 - December 31, 2017
Normally Scheduled Shifts

Radiobiology and associated dosimetry	23%
Radiological physics and chemistry	3.5%
On-line facility development and testing	24.5%
Safety system	4.5%
Accelerator-related repairs/maintenance	10%
Other repairs and maintenance	2.5%
Off-line facility development	83%

irradiation platforms through film irradiations. There was also significant time dedicated to the multiple microfluidic and analysis tools using the PMM endstation. This is about average for the last five years and slightly more than last year.

The accelerator was opened twice in 2017, primarily for ion source replacements. The opportunity was also taken for general accelerator maintenance of diode replacement in the charging system, verification of the electrical generation systems, and measurements for the DREEBIT Heavy Ion Source installation. These openings typically take 5 days but were extended this year as needed for the other projects.

DREEBIT Heavy Ion Source

The DREEBIT Heavy Ion Source development is ongoing. The DREEBIT has been extensively tested this year using an off-line test bed. We reconfirmed the factory tests and made slight improvements that will facilitate the installation in the Singletron, in particular, the ultra-high vacuum needs of the EBIT system. We anticipate the mechanical installation testing of the DREEBIT in the summer of 2018, with the complete installation and operations in the Fall and Winter of 2018.

Training

REU

Since 2004, we have participated in the Research Experiences for Undergraduates (REU) project in collaboration with the Columbia University Physics Department. This is a very selective program that attracts highly talented participants. For 9-10 weeks during the summer, each student attends lectures by members of different research groups at Nevis Laboratories, works on a research project, and presents oral and written reports on his or her progress at the end of the program. Among other activities, the students receive a seminar about and take a tour of RARAF.

The 2017 REU participant at RARAF was Sabrina Campelo from Elon University. Sabrina worked with Andrew Harken on the development of the gSTED super resolution imaging system. The 10-week program involved the initial testing of the high-speed detection and measurement system for the gSTED. This included the reprogramming of the time-correlated single photon counting (TCSPC) card to work with our photomultiplier outputs and interfacing with our multiphoton microscopy system – the excitation beam for our STED system. Sabrina was instrumental in the development of the TCSPC system for the gSTED. She presented her work at the REU seminar at the end of the summer and wrote a report about it.

Group Training

In addition to training individuals at RARAF, staff members also participate in training courses presented at other facilities as a means of introducing microbeam concepts and experiments to a broader audience. This

year, Andrew Harken lectured on “High/low LET microbeams” at the NASA Space Radiation Summer School, Brookhaven National Laboratory, Upton, NY, on June 20, 2017. Manuela Buonanno was the chair of the Experimental Methods Section for the NASA Summer School coordinating all the experiments for students.

Microbeam Training Course

The sixth RARAF microbeam training course “Single-Cell Microbeams: Theory and Practice” was given May 22-26, 2017. There were eight students participating, listed in Table III. Dr. Marcelo Vazquez returned as the director of the Microbeam Training Course.

The Course was adjusted to a 5-day schedule this year. The expansion from 3 days led to a more relaxed atmosphere, more time for the students and instructors to interact, and the students had more time to work in the lab and on their beam-time proposals. The course generally followed the same pattern of technical lectures on Day 1, experimental lab sections on Day 2, further lectures on expanded topics on Day 3 with biology experiment tracking, final biology analysis and beam time proposal work on Day 4, and Day 5 was the final proposal reports and discussions. The expansion to 5 days was given a positive review by students and faculty.

A main feature of the course is the experimental design done by each of the students as if they were proposing to come to RARAF to do an experiment. The students work with the RARAF staff to devise potential experiments and then present these proposals at the end of Day 5 as a final demonstration of what they have learned from the course about the nature of microbeams and their potential applications.

Dissemination

Web site

The RARAF website design that was created in 2013 provides clear and effective presentation while improving access to content. Functional menus (including a home page rotating-picture menu) were designed to make navigation through the content easy and interesting, with a hierarchical structure from general information, suitable for a general or non-science audience, to more-detailed technical content.

The site contains information on microbeams in general, as well as detailed technical information on our various microbeams; *in-vitro* and *in-vivo* endpoints that we use; details of available on-line and off-line imaging capabilities; microfluidic systems we are developing; other charged particle and neutron irradiation facilities available at RARAF; our on-line training course materials; publications lists; information on RARAF contacts and directions to the facility. The site is periodically updated to include new radiation facilities, cell handling and analysis capabilities, publications and other information.

Table III. Students for the sixth RARAF Microbeam Training Course.

<i>Name</i>	<i>Position</i>	<i>Affiliation</i>
<i>Sofia Barbieri</i>	Ph.D. Student	University of Pavia, Italy
<i>Pavel Blaha</i>	Ph.D. Student	Czech Technical Universtiy, Czech Republic
<i>Brian Canter</i>	Ph.D. Student	Rutgers University
<i>Kadeshia Earl</i>	M.D./Ph.D. Student	Texas Southern University
<i>Sunny Narayanan</i>	Ph.D. Student	Texas A&M University, Health Science Center
<i>Anna Michaelidesova</i>	Ph.D. Student	Nuclear Physics Institute, ASCR, Czech Republic
<i>Federico Picollo</i>	Professor of Physics	University of Turin, Italy
<i>Emiliano Pozzi</i>	Researcher	CNEA, Argentina

Virtual training course

We have developed an on-line virtual microbeam training course, based on the three-day microbeam training courses. This on-line course was designed to give interested physicists and biologists who could not attend in person a thorough introduction to microbeam technology.

The goal of the online course, as for the face-to-face course, is to facilitate a better understanding of how microbeams work, what experiments can be performed using a microbeam, why these experiments are of biological interest, and how to design / perform these experiments.

The on-line material curriculum consists of audio podcasts and the same handouts that the face-to-face students received. The audio of each podcast is synched with the accompanying PowerPoint slides (viewable on a video iPod, tablet, PC or Mac, or smart phone), as well as a PDF version of the slides. High-resolution video (720p, with audio) was also used to document demonstrations of all aspects of a microbeam experiment, from making microbeam dishes to irradiating cells and performing online analyses. After extensive editing, this resulted in about 4½ hours of video footage. Additional material is added to the on-line course for new course presentations or lecturers.

The on-line training course can be accessed through the RARAF website (www.RARAF.org) and YouTube channel (<http://www.youtube.com/user/RARAFcourses>). The videos can be viewed on any Internet-enabled device supporting YouTube format.

Tours

In addition to training students, tours of the Facility provide a general introduction to the research performed at RARAF and the irradiation facilities that are available. This year we gave tours to more than 30 scientists, students, and members of the public.

As an example, high school seniors who had been offered priority admission to Columbia as physics majors,

some of whom were Columbia I. I. Rabi Scholarship winners, toured RARAF in April along with Dr. John Parsons from the Physics Department at Nevis Labs.

Personnel

The Director of RARAF is Dr. David Brenner, the Director of the Center for Radiological Research (CRR). The accelerator facility is daily managed and operated by Dr. Gerhard Randers-Pehrson and Dr. Guy Garty, the Co-Associate Directors of RARAF.

Dr. Charles Geard, a Senior Biologist Emeritus, continues to visit RARAF frequently lending his considerable expertise.

Dr. Gerhard Randers-Pehrson, a Senior Research Scientist and Chief Physicist, is directly involved in the operations and new developments of RARAF. He lends his considerable expertise to all of the ongoing projects at RARAF.

Dr. Brian Ponnaiya, a Research Scientist, is the biology advisor for RARAF. He collaborates with many of the external users and coordinates with the CRR, where he spends about half his time.

Dr. Guy Garty, an Associate Professor, developed the Flow and Shoot (FAST) system and is developing the CE-LIF system. He spends about half his time working on the CRR Center for Medical Countermeasures against Radiation, for which he is the director of the Irradiation Core.

Dr. Andrew Harken, an Associate Research Scientist, is responsible for the Super Microbeam development with STED imaging. He is also the project leader on the microFACS system.

Dr. Manuela Buonanno, an Associate Research Scientist in radiation biology, collaborates with many external users and performs assays for the mouse ear microbeam irradiations.

Dr. David Welch, an Associate Research Scientist, is responsible for the development of new microfluidic tools and interfaces for microfluidic irradiation tools. His

expertise in microfluidics has been of considerable assistance in the development of our microfluidics applications.

Dr. Veljko Grilj, a Postdoctoral Research Scientist, is responsible for assisting Dr. Harken with the Super Microbeam development. He is also responsible for working with Drs. Ponnaiya and Buonanno operating the accelerator for outside user experiments.

Dr. Christian Siebenwirth, a Postdoctoral Research Scientist, is responsible for the DREEBIT Heavy Ion Source accelerator development project.

Dr. Malek Haj Tahar, a Postdoctoral Research Scientist, is responsible for assisting the modeling of

RARAF ion beam systems. He will be taking the lead in the new development of a small animal irradiation therapy system as a potential future direction.

Ms. Sofia Barbieri, a Ph.D. Candidate at the University of Pavia in Italy, has joined us for a year and will be working on the microFACS project computer programming and user interface. She will also continue her Ph.D. work looking at H2AX focus formation with respect to particle LET.

Mr. Dennis Farrell has joined the RARAF staff on a part time basis. He is performing microbeam irradiations, serving as the Radiation Safety Officer and providing management support for the RARAF staff.

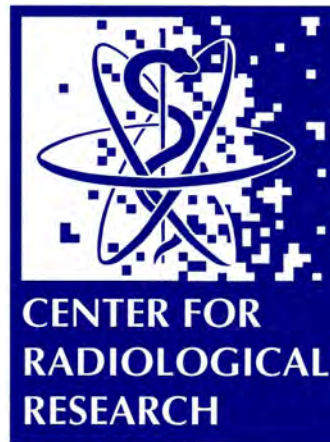


(l to r): Christian Siebenwirth, Andrew Harken, Guy Garty, and Veljko Grilj during an accelerator opening.



Two views of the open Singletron accelerator (above and right).

PUBLICATIONS



Publications

- Broustas CG, Xu Y, Harken AD, Chowdhury M, Garty G and Amundson SA (2017) Impact of Neutron Exposure on Global Gene Expression in a Human Peripheral Blood Model. *Radiat Res* **187**: 433-440.
- Broustas CG, Xu Y, Harken AD, Garty G and Amundson SA (2017) Comparison of gene expression response to neutron and x-ray irradiation using mouse blood. *BMC Genomics* **18**: 2. PMID: PMC5210311.
- Buonanno M, Ponnaiya B, Welch D, Stanislauskas M, Randers-Pehrson G, Smilenov L, Lowy FD, Owens DM and Brenner DJ (2017) Germicidal Efficacy and Mammalian Skin Safety of 222-nm UV Light. *Radiat Res* **187**: 483-491. PMID: PMC5552051.
- England MJ, Bigelow AW, Merchant MJ, Velliou E, Welch D, Brenner DJ and Kirkby KJ (2017) Automated microbeam observation environment for biological analysis—Custom portable environmental control applied to a vertical microbeam system. *Sensors and Actuators B* **239**: 1134-1143.
- Garty G, Xu Y, Elliston C, Marino SA, Randers-Pehrson G and Brenner DJ (2017) Mice and the A-Bomb: Irradiation Systems for Realistic Exposure Scenarios. *Radiat Res* **187**: 465-475. PMID: PMC5525049.
- Hall EJ (2017) 100 Years of Radiation Research in the Footsteps of Failla. *Radiat Res* **187**: 406-412.
- Hei TK and Amundson SA (2017) Preface from the Guest Editors. *Radiat Res* **187**: 405.
- Holmes JA, Chera BS, Brenner DJ, Shuryak I, Wilson AK, Lehman-Davis M, Fried DV, Somasundaram V, Lian J, Cullip T and Marks LB (2017) Estimating the excess lifetime risk of radiation induced secondary malignancy (SMN) in pediatric patients treated with craniospinal irradiation (CSI): Conventional radiation therapy versus helical intensity modulated radiation therapy. *Pract Radiat Oncol* **7**: 35-41.
- Ivanidze J, Charalel RA, Shuryak I, Brenner D, Pandya A, Kallas ON, Kesavabhotla K, Segal AZ, Simon MS and Sanelli PC (2017) Effects of Radiation Exposure on the Cost-Effectiveness of CT Angiography and Perfusion Imaging in Aneurysmal Subarachnoid Hemorrhage. *AJNR Am J Neuroradiol* **38**: 462-468.
- Ivanov VN, Wu J and Hei TK (2017) Regulation of human glioblastoma cell death by combined treatment of cannabidiol, γ -radiation and small molecule inhibitors of cell signaling pathways. *Oncotarget* **8**: 74068-74095. PMID: PMC5650324.
- Kleiman NJ, Stewart FA and Hall EJ (2017) Modifiers of radiation effects in the eye. *Life Sci Space Res (Amst)* **15**: 43-54.
- Jiang M, Li H, Zhang Y, Yang Y, Lu R, Liu K, Lin S, Lan X, Wang H, Wu H, Zhu J, Zhou Z, Xu J, Lee DK, Zhang L, Lee YC, Yuan J, Abrams JA, Wang TC, Sepulveda AR, Wu Q, Chen H, Sun X, She J, Chen X, Que J. (2017) Transitional basal cells at the squamous-columnar junction generate Barrett's oesophagus. *Nature* **550(7677)**: 529-533.
- Kramer R, Cassola VF, Andrade ME, de Araújo MW, Brenner DJ and Khoury HJ (2017) Mathematical modelling of scanner-specific bowtie filters for Monte Carlo CT dosimetry. *Phys Med Biol* **62**: 781-809.
- Laiakis EC, Wang YW, Young EF, Harken AD, Xu Y, Smilenov L, Garty GY, Brenner DJ and Fornace AJ (2017) Metabolic Dysregulation after Neutron Exposures Expected from an Improvised Nuclear Device. *Radiat Res* **188**: 21-34. PMID: PMC5714588.
- Li X, Gao M, Choi JM, Kim BJ, Zhou MT, Chen Z, Jain AN, Jung SY, Yuan J, Wang W, Wang Y and Chen J (2017) Clustered, Regularly Interspaced Short Palindromic Repeats (CRISPR)/Cas9-coupled Affinity Purification/Mass Spectrometry Analysis Revealed a Novel Role of Neurofibromin in mTOR Signaling. *Mol Cell Proteomics* **16**: 594-607. PMID: PMC5383781.
- Liao W, Hei TK and Cheng SK (2017) Radiation-Induced Dermatitis is Mediated by IL17-Expressing $\gamma\delta$ T Cells. *Radiat Res* **187**: 454-464. PMID: PMC5524538.
- Lieberman HB, Panigrahi SK, Hopkins KM, Wang L and Broustas CG (2017) p53 and RAD9, the DNA Damage Response, and Regulation of Transcription Networks. *Radiat Res* **187**: 424-432.
- Pacelli C, Bryan RA, Onofri S, Selbmann L, Shuryak I and Dadachova E (2017) Melanin is effective in protecting fast and slow growing fungi from various types of ionizing radiation. *Environ Microbiol* **19**: 1612-1624.
- Pacelli C, Selbmann L, Zucconi L, Raguse M, Moeller R, Shuryak I and Onofri S (2017) Survival, DNA Integrity, and Ultrastructural Damage in Antarctic Cryptoendolithic Eukaryotic Microorganisms Exposed to Ionizing Radiation. *Astrobiology* **17**: 126-135. PMID: PMC5314979.
- Park JG, Paul S, Briones N, Zeng J, Gillis K, Wallstrom G, LaBaer J and Amundson SA (2017) Developing Human Radiation Biodosimetry Models: Testing Cross-Species Conversion Approaches Using an Ex Vivo Model System. *Radiat Res* **187**: 708-721.
- Miller AC, Gilstad J and Brenner DJ (2017) Military Global Health Engagement and Low-Dose Ionizing Radiation. *Mil Med* **182**: 1677-1679.
- Nagel ZD, Engelward BP, Brenner DJ, Begley TJ, Sobol RW, Bielas JH, Stambrook PJ, Wei Q, Hu JJ, Terry MB, Dilworth C, McAllister KA, Reinlib L, Worth L

- and Shaughnessy DT (2017) Towards precision prevention: Technologies for identifying healthy individuals with high risk of disease. *Mutat Res* **800-802**: 14-28.
- Park JG, Paul S, Briones N, Zeng J, Gillis K, Wallstrom G, LaBaer J and Amundson SA (2017) Developing Human Radiation Biodosimetry Models: Testing Cross-Species Conversion Approaches Using an Ex Vivo Model System. *Radiat Res* **187**: 708-721.
- Pei H, Zhang J, Nie J, Ding N, Hu W, Hua J, Hirayama R, Furusawa Y, Liu C, Li B, Hei TK and Zhou G (2017) RAC2-P38 MAPK-dependent NADPH oxidase activity is associated with the resistance of quiescent cells to ionizing radiation. *Cell Cycle* **16**: 113-122. PMC5270549.
- Repin M, Pampou S, Karan C, Brenner DJ and Garty G (2017) RABiT-II: Implementation of a High-Throughput Micronucleus Biodosimetry Assay on Commercial Biotech Robotic Systems. *Radiat Res* **187**: 492-498.
- Sharma A, Gaidamakova EK, Grichenko O, Matrosova VY, Hoeke V, Klimenkova P, Conze IH, Volpe RP, Tkavc R, Gostinčar C, Gunde-Cimerman N, DiRuggiero J, Shuryak I, Ozarowski A, Hoffman BM and Daly MJ (2017) Across the tree of life, radiation resistance is governed by antioxidant Mn. *Proc Natl Acad Sci U S A* **114**: E9253-E9260. PMC5676931.
- Shuryak I (2017) Advantages of Synthetic Noise and Machine Learning for Analyzing Radioecological Data Sets. *PLoS One* **12**: e0170007. PMC5222373.
- Shuryak I (2017) Quantitative modeling of responses to chronic ionizing radiation exposure using targeted and non-targeted effects. *PLoS One* **12**: e0176476. PMC5404850.
- Shuryak I, Fornace AJ, Datta K, Suman S, Kumar S, Sachs RK and Brenner DJ (2017) Scaling Human Cancer Risks from Low LET to High LET when Dose-Effect Relationships are Complex. *Radiat Res* **187**: 476-482.
- Shuryak I, Loucas BD and Cornforth MN (2017) Seeking Beta: Experimental Considerations and Theoretical Implications Regarding the Detection of Curvature in Dose-Response Relationships for Chromosome Aberrations. *Radiat Res* **187**: 7-19.
- Shuryak I, Loucas BD and Cornforth MN (2017) Straightening Beta: Overdispersion of Lethal Chromosome Aberrations following Radiotherapeutic Doses Leads to Terminal Linearity in the Alpha-Beta Model. *Front Oncol* **7**: 318. PMC5742594.
- Shuryak I, Matrosova VY, Gaidamakova EK, Tkavc R, Grichenko O, Klimenkova P, Volpe RP and Daly MJ (2017) Microbial cells can cooperate to resist high-level chronic ionizing radiation. *PLoS One* **12**: e0189261. PMC5738026.
- Vandermolen J, Einstein A, Shuryak I, Balter S, Meulepas J, King R, Mehta N, Brenner DJ, Gehi A. (2017) Estimating cancer risk associated with ionizing radiation exposure during atrial fibrillation ablation. *J Amer Coll Cardiol* **69(11)**: 502.
- Wang X, Liu Y, Wang J, Nie Y, Chen S, Hei TK, Deng Z, Wu L, Zhao G, Xu, A (2017) Amplification of arsenic genotoxicity by TiO₂ nanoparticles in mammalian cells: new insight from physicochemical interaction and mitochondria. *Nanotoxicology* **11(8)**: 978-995.
- Welch D, Randers-Pehrson G, Spotnitz HM and Brenner DJ (2017) UNLAMINATED GAFCHROMIC EBT3 FILM FOR ULTRAVIOLET RADIATION MONITORING. *Radiat Prot Dosimetry* **176**: 341-346.
- Welch D, Spotnitz HM and Brenner DJ (2017) Measurement of UV Emission from a Diffusing Optical Fiber Using Radiochromic Film. *Photochem Photobiol* **93**: 1509-1512.
- Welch D, Turner L, Speiser M, Randers-Pehrson G and Brenner DJ (2017) Scattered Dose Calculations and Measurements in a Life-Like Mouse Phantom. *Radiat Res* **187**: 433-442. PMC5525046.
- Wu CC, Chaudhary KR, Na YH, Welch D, Black PJ, Sonabend AM, Canoll P, Saenger YM, Wang TJC, Wu CS, Hei TK and Cheng SK (2017) Quality Assessment of Stereotactic Radiosurgery of a Melanoma Brain Metastases Model Using a Mouselike Phantom and the Small Animal Radiation Research Platform. *Int J Radiat Oncol Biol Phys* **99**: 191-201. PMC5675116.
- Wu J, Zhang Q, Wu YR, Zou S and Hei TK (2017) Cytoplasmic Irradiation Induces Metabolic Shift in Human Small Airway Epithelial Cells via Activation of Pim-1 Kinase. *Radiat Res* **187**: 441-453. PMC5539528.
- Wu J and Hei TK (2017) Focus small to find big - the microbeam story. *Int J Radiat Biol*, DOI: 10.1080/09553002.2017.1364801.
- Wu J, Zhang B, Wu YR, Davidson MM and Hei TK (2017) Targeted cytoplasmic irradiation and autophagy. *Mutat Res* **806**: 88-97. PMC5581273. ■



*David Brenner presenting at the TED2017 conference in Vancouver, BC.
Photo: Bret Hartman / TED reproduced under Creative Commons License CC BY-NC 2.0*